

**EFFECTS OF NANOPARTICLES ON RHEOLOGICAL AND FLUID
LOSS CONTROL PROPERTIES OF NON DAMAGING DRILLING
FLUID**

A Thesis submitted to the
University of Petroleum and Energy Studies

For the Award of
Doctor of Philosophy
in
Petroleum Engineering

By
Srawanti Medhi

March 2020

SUPERVISOR(s)
Dr. Dharmendra Kumar Gupta
Dr. Jitendra S. Sangwai



Department of Petroleum Engineering & Earth Sciences
School of Engineering
University of Petroleum and Energy Studies
Dehradun-248007: Uttarakhand

**EFFECTS OF NANOPARTICLES ON RHEOLOGICAL AND FLUID
LOSS CONTROL PROPERTIES OF NON DAMAGING DRILLING
FLUID**

A Thesis submitted to the
University of Petroleum and Energy Studies

For the Award of
Doctor of Philosophy
in
Petroleum Engineering

By
Srawanti Medhi
(SAP ID 500057318)

March 2020

Internal Supervisor
Dr. Dharmendra Kumar Gupta
Professor
Department of Petroleum Engineering and Earth Sciences
University of Petroleum and Energy Studies

External Supervisor
Dr. Jitendra S. Sangwai
Professor
Department of Ocean Engineering
Indian Institute of Technology, Madras



Department of Petroleum Engineering & Earth Sciences
School of Engineering
University of Petroleum and Energy Studies
Dehradun-248007: Uttarakhand

March 2020
DECLARATION

I declare that the thesis entitled “Effects of Nanoparticles on Rheological and Fluid Loss Control Properties of Non Damaging Drilling Fluids” has been prepared by me under the guidance of Dr. Dharmendra Kumar Gupta, Professor of Department of Petroleum Engineering and Earth Sciences, University of Petroleum and Energy Studies and Dr. Jitendra S Sangwai, Professor of Department of Ocean Engineering, Indian Institute of Technology, Madras. No part of this thesis has formed the basis for the award of any degree or fellowship previously.



SRAWANTI MEDHI
Petroleum Engineering and Earth Sciences, School of Engineering
University of Petroleum and Energy Studies
Dehradun, Uttarakhand
Date: 05/08/2020

CERTIFICATE

I certify that Srawanti Medhi has prepared her thesis entitled “**Effects of Nanoparticles on Rheological and Fluid Loss Control Properties of Non Damaging Drilling Fluid**”, for the award of PhD degree of the University of Petroleum and Energy Studies, under my guidance. She has carried out the work at the Department of Petroleum Engineering and Earth Sciences, University of Petroleum & Energy Studies.



Internal Supervisor

Dr. DHARMENDRA KUMAR GUPTA

Professor, Department of Petroleum Engineering and Earth Sciences,
University of Petroleum and Energy Studies

Dehradun, Uttarakhand

Date: 05/08/2020



Department of Ocean Engineering
Indian Institute of Technology Madras, Chennai 600 036

DR. JITENDRA S. SANGWAI
PROFESSOR

Phone: +91-44-2257-4825; Fax: +91-44-2257-4802
jitendrasangwai@iitm.ac.in; jitendrasangwai@yahoo.com

05/08/2020

CERTIFICATE

I certify that Srawanti Medhi has prepared her thesis entitled “**Effects of Nanoparticles on Rheological and Fluid Loss Control Properties of Non Damaging Drilling Fluid**”, for the award of PhD degree of the University of Petroleum & Energy Studies, under my guidance. She has carried out the work at the Department of Petroleum Engineering and Earth Sciences, University of Petroleum & Energy Studies, Dehradun.

Thanking you.

Sincerely,

Dr. Jitendra SANGWAI
Professor
Department of Ocean Engineering
Indian Institute of Technology Madras
Chennai, 600036, India.
Phone: +91-44-2257-4825 (O); +91-9884310593 (m)

ABSTRACT

With an increase in hydrocarbon demand, exploration of oil and gas in extreme conditions has become indispensable. Drilling in these problematic zones necessitate superior drilling fluids, which possess good rheological and fluid-loss control properties and optimized hydraulics. A class of clay free, biopolymer derived drilling fluid known as non-damaging drilling fluid (NDDF) has emerged lately which tackles problems of fluid loss thereby reducing shale swelling and formation damage in the reservoir. However, the thermal stability of NDDF is uncertain as it relies on hydrogel structure of the fluid, which is susceptible to degradation even at moderate to high temperature conditions. In the last few decades, nanotechnology has brought about pronounced amelioration and reforms in day-to-day life. Nanofluids (made up of nanoparticles) find vast application in petrochemical, medicine, pharma and other allied fields. This research work investigates the effect of nanoparticles (NPs) on NDDF and aims to enhance its vital properties. The nanoparticles of interest were silicon dioxide NP, copper oxide NP, aluminium dioxide NP, in-house synthesized zirconium dioxide NP, in-house synthesized graphene oxide nanosheets (NS) and zinc oxide NP. Firstly, rheological measurements were carried out; which included steady state rotational test to evaluate viscosity and shear stress profiles; followed by dynamic oscillation test for gauging viscoelastic properties. All these tests were conducted at 30, 60 and 80 °C. Fluid loss at low pressure (100 psi) at ambient temperature were measured using an API filtrate loss apparatus. To model the fluid behaviour, Herschel Bulkley (HB) parameters were optimally determined by using genetic algorithm (GA) optimization technique. HB parameters were then incorporated in momentum

transfer equation to define various drilling fluids at different temperatures. Computational fluid dynamics (CFD) simulations were carried out by solving the mass and momentum governing equation using finite volume in Ansys FLUENT 19 R3®. Closure equations were simultaneously solved to define phase interaction between solid and liquid phase. Results were presented in terms of cutting volume fraction, percentage retention of cuttings in annular region, velocity profile to visualize flow area and pressure drop along the wellbore length to check for ease of flow. Finally, with a comparative analysis, the effect of each particle on rheological property, fluid loss and hydraulic performance of NDDF were summarized and reported.

ACKNOWLEDGEMENT

I would like to extend my heartfelt gratitude to my supervisor, Prof. D. K. Gupta, for his constant guidance through each stage of the process. His encouragement to pursue research in nanotechnology since my teaching assistantship days with him were the pillars of my work. He has always provided me with immense moral support and the freedom to move forward.

I am forever grateful to Prof. J. S. Sangwai for inspiring my interest in developing innovative technologies in the field of drilling fluids. I would like to thank him for all the relentless hours of discussion during my stay at IIT Madras. His pioneering work has been the defining path of my research.

I would like to thank Prof. S. K. Gupta for his insightful suggestions and enthusiasm throughout this journey.

I would like to extend my gratitude to my research partner, Mr. Satyajit Chowdhury, who was instrumental in ensuring proper execution and providing valuable criticism of the work. For this, I am extremely grateful. Very few are fortunate enough to have similar research interests as their life partners.

I would like to thank IDT, ONGC, Dehradun for helping me initiate preliminary laboratory experiments and providing a head-start. I would like to express my gratitude to Mr. A. K. Joshi for his valuable opinions and inputs during the early stage of my research.

I would also like to thank Dr. Kamal Bansal, Dean, SOE, UPES, Dr. J. K. Pandey, Associate Dean, R&D, UPES and Dr. Sunil Khare, HoD, Department of Petroleum

Engineering and Earth Sciences, UPES for granting me funds and facilities to carry out my work.

I would like to thank all the people whose assistance was incalculable in the completion of my PhD, especially my Rheology and CFD lab students, Mr. Aryab Mazumdar, who accompanied me in all my visits to IDT, ONGC lab and assisted me in conducting experiments while I was testing out the best suitable fluid for my research; Mr. Naman Bhatt along with Kartik Kohli who tirelessly assisted me while conducting CFD studies and Zenitha Aswal for assisting me in preparation of numerous samples of drilling fluids.

Last but not the least, I would like to acknowledge my family and friends for their never-ending support. I am indebted to my parents, D. K. Medhi and Dipali Bora Medhi for always believing in me.

TABLE OF CONTENTS

CHAPTER	CHAPTER DESCRIPTION	PAGE NO.
Chapter 1	INTRODUCTION	1 - 21
1.1.	Overview	1
1.2.	Motivation	5
1.3.	Research Objectives	6
1.4.	Research Methodology	8
1.5.	Chapter Scheme	18
Chapter 2	LITERATURE SURVEY	22 - 36
2.1	Introduction	22
2.2	Limitation of Conventional Drilling Fluid	23
2.3	Recent Progress	23
2.4	Nano Based Drilling Fluids	24
2.4.1	Effect of Metal Oxide NPs on Rheological Properties of Drilling Fluids	25
2.4.2	Effect of Carbon Nanotubes (CNT) on the Rheological Properties of Drilling Fluids	29
2.4.3	Effect of Clay NPs on the Rheological Properties of Drilling Fluids	31
2.4.4	Effect of Graphene on the Rheological Properties of Drilling Fluids	32
2.5	Computational Fluid Dynamics (CFD) Studies to Understand Solid-Liquid Hydrodynamics in Annular Region	33

2.6	Chapter Conclusion	35
Chapter 3	EFFECT OF SILICON DIOXIDE NPs (SiO₂ NP) ON NDDF	37 - 55
3.1	Synthesis of Silica (SiO ₂) NPs	37
3.2	Results and Discussions	38
3.2.1	Yield Point (YP)	38
3.2.2	Viscosity	40
3.2.3	Gel Strength	42
3.2.4	API Filtrate Loss Test Measurements	44
3.3	Determination of Optimal Herschel Bulkley (HB) Parameters by Genetic Algorithm Optimization	46
3.4	Results and Discussions on Flow Behaviour from CFD Studies in Eccentric Wellbore Annulus	48
3.4.1	Effect of SiO ₂ NPs on Cutting Volume Fraction	48
3.4.2	Effect of SiO ₂ NPs on Velocity Profile of NDDF	50
3.4.3	Effect of SiO ₂ NPs on Pressure Drop	54
3.5	Chapter Conclusion	55
Chapter 4	EFFECT OF COPPER OXIDE NPS (CuO NP) ON NDDF	56 - 71
4.1	Synthesis of Copper Oxide (CuO) NPs	56
4.2	Results and Discussions	57
4.2.1	Yield Point	57
4.2.2	Viscosity	58
4.2.3	Gel Strength	60
4.2.4	API Filtrate Loss Test Measurements	61
4.3	Determination of Optimal Herschel Bulkley (HB) Parameters by Genetic Algorithm Optimization	63
4.4	Results and Discussion on Flow Behaviour from CFD Studies in Eccentric Wellbore Annulus	64

4.4.1	Effect of CuO NP on Cutting Volume Fraction	64
4.4.2	Effect of CuO NPs on Velocity Profile of NDDF	66
4.4.3	Effect of CuO NPs on Pressure Drop	70
4.5	Chapter Conclusion	70
Chapter 5	EFFECT OF ALUMINUM OXIDE NPS (Al₂O₃ NPs) ON NDDF	72 - 89
5.1	Rheology Measurements	72
5.1.1.	Steady Shear Rotational Test Measurements	72
5.1.2.	Amplitude Sweep Test Measurements	73
5.1.3.	Frequency Sweep Test Measurement	74
5.1.4.	Time Dependent Flow Behaviour Test Measurements	77
5.1.5.	Temperature Dependent Flow Behaviour Test Measurements	79
5.1.6.	API Filtrate Loss Test Measurements	80
5.2	Determining Optimal Herschel Buckley (HB) Parameters Using Genetic Algorithm (GA)	81
5.3	Results and Discussion on Flow Behaviour from CFD Studies on Eccentric Wellbore Annulus	82
5.3.1	Effect of Al ₂ O ₃ NPs on Cutting Carrying Capacity of NDDF	83
5.3.2	Effect of Al ₂ O ₃ NPs on the Velocity Profile of NDDF	85
5.3.3	Effect of Al ₂ O ₃ NPs on Pressure Drop of NDDF	88
5.4	Chapter Conclusion	88
Chapter 6	EFFECT OF ZIRCONIUM DIOXIDE NPS (ZrO₂ NP) ON NDDF	90 - 112
6.1	Synthesis and Characterization of ZrO ₂ NPs	90
6.2	Rheology Measurements	93
6.2.1	Steady State Rotational Test Measurements	93

6.2.2	Amplitude Sweep Test Measurements	97
6.2.3	Frequency Sweep Test Measurements	99
6.2.4	Temperature Dependent Flow Behaviour Test Measurements	101
6.2.5	Time Dependent Flow Behaviour Test Measurements	102
6.2.6	API Filtrate Loss Test Measurements	103
6.3	Determining Optimal Herschel Buckley (HB) Parameters Using Genetic Algorithm (GA)	105
6.4	Results and Discussion on Flow Behaviour from CFD Studies in Eccentric Wellbore Annulus	106
6.4.1	Effect of ZrO ₂ NPs on Cutting Carrying Capacity of NDDF	106
6.4.2	Effect of ZrO ₂ NPs on the Velocity Profile of NDDF	109
6.4.3	Effect of ZrO ₂ NPs on Pressure Drop of NDDF	111
6.5	Chapter Conclusion	112
Chapter 7	EFFECT OF GRAPHENE OXIDE NANOSHEET (GO NS)	113 - 131
7.1.	Synthesis of Graphene Oxide Nanosheet	113
7.2	Characterization of GO NS	114
7.3	Rheological Measurements	115
7.3.1	Steady State Rotational Test Measurements	115
7.3.2	Amplitude Sweep Test Measurements	118
7.3.3	Frequency Sweep Test Measurements	119
7.3.4	Time Dependent Test Measurements	121
7.3.5	Temperature Dependent Test Measurements	122
7.3.6	API Filtrate Loss Test Measurements	123
7.4	Determination of Optimal Herschel Buckley (HB) Parameter by Genetic Algorithm (GA)	124

7.5	Results and Discussion on Flow Behaviour from CFD Studies in Eccentric Wellbore Annulus	125
7.5.1	Effect of GO NS on Cutting Carrying Capacity of NDDF	125
7.5.2	Effect of GO NS on The Velocity Profile of NDDF	128
7.5.3	Effect of GO NS on Pressure Drop of NDDF	130
7.6	Chapter Conclusion	131
Chapter 8	EFFECT OF ZINC OXIDE NPS (ZnO NPs) ON NDDF	132 - 149
8.1.	Rheology Measurements	132
8.1.1	Steady State Rotational Test Measurements	132
8.1.2	Amplitude Sweep Test Measurements	134
8.1.3	Frequency Sweep Test Measurements	136
8.1.4	Time Dependent Test Measurements	138
8.1.5	Temperature Dependent Test Measurements	139
8.1.6	API Filtrate Loss Test Measurements	140
8.2	Determining Optimal Herschel Buckley (HB) Parameters Using Genetic Algorithm (GA)	142
8.3	Results and Discussion on Flow Behaviour from CFD Studies in Eccentric Wellbore Annulus	143
8.3.1	Effect of ZnO NPs on Cutting Carrying Capacity of NDDF	143
8.3.2	Effect of ZnO NPs on the Velocity Profile of NDDF	145
8.3.3	Effect of ZnO NPs on Pressure Drop of NDDF	148
8.4	Chapter Conclusion	148
Chapter 9	CONCLUSION	150- 162
9.1.	Comparative Analysis of all NP based NDDF	150
9.1.1.	Comparing Steady State Rheological Test Measurements	150

9.1.2	Comparing Amplitude Sweep Test Measurements	151
9.1.3	Comparing Frequency Sweep Test Measurements	152
9.1.4	Comparing API Fluid Loss Test Measurements	155
9.1.5	Comparing Cutting Carrying Capacity	156
9.2	Conclusion	158
9.3	Scope for Future Work	160
Chapter 10	BIBLIOGRAPHY	162- 170
10.1	BIBLIOGRAPHY	162

LIST OF FIGURES

FIGURE NO.	FIGURE DESCRIPTION	PAGE NO.
Fig. 1.1	Types of drilling fluids	3
Fig. 1.2	Typical schematic of a drilling rig	5
Fig. 1.3	Layout of methodology	8
Fig. 1.4	Formulation of nano-based NDDF (NP based NDDF)	9
Fig. 1.5	Mesh Validation	16
Fig. 1.6	Details of geometry, meshing, and boundary condition details in the current study	17
Fig. 1.7	Images of different nanoparticles included in this study. (a) SiO ₂ NP (b) CuO NP (c) Al ₂ O ₃ NP (d) ZrO ₂ NP (e) GO NS (f) ZnO NP	20
Fig. 3.1	XRD of SiO ₂ NP after calcination	38
Fig. 3.2	Yield point of all the SiO ₂ NP based drilling fluids	39
Fig. 3.3	Plastic viscosity of all the SiO ₂ NP based drilling fluids	40
Fig. 3.4	Apparent viscosity of all the SiO ₂ NP based drilling fluids	41
Fig. 3.5	Gel Strength (Gel 0) of all the SiO ₂ NP based drilling fluids after a resting time of 10 secs	42

Fig. 3.6	Gel Strength (Gel 10) of all the SiO ₂ NP based drilling fluids after a resting time of 10 mins	43
Fig. 3.7	Fluid loss vs. time all the prepared drilling fluid samples	44
Fig. 3.8	Fluid loss vs. time all the prepared drilling fluid samples	45
Fig. 3.9	Comparative side view of contours for cutting volume fraction ($V_{inlet} = 0.8$ m/s, cutting density and inlet volume fraction = 2550 kg/m ³ and 10% respectively)	49
Fig. 3.10	Velocity profile at Kick-off Point (KOP) for base and 1% SiO ₂ NP NDDF at BHR and AHR conditions	51
Fig. 3.11	Velocity profile at Drop-off section (DOS) for base and 1% SiO ₂ NP NDDF at BHR and AHR conditions	52
Fig. 3.12	Velocity profile at Build-up section (BUS) for base and 1% SiO ₂ NP NDDF at BHR and AHR conditions	53
Fig. 3.13	Pressure drop of SiO ₂ NP based NDDF	54
Fig. 4.1	XRD of CuO NP	57
Fig. 4.2	Yield Point of all the prepared drilling fluid samples	57
Fig. 4.3	Plastic Viscosity of all the prepared drilling fluid samples	58
Fig. 4.4	Apparent Viscosity of all the prepared drilling fluid samples	59

Fig. 4.5	Gel Strength (Gel 0) of all the prepared drilling fluid samples	60
Fig. 4.6	Gel Strength (Gel 10) of all the prepared drilling fluid samples	60
Fig. 4.7	Fluid loss <i>vs.</i> time for all CuO NP based NDDF	61
Fig. 4.8	Fluid loss <i>vs.</i> time for all CuO NP based BBDF	62
Fig. 4.9	Comparative side view of contours for cutting volume fraction ($V_{inlet} = 0.8$ m/s, cutting density and inlet volume fraction = 2500 kg/m ³ and 8% respectively)	65
Fig. 4.10	Velocity profile at Kick-off Point (KOP) for base and 1% CuO NP NDDF at BHR and AHR conditions	67
Fig. 4.11	Velocity profile at Drop-off section (DOS) for base and 1% CuO NP NDDF at BHR and AHR conditions	68
Fig. 4.12	Velocity profile at Build-up section (BUS) for base and 1% CuO NP NDDF at BHR and AHR conditions	69
Fig. 4.13	Pressure drop for CuO based NDDF	70
Fig. 5.1	(a) Viscosity <i>vs.</i> shear rate at 30 °C, (b) Viscosity <i>vs.</i> shear rate at 60 °C, (c) Viscosity <i>vs.</i> shear rate at 80 °C. Legend: NDDF represents the base with 0 wt% Al ₂ O ₃ NP. 0.5% Al represents 0.5 wt% Al ₂ O ₃ NP NDDF and so on	72
Fig. 5.2	(a) Storage modulus (G') and loss factor <i>vs.</i> shear strain (%) at 30 °C, (b) G' and loss factor <i>vs.</i> shear strain (%) at 60 °C, (c) G' and loss factor <i>vs.</i> shear	73

	strain (%) at 80 °C. Legend: NDDF represents the base with 0 wt% Al ₂ O ₃ NP. 0.5% Al represents 0.5 wt% Al ₂ O ₃ NP NDDF and so on.	
Fig. 5.3	(a) Storage modulus (G') and Loss modulus (G'') vs. angular frequency at 30 °C, (b) G' and G'' vs. angular frequency at 60 °C, (c) G' and G'' vs. angular frequency at 80 °C. Legend: NDDF represents the base with 0 wt% Al ₂ O ₃ NP. 0.5% Al represents 0.5 wt% Al ₂ O ₃ NP NDDF and so on.	75
Fig. 5.4	(a) Complex viscosity vs. angular frequency at 30 °C, (b) Complex viscosity vs. angular frequency at 60 °C, (c) Complex viscosity vs. angular frequency at 80 °C. Legend: NDDF represents the base with 0 wt% Al ₂ O ₃ NP. 0.5% Al represents 0.5 wt% Al ₂ O ₃ NP NDDF and so on.	76
Fig. 5.5	Time dependent rotational thixotropic test for various NDDFs. Legend: NDDF represents the base with 0 wt% Al ₂ O ₃ NP. 0.5% Al represents 0.5 wt% Al ₂ O ₃ NP NDDF and so on.	77
Fig. 5.6	(a) G' , G'' and loss factor vs. temperature, (b) Viscosity and complex	79
Fig. 5.7	Filtrate loss volume vs. time for various Al ₂ O ₃ NP NDDFs. Legend: NDDF represents the base with 0 wt% Al ₂ O ₃ NP. 0.5% Al represents 0.5 wt% Al ₂ O ₃ NP NDDF and so on.	80
Fig. 5.8	Comparative side view of contours for cutting volume fraction ($V_{inlet} = 0.8$ m/s, cutting density and inlet volume fraction = 2550 kg/m ³ and 10% respectively)	83

Fig. 5.9	Velocity profile at Build-up section (BUS) for base and 1% Al ₂ O ₃ NP NDDF at 30° C and 80° C conditions	85
Fig. 5.10	Velocity profile at Drop-off section (DOS) for base and 1% Al ₂ O ₃ NP NDDF at 30° C and 80° C conditions	86
Fig. 5.11	Velocity profile at Kick-off Point (KOP) for base and 1% Al ₂ O ₃ NP NDDF at 30° C and 80° C conditions	87
Fig. 5.12	Pressure drop of Al ₂ O ₃ NP NP based NDDF	88
Fig. 6.1	SEM images of ZrO ₂ NPs produced in this study	91
Fig. 6.2	(a) XRD pattern, (b) FTIR Spectra, (c) N ₂ adsorption/desorption isotherms, (d) Pore size distribution of ZrO ₂ NPs	92
Fig. 6.3	(a) Viscosity vs. shear rate at 30 °C, (b) Viscosity vs. shear rate at 60 °C, (c) Viscosity vs. shear rate at 80 °C, (d) Viscosity vs. shear rate for NDDFs with 0 and 1 wt% ZrO ₂ NPs at 30, 60 and 80 °C. Legend: NDDF represents the base with 0 wt% ZrO ₂ NP. 0.5% represents 0.5 wt% ZrO ₂ NP NDDF and so on.	93
Fig. 6.4	(a) Shear stress vs. shear rate at 30 °C, (b) Shear stress vs. shear rate at 60 °C, (c) Shear stress vs. shear rate at 80 °C, (d) Shear stress vs. shear rate for NDDF and 1 wt% ZrO ₂ NP at 30, 60 and 80 °C. Legend: NDDF represents the base with 0 wt% ZrO ₂ NP. 0.5% represents 0.5 wt% ZrO ₂ NP NDDF and so on.	94

Fig. 6.5	Viscosity <i>vs.</i> shear stress for various NP NDDFs prepared in this study. Legend: NDDF represents the base with 0 wt% ZrO ₂ NP. 0.5% represents 0.5 wt% ZrO ₂ NP NDDF and so on.	96
Fig. 6.6	(a) Storage modulus (G') and loss factor <i>vs.</i> shear strain (%) at 30 °C, (b) G' and loss factor <i>vs.</i> shear strain (%) at 60 °C, (c) G' and loss factor <i>vs.</i> shear strain (%) at 80 °C, (d) G' <i>vs.</i> shear strain (%) for NDDF and 1 wt% ZrO ₂ NP at 30, 60 and 80. Legend: NDDF represents the base with 0 wt% ZrO ₂ NP. 0.5% represents 0.5 wt% ZrO ₂ NP NDDF and so on.	97
Fig. 6.7	(a) Storage modulus (G') and Loss modulus (G'') <i>vs.</i> angular frequency at 30 °C, (b) G' and G'' <i>vs.</i> angular frequency at 60 °C, (c) G' and G'' <i>vs.</i> angular frequency at 80 °C, (d) Complex viscosity <i>vs.</i> angular frequency at 30, 60 and 80° C. Legend: NDDF represents the base with 0 wt% ZrO ₂ NP. 0.5% represents 0.5 wt% ZrO ₂ NP NDDF and so on.	99
Fig. 6.8	(a) G' , G'' and loss factor <i>vs.</i> temperature, (b) Viscosity and complex viscosity <i>vs.</i> temperature for various NDDFs. Legend: NDDF represents the base with 0 wt% ZrO ₂ NP. 0.5% represents 0.5 wt% ZrO ₂ NP NDDF and so on.	101
Fig. 6.9	Time dependent rotational thixotropic test for various NDDFs. Legend: NDDF represents the base with 0 wt% ZrO ₂ NP. 0.5% represents 0.5 wt% ZrO ₂ NP NDDF and so on.	102
Fig. 6.10	Filtrate loss volume <i>vs.</i> time for various ZrO ₂ NP NDDFs. Legend: NDDF represents the base with 0	103

	wt% ZrO ₂ NP. 0.5% represents 0.5 wt% ZrO ₂ NP NDDF and so on.	
Fig. 6.11	Comparative side view of contours for cutting volume fraction ($V_{inlet} = 0.8$ m/s, cutting density and inlet volume fraction = 2550 kg/m ³ and 10% respectively)	107
Fig. 6.12	Velocity profile at Kick-off Point (KOP) for base and 1% ZrO ₂ NP NDDF at 30 and 80 °C conditions	109
Fig. 6.13	Velocity profile at Drop-off section (DOS) for base and 1% ZrO ₂ NP NDDF at 30 and 80 °C conditions	110
Fig. 6.14	Velocity profile at Build-up section (BUS) for base and 1% ZrO ₂ NP NDDF at 30 and 80 °C conditions	111
Fig. 6.15	Pressure drop of ZrO ₂ NP NP based NDDF	112
Fig. 7.1	(a) XRD pattern of synthesized GO NS, peak identifies at $2\theta = 12.11$ (b) TEM image of GO NS showing clear dark and light patches.	114
Fig. 7.2	(a) Viscosity vs. shear rate at 30 °C, (b) Viscosity vs. shear rate at 60 °C, (c) Viscosity vs. shear rate at 80 °C, (d) Viscosity vs. shear rate for NDDFs with 0 and 0.5 wt% NS at 30, 60 and 80 °C. Legend: NDDF represents the base with 0 wt% GO NS, 0.2% represents 0.2 wt% GO NS NDDF and so on.	115
Fig. 7.3	(a) Shear stress vs. shear rate at 30 °C, (b) Shear stress vs. shear rate at 60 °C, (c) Shear stress vs. shear rate at 80 °C, (d) Shear stress vs. shear rate for NDDF and 0.5 wt% GO NS at 30, 60 and 80 °C. Legend: NDDF represents the base with 0 wt% GO NS, 0.2% represents 0.2 wt% GO NS NDDF and so on.	117

Fig. 7.4	(a) Storage modulus (G') and loss factor <i>vs.</i> shear strain (%) at 30 °C, (b) G' and loss factor <i>vs.</i> shear strain (%) at 60 °C, (c) G' and loss factor <i>vs.</i> shear strain (%) at 80 °C. Legend: NDDF represents the base with 0 wt% GO NS, 0.2% represents 0.2 wt% GO NS NDDF and so on.	118
Fig. 7.5	(a) G' , G'' <i>vs.</i> Angular frequency at 30 °C (b) G' , G'' <i>vs.</i> Angular frequency at 60 °C (c) G' , G'' <i>vs.</i> Angular frequency at 80 °C (d) Complex viscosity <i>vs.</i> angular frequency at 30, 60 and 80 °C. Legend: NDDF represents the base with 0 wt% GO NS, 0.2% represents 0.2 wt% GO NS NDDF and so on.	119
Fig. 7.6	Time dependent rotational thixotropic test for various NDDFs. Legend: NDDF represents the base with 0 wt% GO NS, 0.2% represents 0.2 wt% GO NS NDDF and so on.	121
Fig. 7.7	(a) G' , G'' and loss factor <i>vs.</i> temperature, (b) Viscosity and complex viscosity <i>vs.</i> temperature for various NDDFs. Legend: NDDF represents the base with 0 wt% GO NS, 0.2% represents 0.2 wt% GO NS NDDF and so on.	122
Fig. 7.8	Filtrate loss volume <i>vs.</i> time for various NDDFs. Legend: NDDF represents the base with 0 wt% GO NS, 0.2% represents 0.2 wt% GO NS NDDF and so on.	123
Fig. 7.9	Volume fraction of cutting deposition of all the concerned NDDFs at 30, 60 and 80 °C in a deviated eccentric annular wellbore	125
Fig. 7.10	Velocity profile of base and 0.5 wt% GO NS NDDF at KOP	128

Fig. 7.11	Velocity profile of base and 0.5 wt% GO NS based NDDF at DOS	129
Fig. 7.12	Velocity profile of base and 0.5 wt% GO NS based NDDF at BUS-2	129
Fig. 7.13	Pressure drop (Pa) along annular region for the GO NS based NDDFs at 30, 60 and 80 °C. Legend: Base NDDF represents the base with 0 wt% GO NS, 0.2% represents 0.2 wt% GO NS NDDF and so on.	130
Fig. 8.1	(a) Shear stress <i>vs.</i> shear rate at 30 °C, (b) Shear stress <i>vs.</i> shear rate at 60 °C, (c) Shear stress <i>vs.</i> shear rate at 80 °C. Legend: NDDF represents the base with 0 wt% ZnO NP. 0.5% represents 0.5 wt% ZnO NP NDDF and so on	132
Fig. 8.2	(a) Viscosity <i>vs.</i> shear rate at 30 °C, (b) Viscosity <i>vs.</i> shear rate at 60 °C, (c) Viscosity <i>vs.</i> shear rate at 80 °C. Legend: NDDF represents the base with 0 wt% ZnO NP. 0.5% represents 0.5 wt% ZnO NP NDDF and so on	133
Fig. 8.3	(a) Storage modulus (G') and loss factor <i>vs.</i> shear strain (%) at 30 °C, (b) G' and loss factor <i>vs.</i> shear strain (%) at 60 °C, (c) G' and loss factor <i>vs.</i> shear strain (%) at 80 °C. Legend: NDDF represents the base with 0 wt% ZnO NP. 0.5% represents 0.5 wt% ZnO NP NDDF and so on.	134
Fig. 8.4	(a) Storage modulus (G') and Loss modulus (G'') <i>vs.</i> angular frequency at 30 °C, (b) G' and G'' <i>vs.</i> angular frequency at 60 °C, (c) G' and G'' <i>vs.</i> angular frequency at 80 °C. Legend: NDDF represents the base with 0 wt% ZnO NP. 0.5% represents 0.5 wt% ZnO NP NDDF and so on.	136

Fig. 8.5	(a) Complex viscosity <i>vs.</i> angular frequency at 30 °C, (b) Complex viscosity <i>vs.</i> angular frequency at 60 °C, (c) Complex viscosity <i>vs.</i> angular frequency at 80 °C. Legend: NDDF represents the base with 0 wt% ZnO NP. 0.5% represents 0.5 wt% ZnO NP NDDF and so on.	137
Fig. 8.6	Time dependent rotational thixotropic test for various NDDFs. Legend: NDDF represents the base with 0 wt% ZnO NP. 0.5% represents 0.5 wt% ZnO NP NDDF and so on.	138
Fig. 8.7	(a) G' , G'' and loss factor <i>vs.</i> temperature, (b) Viscosity and complex viscosity <i>vs.</i> temperature for various NDDFs. Legend: NDDF represents the base with 0 wt% ZnO NP. 0.5% represents 0.5 wt% ZnO NP NDDF and so on.	139
Fig. 8.8	Filtrate loss volume <i>vs.</i> time for various ZnO NP NDDFs. Legend: NDDF represents the base with 0 wt% ZnO NP. 0.5% represents 0.5 wt% ZnO NP NDDF and so on.	141
Fig. 8.9	Volume fraction of cutting deposition of all the concerned NDDFs at 30, 60 and 80 °C in a deviated eccentric annular wellbore	143
Fig. 8.10	Velocity profile at Kick-off Point (KOP) for base and 1% ZnO NP NDDF at 30 and 80 °C conditions	145
Fig. 8.11	Velocity profile at Drop-off section (DOS) for base and 1% ZnO NP NDDF at 30 and 80 °C conditions	146
Fig. 8.12	Velocity profile at Build-up section (BUS) for base and 1% ZnO NP NDDF at 30 and 80 °C conditions	147
Fig. 8.13	Pressure drop of ZnO NP NP based NDDF	148

Fig. 9.1	Modelled shear stress <i>vs.</i> shear rate of different NP based NDDF considering HB parameters at 80 °C	150
Fig. 9.2	HB parameters optimally determined from GA optimization techniques considering shear stress <i>vs.</i> shear rate values at 80 °C	151
Fig. 9.3	Storage modulus (G') and loss factor <i>vs.</i> shear strain (%) of different NP based NDDF at 80 °C	152
Fig. 9.4	Storage modulus (G') <i>vs.</i> angular frequency of different NP based NDDF at 80 °C	153
Fig. 9.5	Complex viscosity <i>vs.</i> angular frequency of different NP based NDDF at 80 °C	154
Fig. 9.6	Viscoelastic road for different NDDFs	154
Fig. 9.7	Effect of NPs on fluid loss control compared to base NDDF ('-' values denote reduction in fluid loss %, '+' value denote increase in fluid loss %)	155
Fig. 9.8	Effect of NPs in annular cutting retention compared to base NDDF at 80 °C ('-' values denote reduction cutting retention '+' value denote increase cutting retention in %)	156
Fig. 9.9	Contours of cutting volume fraction of base and NP NDDFs in the annular region at 80 °C	157

LIST OF TABLES

TABLE NO.	TABLE DESCRIPTION	PAGE NO.
Table 1.1	Details of geometry, meshing, mesh quality and boundary condition details for validation case	15
Table 1.2	Details of mesh quality (skewness and orthogonal quality)	17
Table 3.1	Optimal values of HB parameters by GA	46
Table 3.2	Percentage volume retention of cuttings in annulus <i>vs.</i> different cases of concentration and temperatures. (Volume fraction of cuttings) _{annulus} – (Volume fraction of cuttings) _{inlet} = (Retention of volume fraction of cuttings) _{annulus}	49
Table 4.1	Optimal values of HB parameters by GA	63
Table 4.2	Percentage volume retention of cuttings in annulus <i>vs.</i> different cases of concentration and temperatures. (Volume fraction of cuttings) _{annulus} – (Volume fraction of cuttings) _{inlet} = (Retention of volume fraction of cuttings) _{annulus}	65
Table 5.1	Optimal Herschel Bulkley (HB) parameters determined by genetic algorithm (GA) for various NDDFs	81

Table 5.2	Percentage volume retention of cuttings in annulus vs. different cases of concentration and temperatures. (Volume fraction of cuttings) _{annulus} – (Volume fraction of cuttings) _{inlet} = (Retention of volume fraction of cuttings) _{annulus}	84
Table 6.1	Optimal Herschel Bulkley (HB) parameters determined by genetic algorithm (GA) for various NDDFs	105
Table 6.2	Percentage volume retention of cuttings in annulus vs. different cases of concentration and temperatures. (Volume fraction of cuttings) _{annulus} – (Volume fraction of cuttings) _{inlet} = (Retention of volume fraction of cuttings) _{annulus}	107
Table 7.1	Optimal Herschel Bulkley (HB) parameters for various NDDFs obtained from genetic algorithm (GA)	124
Table 7.2	Percentage volume retention of cuttings in annulus vs. different cases of concentration and temperatures. (Volume fraction of cuttings) _{annulus} – (Volume fraction of cuttings) _{inlet} = (Retention of volume fraction of cuttings) _{annulus}	127
Table 8.1	Determining optimal Herschel Bulkley (HB) parameters using genetic algorithm (GA) optimization	142
Table 8.2	Percentage volume retention of cuttings in annulus vs. different cases of concentration and temperatures. (Volume fraction of cuttings) _{annulus} – (Volume fraction of cuttings) _{inlet} = (Retention of volume fraction of cuttings) _{annulus}	144
Table 9.1	Summary and Conclusions	159

NOMENCLATURE OF SYMBOLS

Latin letters

C_D	Drag coefficient (dimensionless)
C_l	Lift coefficient (dimensionless)
d	Diameter (m)
d_s	Volume equivalent particle diameter (m)
e	Eccentricity factor (dimensionless)
e_{ss}	Coefficient of restitution (dimensionless)
$g_{o,ss}$	Compressibility transition function (dimensionless)
$\vec{F}_{lift,s}$	Lift force (N)
\vec{F}_s	External body force (N)
$\vec{F}_{td,s}$	Turbulent dispersion force (N)
$\vec{F}_{vm,s}$	Virtual mass force (N)
\vec{g}	Gravitational acceleration (m/s^2)
k_{ls}	Interphase momentum exchange coefficient
K	Fluid consistency index
\dot{m}_{ls}	Mass transfer from phase l to s (kg/s)
\dot{m}_{pq}	Mass transfer from phase p to q (kg/s)
\dot{m}_{qp}	Mass transfer from phase q to p (kg/s)
\dot{m}_{sl}	Mass transfer from phase s to l (kg/s)
n	Flow index
p	Pressure (Pa)

p_s	Solids pressure (Pa)
Re	Reynold's number (dimensionless)
\vec{v}_l	Liquid phase velocity (m/s)
\vec{v}_q	Phase velocity (m/s)
\vec{v}_s	Solid phase velocity (m/s)
\vec{v}_{sl}	Interphase velocity (m/s)

Greek letters

α	Volume fraction (dimensionless)
α_s	Solid phase volume fraction (dimensionless)
β	Coefficient of thermal expansion (K^{-1})
δ	Delta function (units vary)
$\dot{\gamma}$	Shear rate (1/s)
λ_s	Bulk viscosity (Pa.s)
μ_s	Solid phase viscosity (Pa-s)
ρ	Density (kg/m^3)
ρ_q	Phase density (kg/m^3)
ρ_{rq}	Phase density at a radial distance 'r' (kg/m^3)
ρ_s	Solid phase density (kg/m^3)
φ	Cuttings bed porosity (%)
$\tau_{obr.}$	Observed shear stress observed (Pa)
$\bar{\tau}_q$	Stress tensor (Pa)
τ	Shear stress (Pa)
Θ_s	Granular temperature (K)

CHAPTER 1

INTRODUCTION

1.1. OVERVIEW

Drilling fluid is a vital component in drilling operations. Effective and fruitful completion of a well depends significantly on the properties of the drilling fluid (Caenn, Darley, & Gray, 2011). Drilling fluids constitute different mixtures of aqueous, solid and gaseous components that are circulated from the surface through the drill string, bit nozzles to the annular region and eventually return to the surface. It is during this circulation period where a drilling fluid executes multiple functions.

Functions of drilling fluid can be summarized as below:

i. Control formation pore pressure

Drilling fluid induces a hydrostatic head which is greater than the formation pore pressure. This ensures that no influx of formation fluid enters the wellbore. This function is purely controlled and dictated by the density of the fluid. A supervisory check on fluid density is also ensured to keep the equivalent circulation density (ECD) under control so that the formation of fractures can be prevented. Drilling fluids are often known as the first line of defense against blowouts.

ii. Carrying and suspension of cuttings

Rock fragments and chips that are generated near the bit must be continuously cleared for efficient drilling operations. The drilling fluid which jets out of the bit nozzle must have enough momentum and viscosity to carry these rock cuttings out

of the annulus to the surface. Additionally, a drilling fluid must possess thixotropic property (characterized by gel strength) to suspend cuttings as well as weighing materials at times when circulation is stopped.

iii. Formation of filter cake

The exposed formation around the wellbore is porous and permeable. Additionally, a differential pressure (generally overbalanced) exists between the wellbore and formation which forces the drilling fluid to seep into these porous and permeable rocks. Henceforth, a drilling fluid must bear filtration property such that it forms a cake around the wellbore, thereby preventing further fluid losses. A thin, tough and impermeable filter cake is desirable to incur less downhole problems, provide borehole stability and yield a minimal fluid loss.

iv. Cooling and lubrication

As the drill string and drill bit rotate, a significant amount of heat is generated due to friction. The constant flow of drilling fluid along these structures helps in better heat transfer and dissipation; thereby cooling off the string and bit. The drilling fluid also provides lubrication and lowers friction between the borehole wall and the drill string.

Few additional qualities that drilling fluid is expected to own and display are:

- i. It should exhibit low formation damage.
- ii. It maintains borehole stability by being unreactive to the open hole section of the wellbore.
- iii. It cleans the drill bit and its junk areas.
- iv. It assists in running logs and collecting information through mud pulse telemetry.
- v. It maintains a corrosion-less environment by providing a certain degree of alkalinity.

The selection of the type of drilling fluid is a critical part of a drilling operation. Different formations are subjected to varied vulnerabilities that need to be addressed. Modern classification of drilling fluids can be summarized as follows:

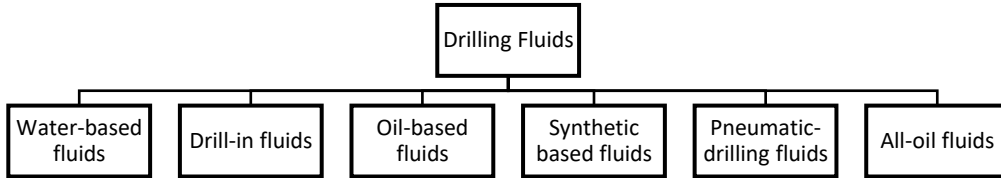


Fig. 1.1: Types of drilling fluids

While drilling for shale gas the key is to maintain borehole wall stability and inhibit shale swelling (Xie, Deng, Su, & Pu, 2013). The conventional use of bentonite drilling fluid while drilling shale reservoirs results in formation damage caused by chemical incompatibility and blocking of pore spaces. The chemical incompatibility often encompasses the reaction between filtrate loss and formation fluids and precipitation of insoluble salts. In some cases, excessive emulsion blockage results in wettability changes in the reservoir. Pore throat blockage is caused by an invasion of solid contents of drilling fluid forming an internal filter cake. These problems related to formation damage are associated with bentonite-based drilling fluids as bentonite is easily hydrated and the mud cake formed cannot be removed and affects productivity. The easy removal of mud cake is desired for good production rates and better cementing during the well construction phase. In the case of bentonite formed mud cake, physical means need to be adapted for its effective removal (Alcheikh & Ghosh, 2017). These problems become more prominent in horizontal wells. To overcome well cleanup difficulties with bentonite when used as rheology enhancing additive, degradable polymers are in use. Unlike conventional bentonite additives, these polymers can naturally degrade within days or even hours. Xanthan gum, modified starch, and modified cellulose products (polyanionic cellulose, PAC) are a few examples of biopolymers that are widely used in the drilling industry. Although biopolymers cost quite more than bentonite,

yet, they enhance production by 40% thereby offsetting the surplus investment (“Why Bentonite Hurts Well Production: The Case for Biopolymer Drilling Fluid,” 2010). Lately, a new generation of drilling fluid free of clay particles has emerged, namely non damaging drilling fluid (NDDF). NDDF is comprised highly of biopolymers which act as viscosifying as well as a fluid loss control agent. The zones susceptible to a high fluid loss like shale zones or production zones that are prone to formation damage are the best candidates for NDDF (Elkatatny, 2019). Potassium chloride (KCl) is often used as a shale inhibitor with biopolymer-based NDDFs. Nonetheless, due to environmental sanctions related to disposable issues, the use of KCl-NDDF has been restricted.

For shale reservoirs, oil based-mud has always been a suitable trouble-free drilling fluid due to its non-invasive nature. However, the oil and gas industry is constantly looking for a replacement of oil-based mud (OBM) as it possesses a lot of environmental adversities, disposal issues as well as associated cost (Elshehabi & Bilgesu, 2015). High performing water-based mud (WBM) is seen as a potential system to replace OBM. Unlike conventional WBMs, these high performing WBMs act as excellent shale inhibitors and encapsulators which reduce downhole problems. A mixture of polyamine derivatives tackles the tendency of reactive clay to hydrate and disperse. For cutting encapsulation, the high molecular weight of partially hydrolyzed polyacrylamide (PHPA) can be used in conjunction with a polyamine. A more stable monolayer arrangement of molecules can be achieved by using short-chain polyamines. These polyamines integrate the c-spacing of sodium montmorillonite. This further restrains foreign macromolecules from entering the interlayer thereby yielding a more stable monolayer (Li & Thuriere, 2016). Hence, it acts as a superior shale inhibitor. The combination of polyamine and PHPA has resulted in a reduction of clay swelling and an increase in cutting encapsulation that has a cutting carrying ability comparable to that of OBM. Additionally, it eases tripping in/out operations due to its enhanced lubrication properties. The problem of bit balling is also significantly decreased, as it prevents swelling of clay cuttings which tend to deposit in the junk areas of a bit (Leaper et al., 2007). Hence,

polyamine when used with biopolymers as viscosifying and fluid loss control agents can be used as NDDF for drilling shale gas reservoir with limited formation damage.

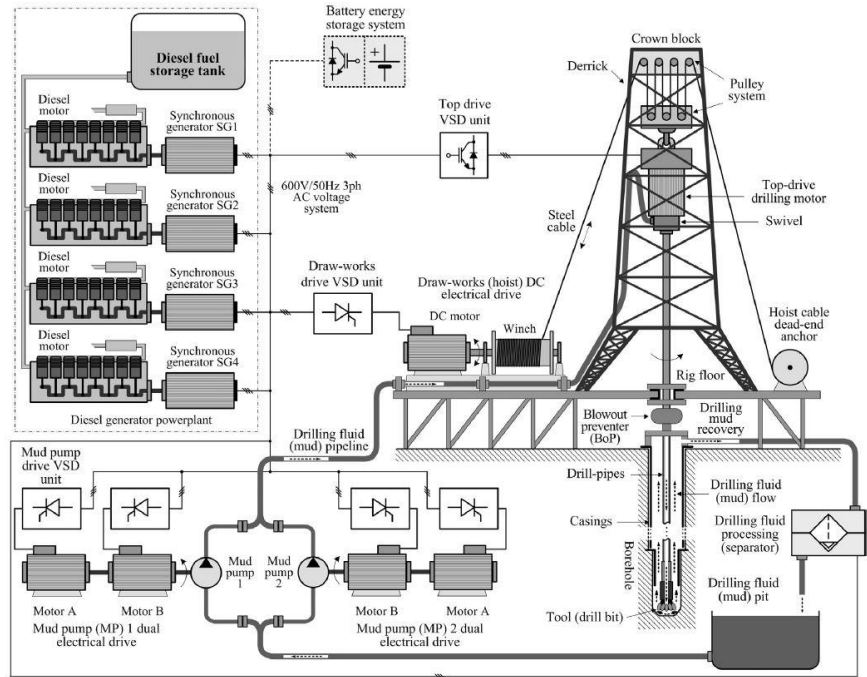


Fig. 1.2: Typical schematic of a drilling rig

1.2. MOTIVATION

Biopolymer based drilling fluids like NDDFs are prone to degradation under high temperatures. Such deterioration at a molecular level leads to the severe loss of rheological properties such as viscosity, yield point, gel strength, elasticity as well as fluid loss control ability of drilling fluids (Bradshaw et al., 2006). This subsequently can lead to sagging of weighing fraction and even rock cuttings; thereby resulting in equivalent circulation density (ECD) problems and pipe stuck-ups. These problems often limit the application of NDDFs to low and moderate temperature drilling conditions (Galindo, Zha, Zhou, & Deville, 2015).

Nanotechnology, which has aided in developing new materials for a wide

range of uses (Wong & De Leon, 2010) in the last decades, can be utilized to improve these limitations of NDDF. Drilling fluids that have at least one component with a size ranging between 1-100 nm are labeled as nano-based drilling fluids (Nabhani & Emami, 2012). A high surface to volume ratio makes nanoparticles (NPs) unique and technology of high applicability (Peng et al., 2018). NPs, when used in concentrations even less than 1 wt%, have the ability to change the van der Waal, molecular and atomic forces thereby altering bulk fluid properties (Abdo & Haneef, 2012; Sidik, Mohammed, Alawi, & Samion, 2014). Taking advantage of these unique properties, researchers have tried to study the impact of NPs on the properties of drilling fluids (Ponmani, Nagarajan, & Sangwai, 2013). Pourafshary et al., (2009) conducted an analytical hierarchy process to study the feasibility of application of nanotechnology in the field of oil and gas industry stating that it can be a useful tool to enhance properties of drilling fluids, especially under high pressure high temperature (HPHT) conditions.

Many researchers have studied the effect of NPs in bentonite-based drilling fluids and oil-based drilling fluids. However, to the best of the author's knowledge, scientific inquiry to further enhance and stabilize the rheological properties of NDDF has not been reported. Moreover, the effect of NPs on the elasticity of drilling fluids can significantly affect the cutting carrying/suspending ability to drill fluid which still rests a void for further study. Additionally, this enhancement or ramification in rheological properties due to the addition of NPs has not yet been quantified by computational fluid dynamics (CFD) studies to appraise hydraulic performance. Summarizing, a comprehensive study needs to be conducted to investigate the effect of NPs on rheological properties and the hydraulic performance of NDDF for a holistic understanding. Hence, these problem statements act as the key motivation for this research.

1.3. RESEARCH OBJECTIVES

The main objective of this research is to investigate the effect of NPs on NDDFs. The effect herein mentioned is in terms of rheological and fluid loss

control properties. Additionally, CFD studies are conducted to evaluate hydraulic performance (cutting carrying capacity, velocity profiles, and pressure drop) of each fluid by solving the governing equations for multiphase fluid flow using finite volume in ANSYS FLUENT®. The experimental observations/measurements are bridged and allied with the CFD simulations by defining Herschel Buckley (HB) parameters in the momentum conservation equation for each fluid. The following points are briefed to define the key objectives of this research study:

1. To study and investigate the effects of NPs on rheological properties of NDDF.
2. To study and investigate the effects of NPs on fluid loss control property of NDDF.
3. To define the rheological model and conduct a CFD analysis of nano-based NDDF.
4. To compare and analyze the hydraulic performance of all the prepared drilling fluids.

1.4. RESEARCH METHODOLOGY

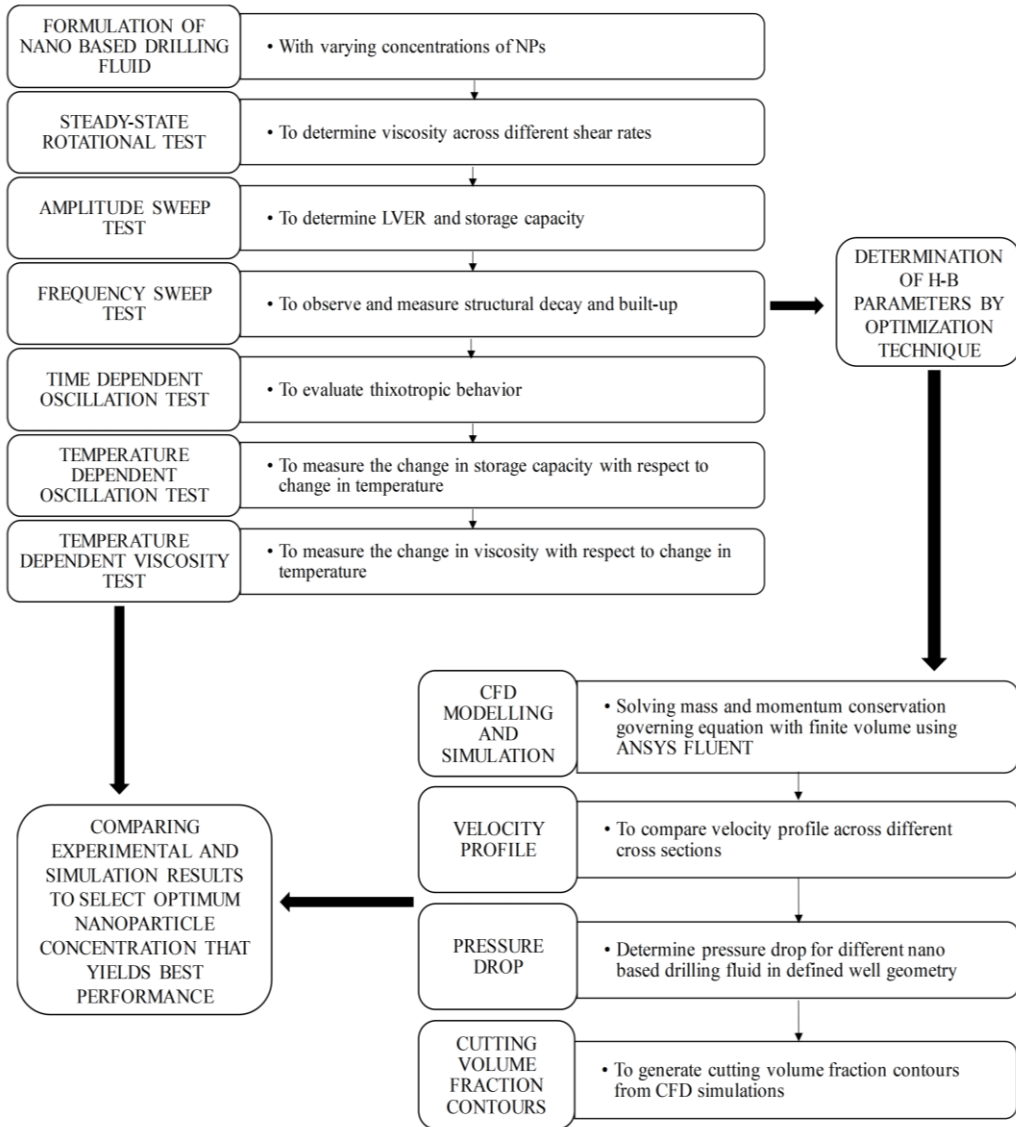


Fig. 1.3: Layout of methodology

The research methodology adopted is elaborated and briefed as follows:

i. Formulation of NP based NDDF

NP based NDDF is formulated by sonicating the desired concentration of NPs in 250 ml deionized (DI) water through a probe-sonicator for homogenous and

uniform dispersion. Constituent additives are mixed at definite proportions to bring out different properties within the drilling fluid.

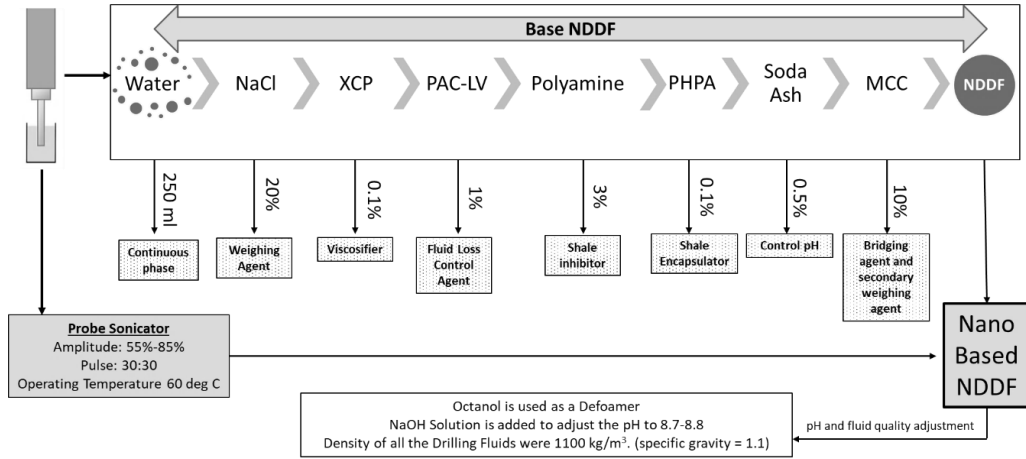


Fig. 1.4: Formulation of nano-based NDDF (NP based NDDF)

ii. Rheological measurements

All the rheological measurements were conducted in an Anton Paar rheometer (MCR 92). Steady-state rotational test measurements were conducted in a concentric cylinder (CC) system while the dynamic oscillation test measurements were conducted in a parallel-plate (PP) system.

a. Steady-state rotational test

The steady-state rotational test was conducted for all the fluids at 30, 60 and 80 °C. Data were logged in terms of viscosity ($mPa\cdot s$) and shear stress (Pa) at different shear rates (sec^{-1}).

b. Amplitude sweep test

An amplitude sweep test was performed to evaluate the linear viscoelastic range (LVER) for all the fluids. The frequency was kept constant at 1 Hz and corresponding storage and loss modulus (G' and G'') were measured. This test

indicates the viscoelastic nature of the fluid. A higher G' than G'' would confirm a viscoelastic solid behaviour. If the G'' is greater than G' , the fluid-structure would indicate viscoelastic liquid nature. Loss factor (G''/G') is another vital indicator to categorize the viscoelastic nature of the fluid in terms of solid and liquid. A fluid that displays loss factor greater than unity is viscoelastic solid in nature, whereas if it is less than unity the fluid is liquid in nature. All the tests were measured at 30, 60 and 80 °C.

c. Frequency sweep test

Frequency sweep test was conducted to measure G' and G'' over a varied frequency range at 30, 60 and 80 °C. The shear strain (%) was kept constant below the LVER region determined from the amplitude sweep test to avoid any structural deformation. Complex viscosity and loss factors were also logged to evaluate viscoelasticity and gel strength at low frequencies.

d. Temperature dependent flow behaviour (temperature sweep)

A temperature sweep test measures the values of G' and G'' as the temperature is ramped up (0.5 °C/sec) from a lower to higher magnitude (30 to 100 °C). The corresponding values of complex viscosity and loss factors were also noted to determine the working range of each fluid. In this set of tests, the frequency and shear strain (%) were kept constant.

e. Viscosity vs. temperature

This test is a rotational test where the viscosity of the fluids at a constant shear rate was measured with a gradual rise in temperature (0.5 °C/sec).

f. Time-dependent rotational test

Time-dependent rotational test evaluates the thixotropic ability of a fluid. The viscosity of the fluid is measured at a very low shear rate (0.25 s⁻¹) to simulate near static state. Further, it is sheared at a high shear rate (1000 s⁻¹), which breaks down

the fluid structure. After a rest period of 4 secs, the viscosity of the fluid is again measured at 0.25 s^{-1} . The fluid viscosity is expected to rise and subsequently and subsequently reach the original viscosity. Time taken to achieve the original viscosity represents the thixotropic property of a drilling fluid.

iii. Fluid loss measurements

Fluid loss of all the drilling fluids was measured in an OFITE API Filter Press apparatus. Here, the fluid is contained in a stainless-steel cylinder having a filter paper supported by a metal screen at the bottom end, and is subjected to a pressure of 100 and 200 psi from a nitrogen cylinder for 30 minutes. Due to this differential pressure, a certain amount of fluid is lost across the filter paper which is collected in a graduated cylinder. The volume collected is termed as fluid loss.

iv. Determination of optimal Herschel Buckley (HB) parameter

Drilling fluid, in general, follows the HB model. The main objective related to this model is the accurate determination of equation model parameters which are: yield stress (τ_o), fluid consistency index (K) and the flow index (n). The equation is given by:

$$\tau = \tau_o + K\dot{\gamma}^n \quad \text{Eqn. (1.1)}$$

In this study, genetic algorithm (GA) optimization technique is used to minimize an objective function which is given by sum of squared error (SSE). SSE is calculated between the model shear stress function and observed values from the rheometer against each shear rate as expressed below:

$$SSE = \sum_{i=1}^6 (\tau_{obr.} - (\tau_o + K\dot{\gamma}^n))^2 \quad \text{Eqn. (1.2)}$$

GA minimizes the value of SSE so that the HB parameter defines a function curve which fits the observed value. Each generation of parameters is updated to a new generation after initialization and similar evolving values are considered

subsequent to each iteration. Parameters resulting in a decrease in SSE are included in the next generation of the population while increasing values are removed. This process is repeated until there is no significant change between consecutive iterative values. MATLAB Toolbox is use to run GA tool for minimizing the objective function.

v. Study of hydraulic performance of NDDFs through computational fluid dynamics (CFD) simulation and analysis

a. Numerical formulation

Equation of continuity and momentum conservation equation is considered for both the non-Newtonian NDDFs and rock cuttings. The HB parameters obtained from GA calculations are coupled with momentum conservation equation to describe the concerned NDDFs.

Equation of continuity:

$$\frac{1}{\rho_{rq}} \left(\frac{\partial}{\partial t} (\alpha_q \rho_q) + \nabla \cdot (\alpha_q \rho_q \vec{v}_q) \right) = \sum_{p=1}^n (\dot{m}_{pq} - \dot{m}_{qp}) \quad \text{Eqn. (1.3)}$$

Momentum conservation equation for fluid and solid:

$$\frac{\partial}{\partial t} (\alpha_s \rho_s \vec{v}_s) + \nabla \cdot (\alpha_s \rho_s \vec{v}_s \vec{v}_s) = -\alpha_s \nabla_p - \nabla_{p_s} + \nabla \cdot \bar{\tau}_q + \alpha_s \rho_s \vec{g} + \sum_{l=1}^N (K_{ls} (\vec{v}_l - \vec{v}_s) + \dot{m}_{ls} \vec{v}_{ls} - \dot{m}_{sl} \vec{v}_{sl}) + (\vec{F}_s - \vec{F}_{lift,s} + \vec{F}_{vm,s} + \vec{F}_{td,s}) \quad \text{Eqn. (1.4)}$$

Thus, the final equation for momentum conservation after neglecting turbulent dispersion force and mass transfer parameters becomes:

$$\frac{\partial}{\partial t} (\alpha_s \rho_s \vec{v}_s) + \nabla \cdot (\alpha_s \rho_s \vec{v}_s \vec{v}_s) = -\alpha_s \nabla_p - \nabla_{p_s} + \nabla \cdot \bar{\tau}_q + \alpha_s \rho_s \vec{g} + \sum_{l=1}^N (K_{ls} (\vec{v}_l - \vec{v}_s)) + (\vec{F}_s - \vec{F}_{lift,s} + \vec{F}_{vm,s}) \quad \text{Eqn. (1.5)}$$

The finite volume technique is used to discretize and solve the governing partial

differential equation using Ansys FLUENT® (Fluent, 2013) with prescribed initial and final boundary conditions. Since the flow is incompressible, the pressure-based solver was incorporated. Due to the low dispersion of solids in the liquid phase, Euler-Euler multiphase model was used. The implicit scheme was used for this steady-state study. Reynolds seven stress was used as viscous turbulent modeling, as it is effective for rotating flow. As the primary phase mostly contributes to the turbulent flow, the dispersed model in the Reynolds Stress Model (RMS) was used for simulations.

Other mathematical closures describing particular flow, effect and interaction are as follows:

Syamlal-O'Brien Granular viscosity equation (Syamlal & O'Brien, 1988)

$$\mu_s = \frac{\alpha_s d_s \rho_s \sqrt{\pi}}{6(3-e_{ss})} \left[1 + \frac{2}{5} g_{o,ss} \alpha_s (1 + e_{ss}) (3e_{ss} - 1) \right] \quad \text{Eqn. (1.6)}$$

Lun-et.al. Granular bulk viscosity equation (Lun & Savage, 1987):

$$\lambda_s = \frac{4}{3} \alpha_s^2 \rho_s d_s g_{o,ss} (1 + e_{ss}) \left[\frac{\Theta_s}{\pi} \right]^{1/2} \quad \text{Eqn. (1.7)}$$

Lun-et.al. Solid pressure equation (Lun & Savage, 1987):

$$p_s = \alpha_s \rho_s \Theta_s + 2p_s (1 + e_{ss}) \alpha_s^2 g_{o,ss} \Theta_s \quad \text{Eqn. (1.8)}$$

Schiller-Naumann Drag co-efficient equation (Schiller & Naumann, 1935):

$$C_D = \left\{ \frac{24}{Re} (1 + 0.15 Re^{0.687}) \right\} \quad \text{Eqn. (1.9)}$$

Moraga Lift Equation (Moraga, Larreteguy, Drew, & Lahey, 2003):

$$C_l = \left\{ - \left(0.12 - 0.2 e^{-\frac{\varphi}{3.6} \times 10^{-5}} \right) e^{\frac{\varphi}{3} \times 10^{-7}} \right\} - 0.653$$

$$\varphi \leq 6000,$$

$$6000 < \varphi < 5 < 10^7,$$

$$\varphi \geq 5 \times 10^7 \quad \text{Eqn. (1.10)}$$

b. Steady state simulation approach

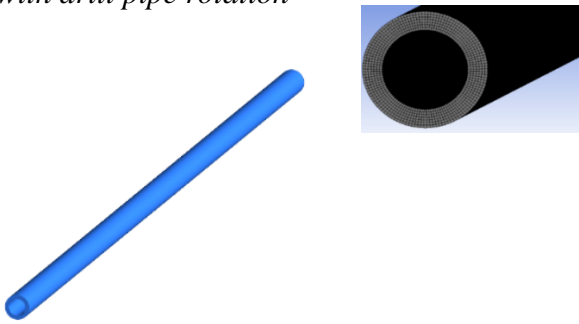
Reynolds Average Navier Stokes (RANS) is solved using the finite volume technique using Ansys FLUENT®. For the pressure-velocity coupling scheme, Semi-Implicit Method for Pressure Linked Equations (SIMPLE) is implemented. While, Quadratic Upstream Interpolation for Convective Kinematics (QUICK) which is a high order differencing method is used for spatial discretization of momentum, volume fraction, turbulent kinetic energy and Reynold's stresses. The solution is initialized using inlet boundary conditions. To ensure convergence a standard value of 10^{-4} is set as residuals value. Pressure drops, velocity profiles and contour plots of cutting volume fraction for each drilling fluid at different temperatures are obtained through CFD post.

c. Validation with experimental results

The proposed mathematical model was validated against the experimental values obtained from the works of (Han et al., 2010). The results obtained showed a similar trend and values as that of the experimental. However, the relatively additional deviation can be seen for the high velocity at high drill-pipe rotation per minute (rpm) as compared to low velocity and low rpm. This is due to the commencement of turbulence and inconsideration of cutting shape. Realistic particle size during drilling operations is relatively larger than the assumed particle size in the present model. This is due to the limitation of control volume in Eulerian-Eulerian equations for solid phase treatment (Cleminš, 1988; Fan and Zhu, 2005; Gómez and Milioli, 2005). Although Lagrangian-Eulerian models accomplish better prediction related to larger particle size; computational cost is substantially higher than Eulerian-Eulerian continuum equations. On the other hand, the Lagrangian Particle Tracking model has a limitation of handling higher solid

volume fraction. The Eulerian-Eulerian model considers for continuous and dispersed phases as continuous media and accounts for phase interaction and incorporates turbulence automatically (Faeth, 1987). However, a drawback of this model is that it requires robust closure equations to define the physical phenomena. Considering the Eulerian-Eulerian model and defined closure equations; pressure difference between inlet and outlet from simulations were coursed to attain grid independency. A mesh independency study showed that 7,92,000 elements were enough to obtain accurate and persistent results.

Table 1.1 Details of geometry, meshing, mesh quality and boundary condition details for validation case

Geometry	Meshing	Mesh quality	
		<i>Skewness</i>	<i>Orthogonal quality</i>
<p><i>Slim hole inclined well with drill pipe rotation</i></p> 	<p>Number of nodes: 968000</p>	Min:	Min:
		0.019417	0.99975
<p>OD/ID = 44 mm/30 mm</p> <p>Length = 1.8 m</p> <p>Drill pipe Rotation = 100 rpm</p>	<p>Number of elements: 721125</p> <p>Body sizing: 0.001</p>	Max:	Max:
		0.48668	0.99988
		Average:	Average:
		0.27927	0.99981

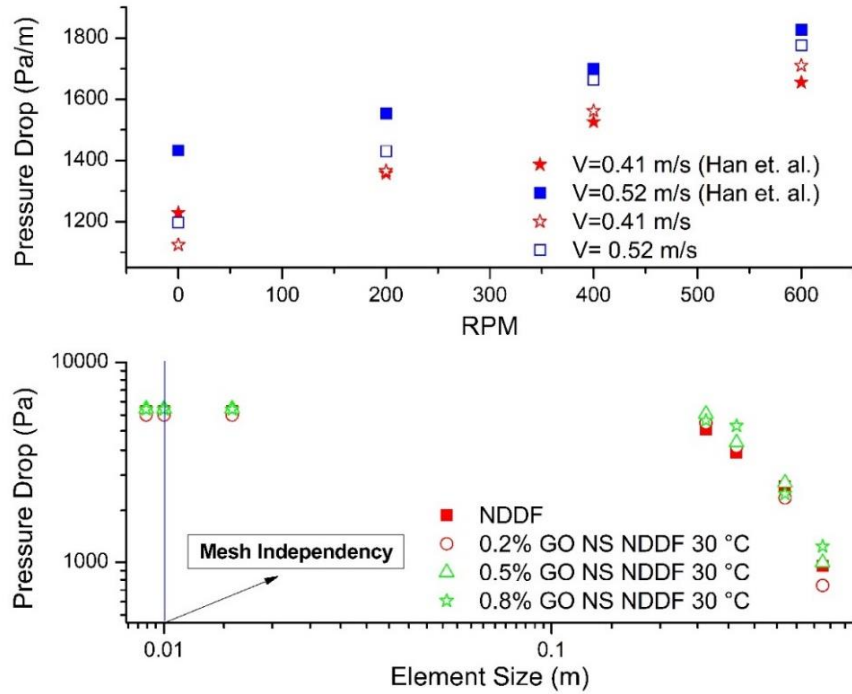
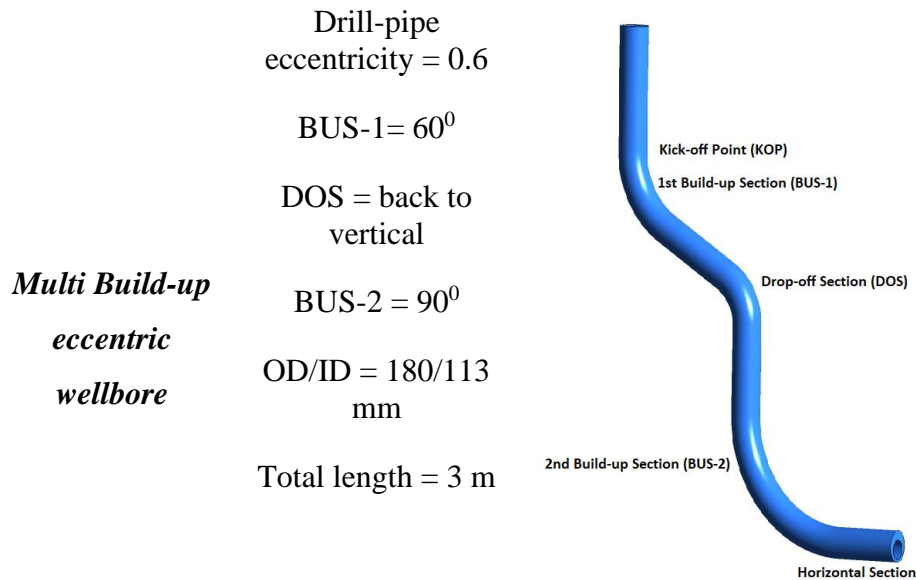
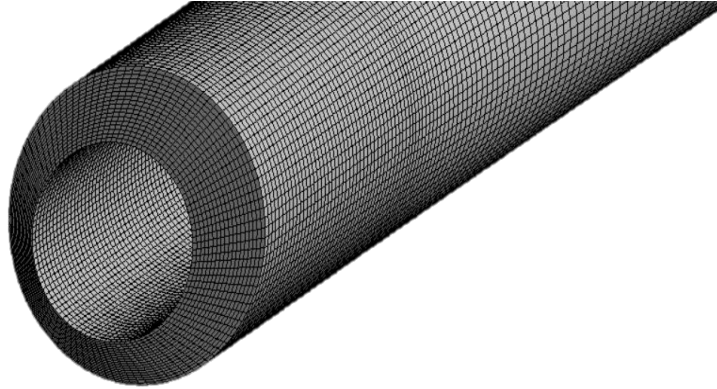


Fig. 1.5: Mesh Validation

Geometry



Meshing



Number of nodes: 837900

Number of elements: 792000

Body sizing element size: 0.01m

Fig. 1.6: Details of geometry, meshing, and boundary condition details in the current study

Table 1.2 Details of mesh quality (skewness and orthogonal quality)

Mesh quality	
<i>Skewness</i>	<i>Orthogonal quality</i>
Minimum: 0.017481	Minimum: 0.65929
Maximum: 0.48668	Maximum: 0.9997
Average: 0.27927	Average: 0.88662

The following assumptions and parameters are considered for the flow model:

- ✓ Drilling fluid is in a continuous phase with rock cuttings as dispersed phase.
- ✓ No slip between the wellbore wall or drill pipe and the drilling fluid.
- ✓ Spherical (1 mm) cuttings with a density of 2550 kg/m^3 with an inlet volume fraction of 10%
- ✓ No mass exchange and change in shape due to solid-solid interaction.
- ✓ Fluid inlet velocity = 0.8 m/s
- ✓ Fluid density = 1100 kg/m^3

vi. Comparing results

Steady-state rotational results are compared in terms of shear stress/viscosity at different concentrations and varied temperatures (30, 60 and 80° C). Similar comparisons are carried out for amplitude, frequency, time dependent and temperature sweep to compare viscoelastic properties and stability of gel structure. CFD results are then presented in terms of cutting volume fraction deposits along the wellpath. Velocity plots are further obtained at kick off point (KOP), drop off point (DOS) and 2nd build up section (BUS-2) for the best and worst performing fluids as decided from the previous step. Velocities are compared with base NDDF at 30 and 80° C to draw a comparison of the profiles across the annular diameter. Furthermore, the pressure drop across the length of the wellbore is calculated to check fluid flowability and required inlet pressure.

1.5. CHAPTER SCHEME

The thesis of the work is reported in six chapters which are briefed as follows:

- Chapter 1: Introduction

This chapter presents an overview of drilling fluids; its functions and its importance. It also throws light on the limitations of conventional drilling fluid, its effect on formation damage and the requisite for non-damaging drilling fluid (NDDF). Additionally, it highlights that these biopolymer-based drilling fluids are

thermally unstable and a need for a study to address this issue holds great significance. The chapter also describes the importance of nanotechnology in today's world. The aim to incorporate nanotechnology to study its effect on NDDF and observe its enhancement emerges as the motivation for this research. Furthermore, it also elaborates on the methodology adopted to investigate the effect of different NPs of NDDF by both experimental and computational techniques.

- Chapter 2: Literature Survey

A comprehensive literature review is presented by reporting studies conducted by various researchers. The chapter extends these representations into two broad verticals of information: (a) effect of NPs on drilling fluids (b) review of CFD studies to evaluate the performance of drilling fluids.

- Chapter 3: Effect of Silicon dioxide NPs (SiO_2 NP) on NDDF

This chapter presents a study of the effect of SiO_2 NP on NDDF. The concentration of SiO_2 NP considered were 0.5, 0.8 and 1 wt%. All the measurements are made before and after aging the fluid in a hot rolling oven for 16 hours. Measurements before treatment in the oven are termed as before hot roll (BHR) while, measurements after treatment are termed as after hot roll (AHR). Rheological studies by steady state rotational measurements through a Brookfield viscometer are reported in terms of plastic viscosity (PV), apparent viscosity (AV) and gel strength. CFD simulations are then set forth to draw comparisons at 30 and 80 °C for all the concentrations in terms of volume fraction and pressure drops. Velocity plots are compared between base and 1 wt% SiO_2 NP NDDF to distinguish differences in their respective profiles at BHR and AHR conditions.

- Chapter 4: Effect of Copper oxide NPs (CuO NP) on NDDF

This chapter reports the effect of 0.5, 0.8 and 1 wt% CuO NP on rheological properties, fluid loss control and hydraulic performance of NDDF. Steady state rotational rheological properties are reported in terms of PV, AV and gel strength.

CFD studies are drawn similarly to Chapter 3. Simulation results are presented in terms of cutting volume fractions, velocity profiles and pressure drop at BHR and AHR conditions.

- Chapter 5: Effect of Aluminum oxide NPs (Al_2O_3 NP) on NDDF
- Chapter 6: Effect of Zirconium dioxide NPs (ZrO_2 NP) on NDDF
- Chapter 7: Effect of Graphene oxide nanosheets (GO NS) on NDDF
- Chapter 8: Effect of Zinc oxide NPs (ZnO NP) on NDDF



Fig. 1.7: Images of different nanoparticles included in this study. (a) SiO_2 NP (b) CuO NP (c) Al_2O_3 NP (d) ZrO_2 NP (e) GO NS (f) ZnO NP

Chapter 5 – 8 has identical methodologies for different NPs and therefore their chapter scheme can be merged within the same description. The steady state rheological measurements are carried out in rheometer. Viscoelastic properties are determined at various amplitude, frequency and temperature through dynamic oscillation tests. The thixotropic nature of each fluid is also determined in terms of recovery time and reported. Further, rotational data are considered to determine HB parameters through the GA optimization technique which are used in numerical modelling and CFD simulations. The results from CFD studies are presented in terms of cutting volume fraction and pressure drops for all fluids. Velocity profiles are obtained for the NP NDDFs displaying the highest effect and compared with base NDDF at 30 and 80 °C.

- Chapter 9: Conclusion and future work

This chapter presents a comparative study of all the concerned NPs that are investigated in this study. The best performing NPs are considered from each

chapter's conclusions to draw relative contrast amongst themselves from rheological, fluid loss and CFD standpoint.

- Chapter 10: Bibliography and References

CHAPTER 2

LITERATURE SURVEY

2.1 INTRODUCTION

The exploitation of the oil and gas reserves from the subsurface reservoir is achieved by drilling a borehole through multiple rock formations into a hydrocarbon reservoir. The borehole, commonly referred to as an oil well may be of different trajectories which can extend up to a depth of several thousand feet. A drill bit is used to break the rock formations under the application of sufficient compressive force (weight on bit) as provided by the drill string through the bottom hole assembly (BHA). During this process, the drill bit scrapes and grinds the rock to produce fragments called cuttings, which are to be removed out of the well bore, continuously and efficiently. This action is performed by the drilling fluid, which acts as a medium to transport the rock cuttings to the surface through the annulus region of a well bore. Moreover, the drilling fluid, commonly referred to as the drilling mud, acts as the primary safety barrier during overbalance drilling operations. It provides a sufficient hydrostatic head that is greater than the formation pore pressure, thereby minimizing the chances of a kick.

An efficient drilling fluid plays an elemental role in achieving better drilling performance. The rate of penetration (ROP) during drilling increases as the efficiency of the drilling fluid to lift and transport the cuttings increases. This, in turn, is dependent on the rheological properties of the mud such as viscosity, gel strength and yield point. Moreover, a drilling fluid is expected to pose fluid loss control ability, which prevents shale swelling as well as formation damage at pay

zones in the reservoir. Thus, selecting an optimized drilling fluid system is of utmost relevance in order to enhance the efficiency of the drilling process.

2.2 LIMITATION OF CONVENTIONAL DRILLING FLUID

The conventional drilling fluids may witness degradation in properties when subjected to severe downhole conditions. The fluids may lose thermal stability in the case of High Pressure High Temperature (HPHT) wells, which may result in severe downhole complications such as inefficient cutting transport, bit balling and hence reduced ROP. This condition is more prominent in the case of water based drilling fluid. Barite sagging is another common complication that takes place due to an inefficient drilling fluid. The cutting carrying capacity of the drilling fluid may also be adversely affected by the loss in viscosity on account of the constant shear experienced. Additionally, a drilling fluid must also be capable of generating an impermeable filter cake of optimum thickness on the walls of the wellbore, in order to minimize the filtrate losses. The type of drilling fluid being used is largely dependent on the characteristics of the formations through which the well is being drilled. Shale formations cannot be drilled using conventional water based drilling fluid. Shale, being a clay swells when in contact with water which reduces the effective well bore diameter, thereby increasing annular pressure drop and increasing the probability of pipe stuck conditions.

2.3 RECENT PROGRESS

In recent years, studies are being carried out to enhance drilling fluid properties by means of polymers and clay hybrids. Polymer composites majorly constitute polyanionic cellulose (PAC), carboxymethyl cellulose (CMC) and sodium carboxymethyl cellulose (NaCMC) (García-Ochoa, Santos, Casas, & Gómez, 2000; Lahalih, Dairanieh, & Division, 1989; Pérez, Siquier, Ramírez, Müller, & Sáez, 2004; Wan, Zang, Wang, Zhang, & Sun, 2010). The clay hybrids comprise of palygorskite and hydrous clays. The application of such polymers and clays is limited to certain wellbore conditions and cannot be

applied to drill in adverse conditions. So, in order to overcome this issue, NPs have been used as an additive in the water-based and oil-based drilling fluids to boost their performance. These nano-enhanced drilling fluids often exhibit higher gel-strength, lower drag and are anti-corrosive nature (Aftab et al., 2017; Contreras et al., 2014; Contreras and Husein, 2014; Mahmoud et al., 2016; Ragab and Noah, 2014; Wang et al., 2018; Yu et al., 2017; Zakaria et al., 2012).

2.4 NANO BASED DRILLING FLUIDS

Drilling fluids that have at least one additive with a particle size ranging between 1-100 nm are termed as nano-based drilling fluids (Santoyo et al. 2001). Amanullah et al. (2011) observed the effects caused by the nano-based drilling fluids during drilling operations. They formulated several nano-based drilling fluids using three commercial NPs (NP). The qualitative assessment report showed the stability of the nanofluids by making short and long term observations of the fluid behaviour. After measuring the rheological properties, API fluid loss and mud cake thickness in case of nano-fluid and comparing it with the bentonite based one, it was found that the nano-based drilling fluids can play an important role in controlling loss circulation, eliminate spurt loss, and form a thin mud cake which may lead to a drastic decrease the chances of differential pipe sticking in highly permeable formation.

Further studies conducted by Srivatsa & Ziaja, (2012) to reduce fluid loss with the addition of NPs based biopolymer-surfactant fluid blend showed prospective results. They also tested the rheological properties with this new fluid loss additive. They concluded that polymer-surfactant blend had better properties as compared to only polymer or only surfactant based fluid.

These next generation drilling fluids must possess enhanced rheological properties along with superior thermal and filtration control properties. Major obstacles to be faced by these fluids include instability of additives, excessive fluid loss and disintegration of polymers, which result in sagging of weighing agents and rock cutting.

2.4.1 EFFECT OF METAL OXIDE NPs ON RHEOLOGICAL PROPERTIES OF DRILLING FLUIDS

Metal NPs tend to increase yield point, viscosity and gel strength of the drilling fluid due to their ability to form ionic bonds. However, oxides of some transition metals can be toxic and harmful to the environment.

2.4.1.1 EFFECT OF IRON OXIDE NPs

Barry et al., (2015) investigated the effect of iron oxide NPs on the viscosity and fluid loss control property of bentonite containing low solid particles. They observed that the viscosity and flow stress increased for 3 nm iron oxide NPs under LPLT and HPHT conditions as compared to 30 nm NPs. This increment in flow stress could be credited to increment in interaction strength related to the synergy effect of both homocoagulation and heterocoagulation between the particles in the drilling fluid. The addition of iron oxide NPs decreased the fluid loss at HTHP conditions as the NPs altered the surface charge leading to a restructuring of clay platelet interaction.

Arkoudeas et al., (2015) conducted experiments with iron oxide NPs in WBM and observed enhanced fluid loss control properties. They utilized LPLT and HPHT filter press to measure the fluid loss. They also observed that the small size of NPs seals the porous formations, thereby reducing formation damage.

Vryzas et al., (2016) examined iron oxide NPs for their effect on the rheological and fluid loss control properties of WBM. They concluded that the yield stress, flow consistency index (K) and flow behaviour index (n) increased at elevated temperatures with the addition of iron oxide NPs. Additionally, the fluid loss decreased with the formation of a thicker filter cake with the NPs.

Mohammed, (2017) investigated the temperature effect of iron oxide NPs based WBM for the rheological and weight loss properties. He observed that the yield point, plastic viscosity and apparent viscosity increased with the increase in bentonite content at room temperature.

2.4.1.2 EFFECT OF ZINC OXIDE NPs

Sayyadnejad et al., (2008) investigated the efficiency of bulk and nano zinc oxide particles to remove poisonous hydrogen sulfide from water based drilling fluid. They observed that the NPs of zinc oxide were able to remove hydrogen sulfide in 15 minutes during their laboratory trials, whereas, bulk zinc oxide required 90 minutes to do the same. They concluded that the use of NPs of zinc oxide to remove hydrogen sulfide from water based drilling fluids could minimize environmental pollution and prolong the availability of natural resources.

Aftab et al., (2016) investigated the effects of zinc oxide NPs-acrylamide composite (ZnO-Am) on the rheological and shale swelling property of WBM. They observed an increase in the thermal and chemical stability of the drilling mud with the addition of these NPs. The gel strength, viscosity, lubricity and fluid loss control properties were also improved. Additionally, shale swelling was also reduced with ZnO-Am NPs. Thus, they concluded that the ZnO-Am composite could be an appropriate drilling fluid additive to improve rheological and shale swelling properties of drilling fluids at elevated temperature conditions.

Afolabi et al., (2018) investigated the impact of zinc oxide NPs on the fluid loss control property of drilling fluids. The kinetics of filter cake formation and colloidal behaviour of the NPs were observed to derive a novel model predicting the effect of NPs on the filtration process. The fluid loss volume decreased with the zinc oxide NPs as these NPs reduced the permeability of the filter cake owing to their ability to form fine dispersions and tight packing structures (plugging capability of NPs).

2.4.1.3 EFFECT OF SILICA (SiO₂) NPs

Various researches have performed experiments with SiO₂ NPs as an additive to enhance the rheological properties of the drilling fluid due to its ease of availability. Initial researches by Javeri et al., (2011) involved the use of SiO₂ NPs (40-130 nm) to develop an all-new drilling fluid which successfully

reduced the formation damage by increasing the thickness of the mud cake by 34%.

Mao et al., (2014) used a hydrophobic polymer based SiO₂ nano-composite formed by inverse micro-emulsion and sol-gel method. The results were quite drastic as 0.5% of the nano-composite enhanced the rheological properties as well as provide better thermal stability and lubricity. It also helped in reducing the filtrate losses up to 69% under high temperature and pressure conditions.

Li et al., (2016) focused on mixing common materials like Bentonite (22.5 grams), Potassium Chloride (KCl) (0.25% by weight) and SiO₂ NPs (0.20 g) to freshwater (350 mL) to design a WBM. The addition of these NPs enhanced the rheological properties and reduced the filtrate losses. The concept of Smart water-based muds using SiO₂ NPs (0.1%-03% by weight) is gaining popularity as it can replace the oil-based muds in a directional and horizontal well, thereby reducing the drilling and completion problems in the wellbore. Further, SiO₂ is quite sensitive to pH and hence it enhances the properties of the mud at high values of pH according to Salih et al., (2016).

Investigations were carried out by Ismail et al., (2016) to study the effect of SiO₂ NPs on polymers such as High Viscosity Carboxymethyl Cellulose (HV-CMC), Low Viscosity Carboxymethyl Cellulose (LVCMC), xanthan gum and Potassium Chloride or Sodium Chloride treated Bentonite drilling fluids. It was observed that by mixing 0.2 g of LV-CMC and 0.3 g of xanthan gum to 25 g/500 g of Bentonite and 2.5 g KCl, also adding 0.25 g of SiO₂ NPs results to the maximum yield stress of 10 Pa. API filtration tests showed that 4.5% reduction in filtrate loss. However, adding 0.2 g and 0.3 g of SiO₂ NPs resulted in an increase in the fluid loss by 8.7% and 13%.

Kang et al., (2016) utilized 10-20 nm SiO₂ spheres with WBM and OBM for strengthening shale wellbore. Due to the high thermal stability and ion compatibility of SiO₂ NPs, they increased the plastic viscosity and yield point of the drilling fluids as well as decreased fluid loss. Additionally, the SiO₂ NPs

decreased the imbibition amount and swelling rate of the shale sample. The plugging effect of SiO₂ improved Young's modulus of shale, thereby strengthening wellbore stability. However, with OBM, the SiO₂ NPs did not have any promising results.

Elochukwu et al., (2017) modified the surface of SiO₂ NP with a cationic surfactant alkyl benzyl dimethyl ammonium chloride to improve the cutting carrying capacity of WBM and compared the results with unmodified SiO₂ NPs. They concluded that with the modified SiO₂ NPs, the yield point and plastic viscosity of the WBM increased. Consequently, the cutting carrying capacity improved as compared to unmodified and base WBM.

2.4.1.4 EFFECT OF COPPER OXIDE (CuO) NPs

William et al., (2014) investigated the enhancement in thermal, electrical and rheological properties of WBM with the addition of CuO NPs. They concluded that the thermal and electrical properties of CuO NP based WBM increased by 35% as compared to base WBM. The thermal stability of nano based WBM further preserved the rheological properties of the mud.

Ponmani et al., (2016) investigated the fluid loss control property of CuO and ZnO NP based WBM in addition to their thermal and electrical property. They concluded that due to the enhanced thermal stability of the CuO NP based WBM, it could prove to be an excellent candidate in HPHT wells. The optimum concentration of CuO NP was observed to be 0.02 wt%.

2.4.1.5 EFFECT OF TITANIUM DIOXIDE NPs

Ismail et al., (2014) conducted experiments with titanium dioxide NPs in WBM. They observed that the yield point, plastic viscosity, gel strength and fluid loss control increased with titanium dioxide NPs as compared with base WBM. The fluid loss reduced by 50% with NPs. The surface tension of the NP based WBM increased with an increase in the concentration of the NPs.

Cheraghian and Hendraningrat, (2016) investigated the effect of titanium dioxide NPs on EOR and drilling fluids. They concluded that the yield

point, consistency index (K) and flow behaviour index (n) increased with the addition of NPs. The thermal conductivity of the WBM also increased with NPs, thereby providing better lubricity and cooling of the drill bit.

2.4.1.6 EFFECT OF ALUMINIUM OXIDE NPs

Amarfio E. M. and Abdulkadir M., (2015) have found that aluminium oxide NPs (Al_2O_3 NP) when dispersed in water based bentonite drilling fluid, shows superior temperature stability by maintaining the shear stress at variable shear rates. Additionally, they developed a predictive model for estimating aluminium oxide mass fractions and shear rates at drilling temperatures above $100\text{ }^\circ\text{C}$.

Sajjad et al., (2016) investigated the effects of two different synthesis methods of aluminium oxide NPs on bentonite free water based drilling fluid. 1% aluminium oxide NPs in the drilling fluid displayed decreased values of plastic viscosity, effective viscosity, dynamic viscosity and yield stress. Furthermore, it increased the amount of friction factor and velocity.

Khaled and Hassan, (2017) have observed an increase in rheological parameters like yield stress and gel strength thereby increasing the bottom hole cleaning efficiency with the use of aluminium oxide NPs in a water based bentonite mud. A substantial decrease of 45% in the fluid loss was also observed with a gradual increase in aluminium oxide NPs concentration from 0.5% to 1.5% with a reduced mud cake thickness. Comparing aluminium oxide with SiO_2 NPs in water based mud, the former showed better enhancement of rheological and filtration properties.

2.4.2 EFFECT OF CARBON NANOTUBES (CNT) ON THE RHEOLOGICAL PROPERTIES OF DRILLING FLUIDS

Samsuri and Hamzah, (2011) conducted studies on the significance of MWCNTs as an additive in water based drilling mud to increase the cutting carrying capacity of the mud. The cutting slip velocity was determined as the percentage of cutting recovery from the bottom of the hole to the surface and

was examined to be increasing with the size of the cuttings. It was also reported that such multi-walled carbon nanotubes increased the viscosity of the mud. They observed that the addition of 0.005% of MWCNTs to the mud increased the cutting carrying capacity by 5-15% and by doubling the amount of MWCNTs to 0.01%, the cutting carrying capacity increased to 5-21%.

Friedheim et al., (2012) suggested that carbon nanotubes can be used to enhance the rheological stability of inverted emulsion drilling fluids at HPHT conditions, but failed to contribute to the control of fluid losses. Subsequent research was carried out to emphasize on nano based drilling fluids having CNTs as a functional additive. The observations made showed a significant increase in the thermal conductivity of CNT water-based mud by 23.2% (using 1% by volume of CNTs) at 27 °C, when the hydrophobic CNT gets treated with acids. In addition to this, the thermal conductivity increased to 31.8% at a temperature of 50 °C for CNT water-based mud. An increase of 43.1% in the thermal conductivity was reported for oil-based muds for the same concentration of CNTs.

Investigations were conducted by Ismail et al., (2014) to study the effect of carbon nanotubes on the rheological and filtration properties of drilling fluids. Studies showed that mixing 0.01 ppb multi-walled carbon nanotubes (MWCNTs) with oil-based drilling fluid tends to increase the yield strength, gel strength and emulsion stability of the drilling fluid. Ismail et al., (2016) additionally conducted a study on the importance of MWCNTs as a constituent in WBM to increase the cutting carrying capacity of the mud which is affected by the changes in downward gravitational force, upward buoyant force, a parallel drag force and a lifting force perpendicular to the direction of mudflow. The results showed that the cutting slip velocity was increased with the size of cuttings. The percentage of cutting from the bottom of the hole to the surface is used to determine the cutting carrying capacity.

Halali et al., (2016) investigated the role of carbon nanotubes (CNT) in drilling fluids to prevent water invasion into shales. Studies were performed to examine the effects of CNT on engineered polymer-based fluids. The

conclusion was made that the combination of CNT with PMMA (Polymethacrylic Acid Methyl Ester) exhibited a higher thermal conductivity at various temperature ranges and the thermal conductivity of the sample increased with temperature. At 394 K, the HPHT filter loss was reduced by 82% and a significant increase in the gel strength was studied. At 422 K, the fluid loss was reduced by 88% and the gel strength was enhanced. Further, at 450 K, the fluid loss was reduced by 90% and a slight improvement in the gel strength was noted. The derived conclusion states that CNTs play an important role in increasing the thermal properties of the mud and these enhanced fluids can be used in HPHT conditions.

2.4.3 EFFECT OF CLAY NPs ON THE RHEOLOGICAL PROPERTIES OF DRILLING FLUIDS

In a research conducted by Abdo and Haneef, (2013) synthesis of palygorskite, hydrous clay, was carried out to form a needle shaped structure with a diameter of 10-20 nm. The prime objective of this research was to study its stability and applicability in HPHT conditions. Comparing the results of palygorskite and montmorillonite clays showed that using montmorillonite alone did not enhance the rheological properties to much extent. However, using palygorskite NPs in small concentrations along with montmorillonite helped to enhance the rheology. The thermal stability of palygorskite enables it to be used as a rheology modifier and eliminate the use of expensive drilling fluid additives. Therefore, for optimized drilling performance including lubricity and wellbore stability, drilling fluids with palygorskite NPs could be utilized.

Shakib et al., (2016) investigated the effect of nano clay as well as some other NPs on the fluid loss control property of WBM. Nano clay was able to reduce fluid loss by 5 % more in comparison to other additives as it increased the viscosity of the WBM and formed a low permeability filter cake.

2.4.4 EFFECT OF GRAPHENE ON THE RHEOLOGICAL PROPERTIES OF DRILLING FLUIDS

Graphene has emerged as one of the most promising NPs because of its unique properties. Graphene is the thinnest material known to man and is also incredibly strong - about 200 times stronger than steel. It is a great conductor of electricity, heat and is optically transparent, yet so dense that it is impermeable to gases. It has interesting light absorption abilities. It shows enhanced physical as well as electrical properties, such as high tensile strength, Young's modulus, thermal conductivity and electron mobility (James and Tour, 2012). There have been significant studies to investigate the effect of graphene oxide on the rheology of drilling fluids. A study conducted by Kosynkin et al., (2012) showed that a combination of large flake graphene oxide and powdered graphene oxide in a 3:1 ratio in an aqueous dispersion of xanthan gum solution showed an average fluid loss of 6.1 ml over 30 minutes with a thin filter cake of approximately 20 μm . The cross polarised microscopy of the water-based solution of graphene oxide showed the presence of a crystalline domain that enhances the filtration loss control of graphene oxide. Aftab et al., (2017) found that an increase in plastic viscosity (PV) was directly proportional to the graphene nanoplate (GNP) concentration with reduced filtrate loss. This gave a possible explanation of the increase in PV by the addition of GNP due to the increase in resistance between the nanoplatelets, micro additives and the liquid medium of mud. In a study conducted by Ho et al., (2016), the rheological effect of hydrogenated oil-based drilling fluid when dispersed with graphene sheets, showed an increase in viscosity. Similar results were obtained by researchers such as Kole and Dey, (2013) who concluded in their studies that the thermal conductivity and viscosity also increased with the addition of graphene sheets. Graphene nanosheet is the thinnest two dimensional material in the world and this exceptional carbon nanostructure has proved to be a promising technology for application in several fields (Li et al., 2008).

2.5 COMPUTATIONAL FLUID DYNAMICS (CFD) STUDIES TO UNDERSTAND SOLID-LIQUID HYDRODYNAMICS IN ANNULAR REGION

Several researchers have conducted extensive experimental investigations on various drilling parameters. The ever-changing drilling programs and equipment functioning through several well geometries affect the performance of the drilling fluids. The performance of drilling fluids vastly depends on their cutting carrying capacity which is driven by their rheological properties. Rheology of drilling fluid is a study of prime importance as it helps us to comprehend its downhole performance. In addition to several functions, one of the most crucial roles of drilling fluid is to continuously clear and carry cuttings from downhole to surface. This effectiveness directly influences the rate of penetration (ROP), prevents downhole problems like pipe stuck-ups and maintains a fair magnitude of bottom-hole torque and drag.

Al-Kayiem et al., 2010 studied the effect of drilling fluid on cutting sphericity and concluded that spherical particles are much easily cleared as compared to non-spherical particles. Various studies and field experiences have shown that the cuttings tend to sag at the lower part of the annulus due to gravity. Wei et al., (2013) studied a cutting transport model during underbalanced drilling where they found that the larger cuttings tend to deposit on the lower side of the annulus.

This progressive deposition of the cutting bed in most cases results in excessive torque and drag. If persistent, this situation may also result in mechanical pipe stuck, thereby increasing non-productive time (NPT) (Eren et al. 2013). Any inadequacy in this attribute will lead to sagging of cuttings especially in an inclined well or directional well. Hence, improving the rheological properties of drilling fluids can tackle and mitigate this problem.

Moreover, drill pipe rotation also induces a tangential velocity or a swirling effect to the cutting phase which helps in their effective removal (Ozbayoglu et al., 2008; Sanchez et al., 1997).

To quantify and perceive the cutting carrying capacity of drilling fluid, Han et al. (2010) proposed a set of numerical multiphase models with a solution that

was validated by an experimental flow loop hydrodynamic study. They also emphasized on the importance of the viscoelastic nature of drilling fluids for suspension of cuttings. Experimental flow loop results in terms of pressure and volume fractions were compared to a proposed mathematical model. The simulation results were consistent with the experimental observations. Although in his mathematical model, the drilling fluid was considered to be a Power Law fluid.

In a CFD study, Ofei et al. (2014) considered the drilling fluid as yield Power Law fluid (HB model) and found that fluids having a higher consistency index (K) clear more cutting in the larger section of the annulus, while for fluids having a lower consistency index (K), cutting velocity at the lower part is higher. Additionally, they considered an eccentric annular geometry for their study. A CFD-DEM was adopted by Akhshik et al., (2015) to study the effects of drill pipe rotation on the cutting transport ability of drilling fluids with drill pipe rotation, well inclination, rate of penetration and fluid inlet velocity. They compared their cuttings concentration and velocity contours with the experimental data and obtained satisfactory results. However, there are a few limitations in this study, namely the drill pipe rotation is fixed about its own axis and the cuttings are assumed to be homogeneously spherical in shape. Dewangan and Sinha, (2016) investigated borehole cleaning by the distribution of the cuttings concentration within the annulus cross section using two phases Eulerian based CFD approach. They observed that the higher bulk viscosity is a more suitable candidate for better removal of cuttings, aided by drill pipe rotation.

Mme and Skalle, (2012) evaluated three different mud types to evaluate the constants of Power Law model and carried out CFD simulations for cutting carrying capacity in the annulus. GAMBIT was used for modelling and FLUENT for simulation. They found that finer sand particles with high sphericity are the easiest to displace from wellbore using low viscosity muds.

In the CFD studies discussed above, the drilling fluids were considered to obey a Power Law model which is a two parametric function for stress values. However, a drilling fluid is best known to fit a Herschel Bulkley (HB) model, a three parametric model equation. Therefore, in our work, HB fluid parameters,

which are calculated from the rheological studies, are incorporated in the CFD model to solve for velocity, pressure and volume fraction for both the drilling fluid and cutting phases using finite volume approach.

2.6 CHAPTER CONCLUSION

Nanotechnology has shown a lot of potential in its application to improve the performance of drilling fluids. This paper provides a summary of the work carried out to address the challenges and limitations of conventional fluids used in the industry. It is concluded that the use of nanotechnology has not been fully utilized for critical situations such as HPHT, drilling of unconventional or deep offshore wells. The main purpose of this review is to present the effect of the NPs on the rheological properties of drilling fluids based on the types of NPs used. Although various researches were carried out in this field, it is still a challenge to make the nano-enhanced drilling fluids homogeneous in composition, cost-effective, periodically stable and environment friendly without compromising the rheological and filtration properties. This review presents a gist upon the effect of NPs on the rheological and filtration properties of drilling fluids. The following conclusions can be drawn on the basis of this review:

1. The concentration and average size of the NPs affect the properties and performance of the drilling fluids.
2. Studies have revealed that these NPs provide a greater surface area to volume ratio and help in enhancing the rheological properties of the drilling mud at HTHP conditions.
3. Studies have also revealed that the NPs are effective under low concentration and could be used under LPLT conditions but there is less room for the lower concentrations of these NPs to be used at HPHT conditions.
4. It has also been concluded that the NPs enhance the cutting carrying capacity of the drilling fluids by increasing the gel strength of the drilling fluids.

5. Studies have revealed that NPs play a vital role to reduce the permeability of the shale formations by occupying the pores of the formation.
6. Studies have also revealed that the NPs provide stability to the wellbore due to their capacity to increase the fracture pressure and hence reduce the chances of kick.
7. The efficiency and stability of the drilling fluids are overall enhanced with the help of NPs.
8. CFD studies can be a useful method of investigation to evaluate currtng carrying performance and hydraulic study of drilling fluids.

CHAPTER 3

EFFECT OF SILICON DIOXIDE NPs (SiO₂ NP) ON NDDF

3.1 SYNTHESIS OF SILICA (SiO₂) NPs

Silica NPs (SiO₂ NP) used in the current study were synthesized by sol-gel process. This process primarily consists of two stages: hydrolysis of the precursor TEOS (Tetraethyl Orthosilicate) and condensation to form the entire SiO₂ structure (Rahman & Padavettan, 2012). During the network formation process, a large amount of solvent is also impregnated in the network and thus a gel is formed. In the current process, 1 gram of TEOS, 3 grams of ammonia and 4 grams of ethanol was added in water and magnetically stirred at ambient conditions for 1.5 hours. Further, 2 grams of TEOS and 8 grams of ethanol were added and stirred for the next 2 hours. A gel-like solution was eventually formed which was kept in the oven for 24 hours at 65 °C. The dried gel in amorphous form was then calcined for 4 hours at 400 °C to obtain a crystalline structure and ground using an agate motor. X-ray diffraction (XRD) patterns of NPs were measured using Bruker Advance D8 X-ray diffractometer with $\lambda = 1.541 \text{ \AA}$. The applied voltage used in the instrument was 40 Kv and the current was 30mA. The θ range was $2\theta = 20$ to 80° . The X-ray data (count) were collected with a scan rate of $10^\circ \text{ min}^{-1}$ and a step size of 0.2° . The crystallite sizes (D) of the samples were calculated using the Scherrer equation (Patterson, 1939) as given by:

$$D = \frac{0.94 \lambda}{\beta \cos \theta} \quad \text{Eqn. (3.1)}$$

Peaks from XRD (Fig. 3.1) were observed at 21.96° , 27.23° and 36.10° . Particle sizes ranging from 22 nm to 48 nm were obtained for SiO₂ NPs.

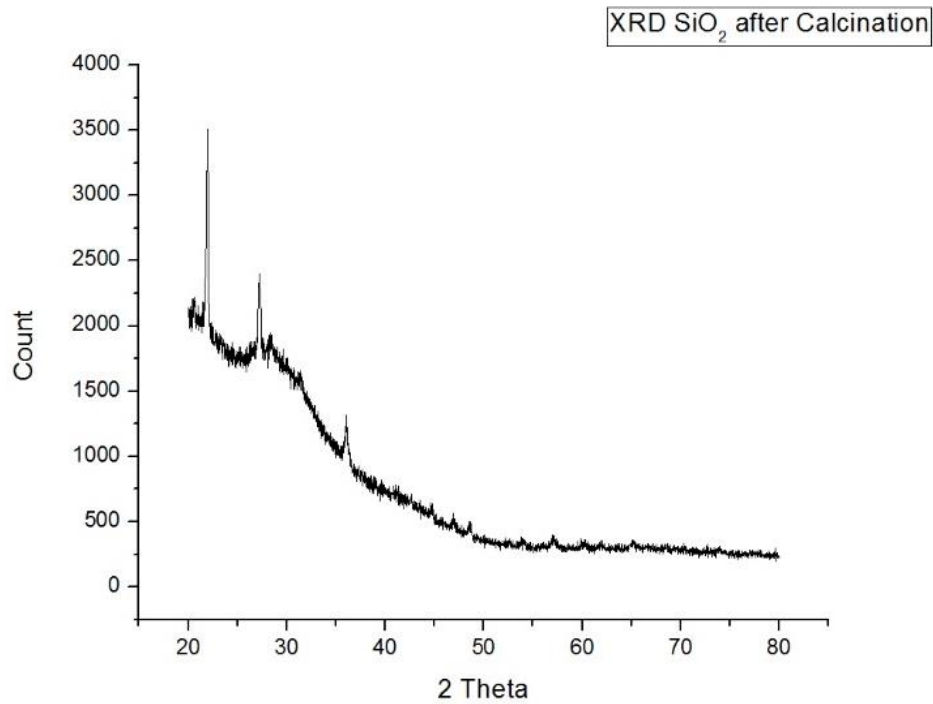


Fig. 3.1: XRD of SiO₂ NP after calcination

3.2 RESULTS AND DISCUSSIONS

3.2.1 YIELD POINT (YP)

Cutting carrying capacity of drilling fluids is greatly affected by the yield point (YP) of the fluid. YP was measured in a Fann viscometer, assuming the fluid behaviour as a Bingham Plastic Model. Hence, the YP from this type of rotational viscometer does not provide the magnitude of the true yield nature of the fluid. Practically, a higher YP often contributes to higher frictional pressure losses. A higher YP is often demanded in large diameter holes for efficient hole cleaning (Power & Zamora, 2003). The YP for the Bingham Plastic model is given by:

$$YP = \theta_{300} - PV \quad \text{Eqn. (3.2)}$$

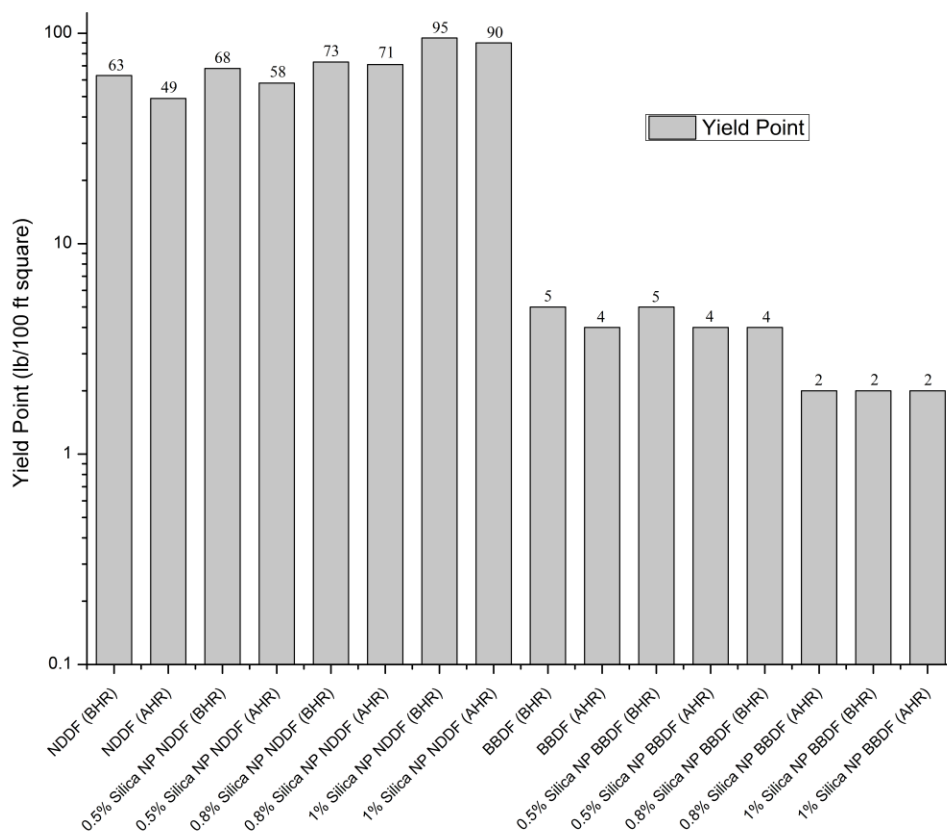


Fig. 3.2: Yield point of all the SiO₂ NP based drilling fluids

From Fig. 3.2, it can be observed that the YP of NDDF increases with the increase in SiO₂ NPs concentration. The addition of 0.5 wt% SiO₂ NPs increases the YP of NDDF by 8 % while the addition of 1 wt% SiO₂ NPs showed a significant increase in YP by 50 %. Besides, with an increase in temperature, fluids often show a decrease in YP and viscosity. Likewise, NDDF showed a reduction in YP by 22 % when exposed to 80 °C. For 0.5 wt% SiO₂ NP NDDF, the margin of reduction was observed to be reduced to 14.7 %. Furthermore, with the increase in the concentration of SiO₂ NPs the magnitude of reduction was further scaled down by 2.7 % for 0.8 wt% SiO₂ NP NDDF and 5.2 % for 1 wt% SiO₂ NP NDDF. Hence, it can be concluded that along with the increasing magnitude of YP, SiO₂ NPs showed a significant amount of temperature stability with the increase in their concentration.

Observations for the addition of SiO₂ NPs with bentonite based drilling fluid (BBDF) showed no change in YP for 0.5 wt% SiO₂ NP BBDF, whereas the YP decreased with an increase in concentration by 20% for 0.8 wt% SiO₂ NP BBDF and 60% for 1 wt% SiO₂ NP BBDF. At high temperatures, a 20% degradation of YP for BBDF was observed; while for 0.5 and 0.8 wt% SiO₂ NP BBDF, the decrease was 20% and 50% respectively. With 1 wt% SiO₂ NP BBDF, no change was observed in the YP.

From the preceding observations, it can be inferred that for the case of NDDF, SiO₂ NPs, for an increasing concentration, shows an exponential rise in YP of the drilling fluid. The magnitude in the reduction of YP at higher temperatures is also narrowed due to the addition of SiO₂ NPs. When doped with BBDF, SiO₂ NPs show a substantial decrease in the YP with an increase in concentration as well as temperature, making them unfeasible for any high temperature applications.

3.2.2 VISCOSITY

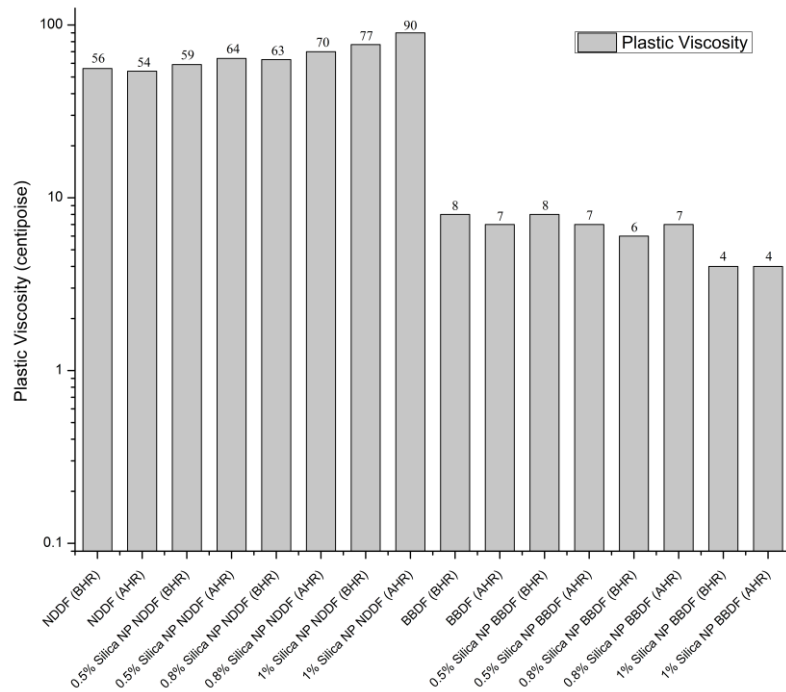


Fig. 3.3: Plastic viscosity of all the SiO₂ NP based drilling fluids

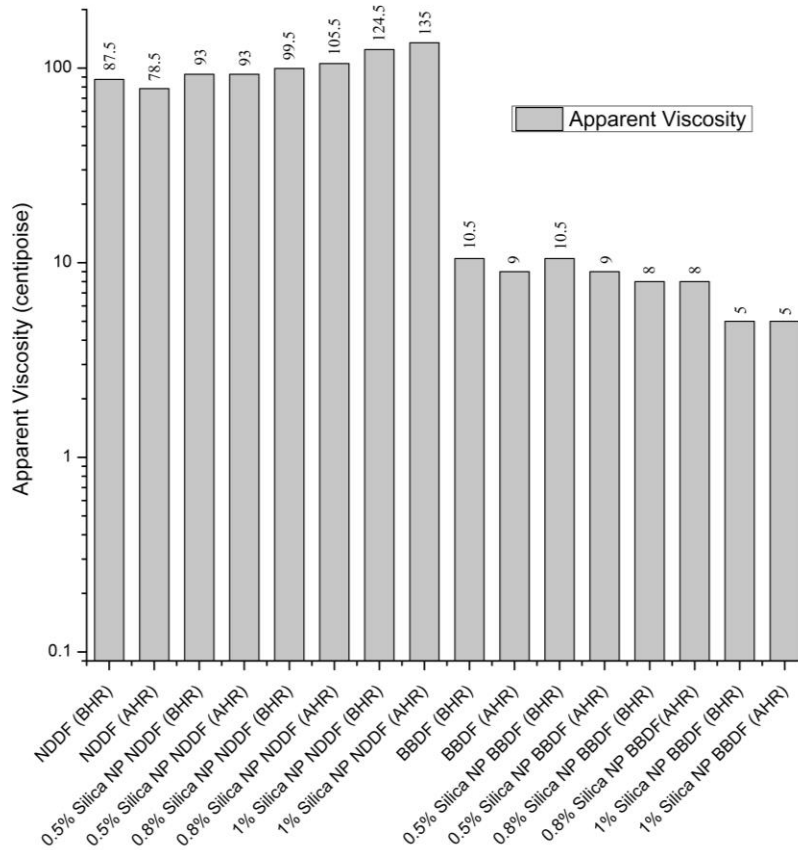


Fig. 3.4: Apparent viscosity of all the SiO₂ NP based drilling fluids

From Fig. 3.3 and 3.4 it can be observed that base NDDF showed a reduction in viscosities; both apparent and plastic with an increase in temperature. For 0.5 wt% SiO₂ NP NDDF, an increase of 5% in viscosity was observed. Furthermore, it was increased by 12.5% and 37.5% for 0.8 and 1 wt% SiO₂ NP NDDF respectively. The addition of 0.5 wt% SiO₂ NP had no effect on the base NDDF whereas; the viscosity was reduced by 25% for 0.8 wt% SiO₂ NP BBDF and 50% for 1 wt% SiO₂ NP BBDF. Overall, the impact of SiO₂ NP with the increase in concentration on the viscosities of BBDF was thinning. This observation can again be explained due to the fact that SiO₂ NPs tend to unite on the clay plates of bentonite and prevent the maintenance of attractive forces between clay plates. This may have resulted due to the deflocculating of clay plated as in the case of SiO₂ NP

based drilling fluid. Mud thickening attribute of SiO₂ NP doped NDDF was observed from the increase of both apparent and plastic viscosities with the increase of NP concentration. The addition of SiO₂ NPs in BBDF causes a reduction in the viscosity of the drilling fluid to a great margin. The mud thinning behaviour of SiO₂ NPs escalates with the gradual increase within its concentration.

3.2.3 GEL STRENGTH

Gel strength (GS) is the measure of the shear stress at a very low shearing rate after the mud is left static for some time. It imparts the ability of mud to suspend cuttings and weighted materials when there is a pause in circulation (Bern, Zamora, Slater, & Hearn, 1996). In situations where excessive barite is used to control high pore pressure, it helps to counter barite sagging problems. An increase in gel strength can be observed due to the introduction of ultra-fine solids in the liquid phase and in these conditions, more circulation pressure is needed to displace the mud after a prolonged static condition.

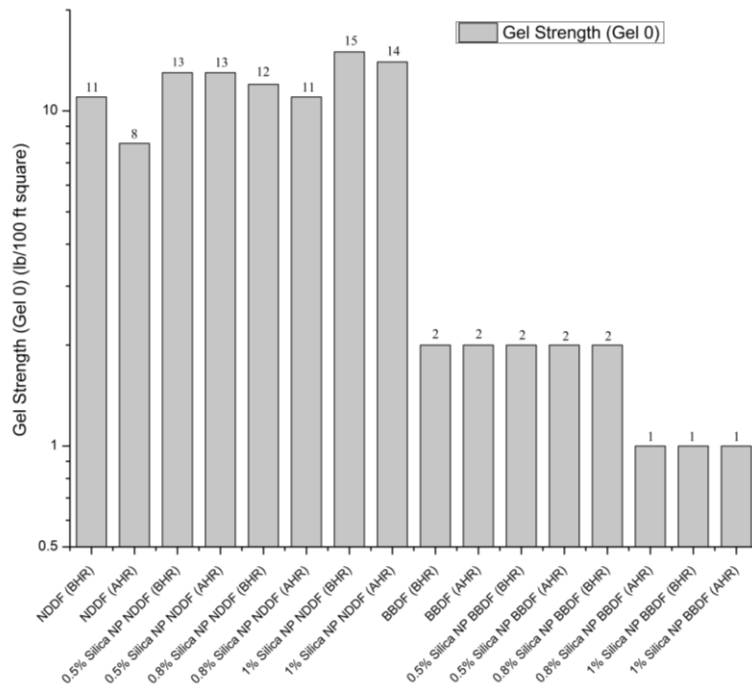


Fig. 3.5: Gel Strength (Gel 0) of all the SiO₂ NP based drilling fluids after a resting time of 10 secs

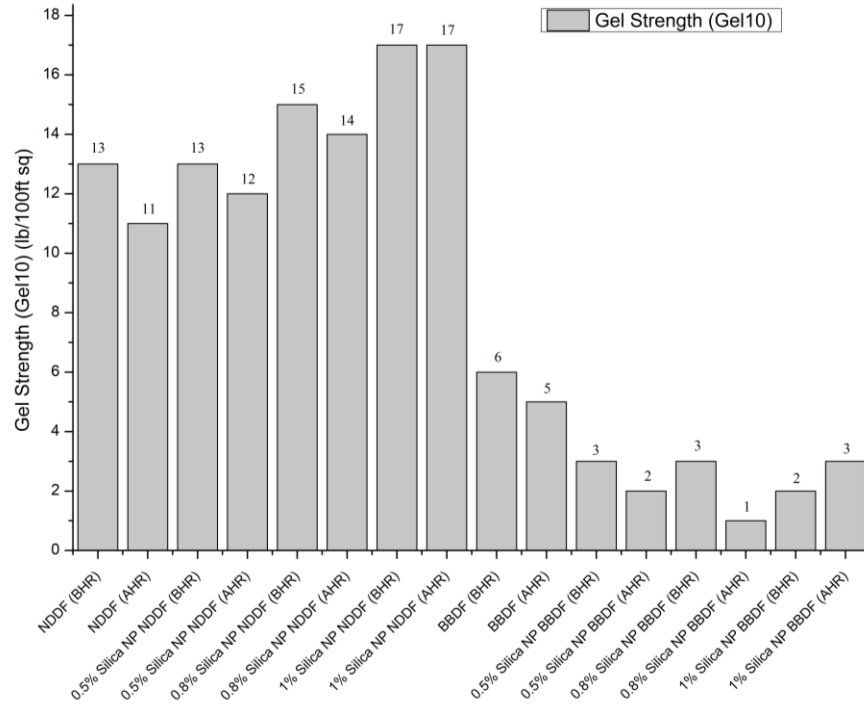


Fig. 3.6: Gel Strength (Gel 10) of all the SiO₂ NP based drilling fluids after a resting time of 10 mins

Apart from observing an increase in gel strength with SiO₂ NP's concentration it also induced the property of thermal stability which aided to preserve the gel strength at bottom hole conditions. This feature will assure proper suspension of rock cuttings and barite thereby preventing sagging issues. An increase in gel strength by 7.6% was observed only for 0.8 wt% SiO₂ NP NDDF while all the other concentrations decreased the gel strength by a very small margin. The variation in gel strength at AHR condition was significant for 0.5 wt% SiO₂ NP BBDF, which decreased it by 27.2 % for Gel 0 and 21.4% for Gel 10 measurements. SiO₂ NPs had a detrimental effect on BBDF. For this type of drilling fluid, it reduced the gel strength significantly in higher concentration as it is deflocculating in nature. The use of SiO₂ NPs is not recommended for high density muds as sagging issues might emerge due to low suspending capacity. SiO₂ NPs when used with NDDF results in a non-linear trend of the gel strength which produces the optimal strength maxima at 0.8% concentration. A detrimental trend

was observed within BBDF with the addition of SiO₂ NPs for all variants of NP concentration.

3.2.4 API FILTRATE LOSS TEST MEASUREMENTS

The resultant pressure at any point in the wellbore is essentially outwards or directed towards the formation. This pressure forces the mud to invade the formation. The solid part of the mud forms a thin plaster around the wellbore and the filtrate moves further into the formation. This filtrate loss in shale formations can cause clay swelling or at production zone can alter the properties like wettability and relative permeability of the pay zone. These all contribute to further complexities and depreciating the integrity of shale formation in the first case and in the later, production from a well (Mahto & Sharma, 2004). Hence minimizing the filtrate loss is of prime importance to impart smooth drilling operations or to avoid production problems.

Fig. 3.7 and 3.8 report fluid loss measurements of SiO₂ NP NDDF at BHR and AHR conditions.

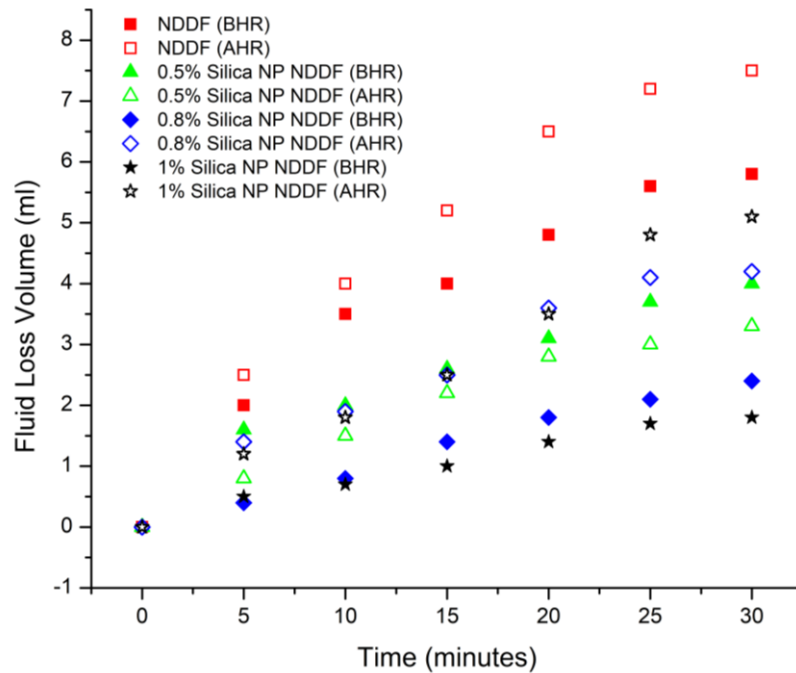


Fig. 3.7: Fluid loss vs. time all the prepared drilling fluid samples

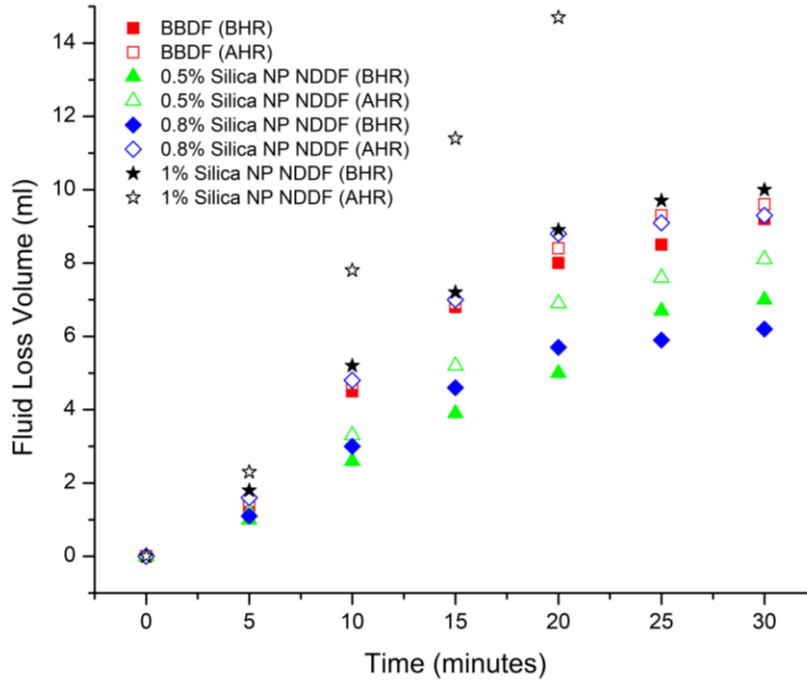


Fig. 3.8: Fluid loss vs. time all the prepared drilling fluid samples

NDDF typically emerged as a fluid loss control fluid, which prevents the contamination of the production zone or in shale sections clay swelling. the addition of 0.5 wt% SiO₂ NPs, reduced fluid loss by 31% while the addition of 0.8 wt% SiO₂ NPs reduced it by 58.6%. The fluid loss is best controlled for 1 wt% SiO₂ NP NDDF that reduced it by 69%. This phenomenon takes place as the NPs block the pore spaces, which prevent to provide a clear passage for the fluid to pass through. But, in cases, with 0.8 and 1 wt% SiO₂ NP NDDF, the fluid loss increased in bottom hole conditions due to excessive agglomeration of SiO₂ NPs. These agglomerations in higher concentrations do not provide enough particles to block the pore throats. It was observed that BBDF has a decrease in fluid loss at surface conditions by 31% when compared to NDDF. It also had a less reduction in fluid loss at the bottom hole condition by 17.5%. Similarly, for the 0.5 wt% SiO₂ NP BBDF fluid loss was reduced by 13.8% at the surface condition and further reduction in fluid loss property in the bottom hole condition was restricted to 4% when compared to 29% for NDDF and 17.5% for BBDF respectively.

On the other hand, with the increase in concentration, the agglomeration of NPs prevailed and hence filtrate loss increased. This phenomenon was seen with 0.8 wt% SiO₂ NP BBDF where the filtrate volume exceeded that of base NDDF by almost 3.4%. SiO₂ NPs, when used in conjunction with BBDF, provided a reduction in filtrate loss by 24% and 33% as seen with 0.5 and 0.8 wt% SiO₂ NP BBDF respectively. Furthermore, an increase in filtrate loss by 8.7% was observed for 1 wt% SiO₂ NP BBDF with even more detrimental results at SiO₂ hole conditions, as it increased by 66%. This can be attributed to the fact that SiO₂ NPs tend to agglomerate at higher concentrations and due to overall viscosity reduction of the fluid.

These observations inferred that NDDF when doped with SiO₂ NP, presented a substantially decreasing trend of fluid loss of the mud with increasing concentration of the NP additive, whereas an increase of fluid loss was observed at the wellbore conditions. A meagerly decreasing trend of fluid loss volume was observed with the addition of SiO₂ NPs in BBDF at increasing concentrations, except at 1 wt% SiO₂ NP BBDF, where the fluid loss increased with the addition of NPs. It also failed in preventing fluid loss in bottom-hole conditions. Hence, SiO₂ NPs, at excessive concentrations are not worthy in terms of fluid loss control.

3.3 DETERMINATION OF OPTIMAL HERSCHEL BULKLEY (HB) PARAMETERS BY GENETIC ALGORITHM OPTIMIZATION

Table 3.1 Optimal values of HB parameters by GA

Drilling Fluid Type	Condition	True YP	<i>K</i>	<i>n</i>	SSE
NDDF	BHR	0.58	1.53	0.58	0.74
	AHR	1.16	0.95	0.63	0.14

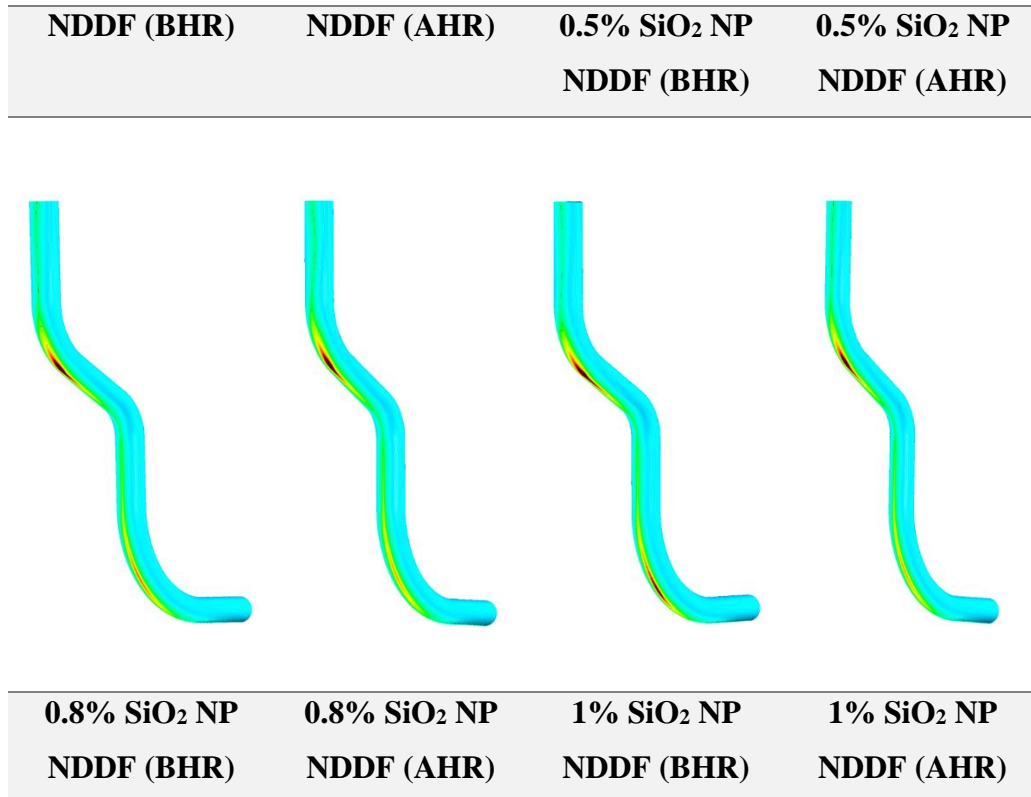
0.5% weight SiO ₂ NP	BHR	0.26	1.75	0.57	0.46
	AHR	1.5	1.13	0.63	0.16
0.8% weight SiO ₂ NP	BHR	0	2.32	0.54	1.4
	AHR	0.82	1.62	0.6	0.32
1% weight SiO ₂ NP	BHR	0.46	2.71	0.55	0.77
	AHR	0.96	2.1	0.60	0.21
Bentonite Base Drilling Fluid	BHR	0.45	0.06	0.75	0.09
	AHR	0.55	0.04	0.81	0.1
0.5% weight SiO ₂ NP	BHR	0.17	0.08	0.71	0.03
	AHR	0.29	0.05	0.77	0.02
0.8% weight SiO ₂ NP	BHR	0.86	0.02	0.86	0.07
	AHR	0.88	0.01	0.98	0.05
1% weight SiO ₂ NP	BHR	0.38	0.03	0.77	0.03
	AHR	0.47	0.01	1.01	0.06

Table 3.1 represents calculated HB parameters by minimizing SSE by means of GA. It can be observed that the consistency index (K) decreases with an increase in SiO₂ NP concentration. Flow index (n) for all the fluids indicates shear thinning nature. The range is typically from 0.55 to 0.64. It is noteworthy to state that at higher temperatures drilling fluid's shear thinning nature increase by a small margin as the value of flow index declines.

3.4 RESULTS AND DISCUSSIONS ON FLOW BEHAVIOUR FROM CFD STUDIES IN ECCENTRIC WELLBORE ANNULUS

3.4.1 EFFECT OF SiO₂ NPs ON CUTTING VOLUME FRACTION

One of the most imperative parameters that govern an effortless drilling operation is cutting deposits. In a complex wellbore geometry, where bends and tortuosity are its essences, the drilling fluid losses a significant momentum due to restrictions and change in directions along its path. In that case, rheological parameters of the drilling fluid play a vital role to lift the cuttings. Fig. 3.9 shows a trend in the sagging of cuttings from the drilling fluid continuous phase along with its flow in the annular region.



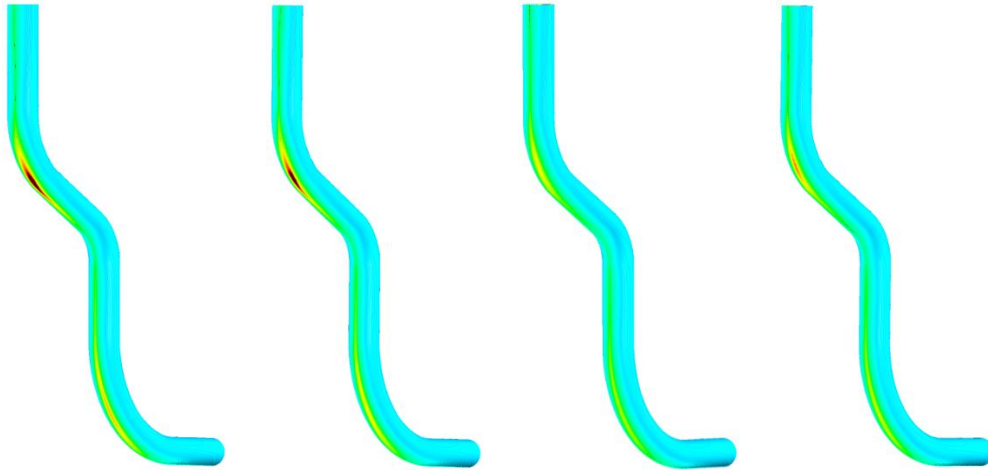


Fig. 3.9: Comparative side view of contours for cutting volume fraction ($V_{inlet} = 0.8$ m/s, cutting density and inlet volume fraction = 2550 kg/m³ and 10% respectively)

Table 3.2: Percentage volume retention of cuttings in annulus *vs.* different cases of concentration and temperatures. $(\text{Volume fraction of cuttings})_{annulus} - (\text{Volume fraction of cuttings})_{inlet} = (\text{Retention of volume fraction of cuttings})_{annulus}$

Cutting retention in terms of % total annular volume				
Sample / Temperature	Base NDDF	0.5 wt% SiO₂ NP NDDF	0.8 wt% SiO₂ NP NDDF	1 wt% SiO₂ NP NDDF
BHR	0.0875	0.0812	0.071	0.051
AHR	0.1025	0.0838	0.080	0.058

From the above CFD simulation results (Fig. 3.9), it is apparent that cutting transport in complex geometry wells is problematic, especially at higher

temperatures. This circumstance emerges owing to the retrogression of rheological properties of drilling fluids at these temperatures. The sagging of cuttings is higher at the upper build-up section as compared to the lower build-up section. Additionally, due to degradation in rheological parameters greater sedimentation of cutting phase can be observed in high temperature cases. Base NDDF at 30 °C shows lesser sagging at lower build-up section than at 80 °C; which shows segregation of cuttings at both the build-up sections. This can be observed in Table 3.2 where percentage retention of cuttings at annulus for BHR conditions is less (0.0875 %). This phenomenon has however been abridged in 0.5 and 0.8 wt% SiO₂ NP NDDF. Sagging at all bends at both 30 °C and 80 °C is barely noticeable for 1 wt% SiO₂ NP NDDF yielding a percentage retention of 0.0512 % and 0.058 % respectively.

3.4.2 EFFECT OF SiO₂ NPs ON VELOCITY PROFILE OF NDDF

To comprehend the variation in sweep efficiency of drilling fluids, the velocity profile is reported from CFD simulations at the onset of the 1st Build-up Section or Kick-off Point (KOP), Drop-off Section (DOS) and 2nd Built-up Section (BUS-2).

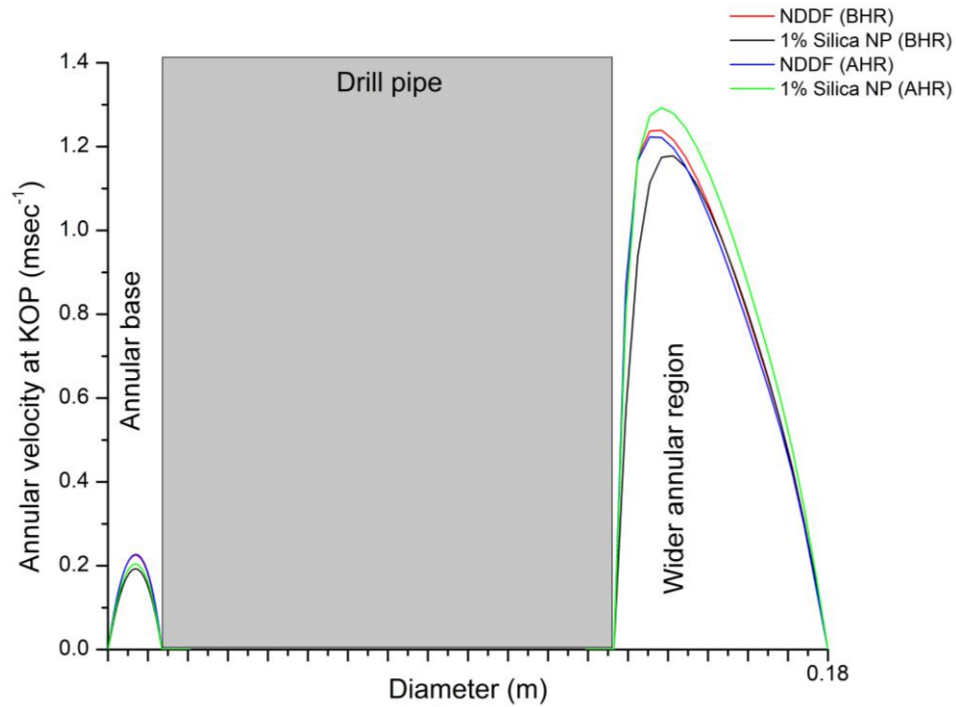


Fig. 3.10: Velocity profile at Kick-off Point (KOP) for base and 1% SiO₂ NP NDDF at BHR and AHR conditions

At the KOP and BHR conditions (Fig. 3.10), the annular velocity at the lower annular region (annular base) is the lowest for 1 wt% SiO₂ NP NDDF. In addition, lesser skewness in flow profile is displayed by 1 wt% SiO₂ NP NDDF compared to base NDDF thus showing superior sweep efficiency.

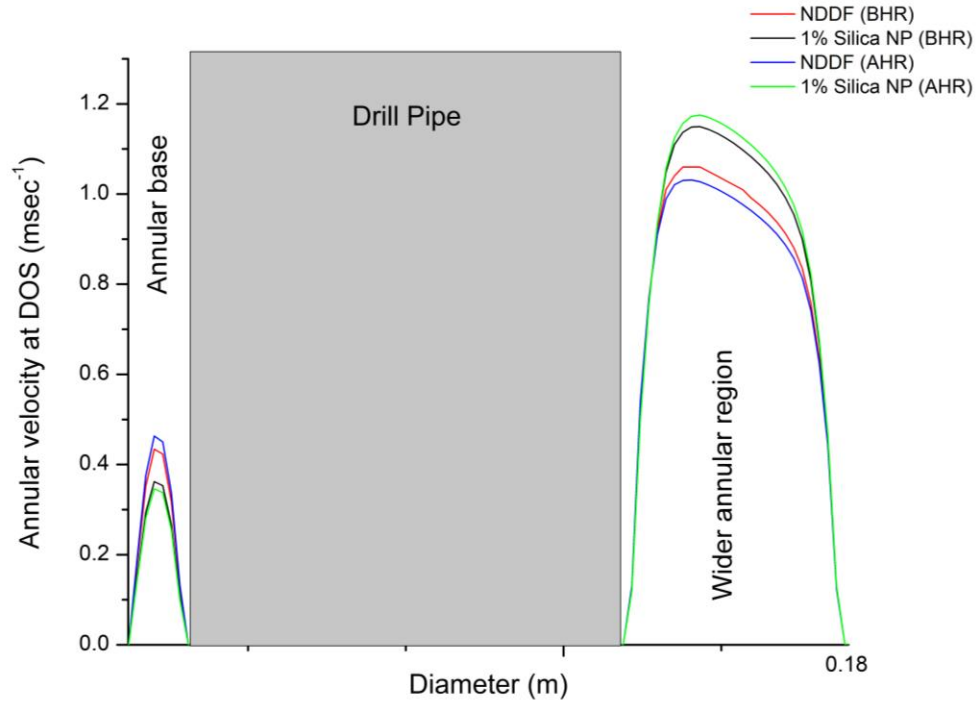


Fig. 3.11: Velocity profile at Drop-off section (DOS) for base and 1% SiO₂ NP NDDF at BHR and AHR conditions

At the drop off section (Fig. 3.11), 1 wt% SiO₂ NP NDDF shows the least velocity in the annular base region but the high velocity at the wider annular region. A blunt flow profile with less skewness can be noticed for 1 wt% SiO₂ NP NDDF at both the temperature conditions. However, compared to KOP profiles, the velocity profile at DOS is less sharp at the leading flow which generates higher sweep. Hence, sagging of cuttings is relatively lesser as compared to that at KOP.

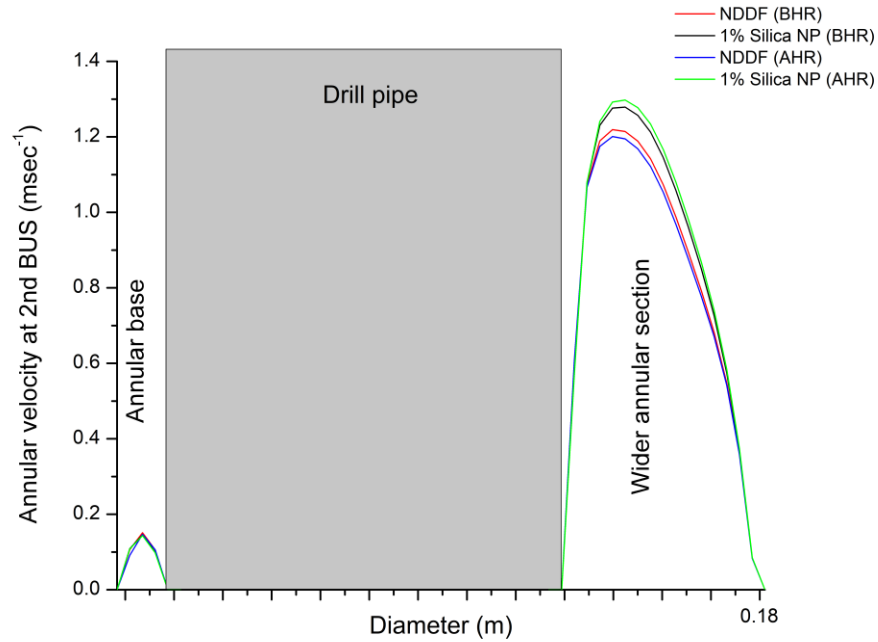


Fig. 3.12: Velocity profile at Build-up section (BUS) for base and 1% SiO₂ NP NDDF at BHR and AHR conditions

In Fig. 3.12, unlike the first build up section, 1 wt% SiO₂ NP NDDF shows greater velocity in the wide annular region, while at the annular base, all fluids bear similar velocity profile. On the contrary, deposition of cuttings is quite prominent in the case of base NDDF whereas, significantly less in the case of 1 wt% SiO₂ NP NDDF. This can be linked with a greater sweep area of 1 wt% SiO₂ NP NDDF. Moreover, alike KOP, the velocity profile is sharp and skewed towards the base side of the annulus.

3.4.3 EFFECT OF SiO₂ NPs ON PRESSURE DROP

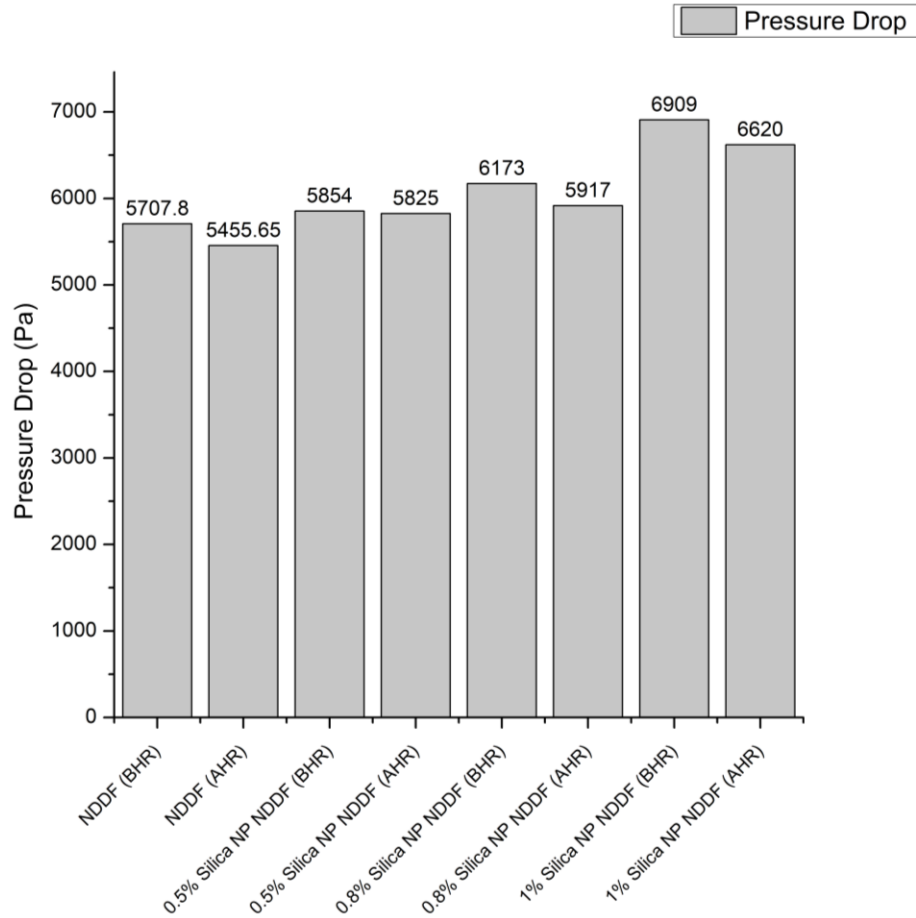


Fig. 3.13: Pressure drop of SiO₂ NP based NDDF

Fig. 3.13 represents values of pressure drop for all the SiO₂ based NDDFs. A general trend of increase in pressure drop can be observed with an increase in SiO₂ NP concentration. This is a consequence of an increase in the rheological properties of NDDFs due to the addition of SiO₂ NP. Pressure drop ranges for 0.08 psi/ft for NDDF (AHR) to 0.1 psi/ft for 1 wt% SiO₂ NP NDDF (BHR) across the entire length of the wellbore. These values are well in the range of flowability from a practical standpoint.

3.5 CHAPTER CONCLUSION

From the simulation studies, it can be concluded that 1 wt% SiO₂ NP NDDF displays the best borehole cleaning efficiency at both low and high temperatures. It owes its performance to good yield stress, a favourable value of flow index (n) and most importantly a higher as well as thermally stable value of consistency index (K). This enhancement in property can be an attribute of SiO₂ adsorption on the polymer chain of XCP due to hydrogen bond. This eventually promotes cross bridging amongst inter and intra molecular domain (Hu et al. 2017). Additionally, 1 wt% SiO₂ NP NDDF shows improved fluid loss control property as compared to base NDDF at both BHR and AHR conditions.

CHAPTER 4

EFFECT OF COPPER OXIDE NPS (CuO NP) ON NDDF

4.1 SYNTHESIS OF COPPER OXIDE (CuO) NPs

Precipitation method was adopted for the synthesis of Copper Oxide (CuO) NPs by using copper chloride (CuCl_2) and copper nitrate ($\text{Cu}(\text{NO}_3)_2 \cdot 3\text{H}_2\text{O}$). 0.1 M solution for each precursor was prepared by dissolving it in deionized water. Sodium Hydroxide (NaOH) solution (0.1 M) was added dropwise under vigorous stirring until a pH of 13-14 was attained. A black precipitate was obtained which was washed repeatedly by deionized water and successively with ethanol to neutralize the pH to 7. The precipitate was then dried at 80 °Celsius for 16 hours. Finally, the dried precipitate was calcined at 500 °C for 5 hours and ground (Malviya, Carpenter, Oswal, & Gupta, 2015). XRD (Fig. 4.1) was carried out for validation and particle sizes were calculated by using the Debye-Scherrer equation, given in Eqn. 3.1. From the XRD data particle size of CuO ranged from 27 nm to 53 nm.

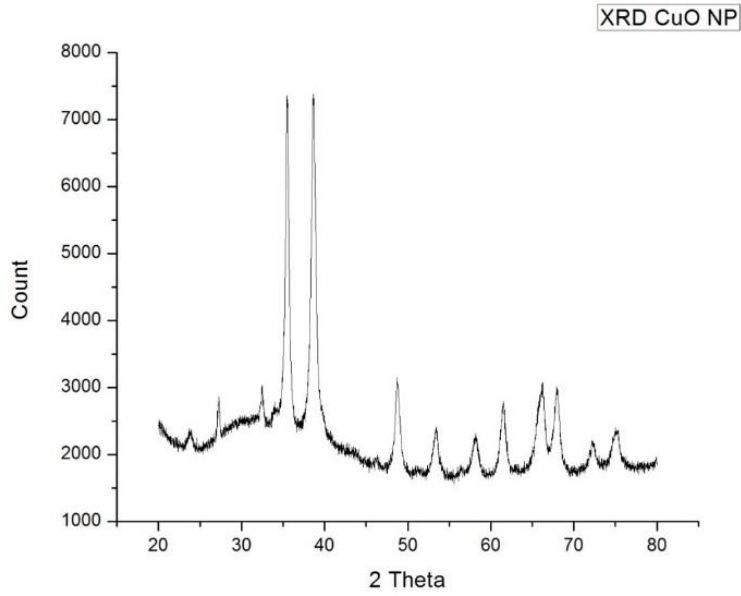


Fig. 4.1: XRD of CuO NP

4.2 RESULTS AND DISCUSSIONS

4.2.1 YIELD POINT

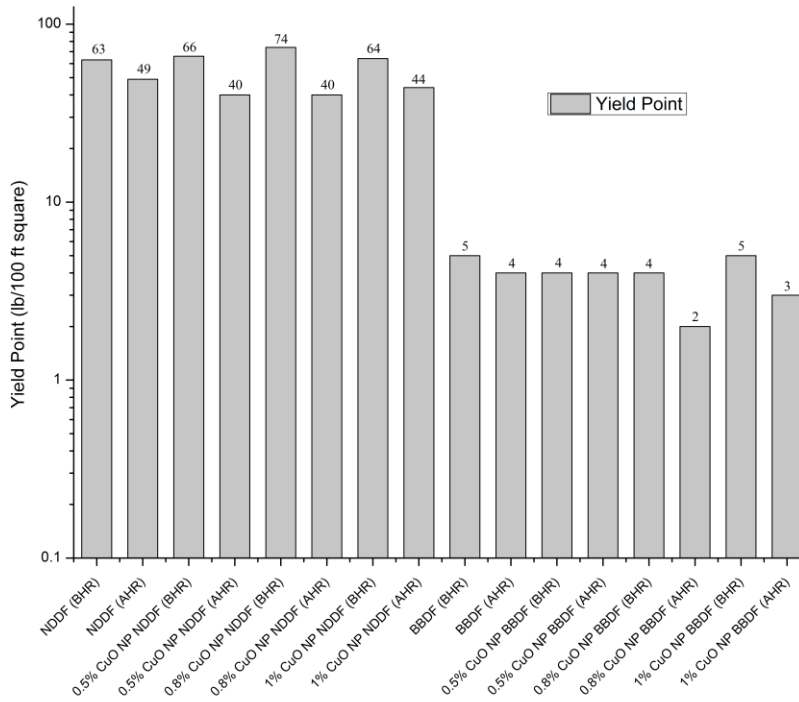


Fig. 4.2: Yield Point of all the prepared drilling fluid samples

Fig. 4.2 represents YP for all CuO NP based drilling fluids. For CuO NP based NDDF, maximum YP can be observed at 0.8 wt% concentration which increases the YP of base NDDF by 17.5%. Addition of 0.5 wt% CuO NP and 1 wt% CuO NP concentration had an insignificant enhancement in YP, which was 4.7% and 1.5% respectively. The concern with CuO NPs was that it showed less resistance to degradation after prolonged exposure (16 hours) at high temperatures (80 °Celsius). With base NDDF, the degradation in YP was observed to be 22.2% while 0.5, 0.8 and 1 wt% CuO NP NDDF showed a reduction in YP by 39%, 45%, and 31.3% respectively.

The effects of CuO NPs on BBDF were fairly constant. 1 wt% CuO NP had no effect on the YP of the fluid but rather showed detrimental effect at AHR conditions by 40%. CuO NPs, when doped in BBDF, show a substantial decrease in the YP trend with the increase in concentration as well as temperature, leading them to be unfeasible for any high-temperature operations.

4.2.2 VISCOSITY

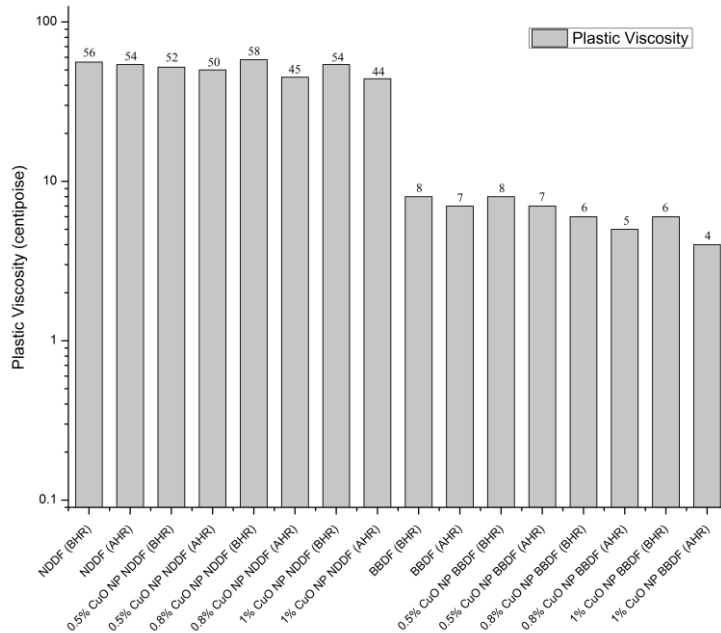


Fig. 4.3: Plastic Viscosity of all the prepared drilling fluid samples

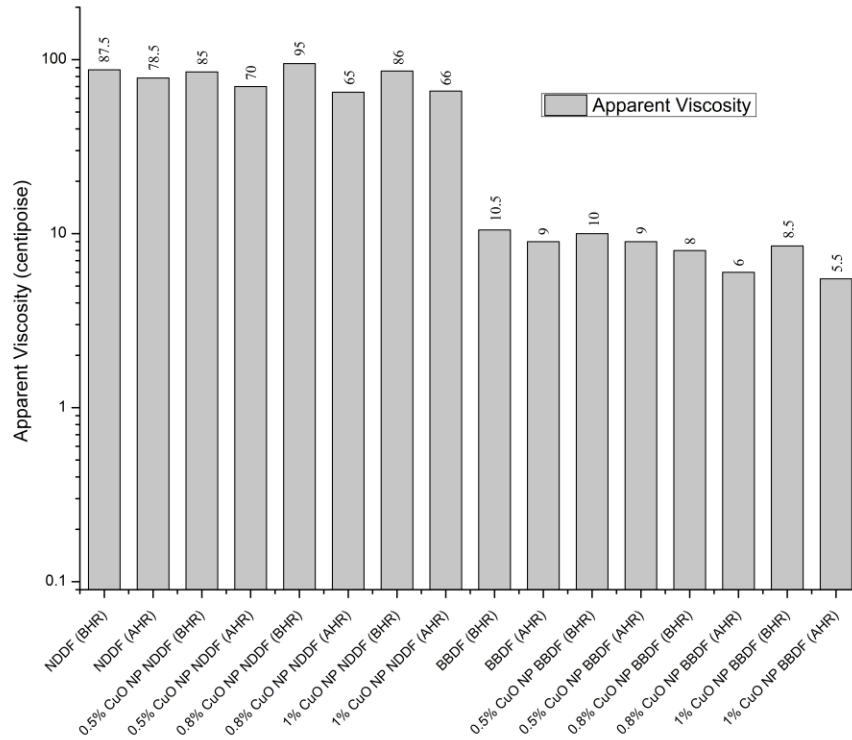


Fig. 4.4: Apparent Viscosity of all the prepared drilling fluid samples

Fig. 4.3 and 4.4 represent values of plastic viscosity (PV) and apparent viscosity (AV) for different concentrations of CuO NPs with NDDF and BBDF. For both 0.5 and 1 wt% CuO NP based NDDF, CuO NPs acted to reduce viscosity while for 0.8 wt% CuO NP plastic viscosity marginally increased by 3.5% and apparent viscosity by 8.5%. The temperature stability of CuO NP in BBDF also seemed to be an issue as it showed incapability to preserve viscosities at AHR conditions. CuO NPs had an effect in the conventional drilling fluid in terms of viscosity, which was lowered with an increase in concentration. Any similar results, however, were not observed with the doping of CuO NPs which presented an overall decreasing trend for both apparent and plastic viscosity with the increase of the NP concentration. The addition of CuO NPs in BBDF causes a reduction in the viscosity of the drilling fluid to a significant margin. The thinning behaviour of CuO NPs escalates with the gradual increase in concentration.

4.2.3 GEL STRENGTH

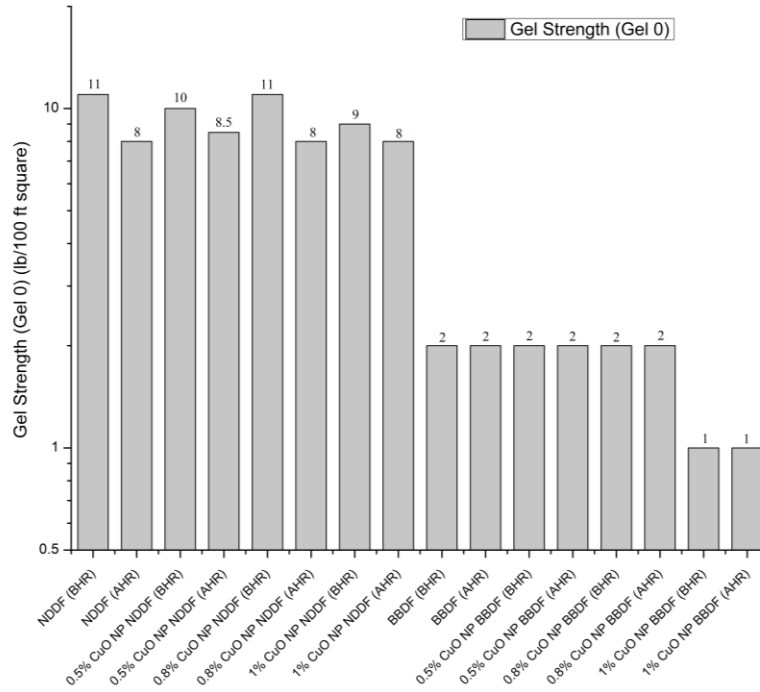


Fig. 4.5: Gel Strength (Gel 0) of all the prepared drilling fluid samples

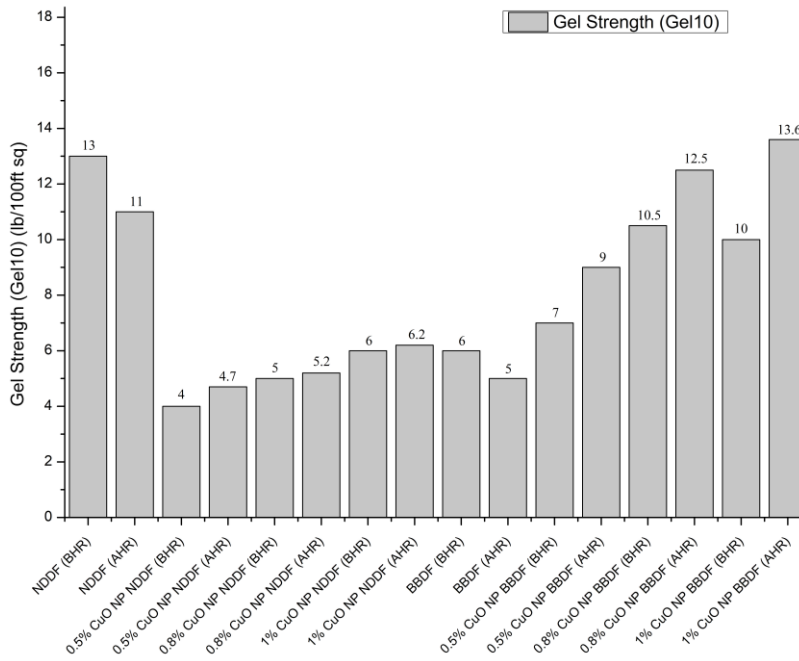


Fig. 4.6: Gel Strength (Gel 10) of all the prepared drilling fluid samples

The effect of CuO NP concentration on gel strength is reported in Fig. 4.5 and 4.6. No significant changes in Gel 0 can be noticed due to the addition of CuO NP in NDDF. However, Gel 0 decreases for 1 %wt CuO NP in BBDF by 50%. Furthermore, with a resting time of 10 mins Gel 10 of CuO NP based NDDF decreases. Contrasting phenomena can be observed for CuO NP based BBDF where the magnitude of Gel 10 rises with an increase in concentration as compared to base BBDF. Lower values of Gel 10 in the case of CuO NP based NDDF indicates inferior cutting suspension capacity than that of CuO NP based BBDF. On the brighter side, the former would require less start-up flow pressure after a prolong rest condition.

4.2.4 API FILTRATE LOSS TEST MEASUREMENTS

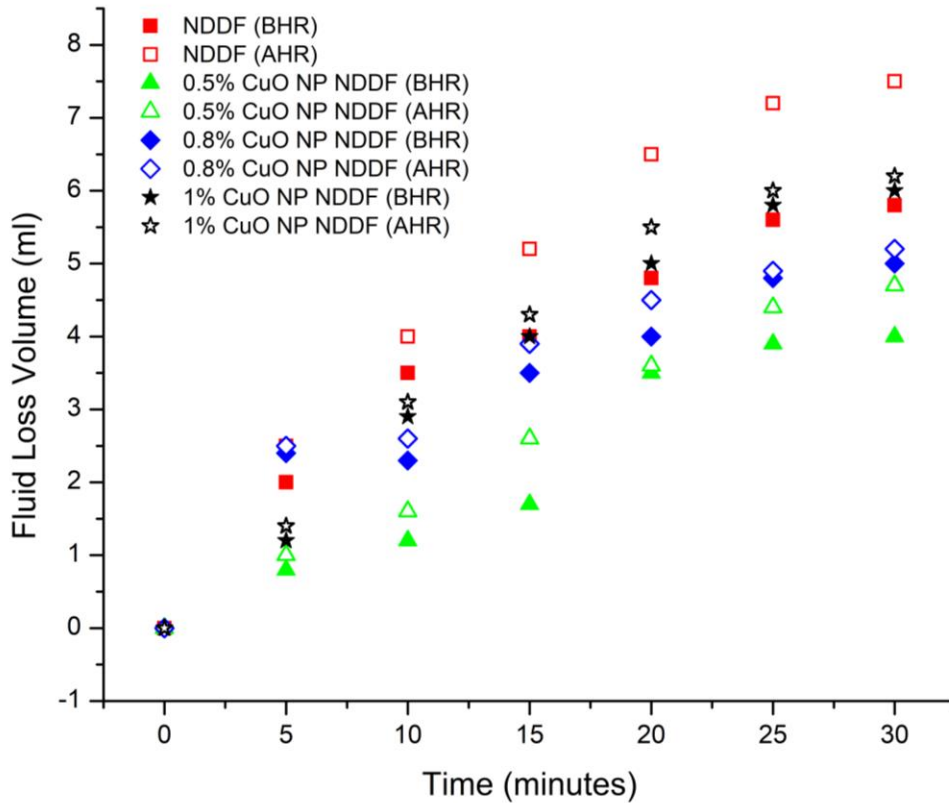


Fig. 4.7: Fluid loss vs. time for all CuO NP based NDDF

Fig. 4.7 reports fluid loss measurements of CuO NP NDDF at BHR and AHR conditions. It is generally noticed that fluid loss increases at AHR conditions as compared to BHR conditions. For base NDDF the increase is observed to be 29% while an increase of 17.5, 4 and 3 % is observed 0.5, 0.8 and 1 wt% CuO NP NDDF. The least fluid loss is shown by 0.5 wt% CuO NP which is 4 and 4.7 ml at BHR and AHR conditions respectively.

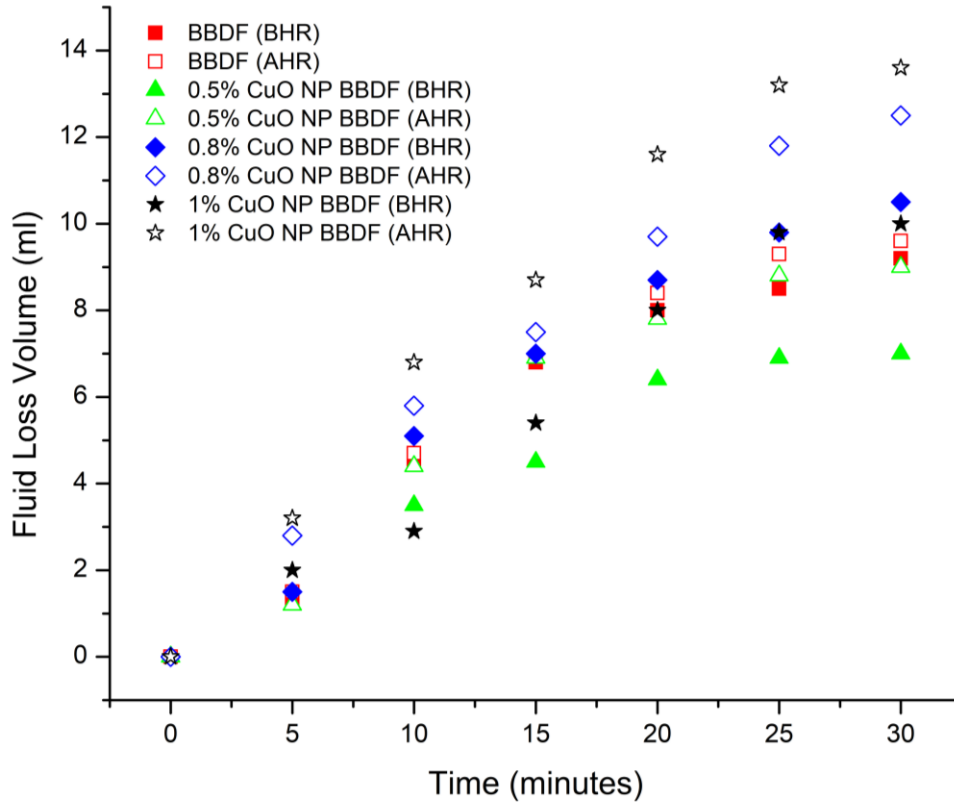


Fig. 4.8: Fluid loss vs. time for all CuO NP based BBDF

Fig. 4.8 represents fluid loss of all CuO NP based BBDFs at both BHR and AHR conditions. This increase in fluid loss volume for base BBDF from BHR to AHR condition is 4.3% while 0.5, 0.8 and 1 wt% CuO NP BBDF yield an increased fluid loss of 28.5, 19 and 36% respectively. However, it is important to note that 0.5 wt% CuO NP BBDF displays a minimum filtrate loss of 7 and 9 ml at BHR and AHR conditions respectively.

4.3 DETERMINATION OF OPTIMAL HERSCHEL BULKLEY (HB) PARAMETERS BY GENETIC ALGORITHM OPTIMIZATION

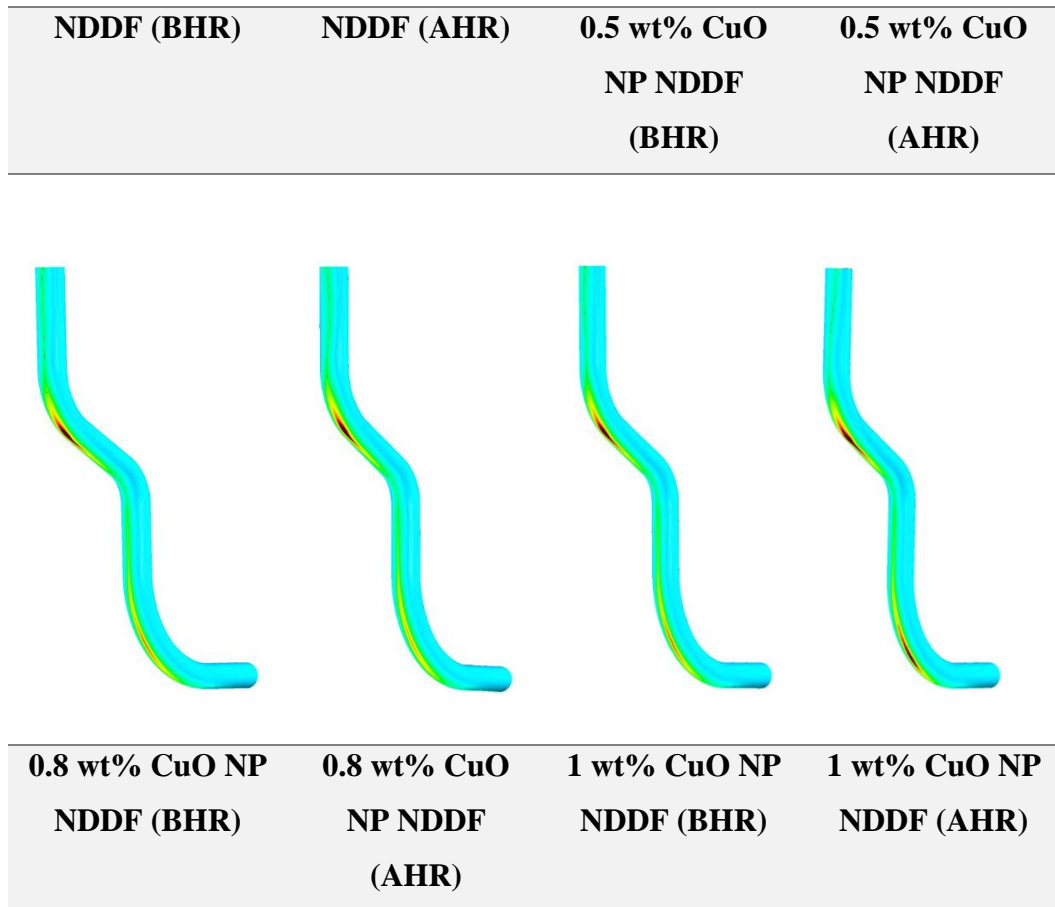
Table 4.1 Optimal values of HB parameters by GA

Drilling Fluid Type	Condition	True YP	<i>K</i>	<i>n</i>	SSE
NDDF	BHR	0.58	1.53	0.58	0.74
	AHR	1.16	0.95	0.63	0.14
0.5% CuO NP NDDF	BHR	0	1.42	0.54	0.18
	AHR	2.28	0.80	0.67	0.32
0.8% CuO NP NDDF	BHR	0	1.39	0.34	1.31
	AHR	1.4	0.73	0.64	0.13
1% CuO NP NDDF	BHR	0.39	1.22	0.58	0.5
	AHR	1.03	0.98	0.6	0.23
BBDF	BHR	0.45	0.06	0.75	0.09
	AHR	0.55	0.04	0.81	0.1
0.5% CuO NP BBDF	BHR	0.53	0.05	0.78	0.09
	AHR	0.62	0.03	0.82	0.54
0.8% CuO NP BBDF	BHR	0.54	0.04	0.76	0.08
	AHR	0.65	0.01	0.98	0.13
1% CuO NP BBDF	BHR	1.02	0.03	0.84	1.06
	AHR	0.62	0.02	0.87	0.16

Table 4.1 represents calculated HB parameters by minimizing SSE by using GA optimization tool in MATLAB. It can be noticed that the addition of CuO NP in NDDF decreases the value of consistency index (K) but promotes high shear thinning nature. On the other hand, this addition in BBDF reduces the shear thinning action which yields a greater value of flow index (n)

4.4 RESULTS AND DISCUSSION ON FLOW BEHAVIOUR FROM CFD STUDIES IN ECCENTRIC WELLBORE ANNULUS

4.4.1 EFFECT OF CuO NP ON CUTTING VOLUME FRACTION



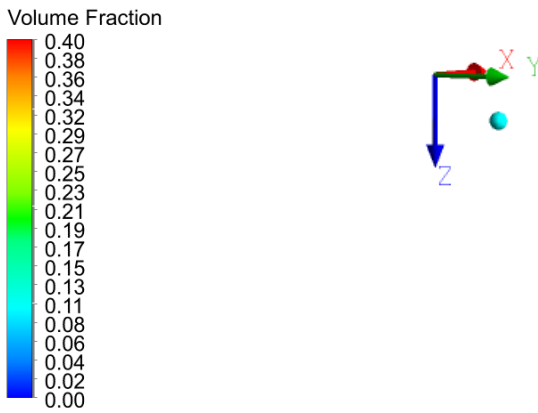
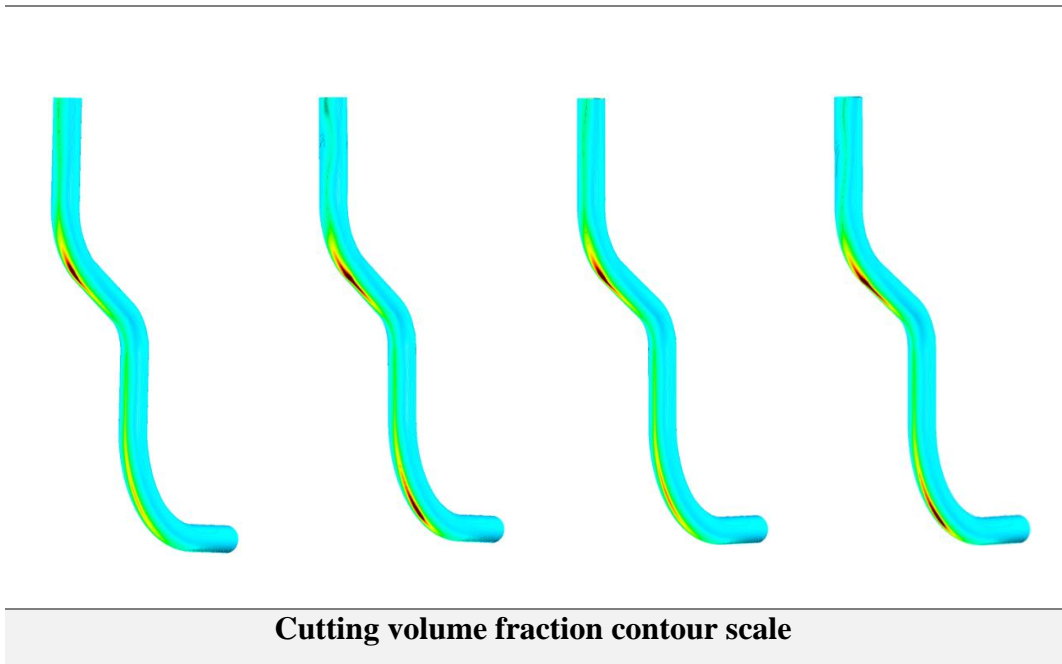


Fig. 4.9: Comparative side view of contours for cutting volume fraction ($V_{inlet} = 0.8 \text{ m/s}$, cutting density and inlet volume fraction = 2500 kg/m^3 and 8% respectively)

Table 4.2: Percentage volume retention of cuttings in annulus vs. different cases of concentration and temperatures. $(\text{Volume fraction of cuttings})_{annulus} - (\text{Volume fraction of cuttings})_{inlet} = (\text{Retention of volume fraction of cuttings})_{annulus}$

Cutting retention in terms of % total annular volume				
Sample / Temperature	Base NDDF	0.5 wt% CuO NP NDDF	0.8 wt% CuO NP NDDF	1 wt% CuO NP NDDF
BHR	0.087	0.0925	0.079	0.088
AHR	0.102	0.108	0.110	0.111

Fig. 4.9 represents contours of cutting deposition along the wellbore path for CuO NP NDDFs. This presents an idea of cutting carrying ability of the drilling fluids. It can be observed that depositions are highly concentrated at the upper bends. Due to degradation in rheological properties cutting sagging is more prominent at AHR conditions as compared to BHR conditions. A dense streak of cutting deposition (at 2nd BUS) appears in the case of 1 wt% CuO NP NDDF at BHR conditions which eventually intensifies at AHR conditions. Hence, compared to all NDDFs base NDDF shows superior cutting carrying capacity when compared to CuO NP based NDDFs. The addition of CuO NP in NDDF does not contribute in improving cutting carrying ability. This can be quantified from Table 4.2, wherein it is conclusive that the addition of CuO NP does not improve cutting removal capacity of NDDF that can be inferred from a reduced % retention compared to all CuO NP NDDFs.

4.4.2 EFFECT OF CuO NPs ON VELOCITY PROFILE OF NDDF

To better understand the phenomena of cutting carrying ability, velocity profiles are plotted from Fig. 4.10 – 4.12. These generate an idea of sweeping profile of the drilling fluid in the eccentric annular region.

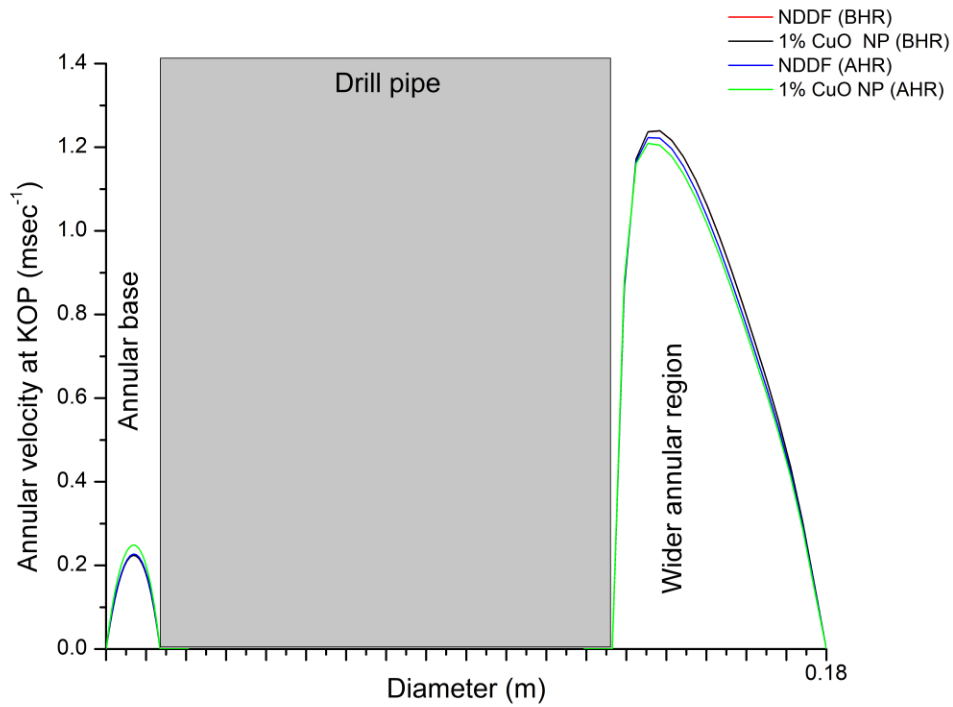


Fig. 4.10: Velocity profile at Kick-off Point (KOP) for base and 1% CuO NP NDDF at BHR and AHR conditions

At the KOP (Fig. 4.10) a sharp velocity profile can be observed for both NDDF and 1 wt% CuO NP NDDF. At BHR conditions the velocity of these two fluids has a close match whereas at AHR conditions velocity of 1 wt% CuO NP NDDF is slightly less than that of base NDDF in the wider annular region. Moreover, a minor increase in skewness is observed for the latter fluid. This increase in skewness/offset can result in less sweep efficiency of 1 wt% CuO NP NDDF due to which cutting sagging is prominent as observed in Fig. 4.9.

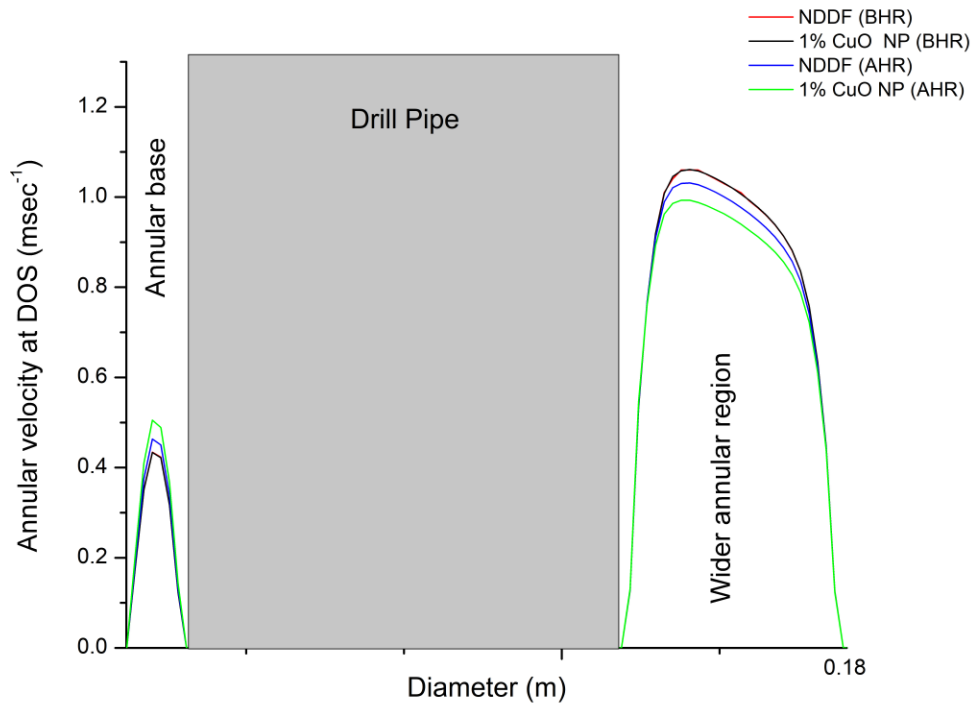


Fig. 4.11: Velocity profile at Drop-off section (DOS) for base and 1% CuO NP NDDF at BHR and AHR conditions

At the drop off section (Fig. 4.11), similar phenomena can be noticed as KOP except velocity profile is relatively blunt; as a result of which less cutting deposition can be observed in this region. However, 1 wt% CuO NP NDDF at AHR condition carries less velocity as compared to base NDDF. Henceforth, (from Fig. 4.9) 1 wt% CuO NP NDDF shows an early deposition of cutting compared to base NDDF when it gets past the DOS section. Having inferior lift velocity adversely affects the cutting carrying capacity of drilling fluid.

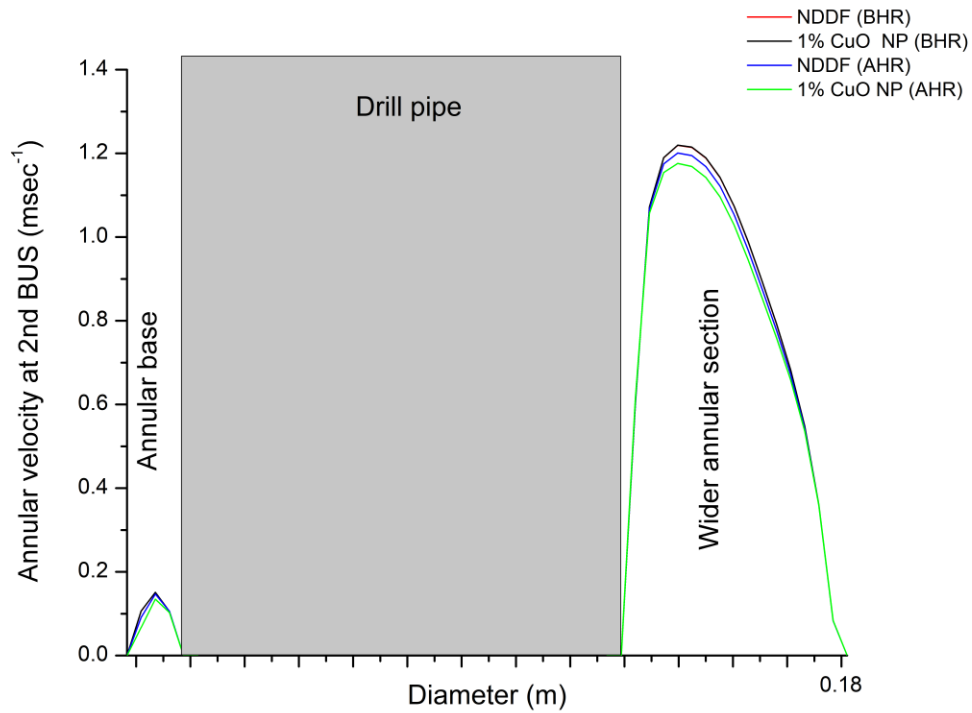


Fig. 4.12: Velocity profile at Build-up section (BUS) for base and 1% CuO NP NDDF at BHR and AHR conditions

Unlike the first BUS or at KOP the velocity profile at 2nd BUS (Fig. 4.12) has a greater sweep area due to which cutting segregation is relatively low. However, due to substandard rheological properties of 1 wt% CuO NP NDDF especially at AHR conditions, cutting deposition is prominent even at 2nd BUS wherein, base NDDF does not show signs of high sagging at this region.

4.4.3 EFFECT OF CuO NPs ON PRESSURE DROP

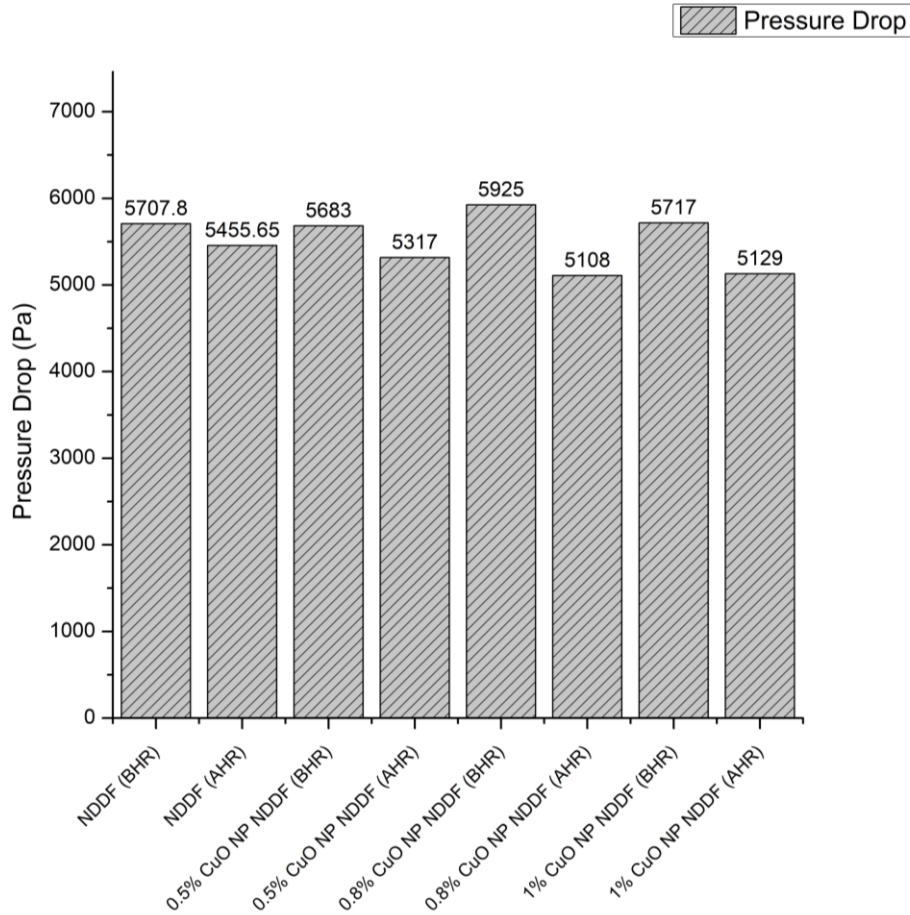


Fig. 4.13: Pressure drop for CuO based NDDF

Fig 4.13 represents the pressure drop for all the NDDFs. It can be observed that pressure drop variation ranges from 5108 to 5925 Pa, which along the wellbore length yields a pressure drop in a range of 0.075 to 0.087 psi/ft. These values are well within the acceptable range ensuing flowability.

4.5 CHAPTER CONCLUSION

From rheological measurements and CFD simulation studies, it can be confirmed that the addition of CuO NP does not contribute to enhancing the essential properties of NDDF. On the brighter side, a potential application of CuO

NP can be in terms of mud thinners. The improvement in thermal stability of CuO NP NDDF is one of the vital advantages of using CuO NP as thinner. They can be used to avoid cases of flocculation which gives rise to excessive gel strength and increases pump start-up power requirement. The detrimental effect of CuO NP addition results in poor cutting carrying ability. However, it shows a positive effect in improving the fluid loss control attribute of NDDF.

CHAPTER 5

EFFECT OF ALUMINUM OXIDE NPS (Al_2O_3 NPs) ON NDDF

5.1 RHEOLOGY MEASUREMENTS

5.1.1. STEADY SHEAR ROTATIONAL TEST MEASUREMENTS

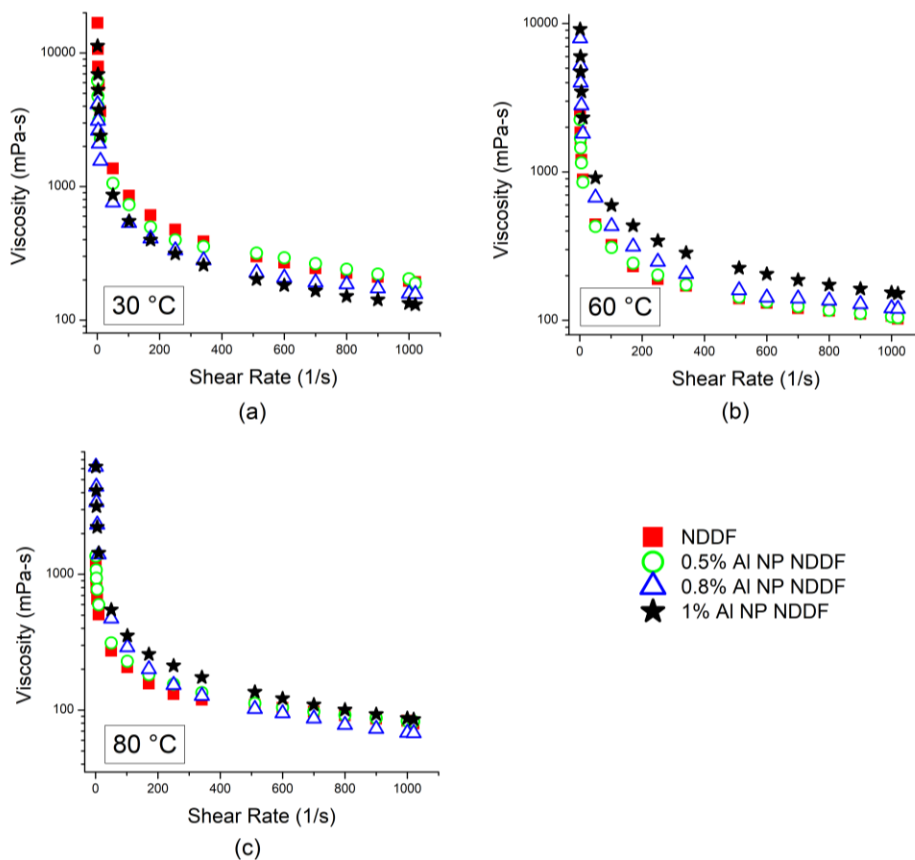


Fig. 5.1: (a) Viscosity vs. shear rate at 30 °C, (b) Viscosity vs. shear rate at 60 °C, (c) Viscosity vs. shear rate at 80 °C. Legend: NDDF represents the base with 0 wt% Al_2O_3 NP. 0.5% Al represents 0.5 wt% Al_2O_3 NP NDDF and so on

At 30 °C (Fig. 5.1 a), the addition of Al₂O₃ NPs shows a reduction in values of shear stress and viscosity at all shear rates. The magnitude of these properties decreases as the concentration of Al₂O₃ NPs increases from 0.5 to 1 wt%. At a temperature of 60 °C (Fig 5.1 b), base NDDF shows a significant reduction in values of shear stress as compared to Al₂O₃ NP DFs. The values of viscosity and shear stress are mostly preserved in the case of 1 wt% Al₂O₃ NP NDDF from a low shearing rate up to 600 s⁻¹. Beyond this shearing rate, both 0.8 wt% Al₂O₃ NP NDDF and 1 wt% Al₂O₃ NP NDDF show degradation in shear stress values. At high shearing rates, 0.5 wt% Al₂O₃ NP NDDF shows superior values in viscosity and shear stress. At 80 °C (Fig 5.1 c), 1 wt% Al₂O₃ NP NDDF shows the highest magnitude of viscosity and shear stress. It was observed that a significant loss of viscosity and shear stress at high temperatures has occurred due to a lack of thermal stability of the Base NDDF. Whereas, Al₂O₃ NP NDDF has shown higher thermal stability resulting in less degradation of rheological properties.

5.1.2. AMPLITUDE SWEEP TEST MEASUREMENTS

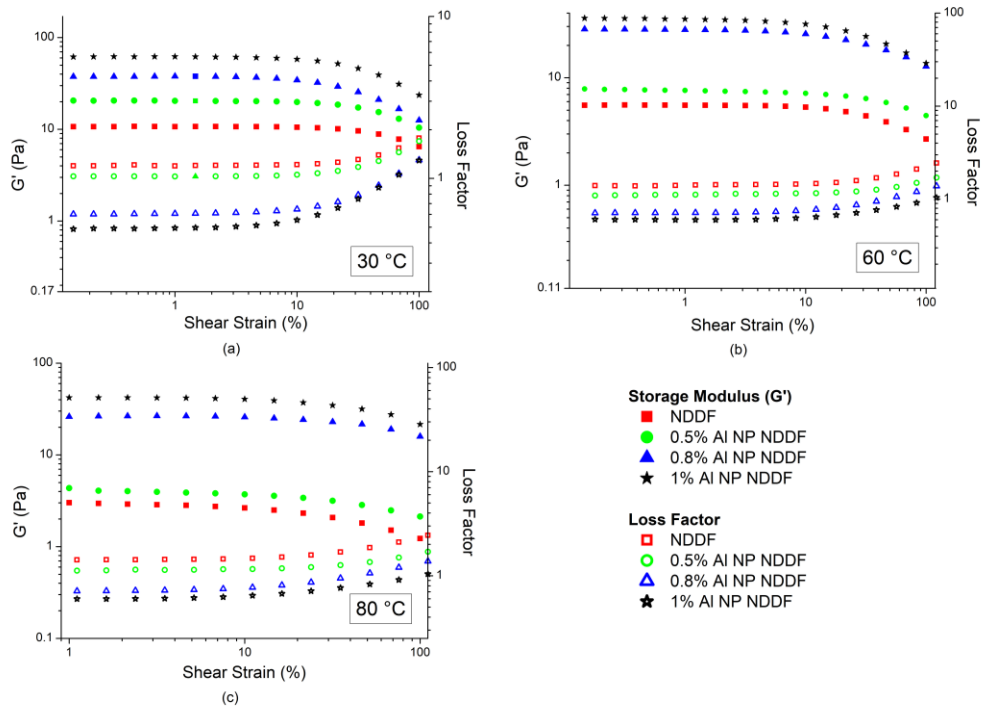


Fig. 5.2: (a) Storage modulus (G') and loss factor vs. shear strain (%) at 30 °C, (b) G' and loss factor vs. shear strain (%) at 60 °C, (c) G' and loss factor vs. shear strain (%) at 80 °C. Legend: NDDF represents the base with 0 wt% Al_2O_3 NP. 0.5% Al represents 0.5 wt% Al_2O_3 NP NDDF and so on.

A reduction in linear viscoelastic range (LVER) is observed for Al_2O_3 NP NDDF with an increase in concentration at 30 °C (Fig 5.2 a). Although the difference in values are quite negligible. 0.8 and 1 wt% Al_2O_3 NP NDDF shows a more dominant viscoelastic solid nature than base NDDF. It can also be observed that a greater difference in G' and G'' pertain in the case of Al_2O_3 NP NDDF with an increase in concentration as indicated by loss factor values. Nature of base NDDF and 0.5 wt% Al_2O_3 NP NDDF shows the complete viscoelastic liquid, while, 0.8 and 1 wt% Al_2O_3 NP NDDF is viscoelastic solid in nature. However, cross over for 0.8 and 1 wt% Al_2O_3 NP NDDF occurs in higher values of shear strain changing its nature to viscoelasticity liquids.

At 60 °C (Fig 5.2 b), a reduction in LVER for both base and 0.5 wt% Al_2O_3 NP NDDF, whereas an increase in LVER for 0.8 and 1 wt% Al_2O_3 NP NDDF can be observed. From the values of loss factor, it can be inferred that the viscoelastic nature of the base and 0.5 wt% Al_2O_3 NP NDDF is liquid in nature and solid for 0.8 and 1 wt% Al_2O_3 NP NDDF.

A substantial increase in LVER can be observed for 0.8 and 1 wt% Al_2O_3 NP NDDF while the LVER for the base and 0.5 wt% Al_2O_3 NP NDDF remains almost the same. Even at this high temperature, the structure for 0.8 and 1 wt% Al_2O_3 NP NDDF remains intact as the value of loss factor is less than 1 (Fig. 5.2 c).

5.1.3. FREQUENCY SWEEP TEST MEASUREMENT

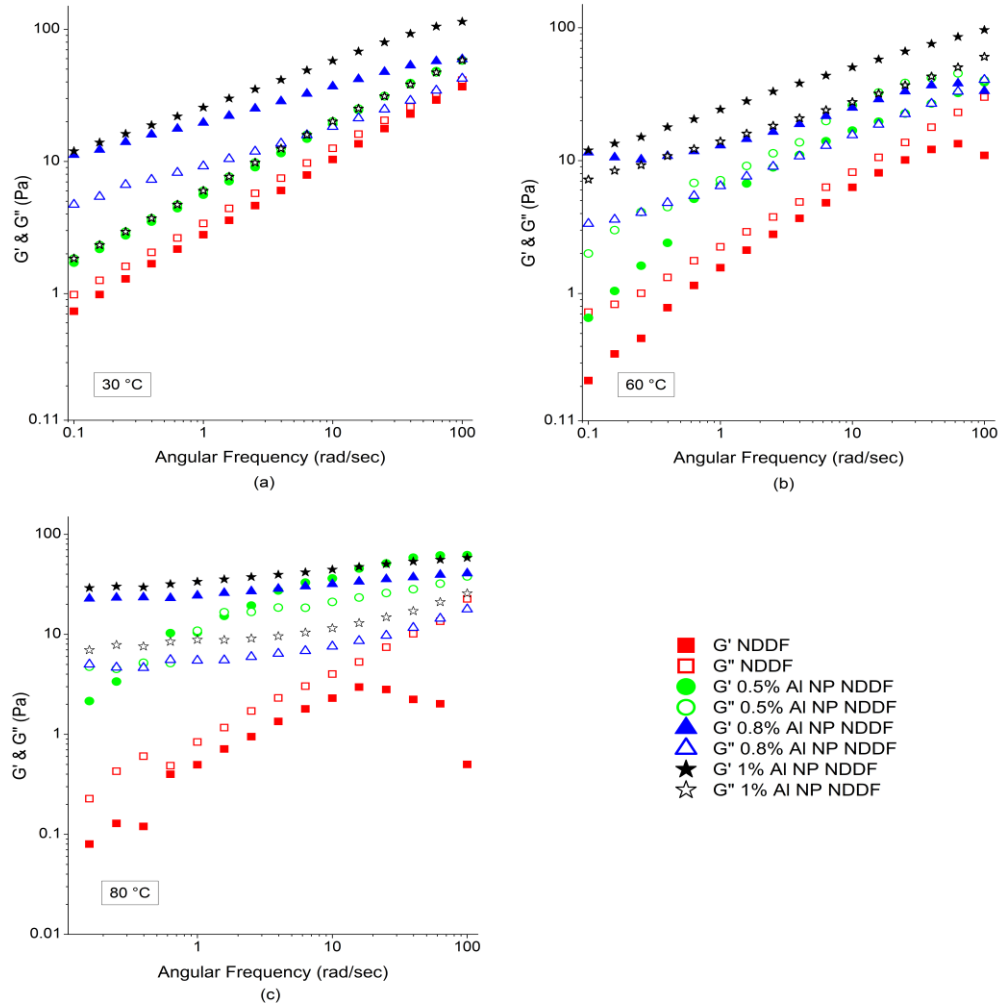


Fig. 5.3: (a) Storage modulus (G') and Loss modulus (G'') vs. angular frequency at 30 °C, (b) G' and G'' vs. angular frequency at 60 °C, (c) G' and G'' vs. angular frequency at 80 °C. Legend: NDDF represents the base with 0 wt% Al_2O_3 NP. 0.5% Al represents 0.5 wt% Al_2O_3 NP NDDF and so on.

At 30 °C (Fig 5.3 a), base NDDF and 0.5 wt% Al_2O_3 NP NDDF exhibit viscoelastic liquid properties due to higher values of G' than G'' . Although this difference is reduced at a higher frequency. 0.8 and 1 wt% Al_2O_3 NP NDDF showed viscoelastic solid i.e. gel behaviour throughout the frequency range. It is important to note that no crossover was observed for these liquids showing no reduction in the degree of crosslinking. From Fig 5.4 (a) no plateau region can be observed which signifies constant structural build-up event at lower frequencies.

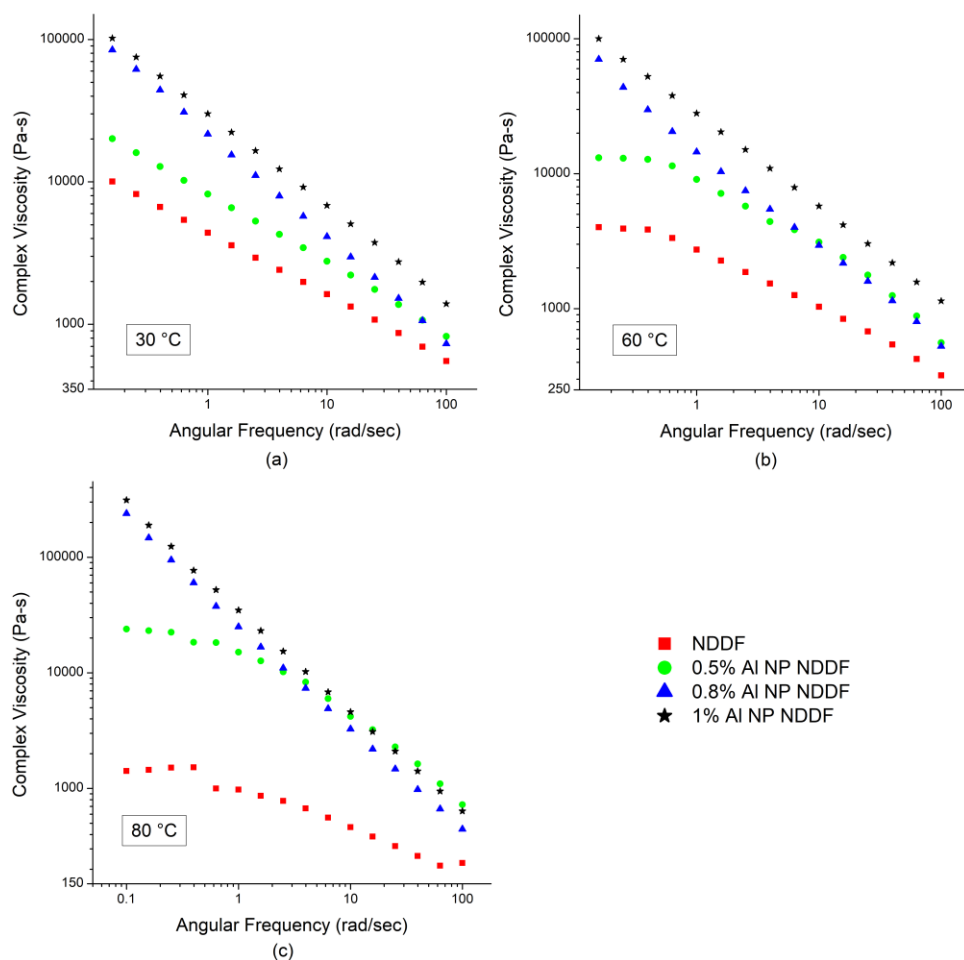


Fig. 5.4: (a) Complex viscosity vs. angular frequency at 30 °C, (b) Complex viscosity vs. angular frequency at 60 °C, (c) Complex viscosity vs. angular frequency at 80 °C. Legend: NDDF represents the base with 0 wt% Al₂O₃ NP. 0.5% Al represents 0.5 wt% Al₂O₃ NP NDDF and so on.

It can be observed that the storage values of base and 0.5 wt% Al₂O₃ NP NDDF at 60 °C (Fig 5.3 b) reduces as compared to its values at 30 °C. The magnitude of loss factor appears irregular showing inconsistency in the fluid structure. However, 0.8 and 1 wt% Al₂O₃ NP NDDF showed high values of storage signifying better structural integrity. It is crucial to mention that base and 0.5 wt% Al₂O₃ NP NDDF shows a plateau region (Fig 5.4 b) in lower frequencies in the

complex viscosity curve. This implies that at lower frequencies or at greater time period, the complex viscosity ceases to increase unlike 0.8 and 1 wt% Al₂O₃ NP NDDF.

At 80 °C (Fig 5.3 c), 0.8 and 1 wt% Al₂O₃ NP NDDF still shows viscoelastic solid behaviour (loss factor < 1) when compared to base NDDF. The value of loss factor for 0.5 wt% Al₂O₃ NP NDDF is more than unity in low frequencies indicating viscous nature while an elastic nature pertains at a higher frequency. However, a crossover can be observed at a frequency of approximately 1 Hz. The start of the plateau region (Fig 5.4 c) for the base and 0.5 wt% Al₂O₃ NP NDDF has shifted towards higher frequency as compared to 60 °C indicating early loss of structure as compared to 30 °C.

5.1.4. TIME DEPENDENT FLOW BEHAVIOUR TEST MEASUREMENTS

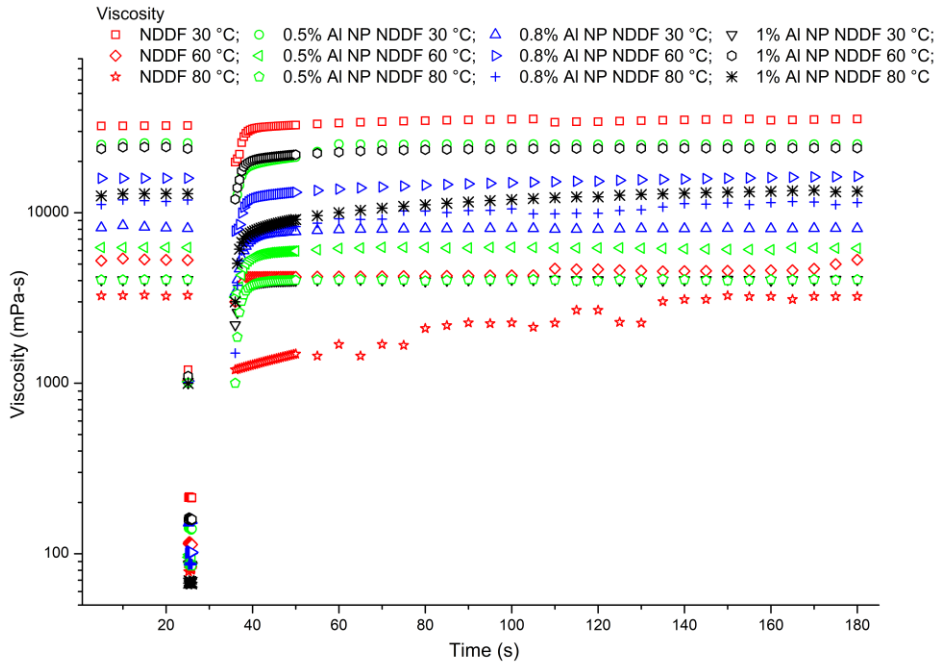


Fig. 5.5: Time dependent rotational thixotropic test for various NDDFs. Legend: NDDF represents the base with 0 wt% Al_2O_3 NP. 0.5% Al represents 0.5 wt% Al_2O_3 NP NDDF and so on.

From Fig. 5.5, rotational test at 30 °C, it can be observed that Base NDDF shows the quickest capability to regain its structure over time. A decrease in the ability of structural recovery against time can be observed with an increase in Al_2O_3 NP concentration from 0.5, 0.8 to 1 wt%. At 60 °C, thixotropic behaviour is more prevailing for 1 wt% Al_2O_3 NP NDDF as it recovers the original viscosity in less duration of time as compared to 0.5, 0.8 wt% Al_2O_3 NP and the base NDDF. The base NDDF was unable to regain its viscosity under the given test time at 80 °C. Although the viscosity of 1 wt% Al_2O_3 NP NDDF decreases with increase in temperature; it is able to regain its initial structural properties within a time which is significantly less than the base, 0.5 and 0.8 wt% Al_2O_3 NP NDDFs.

5.1.5. TEMPERATURE DEPENDENT FLOW BEHAVIOUR TEST MEASUREMENTS

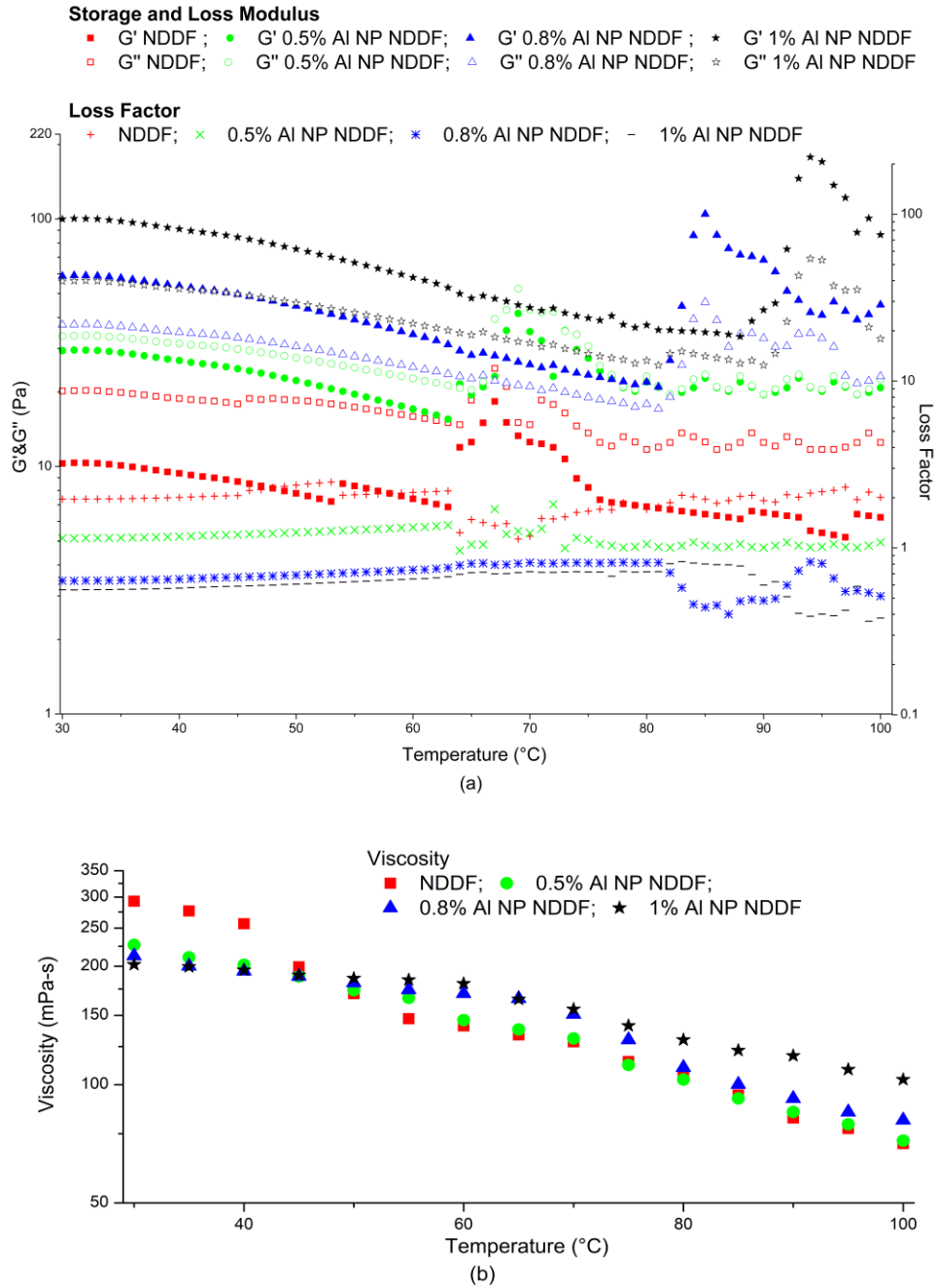


Fig. 5.6: (a) G', G'' and loss factor vs. temperature, (b) Viscosity and complex viscosity vs. temperature for various NDDFs. Legend: NDDF represents the base with 0 wt% Al₂O₃ NP. 0.5% Al represents 0.5 wt% Al₂O₃ NP NDDF and so on.

From Fig. 5.6 (a) and (b), (temperature sweep tests), it can be observed that base and 0.5 wt% Al₂O₃ NP NDDF loses its viscosity just beyond 60 °C. This can be confirmed from the temperature dependent oscillation curve which shows a drastic reduction in *G'* value beyond 60 °C. Moreover, a crossover can be observed for 0.5 wt% Al₂O₃ NP NDDF at 60 °C, which indicates a phase transition. On the other hand, 0.8 and 1 wt% Al₂O₃ NP NDDF shows high temperature stability as there is no crossover and the storage modulus peak appears at 86 °C and 93 °C respectively. This is due to more consistent crosslinking at higher temperatures that 0.8 and 1 wt% Al₂O₃ NP NDDF shows higher viscosity at elevated temperatures than the base and 0.5 wt% Al₂O₃ NP NDDF. As observed and discussed in the previous section, 0.8 and 1 wt% Al₂O₃ NP NDDF shows higher thermal stability.

5.1.6. API FILTRATE LOSS TEST MEASUREMENTS

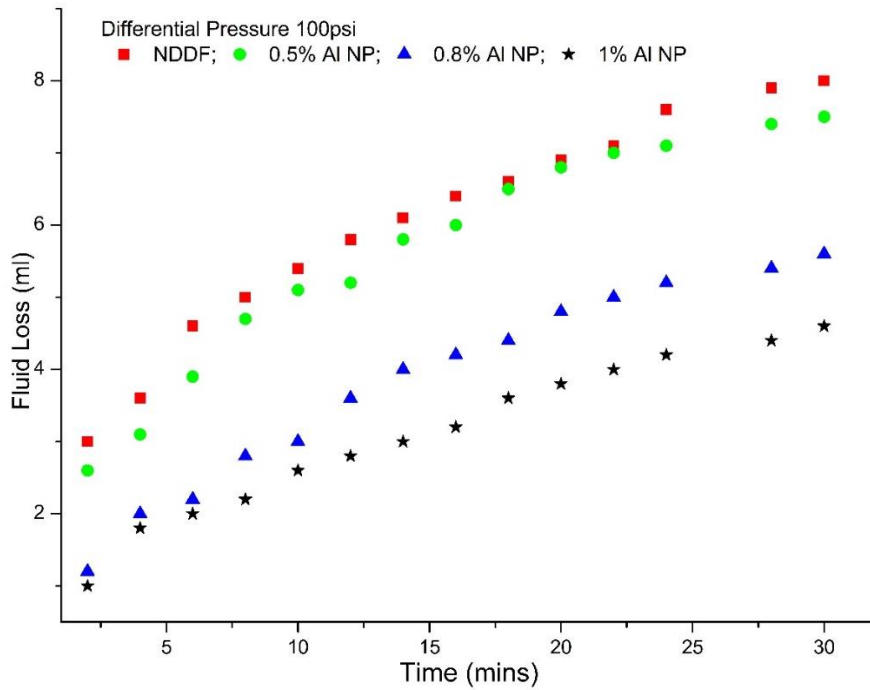


Fig. 5.7: Filtrate loss volume vs. time for various Al₂O₃ NP NDDFs. Legend: NDDF represents the base with 0 wt% Al₂O₃ NP. 0.5% Al represents 0.5 wt% Al₂O₃ NP NDDF and so on.

Fig. 5.7 represents the fluid loss volume data for all the Al₂O₃ NP based and base NDDFs. The static API filtrate loss test shows the highest fluid loss of 8 ml for Base NDDF. Although, the fluid loss decreases with an increase in Al₂O₃ NP concentration from 0.5, 0.8 to 1 wt% yielding a fluid loss volume of 7.5, 5.6 and 4.6 ml respectively after 30 minutes. The filtrate loss test was performed at 30 °C with a differential pressure of 100 psi. At this temperature condition viscosity value of the base and 0.5 wt% Al₂O₃ NP NDDF was much higher as compared to 0.8 and 1 wt% Al₂O₃ NP NDDF. Still, a reduced filtrate volume was observed for 0.8 and 1 wt% Al₂O₃ NP NDDF. This might be due to the plugging of the pore by NPs (Yang, Yue, Cai, Liu, & Wu, 2015). Another possible explanation for this behaviour might be due to a higher storage modulus of 0.8% and 1% Al₂O₃ NP NDDF than its loss modulus. From the frequency sweep data, it can be seen that 0.8 and 1 wt% Al₂O₃ NP NDDF are more resistant to syneresis as the value of loss factor almost lies between 0.2 to 0.3. On the other hand, Base and 0.5 wt% Al₂O₃ NP NDDF shows viscoelastic liquid nature and are prone to syneresis which might result in greater filtrate loss volume.

5.2 DETERMINING OPTIMAL HERSCHEL BUCKLEY (HB) PARAMETERS USING GENETIC ALGORITHM (GA)

Table 5.1: Optimal Herschel Bulkley (HB) parameters determined by genetic algorithm (GA) for various NDDFs

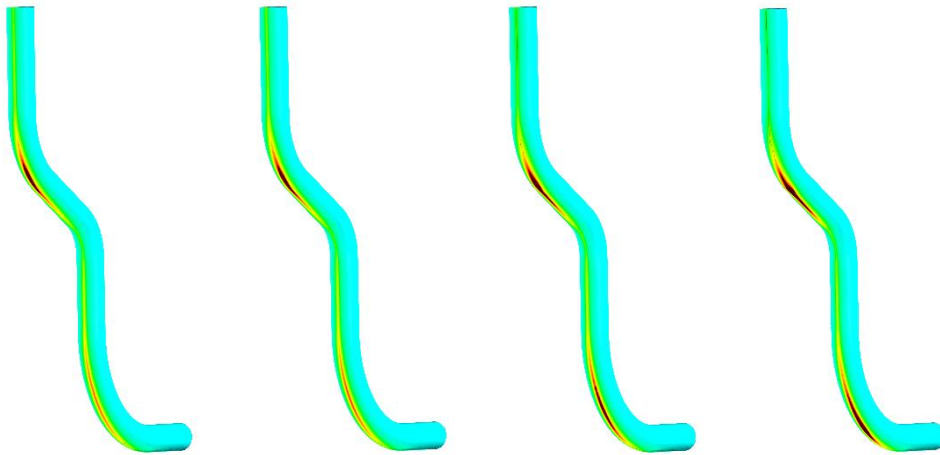
NDDF Sample	Temperature (°C)	Yield Point (Pa)	k (Pa/s ⁿ)	n	SSE
Base NDDF		0	16.34	0.36	94.93
0.5 wt% Alumina NP NDDF	30	0	10.54	0.42	277.84

0.8 wt% Alumina				
NP NDDF	0	5.32	0.50	267.15
1 wt% Alumina NP				
NDDF	3.33	7.99	0.40	96.88
<hr/>				
Base NDDF	0	3.31	0.49	23.93
0.5 wt% Alumina				
NP NDDF	0	2.44	0.55	88.69
60				
0.8 wt% Alumina				
NP NDDF	0	4.73	0.44	197.91
1 wt% Alumina NP				
NDDF	0	8.10	0.36	80.53
<hr/>				
Base NDDF	0	1.50	0.57	11.93
0.5 wt% Alumina				
NP NDDF	0	1.64	0.57	60.37
80				
0.8 wt% Alumina				
NP NDDF	0	2.17	0.53	120.32
1 wt% Alumina NP				
NDDF	0	5.99	0.39	54.55
<hr/>				

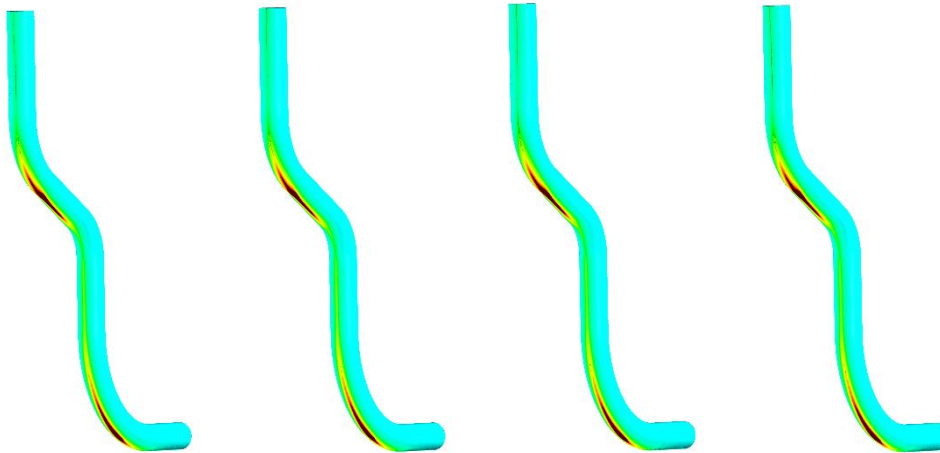
5.3 RESULTS AND DISCUSSION ON FLOW BEHAVIOUR FROM CFD STUDIES IN ECCENTRIC WELLBORE ANNULUS

5.3.1 EFFECT OF Al₂O₃ NPs ON CUTTING CARRYING CAPACITY OF NDDF

Base NDDF	0.5 wt% Alumina NP NDDF	0.8 wt% Alumina NP NDDF	1 wt% Alumina NP NDDF
Cutting deposition at 30 °C			



Cutting deposition at 60 °C



Cutting deposition at 80 °C

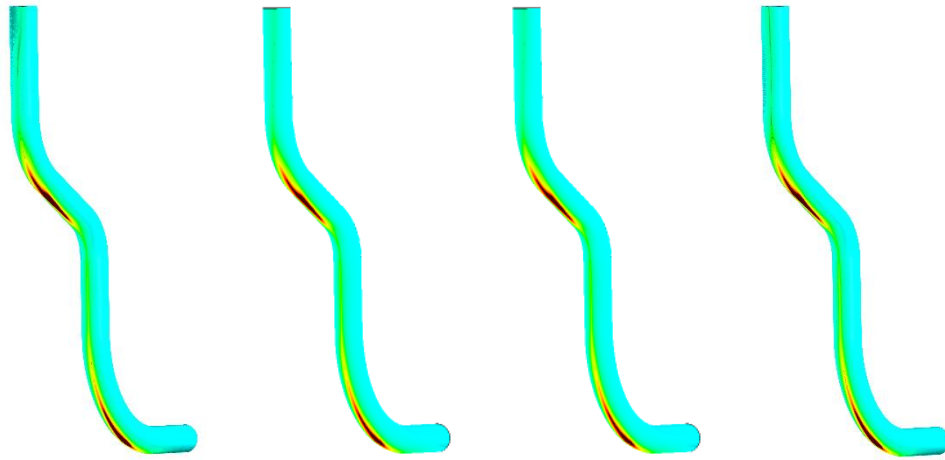


Fig. 5.8: Comparative side view of contours for cutting volume fraction ($V_{inlet} = 0.8$ m/s, cutting density and inlet volume fraction = 2550 kg/m³ and 10% respectively)

Table 5.2 Percentage volume retention of cuttings in annulus vs. different cases of concentration and temperatures. $(\text{Volume fraction of cuttings})_{annulus} - (\text{Volume fraction of cuttings})_{inlet} = (\text{Retention of volume fraction of cuttings})_{annulus}$

Cutting retention in terms of % total annular volume				
Sample / Temperature	Base NDDF	0.5 wt% Alumina NP NDDF	0.8 wt% Alumina NP NP NDDF	1 wt% Alumina NP NP NDDF
30 °C	0.070	0.072	0.086	0.105
60 °C	0.127	0.122	0.132	0.128
80 °C	0.142	0.149	0.139	0.135

Fig. 5.8 represents the contours of cutting volume fraction. It can be observed that at 30° C, sagging of cutting at 2nd BUS increases with an increase in Al₂O₃ NP concentration. Additionally, retention of cuttings within the annular region increases with an increase in temperature. The base and 0.5 wt% Al₂O₃ NP NDDF show better cutting removal efficiency till 60° C. This can be observed from Table 5.2 where percentage (%) retention is 0.127 and 0.122 respectively. However, with an increase in temperature (80° C) the adverse effect of Al₂O₃ NPs trend reverses. At this temperature, the 0.8 and 1 wt% Al₂O₃ NP NDDFs starts to show enhancement in cutting removal efficiency. This is due to the better thermal stability of Al₂O₃ NP NDDF as observed in rheological studies.

5.3.2 EFFECT OF Al₂O₃ NPs ON THE VELOCITY PROFILE OF NDDF

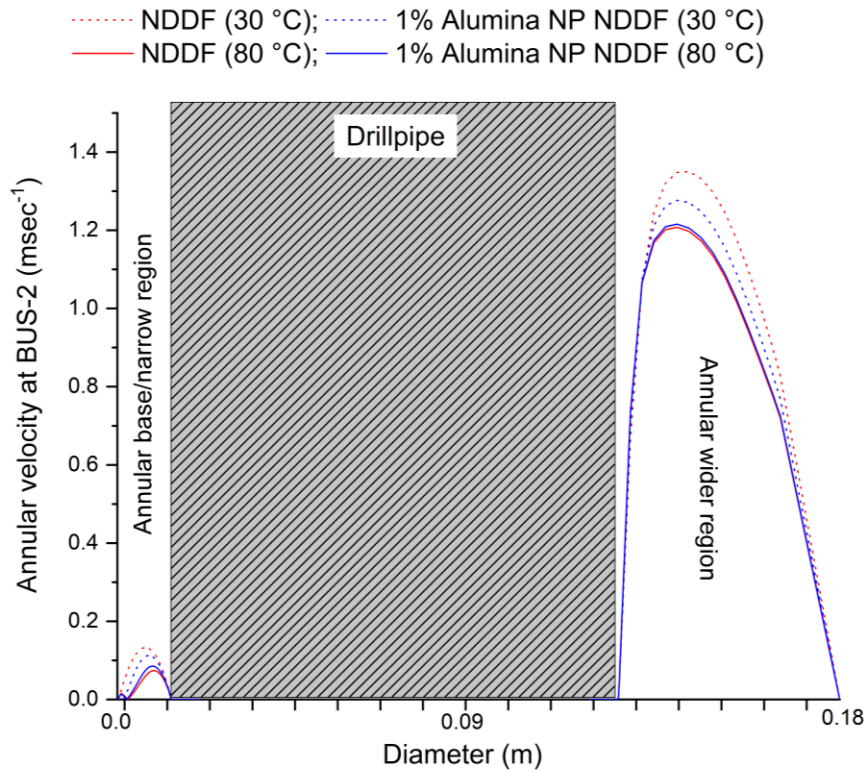


Fig. 5.9: Velocity profile at Build-up section (BUS) for base and 1% Al₂O₃ NP NDDF at 30° C and 80° C conditions

At 2nd BUS (Fig. 5.9) skewed velocity profiles are observed similar to KOP, but with a relatively blunt velocity head. This results in a greater sweep area thereby incurring lesser cutting sedimentation in this zone as compared to KOP. The reported lift velocities of NDDFs in this section are lesser than that of KOP at the annular base.

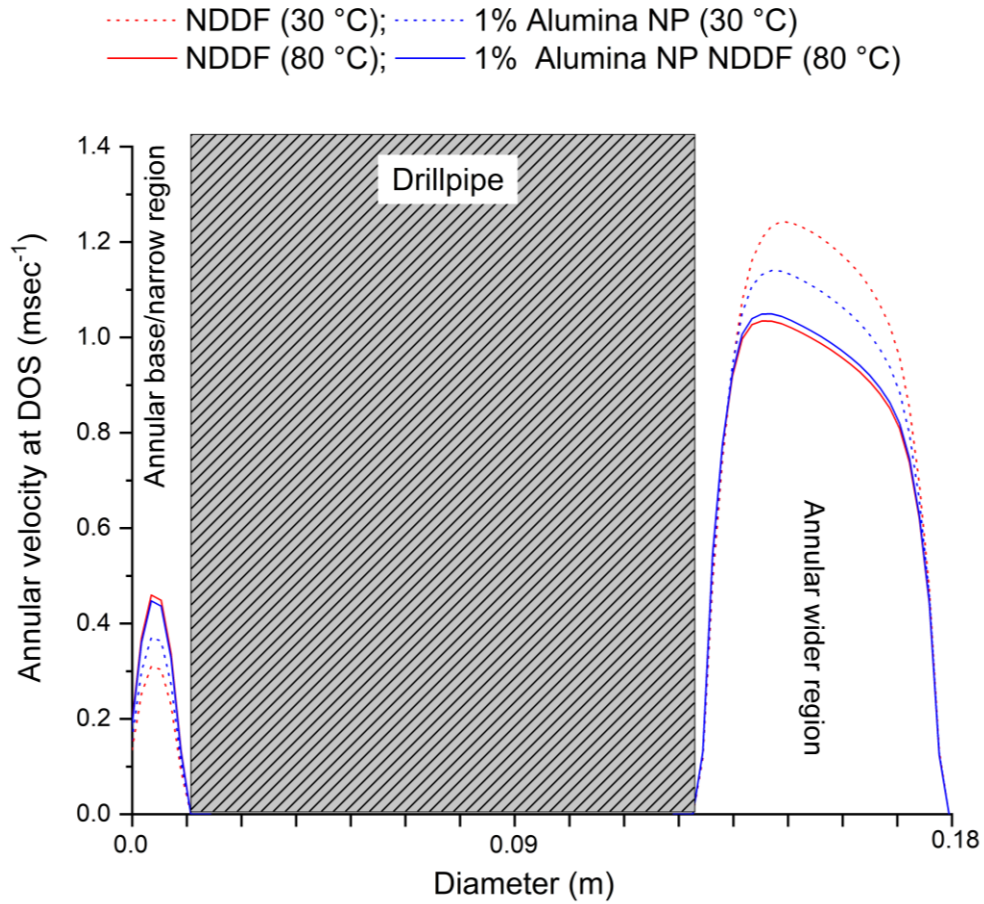


Fig. 5.10: Velocity profile at Drop-off section (DOS) for base and 1% Al₂O₃ NP NDDF at 30° C and 80° C conditions

Fig. 5.10 represents velocity profiles at DOS which has a relatively blunt velocity profile. This blunt profile improves the areal sweep efficiency in the annular region. Furthermore, a similar phenomenon as discussed at KOP is observed wherein the velocity of base and 1 wt% Al₂O₃ NP NDDF are

approximately identical at 80° C. The lift velocities in this section are lesser as compared to KOP and 2nd BUS.

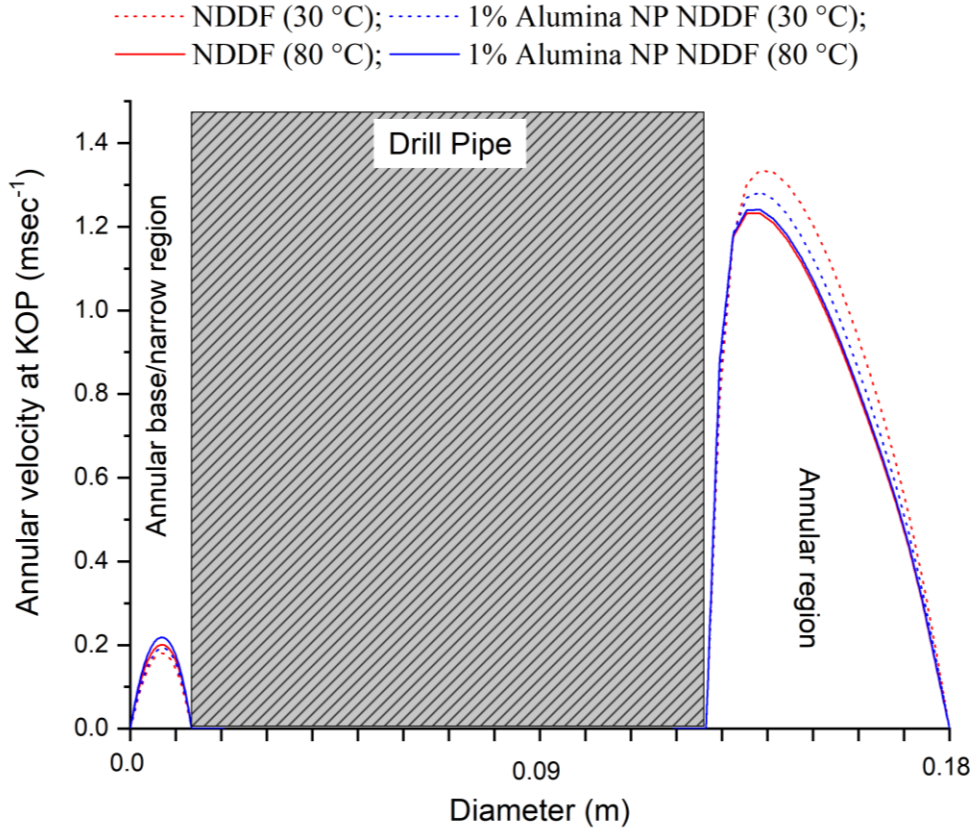


Fig. 5.11: Velocity profile at Kick-off Point (KOP) for base and 1% Al_2O_3 NP NDDF at 30° C and 80° C conditions

At KOP (Fig. 5.11) velocity profiles with high lift velocities were observed. At 30° C, base and 1 wt% Al_2O_3 NP NDDF show clear distinction in velocity profiles due to contrasting consistency index (K) values. However, at 80° C, shear thinning behaviour of 1 wt% Al_2O_3 NP NDDF becomes more dominant which results in similar velocity values and the same degree of skewness as that of base NDDF.

5.3.3 EFFECT OF Al₂O₃ NPs ON PRESSURE DROP OF NDDF

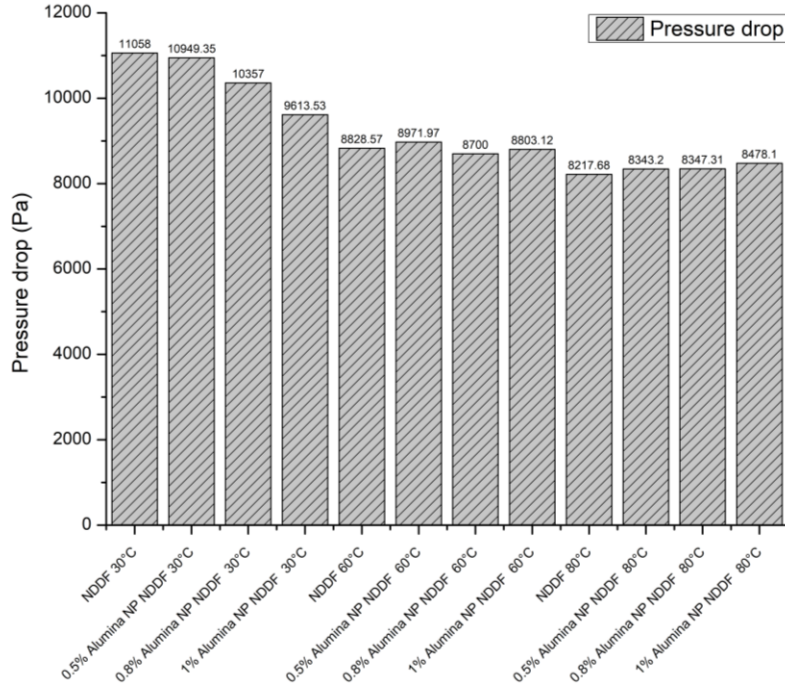


Fig. 5.12: Pressure drop of Al₂O₃ NP NP based NDDF

Fig 5.12 presents comparative values of pressure drop in the annular region for all the NDDFs. At 30° C, pressure drop decreases with an increase in the concentration of Al₂O₃. This can be an attribute of the decreasing value of consistency index (*K*). However, this difference minimizes at higher temperatures where rheological properties of all NDDFs are approximately similar in nature if not the same. It can also be observed that the pressure drop values confirm the flowability of all the fluids.

5.4 CHAPTER CONCLUSION

The addition of Al₂O₃ NP brings about a favorable change in the rheological properties of NDDF, especially at high temperatures. Considering both fluid loss

control studies and cutting carrying performance, it was concluded that 1 wt% Al₂O₃ NP NDDF outperforms other NDDFs. Rheological studies through viscoelastic investigations also suggest more stable structural integrity of the same.

CHAPTER 6

EFFECT OF ZIRCONIUM DIOXIDE NPS (ZrO_2 NP) ON NDDF

In this chapter, investigations on the various properties of the base NDDF and NP NDDFs with varying concentrations of ZrO_2 NPs have been reported. Initially, rotational shear test studies are discussed providing insights into the effect of NPs on the viscosity and thermal stability in terms of variation in rheological properties of NDDFs. Subsequently, dynamic oscillation test results are discussed to evaluate the viscoelasticity at various strain % (amplitude sweep) and frequencies (frequency sweep). Fluid loss results determined from the API filter press apparatus of all the NDDFs are also reported. Subsequently, CFD simulations with a comparative study on the velocity profile, pressure drop and cutting carrying capacity of all the NDDFs are presented to evaluate their performance.

6.1 SYNTHESIS AND CHARACTERIZATION OF ZrO_2 NPs

250 ml of zirconium oxychloride solution (0.5 M concentration in water) in two neck round bottom flask were subjected to continuous stirring at 600 rpm. In one neck of the flask, ammonium hydroxide (30%) added dropwise into it until pH is reached to a value of 10. The precipitate was refluxed through the other neck of the flask for 5 hours at 100 °C. Furthermore, it was cooled down to room temperature and then filtered and washed till a pH of 7 is achieved. The precipitate cake was dried in a hot air oven at 120 °C overnight, thereafter slightly crushed and sieved through 100 μ m sieve screen. The dried sample was calcined in a muffle furnace at 600 °C for 4 hours at 10 °C/min to obtain ZrO_2 NPs (Kumar et al., 2018).

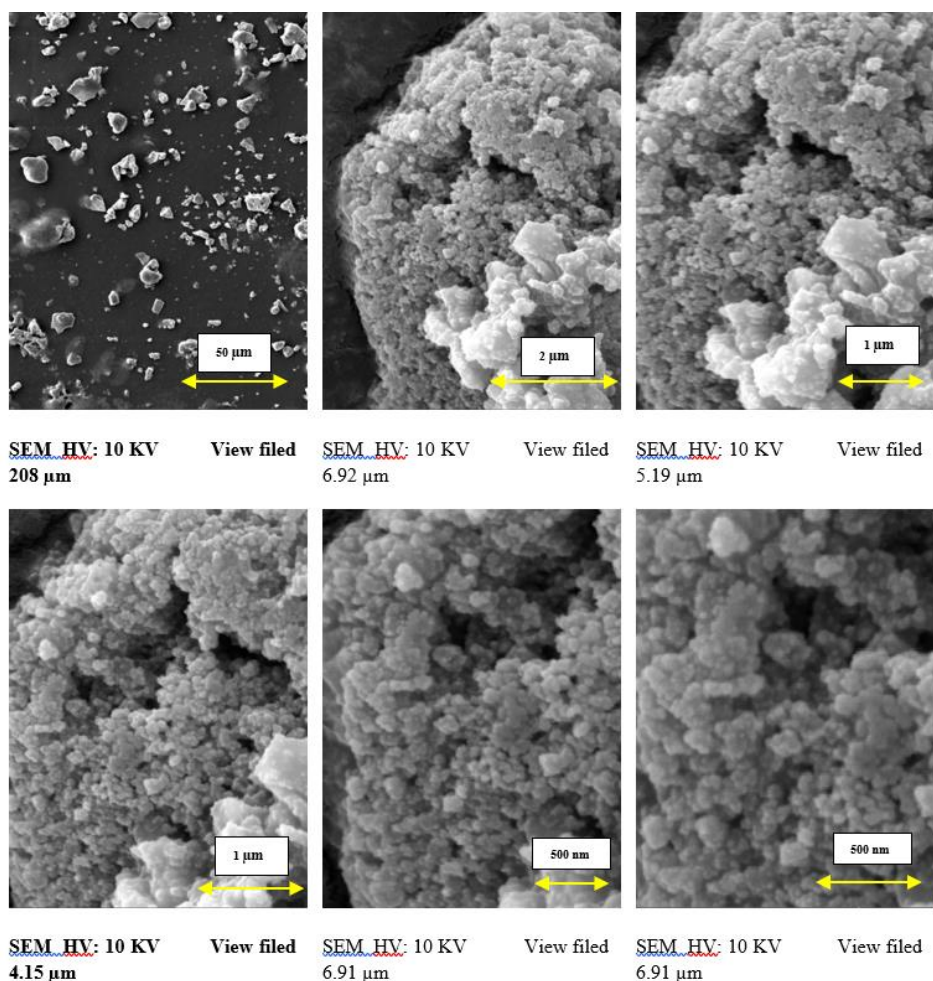


Fig. 6.1: SEM images of ZrO₂ NPs produced in this study

Fig. 6.1 shows the SEM images of prepared ZrO₂ NPs. It is evident that ZrO₂ NPs are spherical in shape having the same average grain size and uniform distribution. Fig. 6.2 shows images of XRD pattern, FTIR spectra and BET.

It is found that the XRD pattern of calcined ZrO₂ NP is in the crystalline phase (Fig. 6.2 a). The most intense peaks obtained at $2\theta = 30.13^\circ, 35.36^\circ, 50.40^\circ, 60.2^\circ, 62.83^\circ$ and 74.5° signify the tetragonal phase against (101), (110), (112), (200), (211), (202) and (220) planes, JCPDS (Joint Committee on Powder Diffraction Standards) card number 80-2155, respectively (Heshmatpour and Aghakhanpour, 2011). The crystallite sizes (D) of the samples were calculated using the Scherrer equation (Patterson, 1939) as given by:

$$D = (0.94 \lambda) / (\beta \cos \theta) \quad \text{Eqn. (6.1)}$$

where λ is the wavelength radiation used ($\lambda = 1.5406 \text{ \AA}$), θ is the Bragg angle ($^\circ$) and β is the line width (radians) at half-maximum height calculated from the full width at half maximum intensity (FWHM). The average crystallite size of these NP materials was found to be 27 nm.

In the FTIR spectrum for ZrO_2 NP (Fig. 6.2 b), the bands at $423\text{--}654 \text{ cm}^{-1}$ correspond to Zr-O-Zr bond (Yamaguchi, 1990). The band at 1625 cm^{-1} can be assigned to the bending mode (H-O-H) of coordinated water and a strong and broad bandwidth at 3398 cm^{-1} is attributed to physisorbed water (Gowri et al., 2014). The band at 1362 cm^{-1} indicates bending vibration of Zr-OH groups (Sinhamahapatra et al., 2011). The broadness of the band around 3200 cm^{-1} indicates the effect of hydrogen bonding and attributes to the O-H stretching vibration of water associated with ZrO_2 (Kumar et al., 2017).

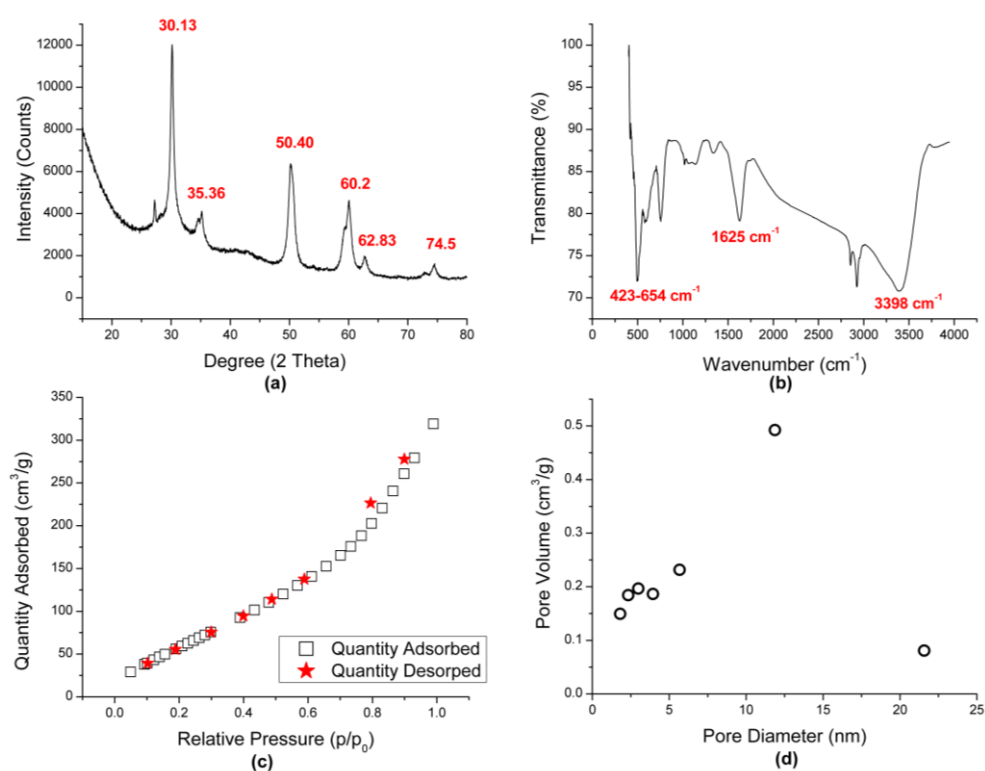


Fig. 6.2: (a) XRD pattern, (b) FTIR Spectra, (c) N₂ adsorption/desorption isotherms, (d) Pore size distribution of ZrO_2 NPs

BET isotherm (Fig. 6.2 c) shows H3 Type hysteresis loops for the ZrO_2 NP samples. Due to the non-rigid aggregates of plate-like particles and the

occurrence of conspicuous hysteresis loops at high relative pressures the material shows mesoporous property (slit-shaped pores). This can be related to weak interaction and capillary condensation associated with large pore channels (Kumar et al., 2015; Sato, 2002). Hysteresis at high relative pressure confirms the maximum pore volume of ZrO₂ NP. Fig. 6.2 (d) shows that the pore size distribution of the pure ZrO₂ is wider and the decrease in particle size to nano-dimensions is the cause for achieving higher surface area and greater pore volume.

6.2 RHEOLOGY MEASUREMENTS

6.2.1 STEADY STATE ROTATIONAL TEST MEASUREMENTS

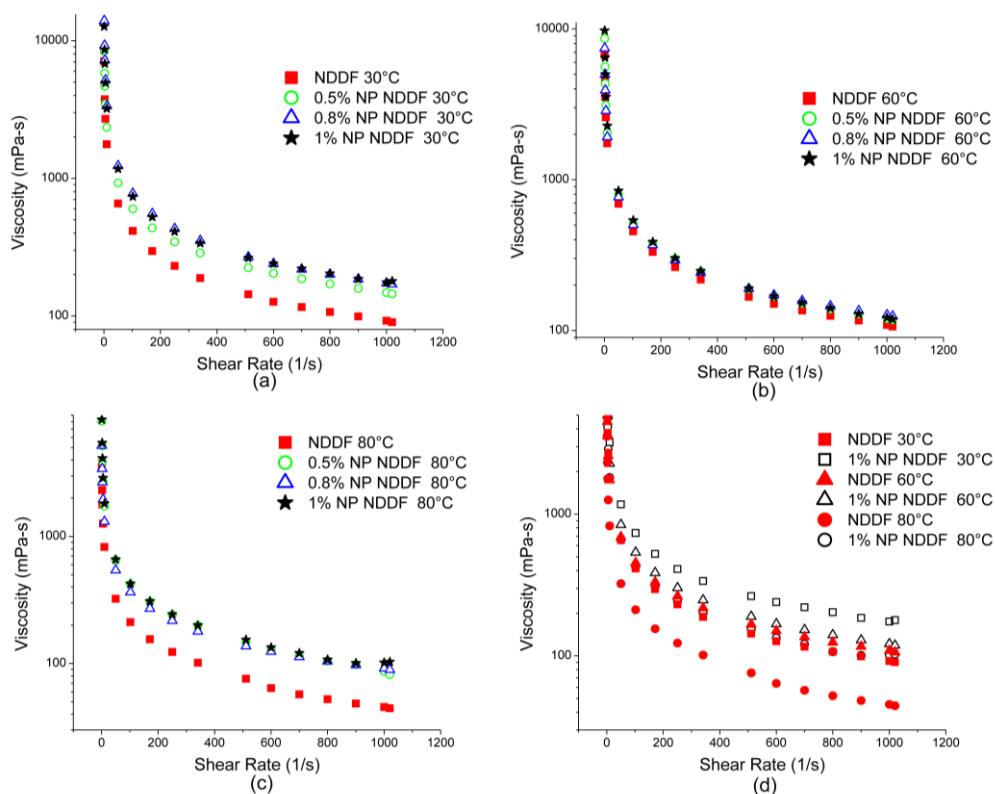


Fig. 6.3: (a) Viscosity vs. shear rate at 30 °C, (b) Viscosity vs. shear rate at 60 °C, (c) Viscosity vs. shear rate at 80 °C, (d) Viscosity vs. shear rate for NDDFs with 0 and 1 wt% ZrO₂ NPs at 30, 60 and 80 °C. Legend: NDDF represents the base with 0 wt% ZrO₂ NP. 0.5% represents 0.5 wt% ZrO₂ NP NDDF and so on.

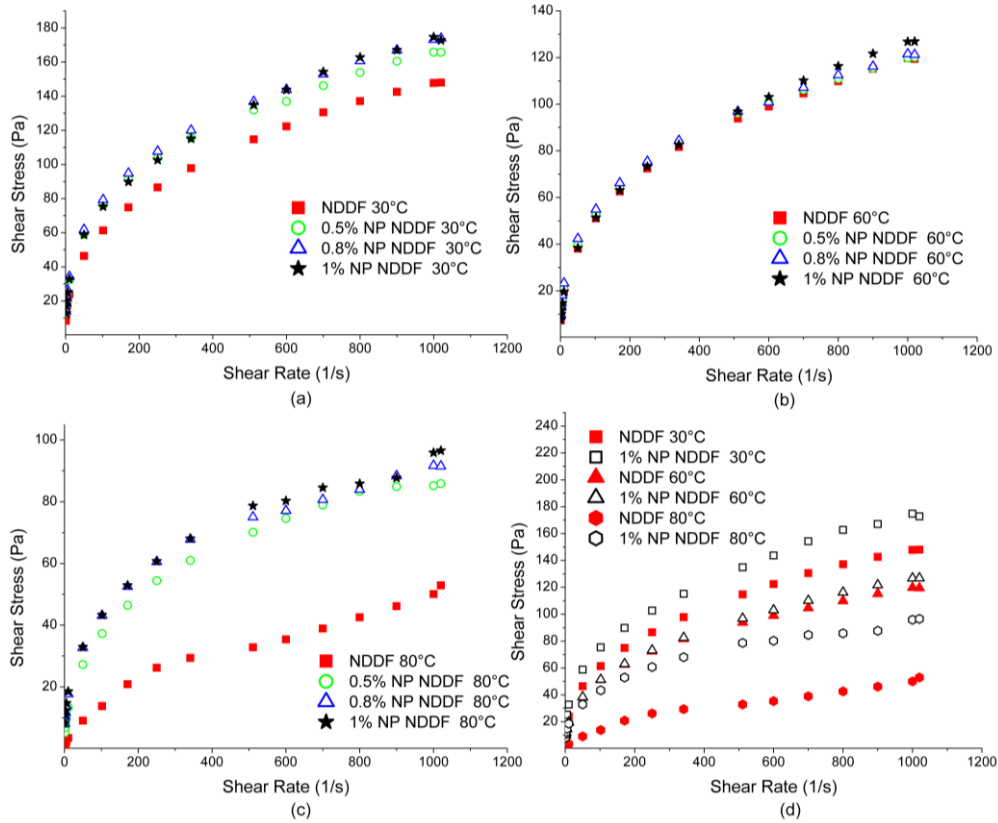


Fig. 6.4: (a) Shear stress vs. shear rate at 30 °C, (b) Shear stress vs. shear rate at 60 °C, (c) Shear stress vs. shear rate at 80 °C, (d) Shear stress vs. shear rate for NDDF and 1 wt% ZrO₂ NP at 30, 60 and 80 °C. Legend: NDDF represents the base with 0 wt% ZrO₂ NP. 0.5% represents 0.5 wt% ZrO₂ NP NDDF and so on.

Figs. 6.3 and 6.4 show the viscosity and shear stress vs. shear rate information for various NDDFs corroborating the effect of concentration of NPs and an increase in temperature. In general, all the NDDFs have shown shear thinning behaviour. At 30 °C (Figs. 6.3 a and 6.4 a), the addition of ZrO₂ NPs significantly increases the viscosity and shear stress of NDDFs. For 0.5 wt% ZrO₂ NP NDDF, the maximum increase in viscosity and shear stress at low shear rates (1 to 100 s⁻¹) as compared to the base NDDF are 44% and 35%, respectively. For intermediate shear rates (100 to 700 s⁻¹), the increase in viscosity and shear stress as compared to the base NDDF is observed to be 60% and 15%, respectively. For high shear rates (>700 s⁻¹), an increase in viscosity and shear stress are around 60% and 12%, respectively, as compared to the base

NDDF. For 0.8 wt% ZrO₂ NP NDDF, the viscosity increase at the low, intermediate and high shear rates were found to be 97, 86 and 87% as compared to the base NDDF. Similarly, the values of shear stress were also found to be increased by 54, 22 and 17% as compared to the base NDDF. At 60 °C (Fig. 6.3 b), all the fluids have a significant reduction in viscosity and shear stress due to an increase in temperature. Although the changes between the fluids are not noteworthy, as the temperature increases from 30 to 60 °C, at high shear rates higher reduction in viscosity can be observed for the base NDDF (0 wt%), 0.5 wt% ZrO₂ NP NDDF and 0.8 wt% ZrO₂ NP NDDF as compared to 1 wt% ZrO₂ NP NDDF. Similar trends can also be observed for the shear stress of all the NDDFs (Fig. 6.4 b). At 80 °C, for base NDDF, viscosity is reduced by 53% at low shear rates, 50% at intermediate shear rates and 51% at high shear rates as compared to the base NDDF at 30 °C. Additionally, at 80 °C (Fig. 6.3 c), for 0.5, 0.8 and 1 wt% ZrO₂ NP NDDFs, the percentage reduction in viscosity at the lower shear rates is 29%, 52%, and 34%, respectively, as compared to 30 °C. Whereas for high and intermediate shear rates reduction in viscosity is found to be the least for 1 wt% ZrO₂ NP NDDF that is 40% and 42% respectively. From Fig. 6.4 (c), it can be observed that the steep rise in shear stress values ceases at 400 s⁻¹ while for ZrO₂ NP NDDF rise in shear stress continues till 700 to 800 s⁻¹. Figs. 6.3 (d) and 6.4 (d) represent viscosity vs. shear rate and shear stress vs. shear rate for the base NDDF and 1 wt% ZrO₂ NP NDDF, respectively, at 30, 60 and 80 °C. It can be observed that the reduction in magnitudes of viscosity and shear stress due to the increase in temperature is quite large for base NDDF. This difference is prominent at high shear rates. On the contrary, the addition of 1 wt% ZrO₂ NP NDDF induces better thermal stability by preserving its viscosity and shear stress.

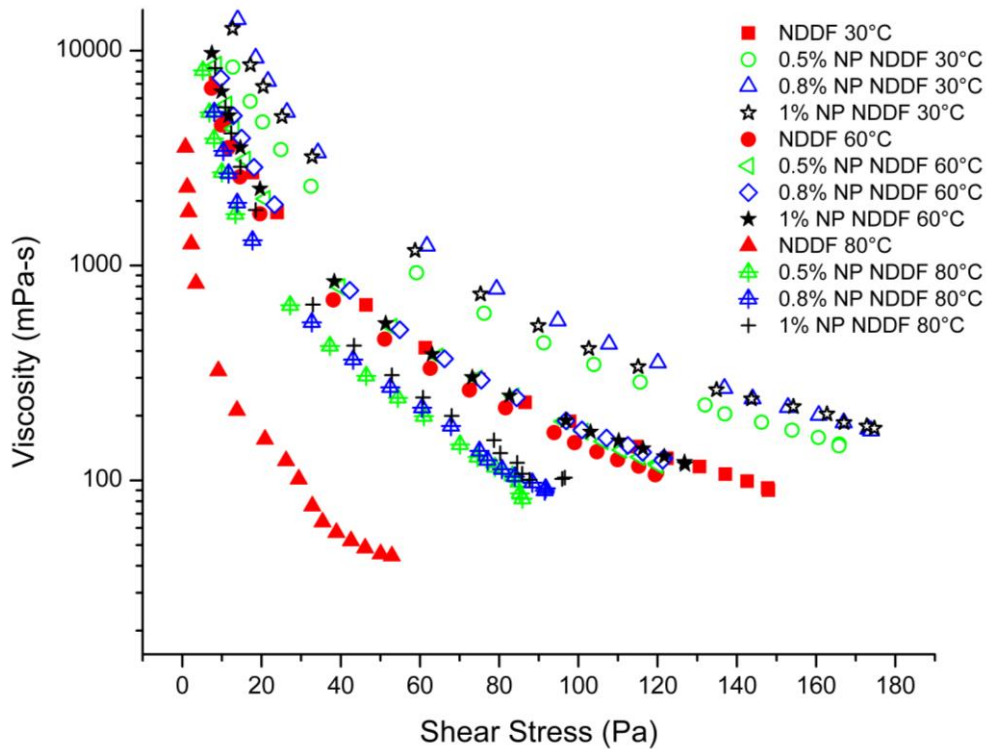


Fig. 6.5: Viscosity vs. shear stress for various NP NDDFs prepared in this study.

Legend: NDDF represents the base with 0 wt% ZrO_2 NP. 0.5% represents 0.5 wt% ZrO_2 NP NDDF and so on.

Fig. 6.5 shows viscosity vs. shear stress curves for all the NDDFs at different temperatures. From Fig. 6.5, at 30 °C, a gradual decrease in viscosity is observed for all the drilling fluids. At 60 °C, the same trend is persistent while yielding a lesser magnitude of viscosity for applied shear stress. At 80 °C, the base NDDF shows a sharp decline in viscosity even for a minor increase in shear stress (0-40 Pa). However, this sharp trend in decline is not observed for ZrO_2 NP NDDF. Comparing the results for all the fluids at different temperatures, it can be observed that the reduction in viscosity is less for 1 wt% ZrO_2 NP NDDF as compared to 0.5, 0.8 wt% ZrO_2 NP NDDF and base NDDF fluids at both low and high shear rates. The addition of polymer in a continuous water phase generally causes an increase in viscosity, forming hydrogel compounds. The rise in viscosity is due to the entanglement of polymers. At low shear rates where the deformation is substantially low, the degree of polymer entanglement is high. Whereas, at high shear rates a gradual decrease in viscosity is observed

typically for shear thinning fluids. This decrease in viscosity is due to the breakage of the entangled chain structure of the polymer within the fluid structure. At high shear rates, the polymer forms linear chains and has little or no inter-linkage within the bulk fluid structure (Hakiki et al., 2015). Maintaining viscosity at low shear rates is more significant than in high shear rates as the latter is often accompanied by the high velocity that aids in cutting removal. However, at low shear rates, the cutting lifting competence is always vetted on the rheological properties of the drilling fluid. This range of low shear rates is more prominent in the upper annular region.

6.2.2 AMPLITUDE SWEEP TEST MEASUREMENTS

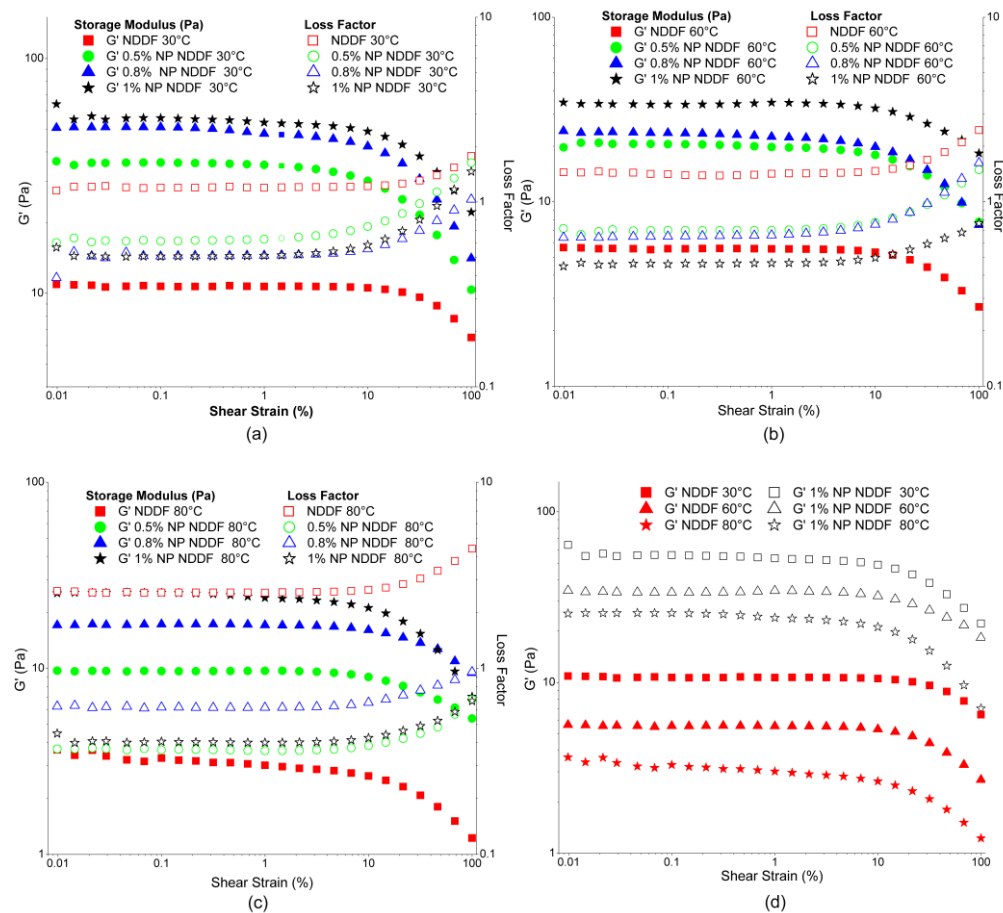


Fig. 6.6: (a) Storage modulus (G') and loss factor vs. shear strain (%) at 30 °C, (b) G' and loss factor vs. shear strain (%) at 60 °C, (c) G' and loss factor vs. shear strain (%) at 80 °C, (d) G' vs. shear strain (%) for NDDF and 1 wt% ZrO_2 NP at 30, 60 and 80. Legend: NDDF represents the base

with 0 wt% ZrO₂ NP. 0.5% represents 0.5 wt% ZrO₂ NP NDDF and so on.

Fig. 6.6 shows the storage modulus (G') and loss factor (G''/G') vs. shear strain (%) for various NDDFs at different temperatures. From Fig. 6.6 (a), it can be observed that at 30 °C, the addition of ZrO₂ NP barely influences the linear viscoelastic range (LVER), which is observed to be 5% shear strain. The storage modulus at 5% shear strain increases from 10.55 Pa for NDDF to 30.13 Pa, 42.2 Pa and 48.9 Pa for 0.5, 0.8 and 1 wt% ZrO₂ NP NDDF, respectively. This indicates that the elasticity component of NDDF is enhanced due to the addition of ZrO₂ NPs. Besides, NDDF behaves as a viscoelastic liquid as the value of the loss factor is greater than unity. Upon the addition of ZrO₂ NPs, the fluid transforms into viscoelastic in nature. A crossover point ($G' = G''$) can be noted beyond shear strain of 60% for all the ZrO₂ NPs NDDF. At 60 °C (Fig. 6.6 b), there is a reduction in G' for all the fluids with base NDDF bearing the highest of 57% at 10% shear strain. The least reduction in G' value was shown by 1 wt% ZrO₂ NP NDDF by 38%. At 80 °C (Fig. 6.6 c), a decline in values of G' can be observed for all the fluids. The highest percentage decline for base NDDF was found to be 73%. The percentage decline for 0.5, 0.8 and 1 wt% ZrO₂ NP NDDF were 72%, 63% and 54%, respectively.

Higher thermal stability (Fig. 6.6 d) of 1 wt% ZrO₂ NP NDDF concerning storage modulus (G') indicates superior anti-sagging properties as compared to other fluids due to a higher degree of crosslinking. It can find applications in high temperature wells where sagging of cuttings is a persistent issue. Higher dynamic yield point (or LVER) in case of 0.8 and 1 wt% ZrO₂ NP NDDF shows anti-sagging properties.

6.2.3 FREQUENCY SWEEP TEST MEASUREMENTS

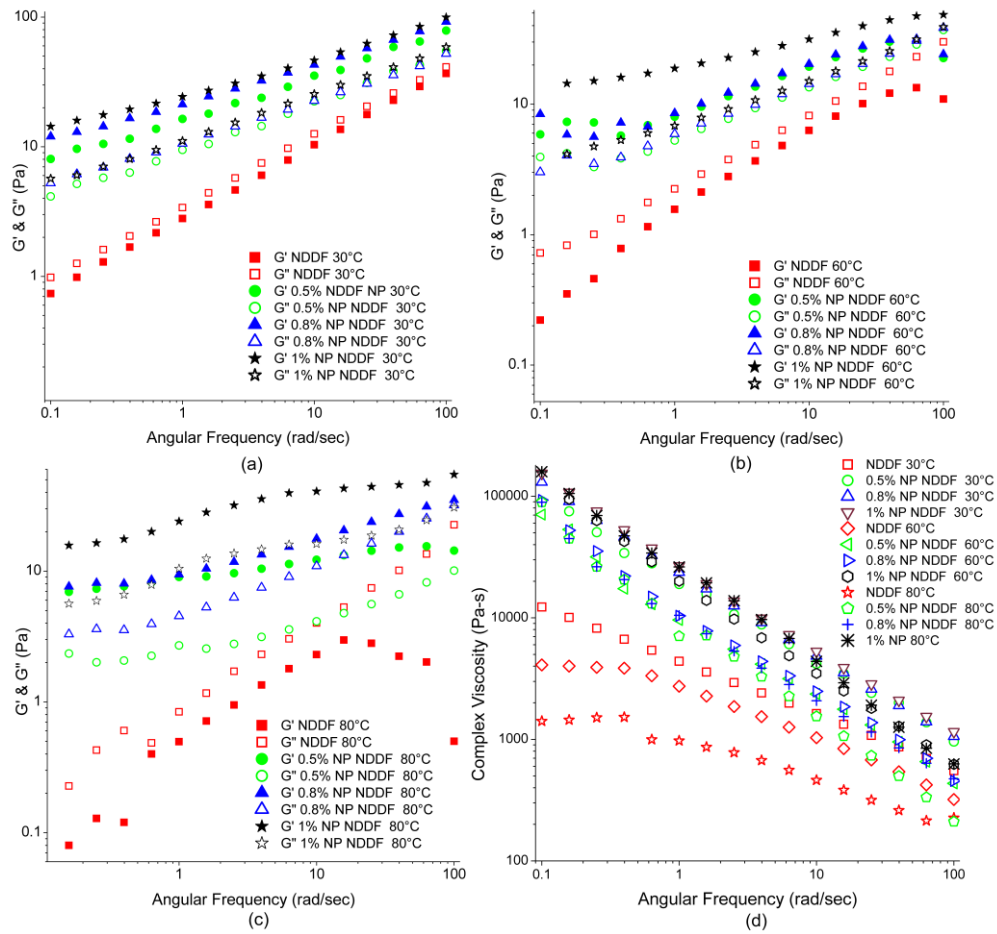


Fig. 6.7: (a) Storage modulus (G') and Loss modulus (G'') vs. angular frequency at 30 °C, (b) G' and G'' vs. angular frequency at 60 °C, (c) G' and G'' vs. angular frequency at 80 °C, (d) Complex viscosity vs. angular frequency at 30, 60 and 80° C. Legend: NDDF represents the base with 0 wt% ZrO₂ NP. 0.5% represents 0.5 wt% ZrO₂ NP NDDF and so on.

Fig. 6.7 shows storage modulus (G'), loss modulus (G'') and complex viscosity vs. angular frequency for various NDDFs at different temperatures. At 30 °C (Fig. 6.7 a), base NDDF shows viscoelastic liquid behaviour throughout the frequency range. On the other hand, ZrO₂ NP based NDDF at all concentrations shows viscoelastic solid nature at all frequencies with a linear rise in complex viscosity like base NDDF. Fig. 6.7 (b) shows a sudden drop in the storage modulus of the base NDDF at high frequencies. 0.5, 0.8 and 1 wt% ZrO₂ NP NDDF do not show such loss in elasticity at higher frequencies. At 80

°C (Fig. 6.7 c), at high frequencies, G' and G'' of the fluids decrease as compared to the corresponding values at 30 °C. A complete breakdown of the structure may be expected for the base NDDF as G' decreases. Even at large intervals of time (low frequency), its failure to recover its structure is evident from the plateau region of the complex viscosity curve. This phenomenon can also be observed for 0.5 wt% ZrO₂ NP NDDF. 1 wt% ZrO₂ NP NDDF shows a striking property to retain structure even at high temperatures. The property of structure build up even at low frequencies displays its potential to regain elasticity rapidly and uniformly. Additionally, at both 60 and 80 °C (Fig. 6.7 d), plateau regions are observed for base NDDF in complex viscosity curves, although, no such phenomena are observed for other fluids doped with ZrO₂ NPs. A constant value of loss factor indicating a better stable structure of all ZrO₂ NP NDDFs even at higher temperatures is observed. On the contrary, base NDDF shows a high increase in loss factor at higher frequencies, especially at elevated temperatures.

Higher values of G' in case of 0.8 and 1 wt% ZrO₂ NP NDDF at low frequencies show better crosslinking firmness as compared to 0.5 wt% ZrO₂ NP NDDF and base NDDF. Superior structural stability at higher temperatures gives better applicability to prevent cutting sagging issues for high temperatures and deviated wells. Similar results were also observed in the amplitude sweep tests. However, it is to be noted that higher G' values are often accompanied by higher pumping power for startup flow. Once the structure is broken beyond the dynamic yield point, viscous forces shall dominate.

6.2.4 TEMPERATURE DEPENDENT FLOW BEHAVIOUR TEST MEASUREMENTS

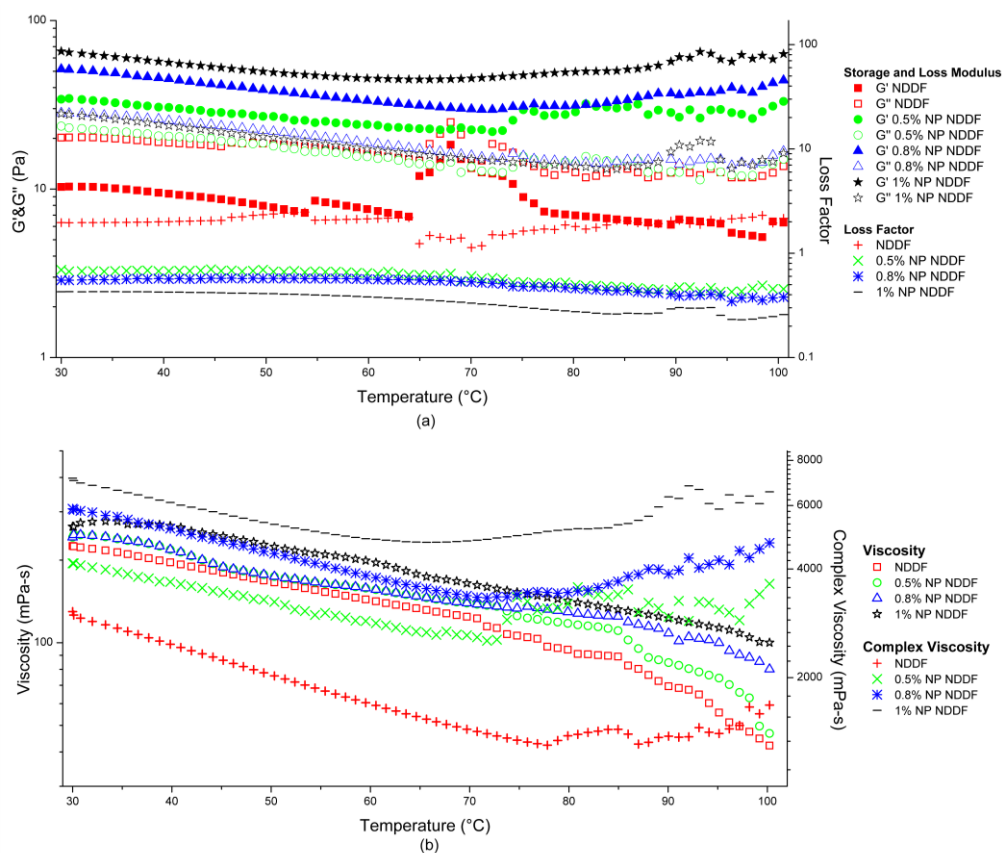


Fig. 6.8: (a) G' , G'' and loss factor vs. temperature, (b) Viscosity and complex viscosity vs. temperature for various NDDFs. Legend: NDDF represents the base with 0 wt% ZrO₂ NP. 0.5% represents 0.5 wt% ZrO₂ NP NDDF and so on.

From the temperature sweep measurements as shown in Fig. 6.8 (a), it can be observed that the base NDDF behaves as a viscoelastic liquid throughout the temperature range. The minimum value of G' for the base NDDF at a moderate temperature of 53 °C is 7.03 Pa which signifies the start of cross linking (curing temperature, T_{CR}) beyond which it rises and falls sharply indicating disintegration of the polymer structure. The value of T_{CR} increases with the addition of ZrO₂ NPs, notably 21.88 Pa at 72 °C, 29.57 Pa at 72 °C, 44.08 Pa at 64.97 °C for 0.5, 0.8 and 1 wt% ZrO₂ NP NDDF, respectively. Higher storage modulus with an increase in ZrO₂ NP concentration indicates a

higher degree of crosslinking. A sudden increase in G' at higher temperatures indicates the crystallization of polymer compounds due to the evaporation of the water phase. This spike in G' is delayed with the addition of ZrO_2 NP showing better thermal stability and reduction in the tendency to swelling at higher temperatures. A similar trend, as shown in Fig. 6.8 (b), can also be observed from viscosity and complex viscosity vs. temperature curves. This is due to the high thermal expansion of liquids as they are more sensitive to temperature (Hakiki et al., 2017). This also holds true for hydrogel colloids like drilling fluids. A linear decline in both the viscosities can be observed for base NDDF up to 67 °C. The highest stability is exhibited by 0.8 and 1 wt% ZrO_2 NP NDDF up to 90 and 95 °C, respectively. At low temperatures, due to similar viscosity and storage properties, all the fluids shall perform relatively similarly. However, at high temperature conditions, superior performance shall always prevail in the case of 0.8 and 1 wt% ZrO_2 NP NDDF as compared to 0.5 wt% and base NDDF.

6.2.5 TIME DEPENDENT FLOW BEHAVIOUR TEST MEASUREMENTS

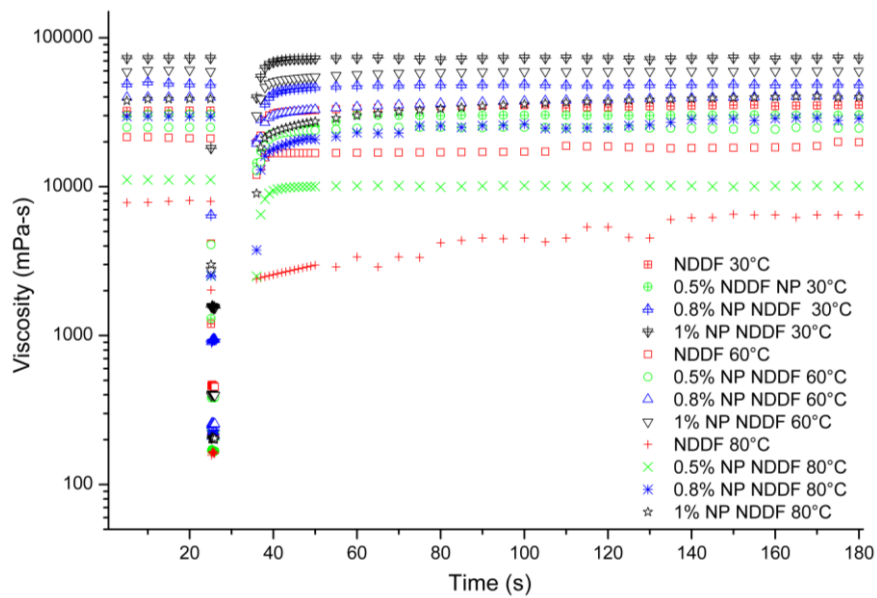


Fig. 6.9: Time dependent rotational thixotropic test for various NDDFs.

Legend: NDDF represents the base with 0 wt% ZrO_2 NP. 0.5% represents 0.5 wt% ZrO_2 NP NDDF and so on.

The viscosity build up for all fluids at the near static shear rates was studied for 180 seconds (3 minutes) as shown in Fig. 6.9. At 30 °C, complete structural regain was observed at 40, 60, 20 and 180 seconds for the base NDDF, 0.5, 0.8 and 1 wt% ZrO₂ NP NDDFs, respectively. At 60 °C, the base NDDF and 0.5 wt% ZrO₂ NP NDDF were able to regain only 95.2% and 98.8% of its original viscosity while 0.8 and 1 wt% ZrO₂ NP NDDF recovered at 135 and 100 seconds, respectively. At 80 °C, base NDDF, 0.5 and 0.8 wt% ZrO₂ NP NDDF recovered 79.9%, 91.01% and 96.64% of its original viscosity while 1 wt% ZrO₂ NP NDDF regained its complete structure within 125 seconds. All the fluids except 1 wt% ZrO₂ NP NDDF at higher temperatures show an inability to regain complete structural integrity. This would indicate failure to hold and suspend cuttings at a near static condition.

6.2.6 API FILTRATE LOSS TEST MEASUREMENTS

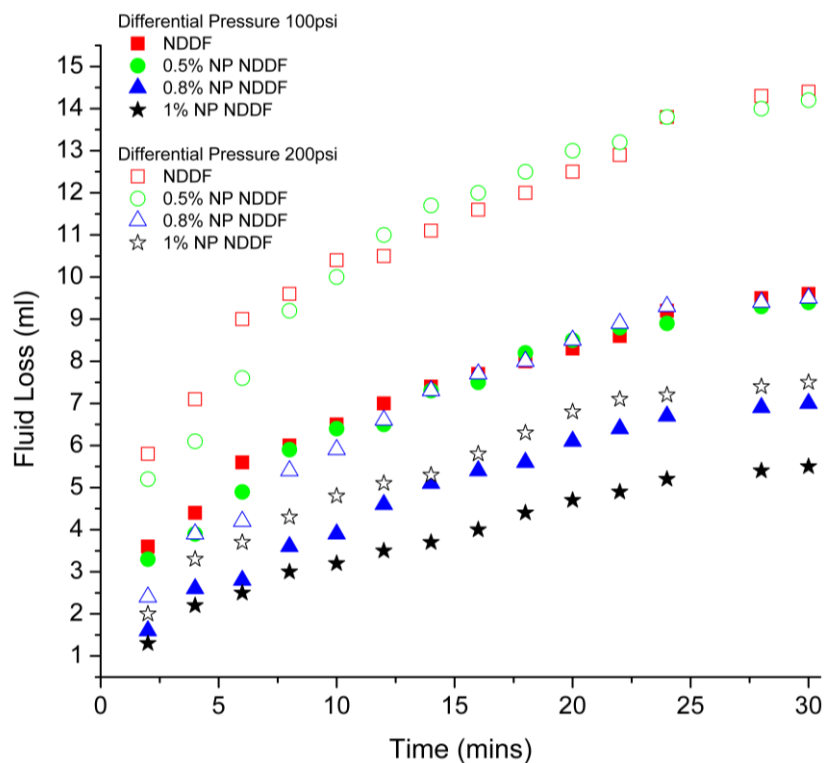


Fig. 6.10: Filtrate loss volume vs. time for various ZrO₂ NP NDDFs. Legend: NDDF represents the base with 0 wt% ZrO₂ NP. 0.5% represents 0.5 wt% ZrO₂ NP NDDF and so on.

Fig. 6.10 shows fluid loss volume of all the concerned drilling fluids at 689 kPa (100 psi) and 1378 kPa (200 psi). At 689 kPa (100 psi) of pressure differential, base NDDF has a filtrate loss of 9.6 ml at 30 minutes. 0.5 wt% ZrO₂ NP NDDF has a fluid loss of 9.4 ml which is only 2% less than the base NDDF. However, 0.8 and 1 wt% ZrO₂ NP NDDF have a fluid loss of 7 ml and 5.5 ml, respectively, which is 27.08 and 42.7% less than the base NDDF. At a differential pressure of 1378 kPa (200 psi), the fluid loss for base NDDF is 14.4 ml indicating a 50% increase as compared to 689 kPa (100 psi). Identical observations can also be made for 0.5 wt% ZrO₂ NP NDDF with a fluid loss volume of 14.2 ml. Fluid loss volume of 0.8 wt% and 1 wt% ZrO₂ NP NDDF at 1378 kPa (200 psi) are 9.5 and 7.5 ml, respectively, which are about 35.71 and 36.37 % more than the filtrate loss at 689 kPa (100 psi).

From the above filtration loss studies, it can be observed that 1 wt% of ZrO₂ NP NDDF has the least fluid loss volume at both 689 kPa (100 psi) and 1378 kPa (200 psi) differential pressure (Figure 6.10). This decrease in fluid loss can be due to the blocking of pore spaces by the ZrO₂ NPs (Yang et al., 2015). Since the measurements are done in a static condition, a higher G' value shall also have a role to play (as observed in Fig. 6.7 a for 1 wt% NP NDDF) for a reduced filtrate loss due to higher elasticity and higher dynamic yield point. In practicality, the velocity at walls of the wellbore is almost zero, hence; it is envisaged that the higher elasticity shall prevent the release of water that outflows as filtrate into the formation. Additionally, from the frequency sweep data, it can be noted that loss factor value lies in the range of 0.2 to 0.3. Within this range, polymer fluids are resistant to syneresis contributing to this significant reduction of filtrate loss.

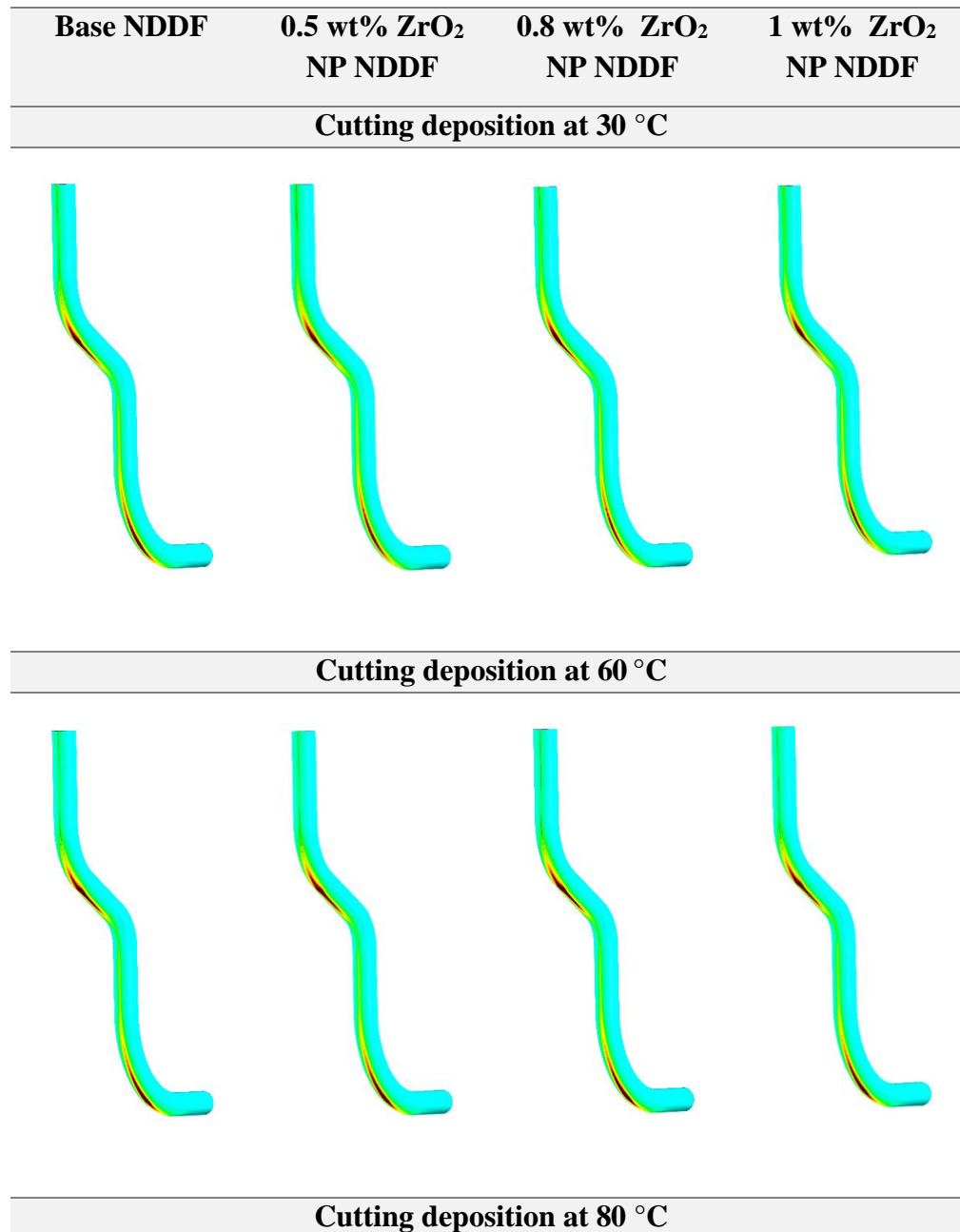
6.3 DETERMINING OPTIMAL HERSCHEL BUCKLEY (HB) PARAMETERS USING GENETIC ALGORITHM (GA)

Table 6.1 Optimal Herschel Bulkley (HB) parameters determined by genetic algorithm (GA) for various NDDFs

NDDF Sample	Temperature °C	Yield Point (Pa)	k (Pa/s ⁿ)	n	SSE
Base NDDF	30	0	10.12	0.389	5.11
0.5% NP NDDF		2.33	13.85	0.357	18.14
0.8% NP NDDF		3.16	13.95	0.362	12.50
1% NP NDDF		1.49	13.13	0.370	1.02
Base NDDF	60	0	8.81	0.378	13.27
0.5% NP NDDF		0	9.75	0.365	17.14
0.8% NP NDDF		0	10.8	0.350	6.37
1% NP NDDF		0	8.0	0.399	2.08
Base NDDF	80	0	1.55	0.569	31.58
0.5% NP NDDF		0	3.65	0.313	82.54
0.8% NP NDDF		0	5.87	0.398	7.23
1% NP NDDF		0	9.84	0.326	45.74

6.4 RESULTS AND DISCUSSION ON FLOW BEHAVIOUR FROM CFD STUDIES IN ECCENTRIC WELLBORE ANNULUS

6.4.1 EFFECT OF ZrO₂ NPs ON CUTTING CARRYING CAPACITY OF NDDF



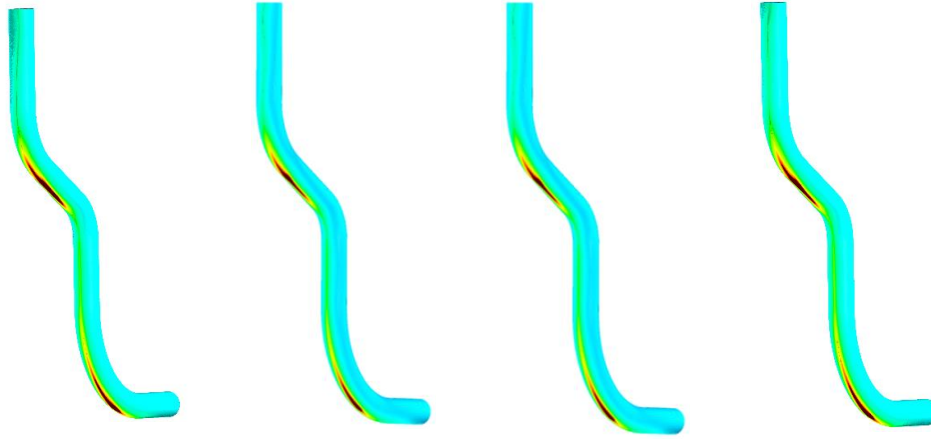


Fig. 6.11: Comparative side view of contours for cutting volume fraction ($V_{\text{inlet}} = 0.8 \text{ m/s}$, cutting density and inlet volume fraction = 2550 kg/m^3 and 10% respectively)

Fig. 6.11 shows the contours of cutting volume fraction for all the concerned NDDFs. The cutting volume fraction is a direct indicator of the drilling fluid's performance in the wellbore annular region. A low cutting fraction is an indication of better drilling fluid performance in the removal of cuttings.

Table 6.2: Percentage volume retention of cuttings in annulus vs. different cases of concentration and temperatures. $(\text{Volume fraction of cuttings})_{\text{annulus}} - (\text{Volume fraction of cuttings})_{\text{inlet}} = (\text{Retention of volume fraction of cuttings})_{\text{annulus}}$

Cutting retention in terms of % total annular volume				
Sample / Temperature	Base NDDF	0.5 wt% ZrO ₂ NP NDDF	0.8 wt% ZrO ₂ NP NDDF	1 wt% ZrO ₂ NP NDDF
30 °C	0.098	0.088	0.084	0.085

60 °C	0.116	0.115	0.114	0.111
80 °C	0.152	0.150	0.145	0.136

The cutting sedimentation is greater in the upper build-up section as compared to the lower one as observed in Table 6.2. At 30 °C, cutting sedimentation is minimal as compared to that at higher temperatures. The amount of cutting accumulated declines with an increase in wt% of ZrO₂ NP. The lowest cutting retention at 30 °C is calculated to be 0.084% of total annular volume for 0.8% ZrO₂ NP as observed in Table 6.3. At 60 °C, a reduction for base NDDF's performance can be observed with the cuttings occupying 0.116% of total annular volume and 0.111% for 1 wt% of ZrO₂ NP NDDF. At 80° C, a significant increase in performance of 1 wt% of ZrO₂ NP NDDF with cutting retention of 0.136% as compared to that of base NDDF yielding 0.152%.

From the above results, it can be clearly inferred that the addition of ZrO₂ NP greatly improves the cutting carrying capacity of the mud. Hence, it can be effectively used as an additive in muds to prevent severe sagging problems and better cutting removal.

6.4.2 EFFECT OF ZrO₂ NPs ON THE VELOCITY PROFILE OF NDDF

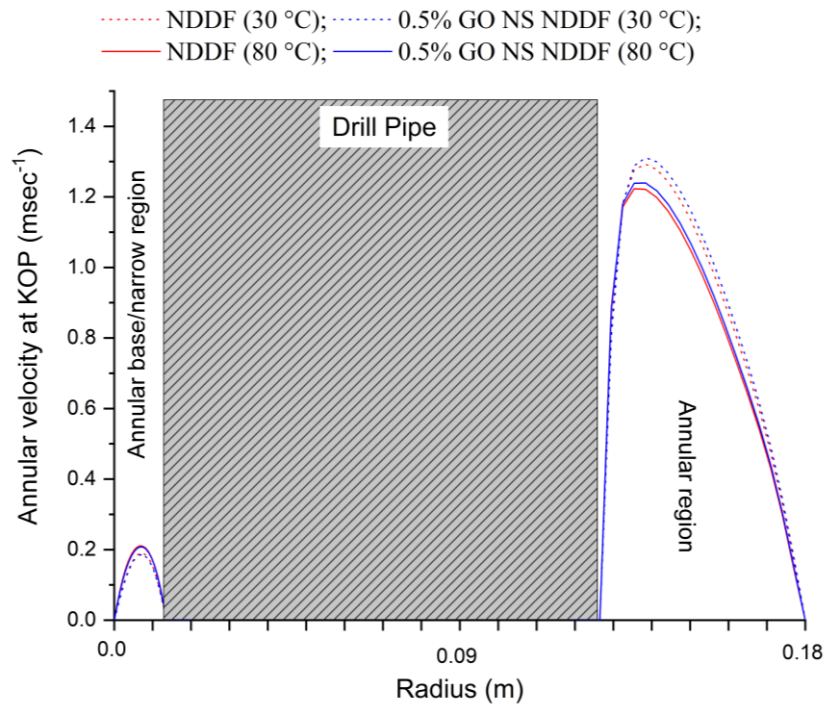


Fig. 6.12: Velocity profile at Kick-off Point (KOP) for base and 1% ZrO₂ NP NDDF at 30 and 80 °C conditions

At the KOP (Fig. 6.12), a sharp velocity profile is observed for all the fluids at both 30 and 80 °C. The addition of ZrO₂ NP results in a slightly higher mean lift velocity at both 30 and 80 °C. From Table 6.3 it can be clearly observed that at 80 °C, the fluid has lower lift velocity and a lower wellbore cleaning efficiency as compared to 30 °C with 1 wt% of ZrO₂ NP NDDF showing better of both. Moreover, it can be observed that skewness of 1 wt% of ZrO₂ NP NDDF is relatively less than base NDDF at both 30 and 80 °C.

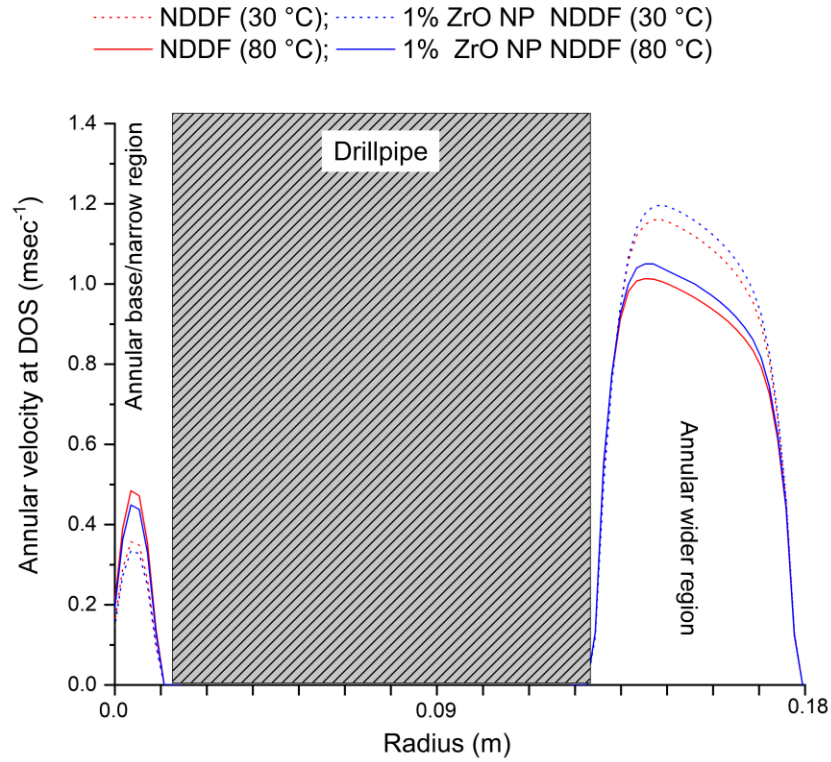


Fig. 6.13: Velocity profile at Drop-off section (DOS) for base and 1% ZrO₂ NP NDDF at 30 and 80 °C conditions

At the DOS (Fig. 6.13), a blunt velocity profile can be observed as compared to KOP (Fig. 6.12) as a result of which, it is evident that there is significantly less cutting deposition. The lift velocity at DOS is lower for 80°C. In addition to this, the inclusion of ZrO₂ NP leads to a reduced velocity drop in the annular region, thereby enhancing the mud performance.

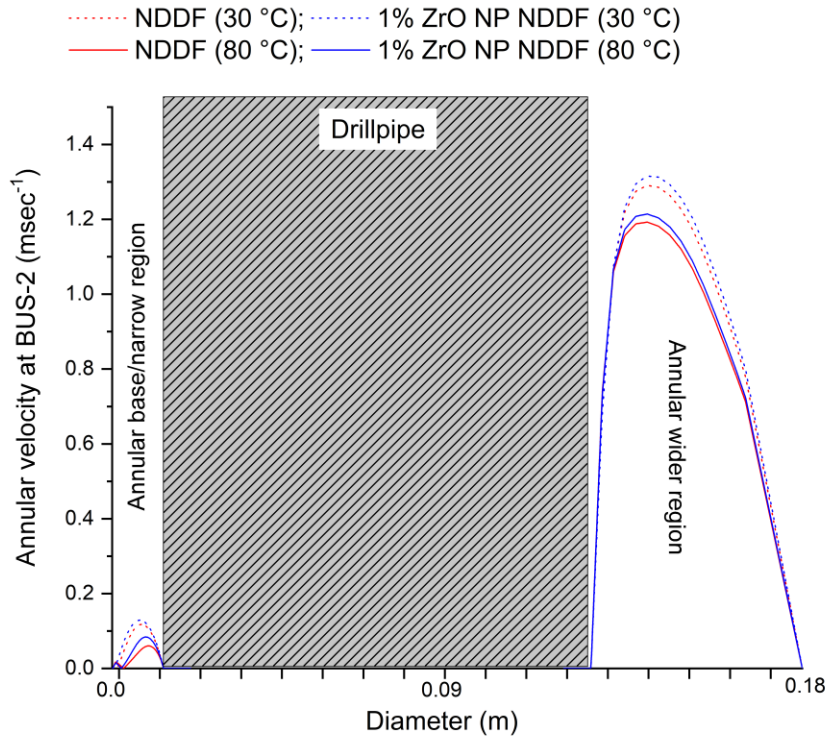


Fig. 6.14: Velocity profile at Build-up section (BUS) for base and 1% ZrO₂ NP NDDF at 30 and 80 °C conditions

The 2nd BUS (Fig. 6.14) exhibits less sharpness of velocity as compared to that at KOP. This is one of the reasons because of which cutting deposition is higher at KOP as compared to 2nd BUS. However, no significant differences in velocities can be drawn between the base and 1 wt% of ZrO₂ NP NDDF at 2nd BUS.

6.4.3 EFFECT OF ZrO₂ NPs ON PRESSURE DROP OF NDDF

Pressure drop calculations are presented which throws light on the flowability of the drilling fluids (Fig. 6.15). The highest pressure drop is shown by 0.8 wt% of ZrO₂ NP NDDF at 30°C which is 10420.22 Pa and a least of 7993.01 Pa. Hence, pressure drop lies within a limit of 0.11 psi/ft to 0.15 psi/ft which lies within an acceptable range. A decrease in pressure drop can be observed with a rise in temperature which is a consequence due to degradation of rheological properties.

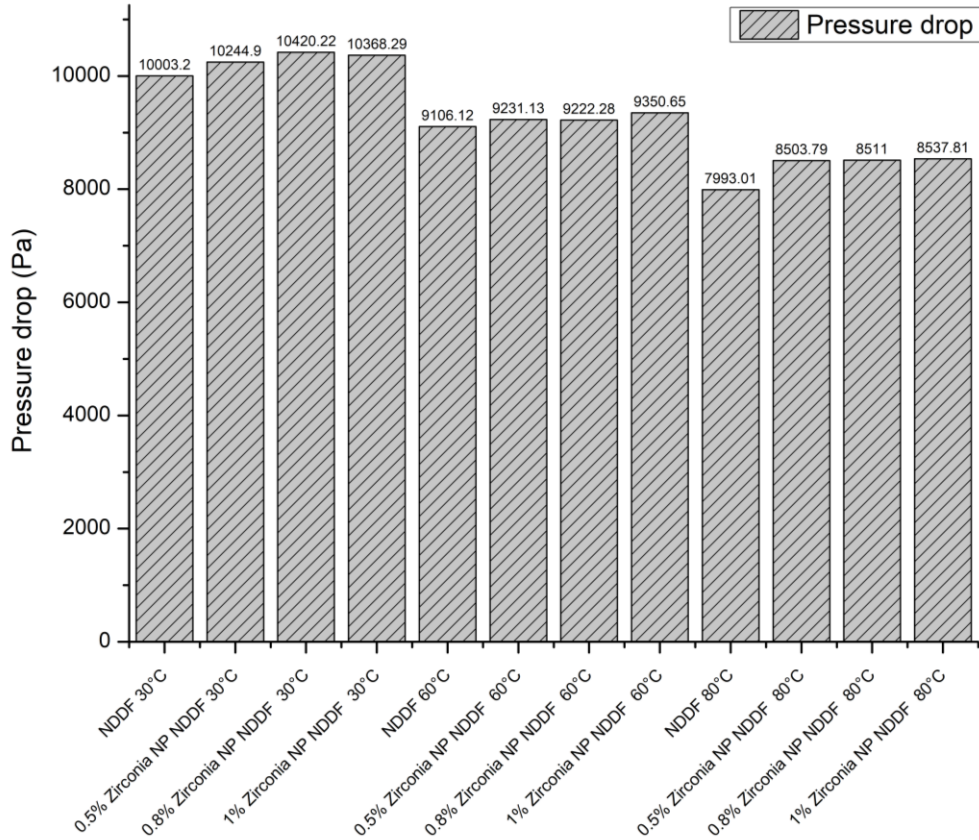


Fig. 6.15: Pressure drop of ZrO₂ NP NP based NDDF

6.5 CHAPTER CONCLUSION

With the addition of ZrO₂ NP, a significant enhancement of properties was observed from a rheological standpoint. Viscoelastic studies indicate that elastic nature was induced in the NDDF with the addition of ZrO₂ NPs. Notably, 1 wt% ZrO₂ NP NDDF proved to be the best when investigated for fluid loss control as well as cutting displacement efficiency.

CHAPTER 7

EFFECT OF GRAPHENE OXIDE NANOSHEET (GO NS) ON NDDF

In this chapter, the effect of in-house synthesized graphene oxide nanosheet (GO NS) on NDDF through steady-state rotational and dynamic oscillation rheological measurements; along with fluid loss estimation. Herschel Bulkley parameters are then determined to carry out computational fluid dynamics (CFD) simulations and to quantify the effect of GO NS on the performance of NDDF. Synthesis of graphene oxide nanosheets (GO NS) was conducted by following the Hummers method. Characterization of GO NS was carried out by x-ray diffraction (XRD) spectroscopy and transmission electron microscopy (TEM).

7.1. SYNTHESIS OF GRAPHENE OXIDE NANOSHEET

To synthesize graphene oxide nanosheets (GO NS), the hummers method was followed (Hummers Jr. & Offeman, 1958; Krishnakumar et al., 2020; Shaygan Nia et al., 2014). First, a mixture of graphite flakes (1g) and sodium nitrate (0.5g) was made after which sulphuric acid was added by keeping the mixture in an ice bath (0 °C). The mixture was further catalysed by slowly adding potassium permanganate (3 mg) at 20 °C and kept for further stirring at 35 °C for 10-12 hours. The mixture was then cooled at 25 °C. Coldwater (130 ml) along with 30% hydrogen peroxide (3ml) was added to it. The precipitate was then washed with ethanol and hydrochloric acid for 3-4 times and centrifuged. The GO sample was dried at 120 °C and flaky GO powder was obtained. Synthesized GO was then analysed through x-ray diffraction (XRD) spectroscopy and transmission electron microscopy (TEM).

7.2 CHARACTERIZATION OF GO NS

In this section, the characterization of the synthesized GO NS and the rheological measurements on its addition to the base NDDF has been investigated. The characterization of GO NS is analysed through XRD and TEM images.

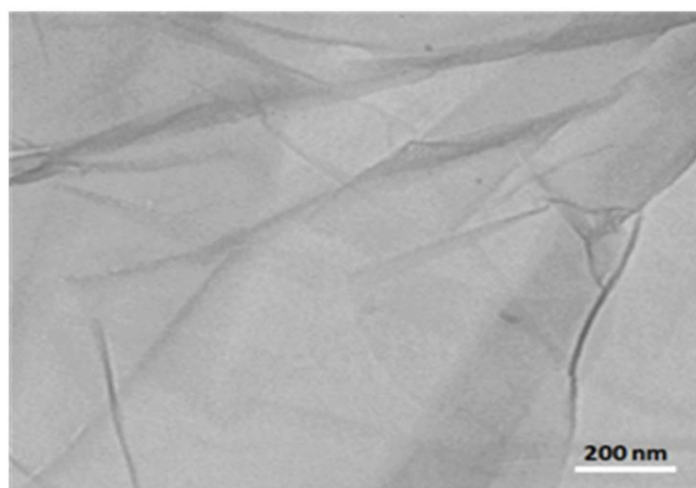
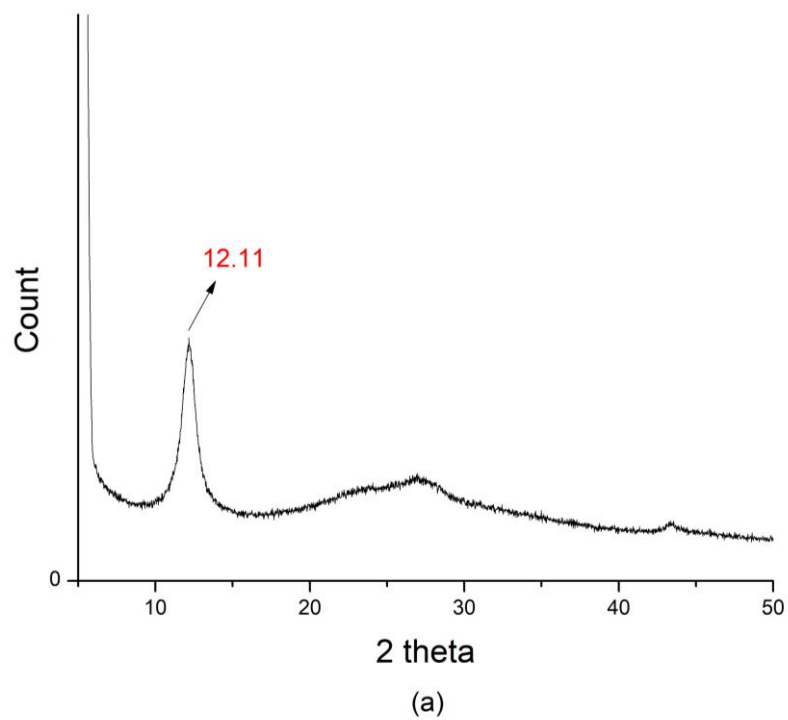


Fig. 7.1: (a) XRD pattern of synthesized GO NS, peak identifies at $2\theta = 12.11$
(b) TEM image of GO NS showing clear dark and light patches.

By using the Scherrer equation (Sahoo & Mallik, 2015; Scherrer & Debye, 1918) the crystal size was calculated to be 2.4 nm at $2\theta = 12.11$ as seen in Fig. 7.1 a. Interplanar distance as determined by Bragg's Law (Aladekomo & Bragg, 1990) was 0.63 nm. Additionally, the number of graphene layers can be quantified by dividing the crystal size by interplanar distance. Hence, around four graphene layers were observed from this synthesis. Fig. 7.1 b, translucent nature from TEM images shows a higher degree of oxidation. Darker patches specify stacked GO layer whereas lighter layer represents monolayers.

7.3 RHEOLOGICAL MEASUREMENTS

7.3.1 STEADY STATE ROTATIONAL TEST MEASUREMENTS

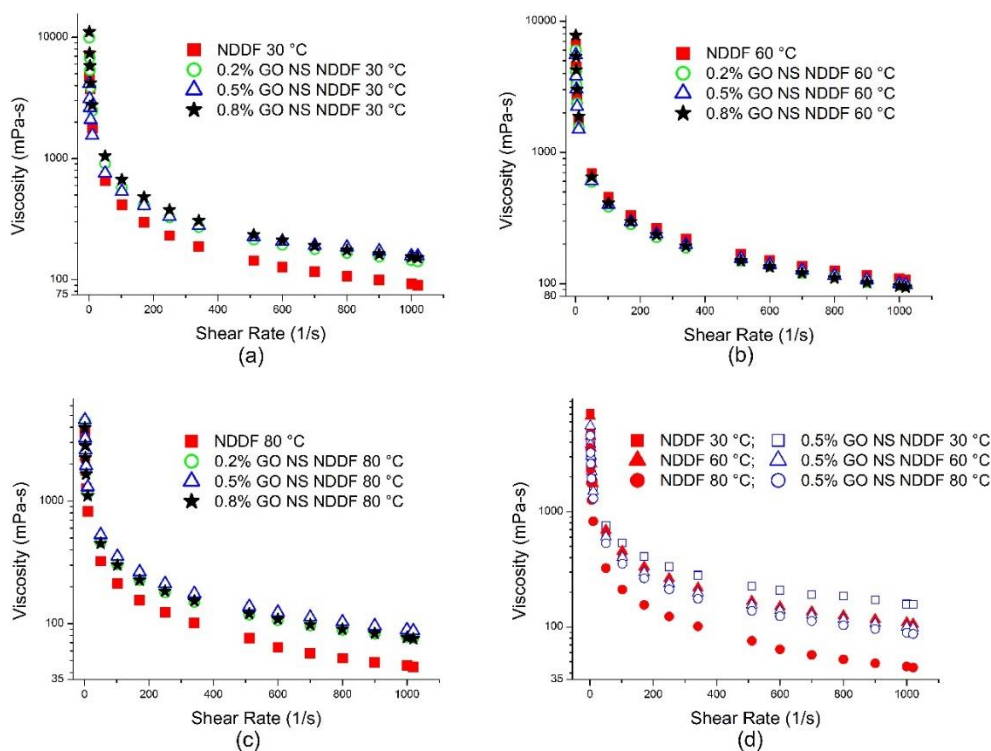


Fig. 7.2: (a) Viscosity vs. shear rate at 30 °C, (b) Viscosity vs. shear rate at 60 °C, (c) Viscosity vs. shear rate at 80 °C, (d) Viscosity vs. shear rate for NDDFs with 0 and 0.5 wt% NS at 30, 60 and 80 °C. Legend: NDDF represents the base with 0 wt% GO NS, 0.2% represents 0.2 wt% GO NS NDDF and so on.

Fig. 7.2 shows viscosity vs. shear rate for the base NDDFs at different temperatures (30, 60 and 80 °C) and concentrations (0, 0.2, 0.5 and 0.8 wt%) of GO NS. With the addition of GO NS at 30 °C (Fig. 7.2 a), viscosity at low shear rates (1 to 100 s⁻¹) is increased by a maximum of 42, 15 and 59 % for 0.2, 0.5 and 0.8 wt% GO NS NDDF as compared to the base NDDF. This increase in viscosity increases further at intermediate shear rates (100 s⁻¹ to 500 s⁻¹) by 53, 63 and 66 % for 0.2, 0.5 and 0.8 wt% GO NS NDDF. The increasing trend continued for high shear rates (>500 s⁻¹) for 0.2, 0.5 and 0.8 wt% GO NS NDDF with a percentage increase of 57, 74 and 67%. From Fig. 7.2 (b), at 60 °C, the overall viscosity of GO NS NDDF decreases as compared to base NDDF. The highest reduction is shown by 1% GO NS NDDF by 11% for both intermediate and high shear rates. At 80 °C (Fig. 7.2 c), one can observe a sudden drop in viscosity of base NDDF. Amongst all fluids, 0.5% shows the highest retention in viscosity, exceeding that of base NDDF by 64, 94 and 98% at low, intermediate and high shear rates respectively. From the above observations, it can be inferred that at 30 °C, the addition of GO NS promotes the shear thinning nature of the fluid. However, at elevated temperatures, one can observe that viscosity retention increases with GO NS doping. This phenomenon is greatest with 0.5 wt% GO NS NDDF (Fig. 7.2 d).

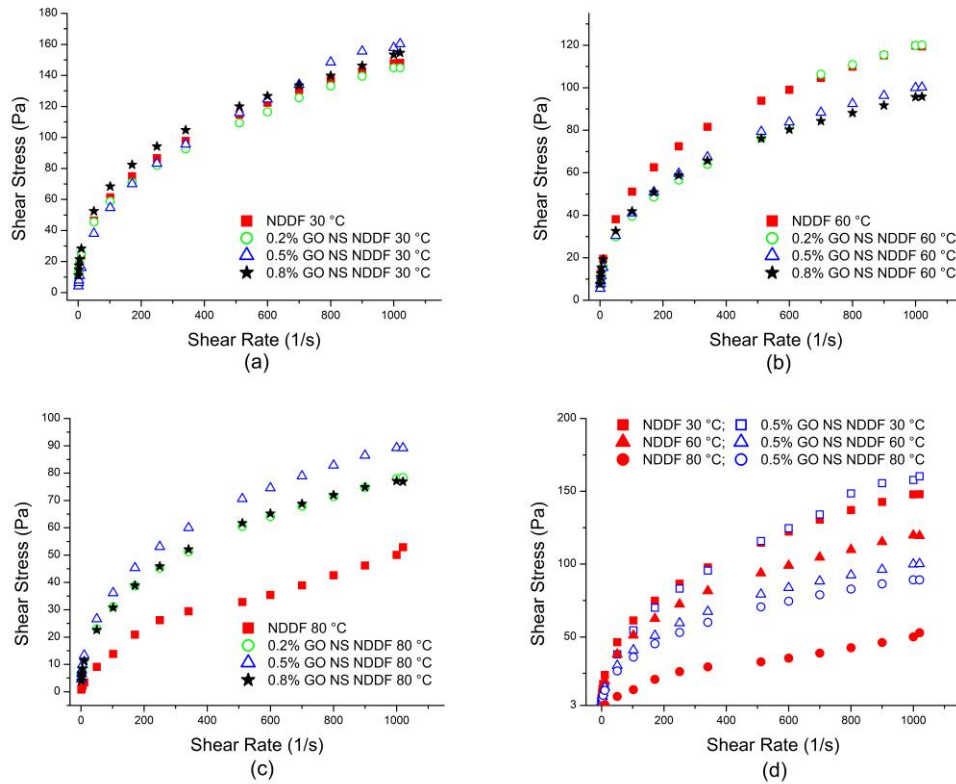


Fig. 7.3: (a) Shear stress vs. shear rate at 30 °C, (b) Shear stress vs. shear rate at 60 °C, (c) Shear stress vs. shear rate at 80 °C, (d) Shear stress vs. shear rate for NDDF and 0.5 wt% GO NS at 30, 60 and 80 °C. Legend: NDDF represents the base with 0 wt% GO NS, 0.2% represents 0.2 wt% GO NS NDDF and so on.

The trend, for shear stress vs. shear rate (Fig. 7.3) is however similar to viscosity as expected.

7.3.2 AMPLITUDE SWEEP TEST MEASUREMENTS

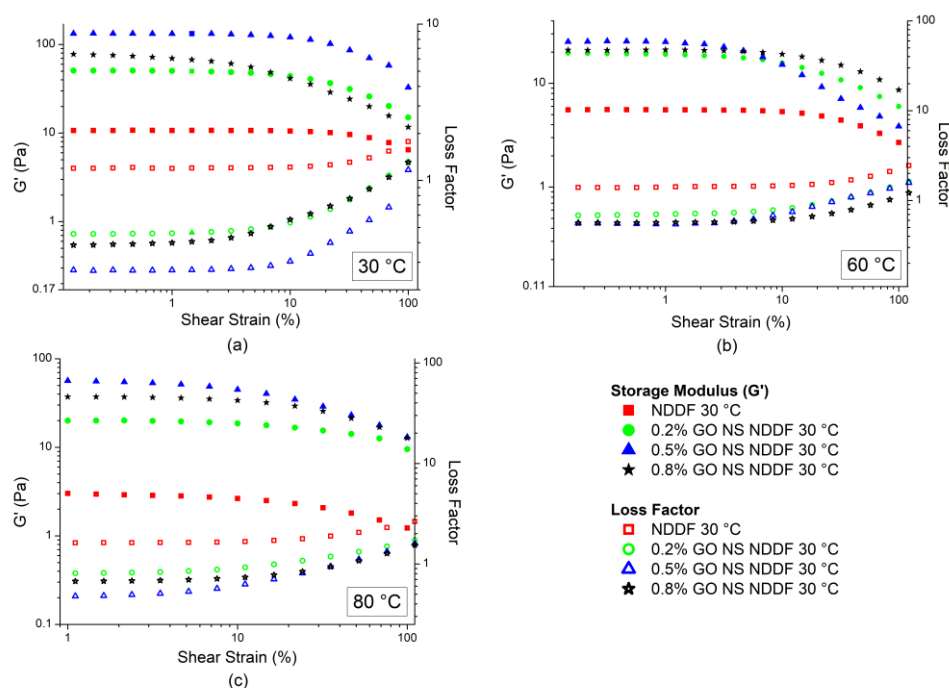


Fig. 7.4: (a) Storage modulus (G') and loss factor vs. shear strain (%) at 30 °C, (b) G' and loss factor vs. shear strain (%) at 60 °C, (c) G' and loss factor vs. shear strain (%) at 80 °C. Legend: NDDF represents the base with 0 wt% GO NS, 0.2% represents 0.2 wt% GO NS NDDF and so on.

Fig. 7.4 represents storage modulus (G') vs. shear strain (%) for the base and 0.5 wt% GO NS NDDF from amplitude sweep measurements. From Fig. 7.4 (a), it can be observed that 0.5 wt% GO NS NDDF shows the highest value of G' at 131 Pa while the base NDDF shows a G' value of 11 Pa. From Fig. 7.4 (b), it can be noted that the base NDDF exhibits viscoelastic liquid nature as the value of loss factor is above unity across all shear strain. With the addition of GO NS, a gradual increase in elastic property can be observed as loss factor approaches less than unity with the increase in concentration. At 80 °C, Fig. 7.4 (c), G' of the base and 0.2 wt% GO NS NDDF completely degrades to 3.6 and 19.8 Pa. On the contrary, 0.5 and 0.8 wt% GO NS NDDF has 57.6 and 37.1 Pa within the linear viscoelastic range (LVER). It is interesting to note that 0.5 wt%

GO NS NDDF shows a more viscoelastic solid nature than 0.8 wt% GO NS NDDF. Higher storage modulus or capacity (G') suggests better crosslinking within the colloidal hydrogel structure. In one of our recent studies, we found that the fluids having higher G' values have better cutting carrying ability. Hence, it can be construed that cutting carrying ability of 0.5 wt% GO NS NDDF shall be superior to that of other NDDFs.

7.3.3 FREQUENCY SWEEP TEST MEASUREMENTS

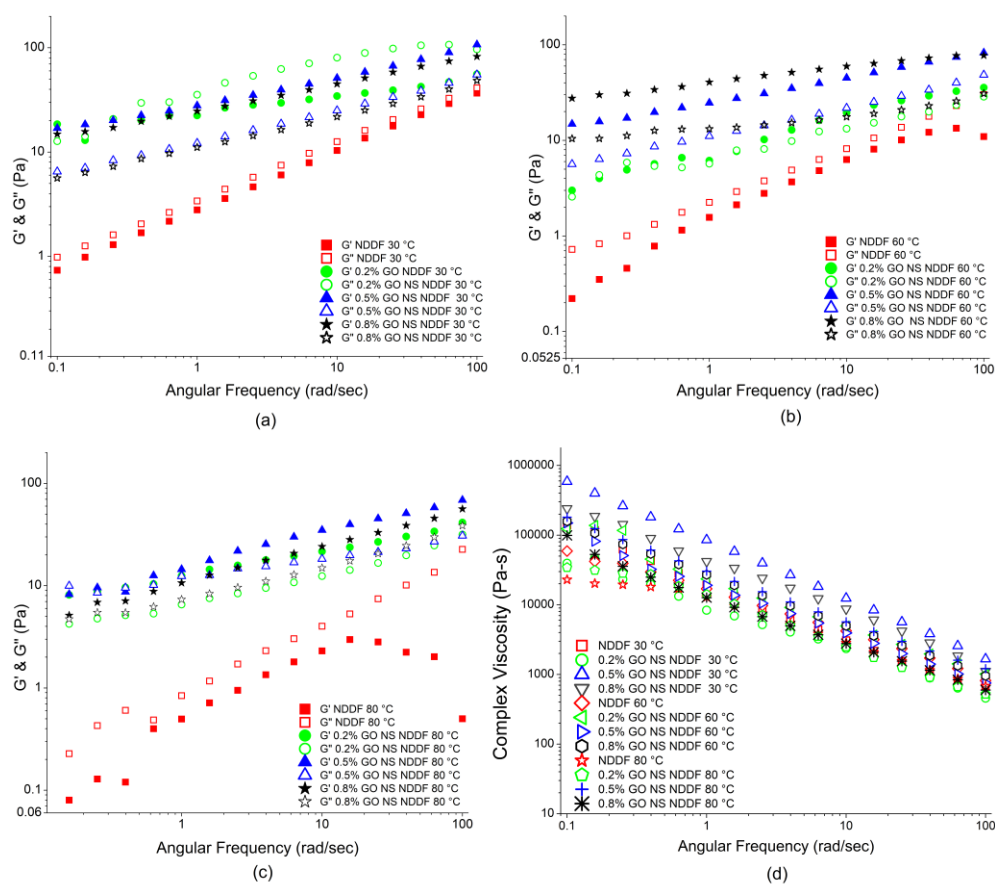


Fig. 7.5: (a) G' , G'' vs. Angular frequency at 30 °C (b) G' , G'' vs. Angular frequency at 60°C (c) G' , G'' vs. Angular frequency at 80 °C (d) Complex viscosity vs. angular frequency at 30, 60 and 80 °C. Legend: NDDF represents the base with 0 wt% GO NS, 0.2% represents 0.2 wt% GO NS NDDF and so on.

Fig. 7.5 (a-c) represents frequency sweep measurements for the base and 0.5 wt% GO NS NDDF at 30, 60 and 80 °C. The base NDDF shows a consistent

viscoelastic liquid nature throughout all frequency range at 30 °C. However, this steady trend is completely derailed at 80 °C as the value of G' is drastically reduced and its difference with G'' intensifies. This suggests a complete breakdown of the base NDDF at high temperatures. On the contrary, a very stable and consistent viscoelastic solid structure can be observed for 0.5 wt% GO NS NDDF. Even at a temperature of 80 °C, the structural integrity is preserved.

Fig. 7.5 (d) shows complex viscosity vs. angular frequencies for all the concerned fluids at 80 °C. Complex viscosity for the base NDDF and 0.2 wt% GO NS NDDF at high temperature and at lower frequencies ceases to build up at high temperature displaying a plateau region. This signifies that structural build-up has paused for these fluids and has reached the maximum possible integrity at 0.9 rad/sec. A contrasting case can be observed for 0.5 and 0.8 wt% GO NS NDDF. These fluids show a highly consistent viscoelastic solid nature and display persistent structural build-up. One can observe a steady rise in complex viscosity even at lower frequencies. Even though there is no plateau region for 0.5 and 0.8 wt% GO NS NDDF; the former shows a more stable trend with higher G' values. Additionally, it can be observed that 0.2 wt% GO NS NDDF show viscoelastic liquid nature throughout all frequency ranges and a very similar trend to the base NDDF in terms of thermal stability. Although, 0.8 wt% GO NS NDDF shows similar properties as compared to that of 0.5 wt% GO NS NDDF.

7.3.4 TIME DEPENDENT TEST MEASUREMENTS

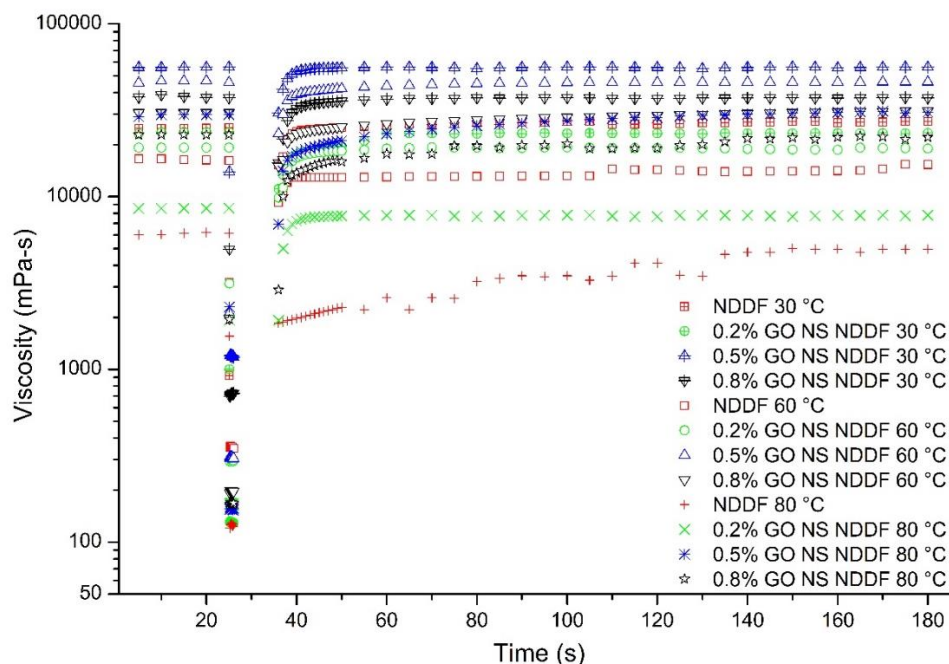


Fig. 7.6: Time dependent rotational thixotropic test for various NDDFs. Legend: NDDF represents the base with 0 wt% GO NS, 0.2% represents 0.2 wt% GO NS NDDF and so on.

Fig. 7.6 represents the viscosity vs. time values for all the concerned fluids at 30, 60 and 80 °C. Time dependent test was conducted to evaluate the thixotropic ability of all the fluid at different temperatures. The test was conducted for 180 secs. The viscosity of each fluid was measured at 0.25 s^{-1} , then sheared at 1000 s^{-1} . The fluid was rested for 8 seconds followed by measurement of viscosity at 0.25 s^{-1} . The gradual increase in viscosity at the last stage was observed and then compared to the initial viscosity to study structural build-up under the near-static shear rate.

Complete structural regain was observed for all the fluids at 30 °C within a range of fewer than 20 secs. At 60 °C, base NDDF and 0.2 wt% GO NS NDDF regained 94.2 and 95.8% at the end of 180 secs of their original viscosity. For 0.5 and 0.8 wt% GO NS NDDF original viscosities were attained at 102 and 131 secs respectively. At 80 °C, base NDDF, 0.2 and 0.8 wt% GO NS NDDF

recovered 72, 89.01 and 93.84% of their initial viscosity while a complete structural reformation was observed for 0.8 wt% GO NS NDDF at 121 secs.

7.3.5 TEMPERATURE DEPENDENT TEST MEASUREMENTS

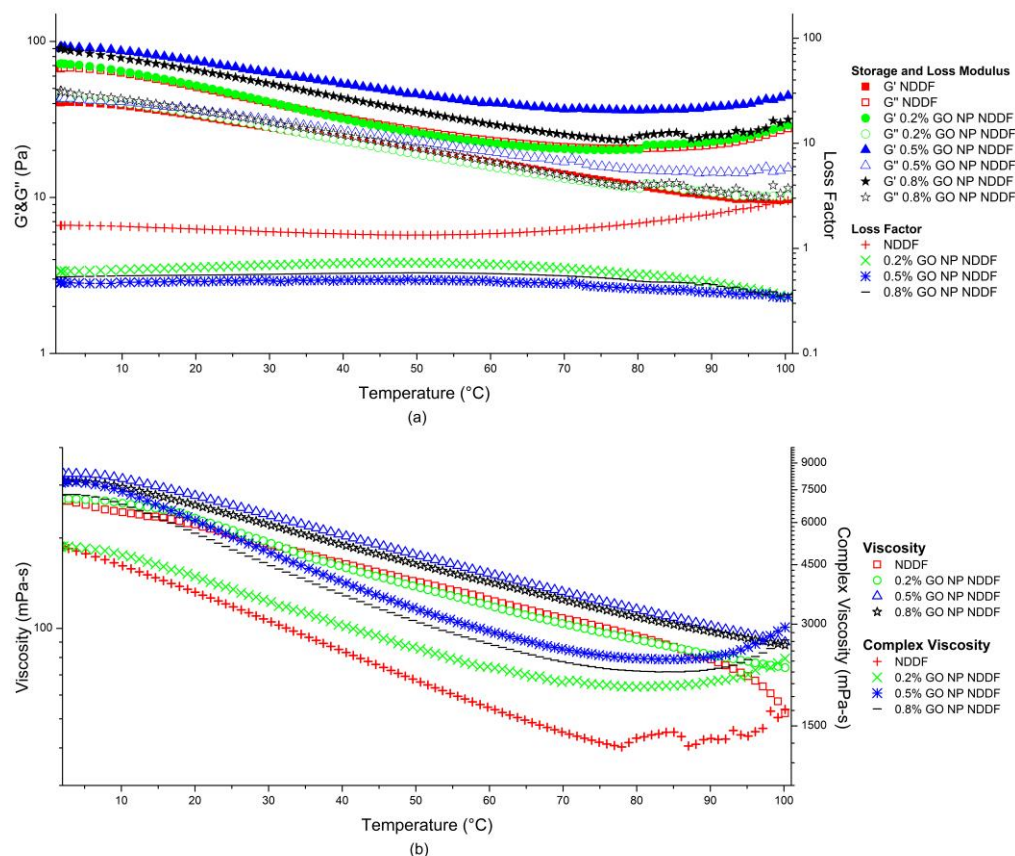


Fig. 7.7: (a) G' , G'' and loss factor vs. temperature, (b) Viscosity and complex viscosity vs. temperature for various NDDFs. Legend: NDDF represents the base with 0 wt% GO NS, 0.2% represents 0.2 wt% GO NS NDDF and so on.

Fig. 7.7 represents the temperature sweep measurement data for all the NDDFs. 0.5 wt% GO NS NDDF demonstrates the highest G' value (Fig. 7.7 a) and consistent structured flow as the variance between G' and G'' does not show an abrupt escalation. This can also be confirmed by a relatively low loss factor value as compared to the base NDDF. From complex viscosity vs. temperature data (Fig. 7.7 b), it can be observed that the base NDDF shows a sudden drop in complex viscosity beyond 70 °C. Fig. 7.7 b also represents a steady state rotational test where a shear rate of 500 s^{-1} was applied at and viscosity was

measured at different temperatures. 0.5 and 0.8 wt% GO NS NDDF shows the highest viscosity, the former showing the greatest. While the base and 0.2 wt% GO NS NDDF show comparable viscosity values. It is noteworthy to mention that the abrupt non-linear fall of viscosity in the case of base NDDF is addressed by the addition of GO NS which shows a linear viscosity down-trend.

7.3.6 API FILTRATE LOSS TEST MEASUREMENTS

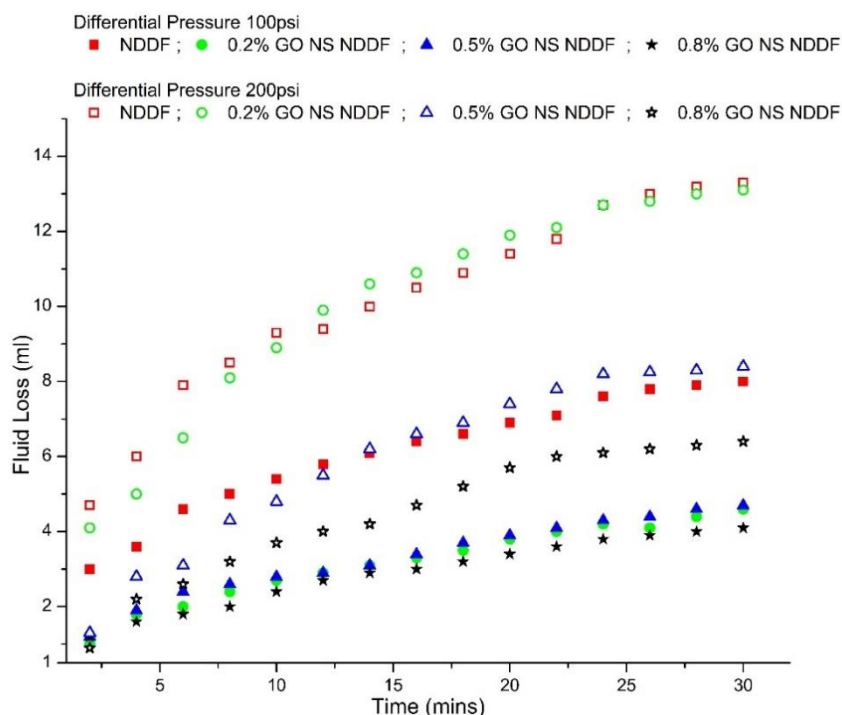


Fig. 7.8: Filtrate loss volume vs. time for various NDDFs. Legend: NDDF represents the base with 0 wt% GO NS, 0.2% represents 0.2 wt% GO NS NDDF and so on.

Fig. 7.8 represents the fluid loss vs. time for all the concerned fluids at 100 and 200 psi differential pressure to represent the rate of fluid loss. The fluid loss was measured by an API OFITE Filter Press apparatus. At 100 psi differential pressure, the addition of GO NS by 0.2 wt% reduces the fluid loss from 8 to 4.7 ml. Further addition of 0.5 and 0.8 wt% GO NS in NDDF yield a fluid loss of 4.6 and 4.1 ml. At a differential pressure of 200 psi, fluid loss of base NDDF increases by 66.25% yielding a volume of 13.3 ml. On the contrary, 0.2, 0.5 and 0.8% GO NS NDDF produces a fluid loss of 8.4, 6.8 and 6.4 ml

respectively. The fluid loss at a static state has shown a significant reduction due to the addition of GO NS. This might be due to superior viscoelastic properties of GO NS NDDF as compared to the base NDDF, this attribute makes it difficult for the former to seep through pore spaces due to strong gel nature. Moreover, from frequency sweep, it was observed that the loss factor of 0.5 and 0.8 wt% GO NS NDDF is between 0.2 and 0.3 which prevents syneresis of polymer liquids contributing to less fluid loss.

7.4 DETERMINATION OF OPTIMAL HERSHEY BUCKLEY (HB) PARAMETER BY GENETIC ALGORITHM (GA)

Table 7.1 Optimal Herschel Bulkley (HB) parameters for various NDDFs obtained from genetic algorithm (GA)

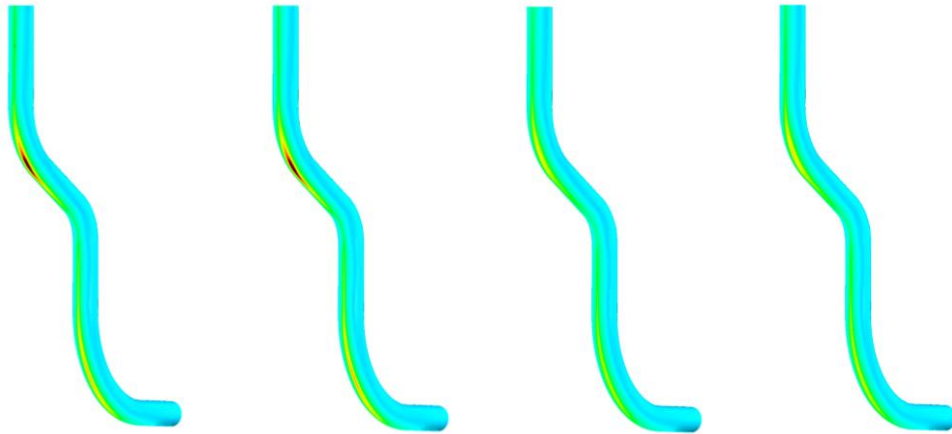
NDDF Sample	Temperature (°C)	Yield Point (Pa)	Flow consistency index (K)	Flow behaviour index (n)	SSE
NDDF	30	1.87	12.55	0.36	2.91
0.2% GO NS NDDF		0.06	12.43	0.36	6.68
0.5% GO NS NDDF		3.95	16.63	0.36	28.90
0.8% GO NS NDDF		2.10	14.89	0.37	2.91
NDDF		0	6.50	0.39	12.44
0.2% GO NS NDDF	0	7.19	0.36	0.15	

0.5% GO NS NDDF	60	0	8.09	0.41	2.26
0.8% GO NS NDDF		0	7.90	0.35	1.64
<hr/>					
NDDF		0	2.56	0.37	3.20
0.2% GO NS NDDF		0	4.81	0.40	1.74
0.5% GO NS NDDF	80	0	6.70	0.41	10.89
0.8% GO NS NDDF		0	5.66	0.40	11.93
<hr/>					

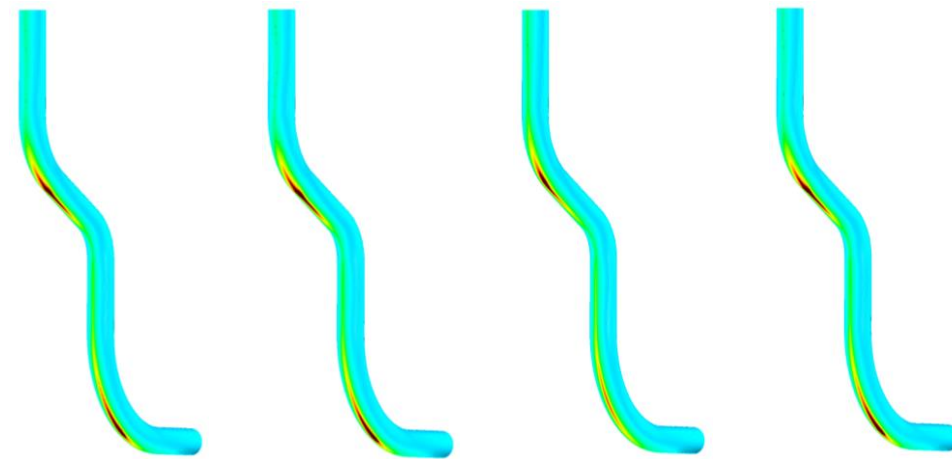
7.5 RESULTS AND DISCUSSION ON FLOW BEHAVIOUR FROM CFD STUDIES IN ECCENTRIC WELLBORE ANNULUS

7.5.1 EFFECT OF GO NS ON CUTTING CARRYING CAPACITY OF NDDF

Base NDDF	0.2 wt% GO NS NDDF	0.5 wt% GO NS NDDF	0.8 wt% GO NS NDDF
Cutting deposition at 30 °C			



Cutting deposition at 60 °C



Cutting deposition at 80 °C

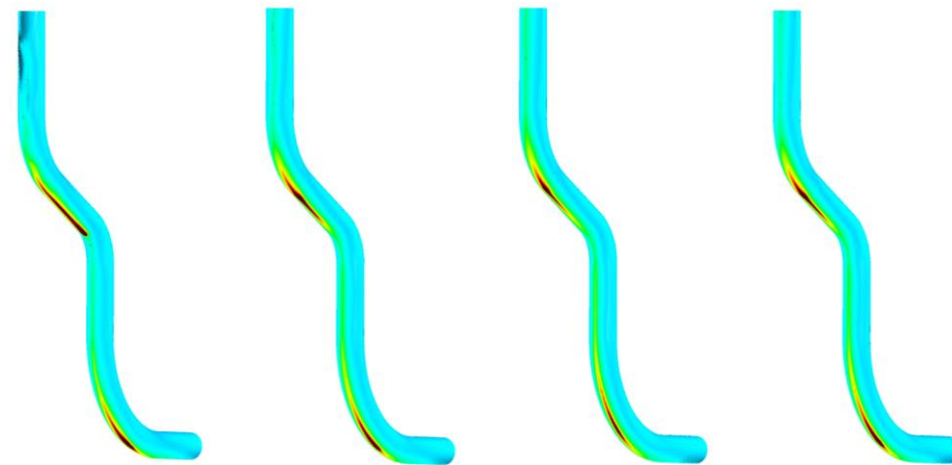


Fig. 7.9: Volume fraction of cutting deposition of all the concerned NDDFs at 30, 60 and 80 °C in a deviated eccentric annular wellbore

Fig. 7.9 represents the volume fraction of cuttings in a deviated eccentric annular wellbore. The volume fraction here reflects the ability of NDDFs to carry solid rock cuttings out of the wellbore from the above combination of contours it can be observed that deposition of cuttings is higher in the bends as compared to straight sections. This fact occurs due to the sudden change in direction of annular velocity. Another striking observation that emerges is that the sedimentation of the cutting phase is maximum in the upper build up section as compared to the lower one. At 30 °C, no severe deposition of cuttings can be observed at the lower build-up section. The base NDDF and 0.2 wt% GO NS NDDF displays a higher degree of sagging compared to 0.5 and 0.8 wt% GO NS NDDF, especially at the upper annulus. At 60 °C, the base NDDF, 0.2 and 0.8 wt% GO NS NDDF shows significant cutting deposition streak at both upper lower build-up section. At 80 °C, the performance of the base NDDF completely degrades and shows severe deposition in all the bend sections. Lowest sagging at this temperature is displayed by 0.5 wt% GO NS NDDF due to its superior ability to retain rheological property even at higher temperatures. From the above simulation results, it is evident that the addition of 0.5 wt% GO NS NDDF enhances cutting carrying capacity compared to the base NDDF. Hence it proves to prevent severe sagging at low shearing rates which are dominant at the upper annular region. These observations as stated above can be quantified from Table 7.2 where 0.5 wt% GO NS NDDF shows less cutting retention in the annular region by a significant margin.

Table 7.2: Percentage volume retention of cuttings in annulus *vs.* different cases of concentration and temperatures. $(\text{Volume fraction of cuttings})_{\text{annulus}} - (\text{Volume fraction of cuttings})_{\text{inlet}} = (\text{Retention of volume fraction of cuttings})_{\text{annulus}}$

Cutting retention in terms of % total annular volume				
Sample / Temperature	Base NDDF	0.2 wt% GO NS NDDF	0.5 wt% GO NS NDDF	0.8 wt% GO NS NDDF
30 °C	0.102	0.125	0.012	0.097
60 °C	0.023	0.091	0.040	0.129
80 °C	0.139	0.135	0.096	0.159

7.5.2 EFFECT OF GO NS ON THE VELOCITY PROFILE OF NDDF

Figs. 7.10-7.12 represent the annular velocity profile of base and 0.5 wt% NS NDDF with respect to the diameter at kick-off point (KOP, Fig. 7.10), drop-off section (DOS, Fig. 7.11) and second build-up section (BUS-2, Fig. 7.12).

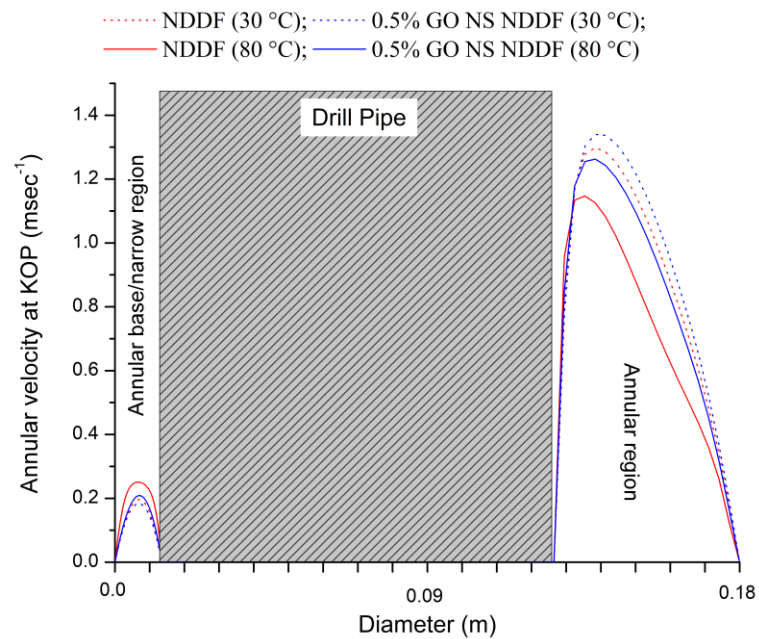


Fig. 7.10: Velocity profile of base and 0.5 wt% GO NS NDDF at KOP

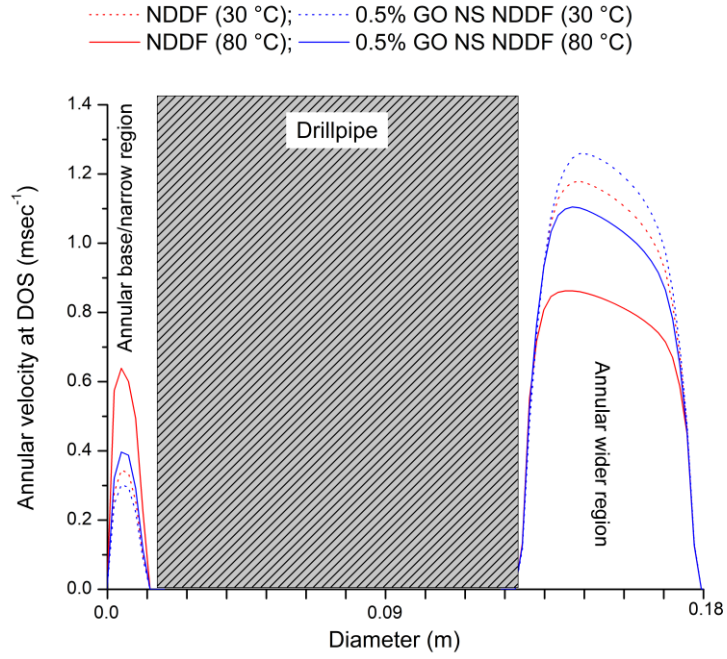


Fig. 7.11: Velocity profile of base and 0.5 wt% GO NS based NDDF at DOS

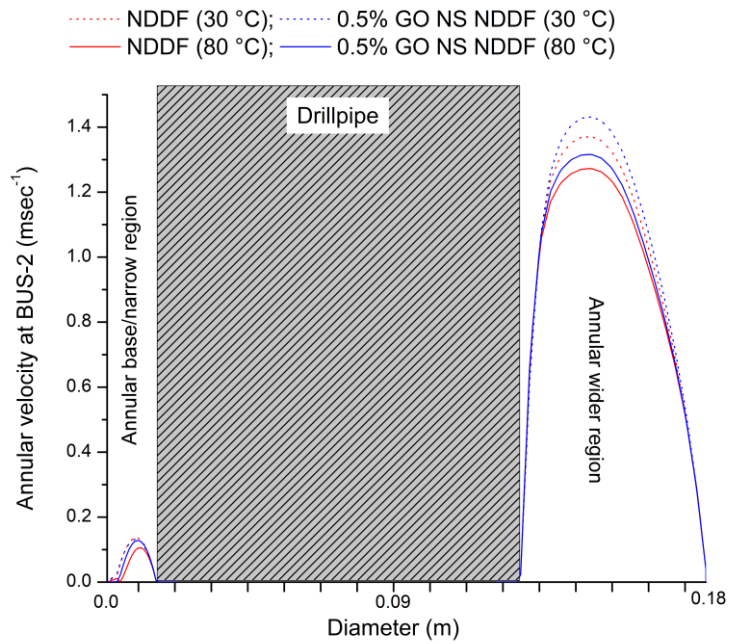


Fig. 7.12: Velocity profile of base and 0.5 wt% GO NS based NDDF at BUS-2

It is evident that both the build-up sections (KOP and BUS-2) have a sharp velocity profile head. Whereas, the drop off section bears a blunt profile. Hence better sweep can be expected at drop off sections as compared to build

up sections, thereby promoting less cutting deposition. This premise is well reflected in the contour plots of cutting volume fraction as shown in Fig. 7.9. The mean velocity of all the drilling fluids decreases as it moves upwards. Although this reduction in velocity is significantly greater for the base NDDF. GO NS doped drilling fluid shows substantial less reduction in velocity thereby preserving more lifting force. 0.5 wt% GO NS NDDF shows the highest velocity amongst all. Additionally, skewness in the leading front towards the annular base can be typically observed for all the drilling fluids. A higher degree of skewness shows a rapid decline of velocity near the drill-pipe wall which adversely affects cutting suspension and lifting. Skewness is, however, less for 0.5 wt% GO NS NDDF.

7.5.3 EFFECT OF GO NS ON PRESSURE DROP OF NDDF

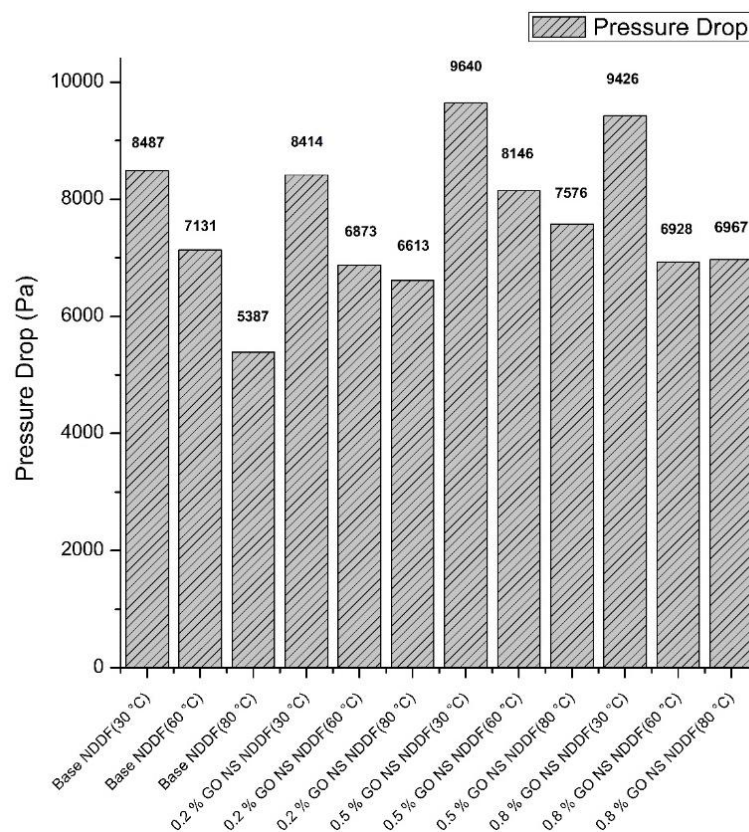


Fig. 7.13: Pressure drop (Pa) along annular region for the GO NS based NDDFs at 30, 60 and 80 °C. Legend: Base NDDF represents the base with 0 wt% GO NS, 0.2% represents 0.2 wt% GO NS NDDF and so on.

From CFD results as presented in Fig. 7.13, the pressure drops of all the fluids ranged from 5387 to 9640 Pa or 0.07 to 0.14 psi/ft in field units. This range confirms that the flowability of all the fluids is within an acceptable range. With the addition of GO NS, the nature of the drilling fluid is transformed from viscoelastic liquid to viscoelastic solid, yet, flowability remains unhindered. 0.5 wt% GO NS NDDF at 80 °C yields a favorable case of 7576 psi along the length of the drill pipe resulting in a pressure drop of 2526 Pa/m or 0.12 psi/ft.

7.6 CHAPTER CONCLUSION

After investigation of the effect of GO NS on NDDF, it can be concluded that GO NS imparts a significant degree of temperature stability. It induces an essence of elasticity within the NDDF fluid structure with a remarkable reduction in fluid loss, especially at 0.5 and 0.8 wt% GO NS NDDF. However, CFD studies indicate that 0.5 wt% GO NS NDDF bears the highest cutting removal ability. Therefore, considering all the pivotal factors 0.5 wt% GO NS NDDF can be interpreted as the best contender.

CHAPTER 8

EFFECT OF ZINC OXIDE NPS (ZnO NPs) ON NDDF

8.1. RHEOLOGY MEASUREMENTS

8.1.1 STEADY STATE ROTATIONAL TEST MEASUREMENTS

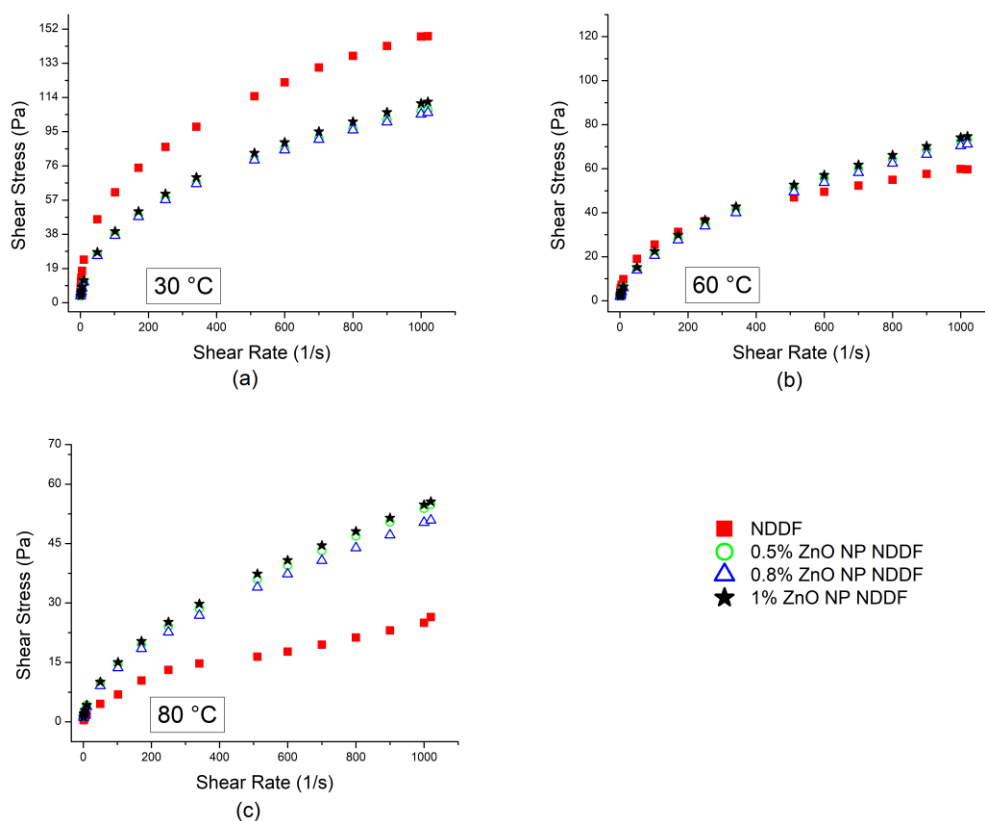


Fig. 8.1: (a) Shear stress vs. shear rate at 30 °C, (b) Shear stress vs. shear rate at 60 °C, (c) Shear stress vs. shear rate at 80 °C. Legend: NDDF represents the base with 0 wt% ZnO NP. 0.5% represents 0.5 wt% ZnO NP NDDF and so on

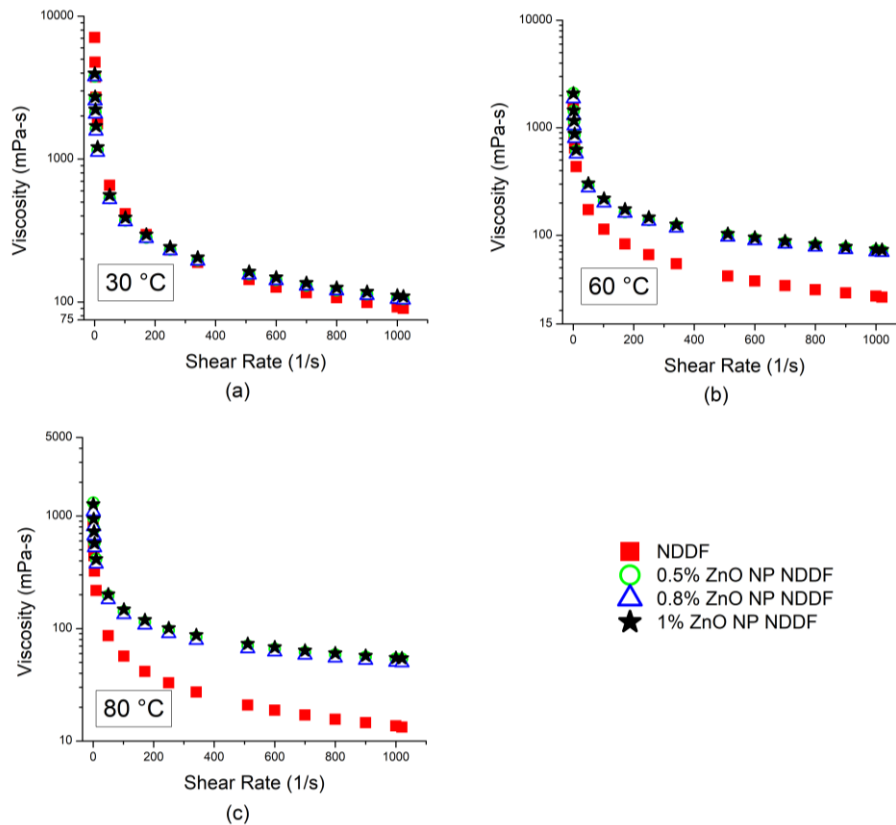


Fig. 8.2: (a) Viscosity vs. shear rate at 30 °C, (b) Viscosity vs. shear rate at 60 °C, (c) Viscosity vs. shear rate at 80 °C. Legend: NDDF represents the base with 0 wt% ZnO NP. 0.5% represents 0.5 wt% ZnO NP NDDF and so on

Fig. 8.1 represents shear stress vs. shear rate data for all the fluids. For ease of comparison, the shear rates have been categorized into low ($1-50 \text{ sec}^{-1}$), intermediate ($100-600 \text{ sec}^{-1}$) and high ($700-1020 \text{ sec}^{-1}$) ranges. Comparisons drawn and reported are with respect to base NDDF at corresponding temperature conditions. It can be observed that the addition of ZnO NP shows a reduction in shear stress at 30 °C. This reduction is 54, 38 and 30 % for 0.5 wt% ZnO NP at low, intermediate and high shear rates respectively. The reduction in shear stress further increased for 0.8 wt% ZnO NP viz. 55, 39 and 30 % at low, intermediate and high shear rates respectively. For 1 wt% ZnO NP, the reduction was 53, 35 and 27% at low, intermediate and high shear rates respectively. At 60 °C, the shear stress reduces for all the fluids, with the base NDDF showing the highest reduction in high shear stress. At low to intermediate shear rates, the shear stress for 0.5, 0.8 and 1 wt% ZnO NP NDDFs

as compared to the base NDDF showed a percentage reduction of 43, 49 and 43 % respectively. At high shearing rates, they show an increase by 22, 19 and 25% for 0.5, 0.8 and 1 wt% ZnO NP NDDF respectively. At 80 °C base NDDF shear stress values are observed to be less than ZnO NP NDDFs. At low shearing rates, shear stress values of 0.5, 0.8 and 1 wt% ZnO NP NDDF exceed that of base NDDF by 224, 170 and 213%. At high shearing rates, all the ZnO NP NDDFs show more than twice the value than that of base NDDF. Fig. 8.2 represents the viscosity *vs.* shear rate. A similar observation can be noticed for all NDDFs as shear stress *vs.* shear rate.

From the above observations, it can be inferred that base NDDF has the highest effect of temperature on its viscosity. However, with the addition of ZnO NPs, the thermal degradation of NDDF is significantly addressed with positivity.

8.1.2 AMPLITUDE SWEEP TEST MEASUREMENTS

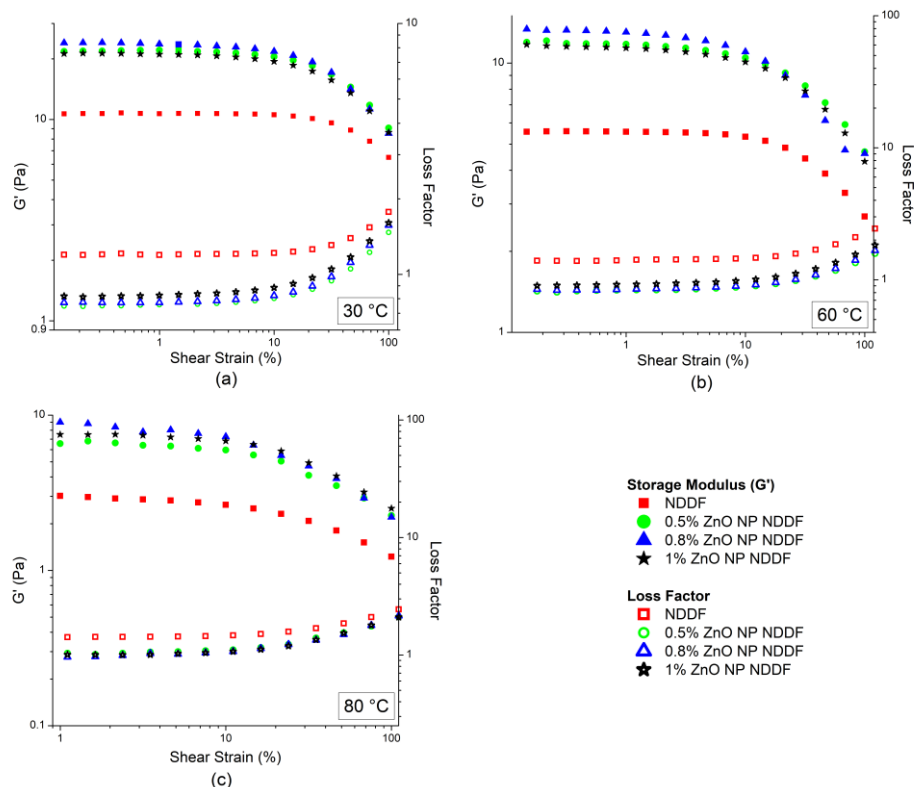


Fig. 8.3: (a) Storage modulus (G') and loss factor *vs.* shear strain (%) at 30 °C, (b) G' and loss factor *vs.* shear strain (%) at 60 °C, (c) G' and loss factor *vs.*

shear strain (%) at 80 °C. Legend: NDDF represents the base with 0 wt% ZnO NP. 0.5% represents 0.5 wt% ZnO NP NDDF and so on.

Fig. 8.3 represents storage modulus (G') and loss factor vs. shear strain (%). The loss factor is the ratio of loss modulus (G'') and storage modulus (G') and a value greater than unity indicates viscoelastic liquid nature. From Fig. 8.3 (a) it can be observed that at 30 °C the base NDDF shows pure viscoelastic liquid nature. With the addition of ZnO NPs, the value of loss factor decreases and approaches values less than one. Hence, it can be settled that the addition of ZnO NP induces an essence of elasticity in the structure of NDDF. Within the linear viscoelastic range (LVER), the base NDDF shows a G' of 10.7 Pa, whereas, 0.5, 0.8 and 1 wt% ZnO NP NDDF bears a value of 21.8, 24.08 and 21.3 Pa respectively. At 60 °C (Fig. 8.3 b), G' for base NDDF reduces to 5.5 Pa. However, the highest value of G' is shown by 0.8 wt% ZnO NP NDDF. Except for the base NDDF, all the ZnO NP NDDFs show viscoelastic solid nature. At 80 °C (Fig. 8.3 c); base, 0.5 and 1 wt% ZnO NP NDDF show viscoelastic liquid nature except, 0.5 wt% ZnO NP NDDF showing a dominant G'' at high shear strain (%). It is interesting to note that 0.8 wt% ZnO NP NDDF shows a slightly greater elastic behaviour than 1 wt% ZnO NP NDDF.

From the above observations, we can infer that all the ZnO NP NDDFs induce viscoelastic solid behaviour but, restricted to a temperature of 60 °C. This would suggest the applicability of ZnO NP NDDF till a moderate temperature range. At high temperatures, ZnO NP NDDF would be susceptible to weak gel formation resulting in the sagging of solid phase (cuttings and other high gravity weighing agents).

8.1.3 FREQUENCY SWEEP TEST MEASUREMENTS

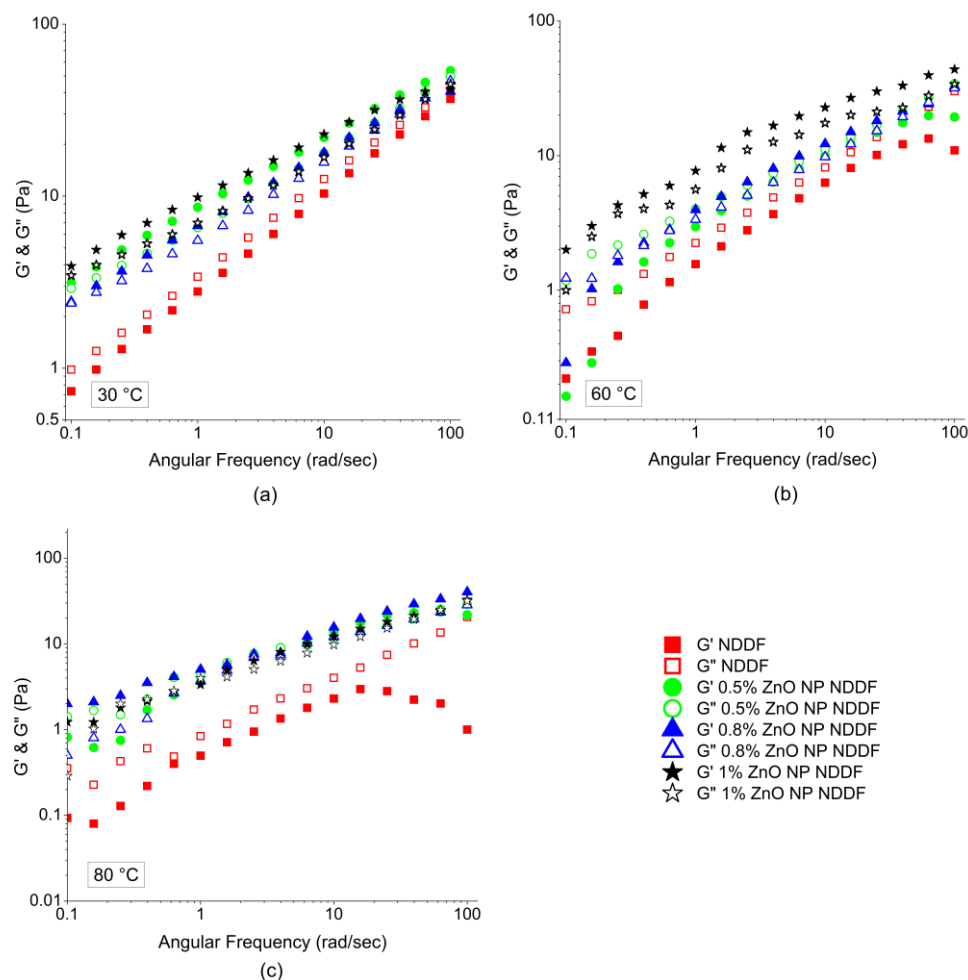


Fig. 8.4: (a) Storage modulus (G') and Loss modulus (G'') vs. angular frequency at 30 °C, (b) G' and G'' vs. angular frequency at 60 °C, (c) G' and G'' vs. angular frequency at 80 °C. Legend: NDDF represents the base with 0 wt% ZnO NP. 0.5% represents 0.5 wt% ZnO NP NDDF and so on.

Fig. 8.4 reports variation of G' and G'' with frequency (rad/s) at 30, 60 and 80 °C. At 30 °C (Fig. 8.4 a), all the ZnO NP NDDFs shows viscoelastic solid nature for all the frequency ranges having a significant distinction between values of G' and G'' . At 60 °C (Fig. 8.4 b), this difference further intensifies with dominant G'' values over G' at low frequencies for all the NDDFs. While base, 0.5 wt% ZnO NP NDDF shows complete viscoelastic liquid nature, 0.8 and 1 wt% ZnO NP NDDF shows elastic dominant nature. However, a cross

over for 1 wt% ZnO NP NDDF can be observed at 0.25 rad/s. At 80 °C (Fig. 8.4 c), the base NDDF undergoes structural degradation displaying erratic behaviour in values of G' and G'' especially at high frequencies. Similar behaviour (viscoelastic liquid) is also exhibited by 0.5 wt% ZnO NP NDDF, more of a stable structure. A crossover can be observed for 1 wt% ZnO NP NDDF at a frequency of 1.58 rad/s beyond which it exhibits viscoelastic liquid behaviour at lower frequencies. 0.8 wt% ZnO NP NDDF shows a stable and stronger gel structure (viscoelastic solid) throughout the entire frequency range.

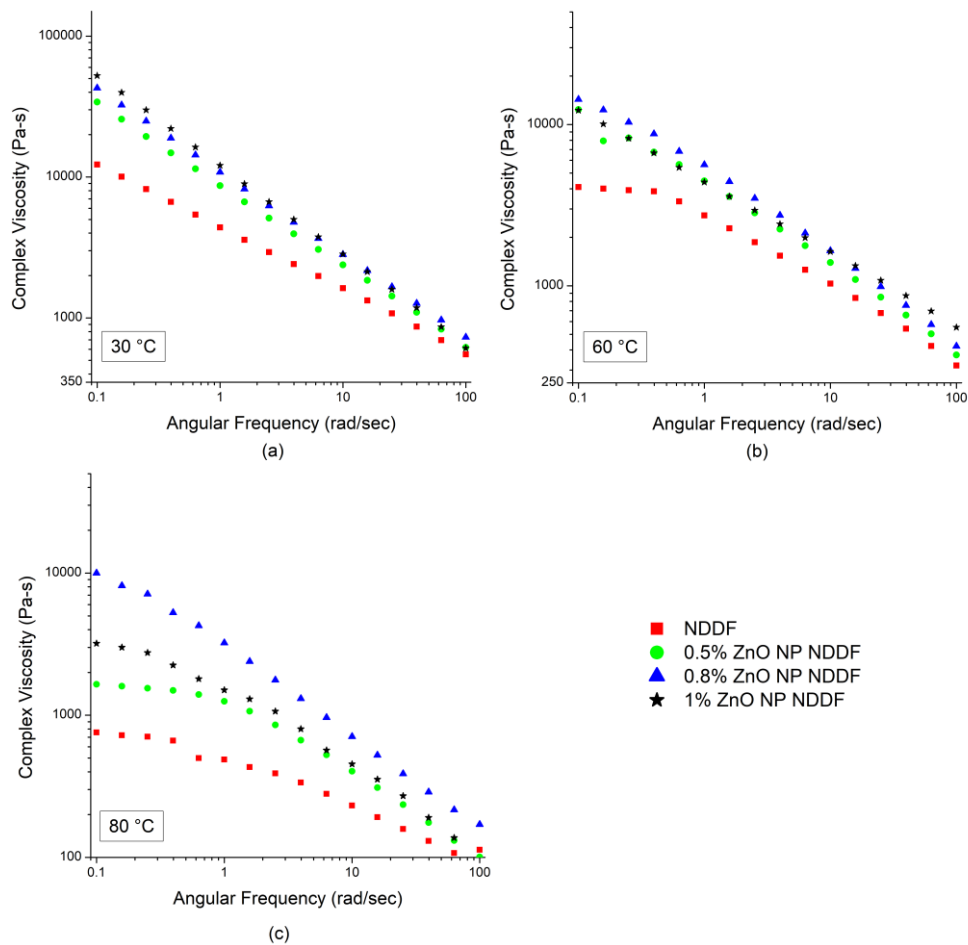


Fig. 8.5: (a) Complex viscosity vs. angular frequency at 30 °C, (b) Complex viscosity vs. angular frequency at 60 °C, (c) Complex viscosity vs. angular frequency at 80 °C. Legend: NDDF represents the base with 0 wt% ZnO NP. 0.5% represents 0.5 wt% ZnO NP NDDF and so on.

Fig. 8.5 indicates a trend in complex viscosity (Pa-s) vs. frequency (rad/s) from which we can have an impression about the structural build-up at

low frequencies or at a greater time period applied shear strain (%). At 30 °C (Fig. 8.5 a), all the fluids show a gradual build-up in structure with 1 wt% ZnO NP NDDF displaying the highest magnitude. From Fig. 8.5 (b) it can be observed that base NDDF shows a plateau region in the rise of complex viscosity at lower frequencies. This region signifies a cease in the structural build-up. Similar observations can be made for the base, 0.5 and 1 wt% ZnO NP NDDF at 80 °C (Fig. 8.5 c). Contrastingly, 0.8 wt% ZnO NP NDDF shows no such phenomena. From Fig. 8.5 (a-c) we can settle that 0.8% wt% ZnO NP NDDF is viscoelastic solid in nature with a greater ability for structural build-up.

8.1.4 TIME DEPENDENT TEST MEASUREMENTS

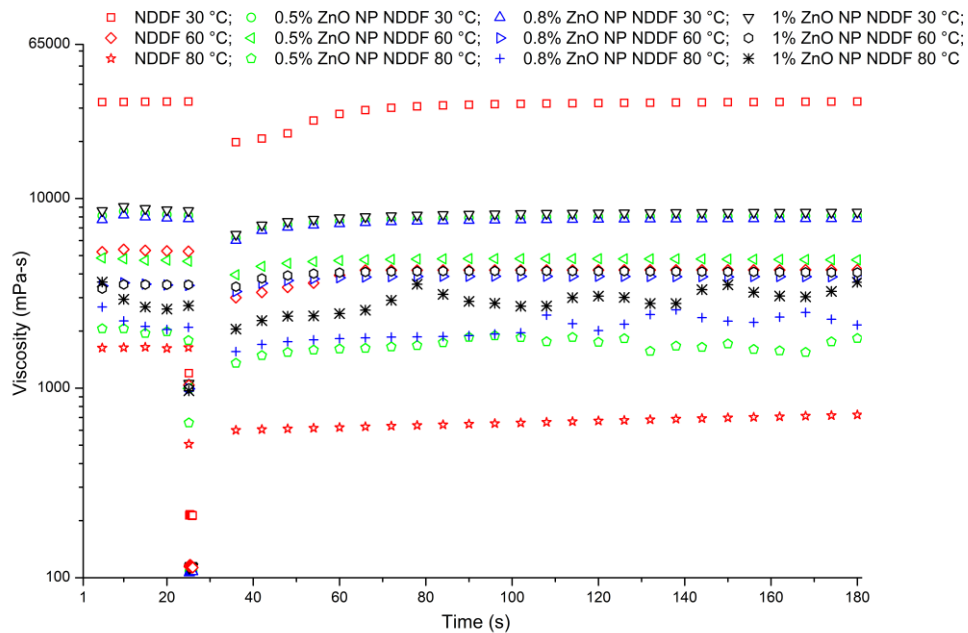


Fig. 8.6: Time dependent rotational thixotropic test for various NDDFs. Legend: NDDF represents the base with 0 wt% ZnO NP. 0.5% represents 0.5 wt% ZnO NP NDDF and so on.

Fig. 8.6 represents time dependent behaviour of all NDDFs under rotational test which measures viscosity under varied shear rates. First, the fluid is deformed under a steady shear rate of 0.25 s^{-1} representing a near static condition followed by a high shear rate of 1000 s^{-1} ; the later deform the fluid

structure. Then the viscosity is measured at 0.25 s^{-1} till 180 secs (3 minutes). For all fluids, a gradual rise in viscosity is observed indicating thixotropic behaviour. A rapid gain in fluid structure (gradual increase in viscosity) characterizes the gel strength of all the NDDFs. At $30 \text{ }^\circ\text{C}$, base NDDF attains its original structural strength at 130 secs while 0.5, 0.8 and 1 wt% ZnO NP NDDF at 172, 176 and 160 secs. At $60 \text{ }^\circ\text{C}$, base NDDF and 0.5 wt% ZnO NP NDDF remains unable to gel up and attains 79 and 97% of their original viscosity respectively. At these conditions, 0.8 and 1 wt% ZnO NP NDDF recovers at 106 and 94 secs. At $80 \text{ }^\circ\text{C}$, structural recovery is 44, 78, 86 and 89% respectively for base, 0.5, 0.8 and 1 wt% ZnO NP NDDF. Additionally, it is interesting to note that all ZnO NP NDDF show inconsistent behaviour at high temperatures as indicated by the erratic trend in viscosity.

8.1.5 TEMPERATURE DEPENDENT TEST MEASUREMENTS

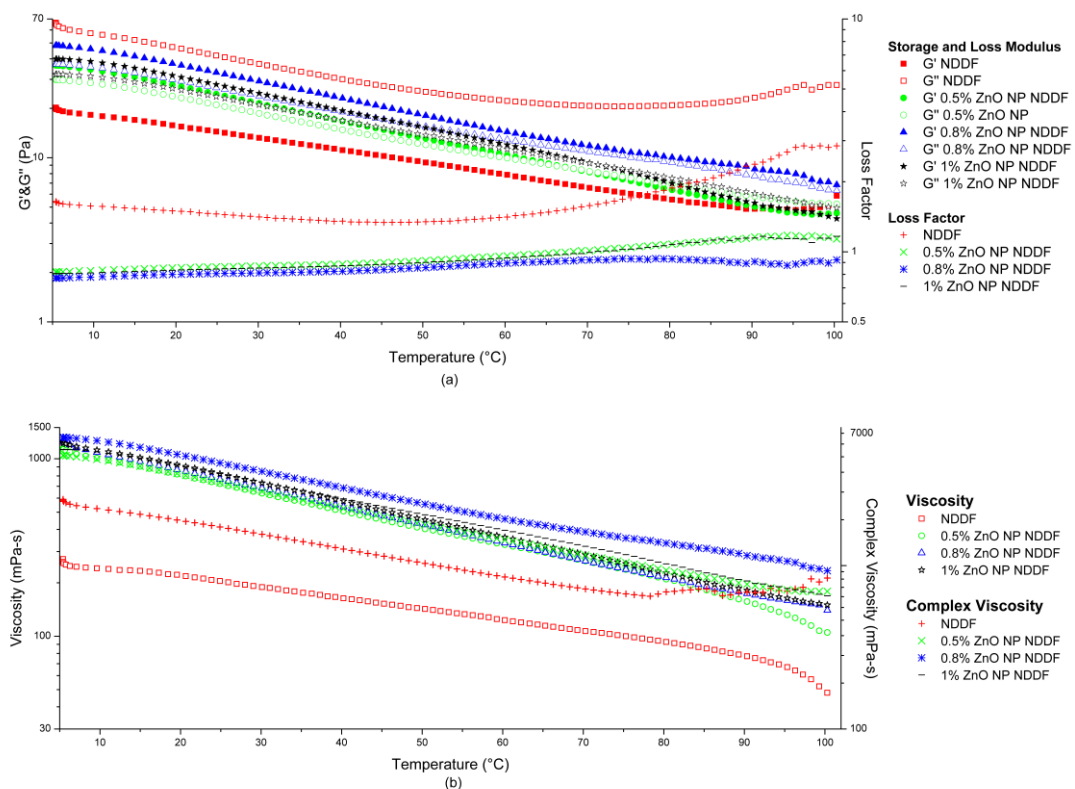


Fig. 8.7: (a) G' , G'' and loss factor vs. temperature, (b) Viscosity and complex viscosity vs. temperature for various NDDFs. Legend: NDDF represents the base with 0 wt% ZnO NP. 0.5% represents 0.5 wt% ZnO NP NDDF and so on.

Fig. 8.7 reports temperature dependent studies (5 – 100 °C) from both oscillation and rotational test. From Fig. 8.7 (a) it can be observed that base NDDF displays complete viscoelastic liquid nature across all temperatures. 0.5 wt% ZnO NP NDDF shows elastic dominant nature at low temperatures, however, an opposite outcome is exhibited at higher temperatures, surely after a crossover point at 68 °C. A similar phenomenon can also be observed for 1 wt% ZnO NP NDDF, however, the crossover point lies at 72 °C, showing a greater range of viscoelastic solid nature as compared to 0.5 wt% ZnO NP NDDF. On the contrary, 0.8 wt% ZnO NP NDDF shows viscoelastic solid nature throughout the temperature range which is a clear indication of a more stable structure less prone to degradation at high temperatures. The viscoelastic nature can be also found true from the loss factor data. From Fig. 8.7 (b), 0.8 wt% ZnO NP NDDF shows higher complex viscosity with a greater degree of stability at high temperatures. Beyond 75 °C, one can observe a clear steep decline in values of complex viscosity as well as viscosity for the base, 0.5 and 1 wt% ZnO NP NDDF. Moreover, base NDDF shows complete breakdown at high temperatures while ZnO NP NDDF shows higher structural integrity, compared to base NDDF. From these observations it can be foreseen that base NDDF will exhibit a higher degree of segregation beyond 70 – 80 °C.

8.1.6 API FILTRATE LOSS TEST MEASUREMENTS

Fig. 8.8 represents fluid loss of all NDDFs at a differential pressure of 100 psi and 200 psi. The measurement is conducted for 30 mins and corresponding fluid loss (ml) is recorded in an interval of 2 mins. A general observation can be drawn with an increase in pressure fluid loss increases. At 100 psi a fluid loss of 8 ml can be seen for base NDDF while 0.5, 0.8 and 1 wt% ZnO NP NDDF yields a fluid loss of 7.3, 5.4, 4.5 ml respectively.

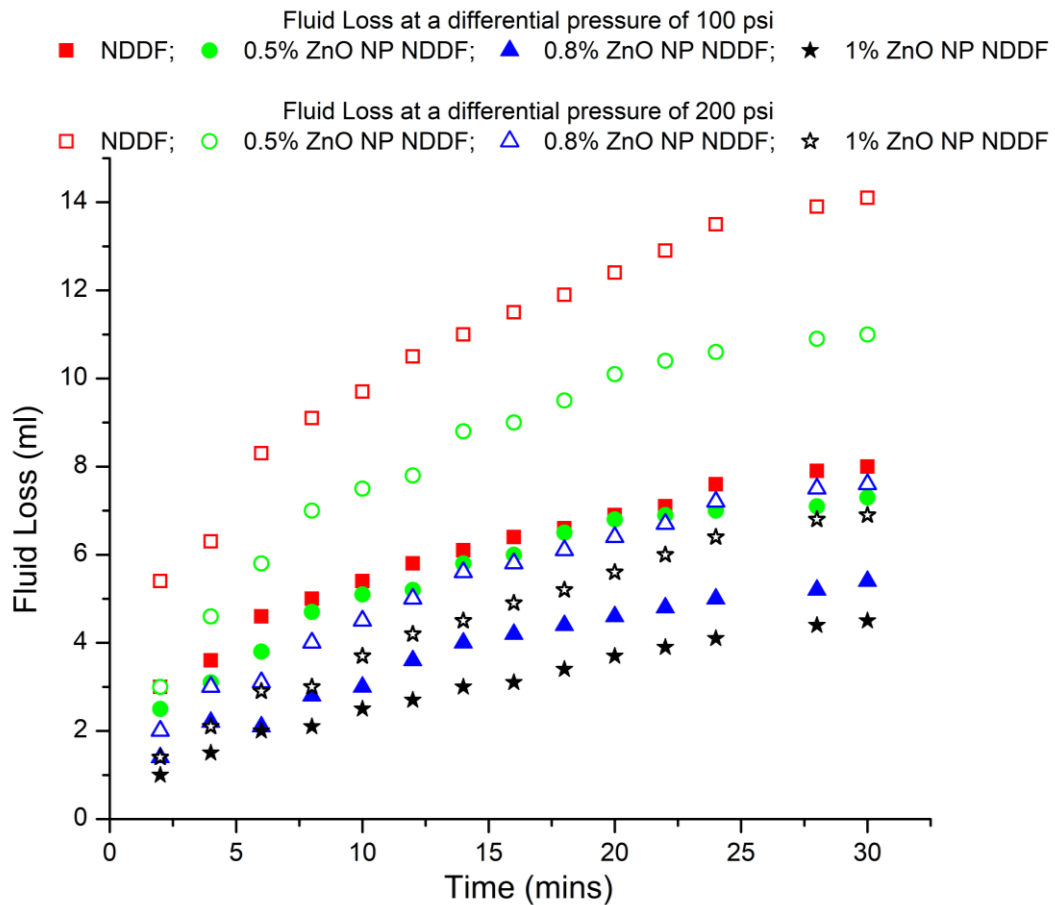


Fig. 8.8: Filtrate loss volume vs. time for various ZnO NP NDDFs. Legend: NDDF represents the base with 0 wt% ZnO NP. 0.5% represents 0.5 wt% ZnO NP NDDF and so on.

When compared to base NDDF at 100 psi 1 wt% ZnO NP NDDF shows a reduction in fluid loss of 49% while 0.5 and 0.8 wt% ZnO NP NDDF shows a reduction of 8% and 32% respectively. At 200 psi fluid loss for base NDDF (14.1 ml) increases by 76% compared to that at 100 psi. While fluid loss of 11, 7.6 and 6.9 ml can be observed for 0.5, 0.8 and 1 wt% ZnO NP NDDF respectively. From the above results, it can be observed that 1 wt% ZnO NP NDDF has the least effect of pressure where an additional increase of only 2.4 ml was observed when pressure was increased from 100 psi to 200 psi.

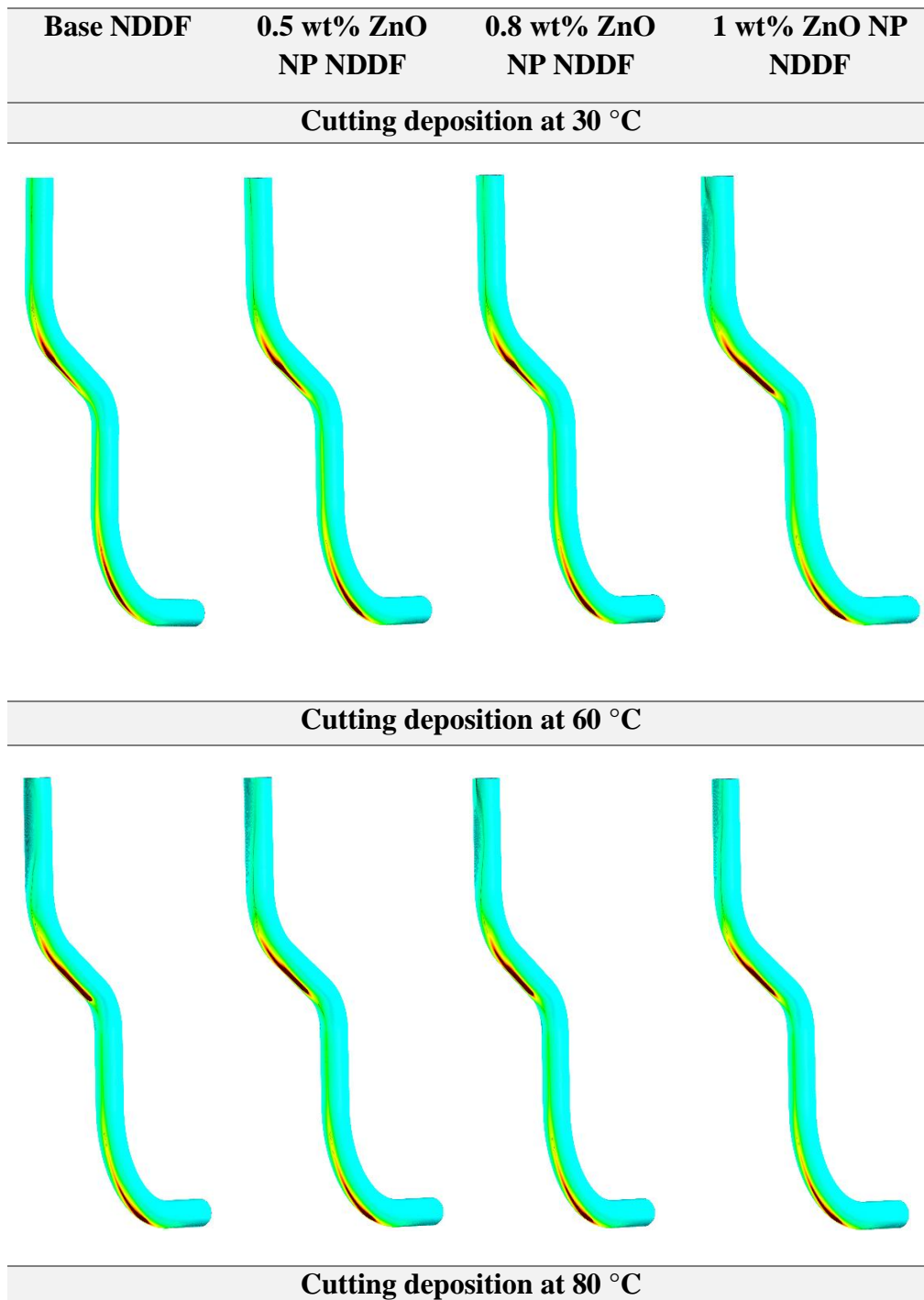
8.2 DETERMINING OPTIMAL HERSCHEL BUCKLEY (HB) PARAMETERS USING GENETIC ALGORITHM (GA)

Table 8.1 Determining optimal Herschel Buckley (HB) parameters using genetic algorithm (GA) optimization

NDDF Sample	Temperature (°C)	Yield Point (Pa)	K (Pa/s ⁿ)	n	SSE
Base NDDF	30	4.07	9.83	0.39	15.52
0.5 wt% NP NDDF		0	4.566	0.456	13.61
0.8 wt% NP NDDF		0	4.48	0.457	17.8
1 wt % NP NDDF		0.45	4.81	0.466	12.45
Base NDDF	60	1.455	1.31	0.380	5.56
0.5 wt % NP NDDF		0.144	1.799	0.535	0.675
0.8 wt % NP NDDF		0	1.76	0.533	0.539
1 wt % NP NDDF		0	2.04	0.52	1.216
Base NDDF	80	0	0.59	0.54	31.58
0.5 wt % NP NDDF		0.65	0.877	0.59	82.54
0.8 wt % NP NDDF		0.29	1.06	0.57	7.23
1 wt % NP NDDF		0.23	1.49	0.56	5.74

8.3 RESULTS AND DISCUSSION ON FLOW BEHAVIOUR FROM CFD STUDIES IN ECCENTRIC WELLBORE ANNULUS

8.3.1 EFFECT OF ZnO NPs ON CUTTING CARRYING CAPACITY OF NDDF



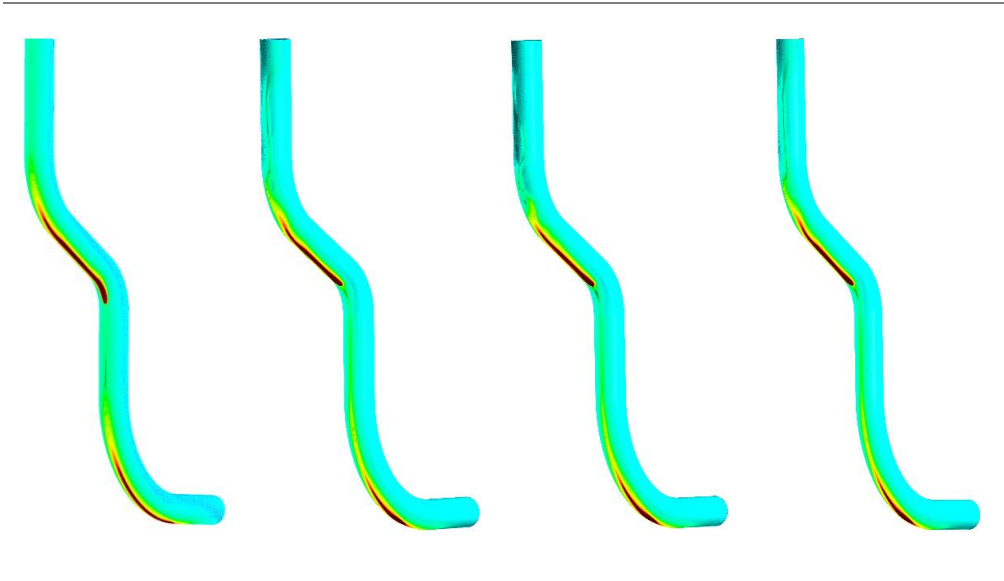


Fig. 8.9: Volume fraction of cutting deposition of all the concerned NDDFs at 30, 60 and 80 °C in a deviated eccentric annular wellbore

Table 8.2 Percentage volume retention of cuttings in annulus vs. different cases of concentration and temperatures. (Volume fraction of cuttings)_{annulus} – (Volume fraction of cuttings)_{inlet} = (Retention of volume fraction of cuttings)_{annulus}

Cutting retention in terms of % total annular volume				
Sample / Temperature	Base NDDF	0.5 wt% ZnO NP NDDF	0.8 wt% ZnO NP NDDF	1 wt% ZnO NP NDDF
30 °C	0.097	0.125	0.126	0.124
60 °C	0.175	0.157	0.159	0.155
80 °C	0.254	0.236	0.189	0.180

Fig. 8.9 represents the contours of cuttings deposits along the wellbore path. At 30 °C, base NDDF shows relatively less cutting deposition while ZnO NP NDDF shows higher sagging issues. This can be well distinguished in the upper bend section. Cutting sedimentation at 60 °C (thick red color) is less for 0.8 and 1 wt% ZnO NP NDDF as compared to base and 0.5 wt% ZnO NP NDDF. At 80 °C, base NDDF shows a higher degree of cutting sagging. This is due to greater degradation in rheological properties as observed from the rheological studies. Among the ZnO NP NDDFs, 1 wt% ZnO NP NDDF shows higher cutting carrying capacity (a less extended dark red patch in the upper bend section). However, the differences in sagging of cuttings amongst the ZnO NP NDDFs can hardly be distinguished from the visual contours, due to the nominal effect of ZnO NP on NDDF. Table 8.2 represents the percentage of cutting retention in the annular region, which indicates a higher degree of retention for Base NDDF and lower for 1 wt% ZnO NP NDDF at 80 °C. However, at lower temperatures, an opposite phenomenon can be observed.

8.3.2 EFFECT OF ZnO NPs ON THE VELOCITY PROFILE OF NDDF

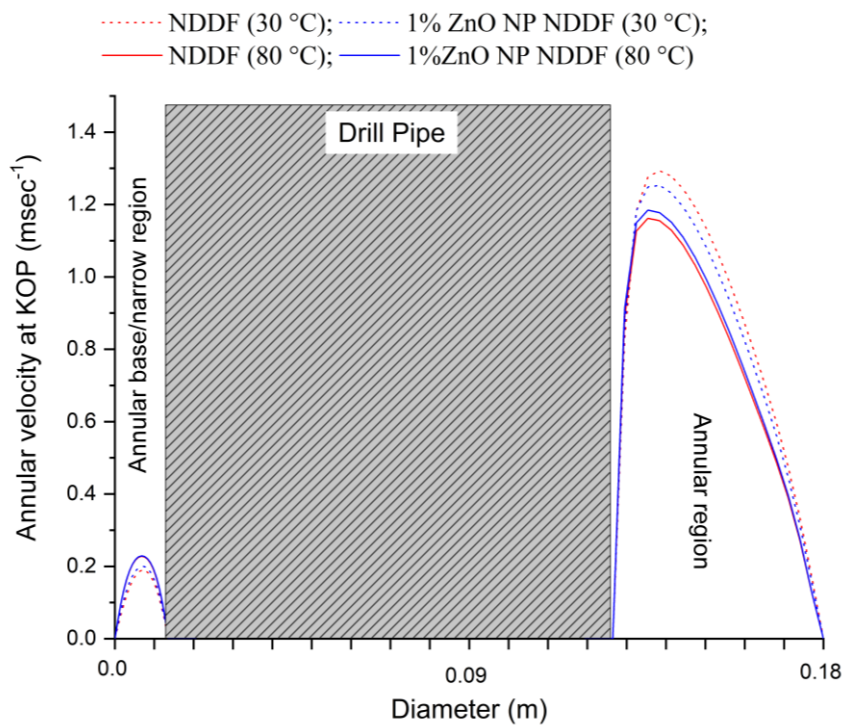


Fig. 8.10: Velocity profile at Kick-off Point (KOP) for base and 1% ZnO NP NDDF at 30 and 80 °C conditions

From Fig 8.10 it can be noticed that at KOP, the NDDFs have a sharp and fairly skewed velocity profile. At 30° C, base NDDF has a higher lift velocity and a better borehole cleaning efficiency with percentage retention of 0.097 % (from Table 8.2) as compared to 1 wt% ZnO NP NDDF. Furthermore, at higher temperature (80° C), the Base NDDF has a lower lift velocity and poorer percentage retention of 0.254 %. However, at high temperature 1 wt% ZnO NP NDDF shows marginally higher velocity as compared to base NDDF with lesser retention in the annular region.

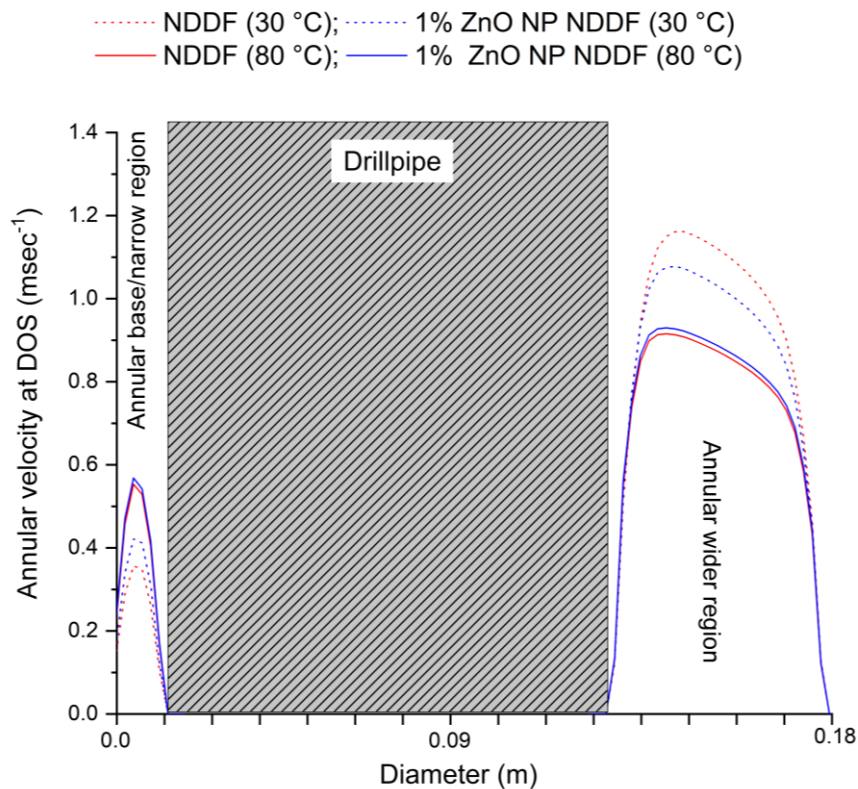


Fig. 8.11: Velocity profile at Drop-off section (DOS) for base and 1% ZnO NP NDDF at 30 and 80 °C conditions

From Fig 8.11 it can be observed that at the DOS section, the velocity profile are relatively blunt and have lower lift velocities. These profiles explain the better areal sweep of cuttings in this zone. At 30° C, Base NDDF displays high lift velocity and exceptionally good cutting removal efficiency. The

addition of ZnO NP NDDF at this temperature has a similarly detrimental effect on cutting carrying efficiency at all concentrations. However, at higher temperatures, ZnO infused NDDFs display a marginally higher lift velocity and a better cleaning performance.

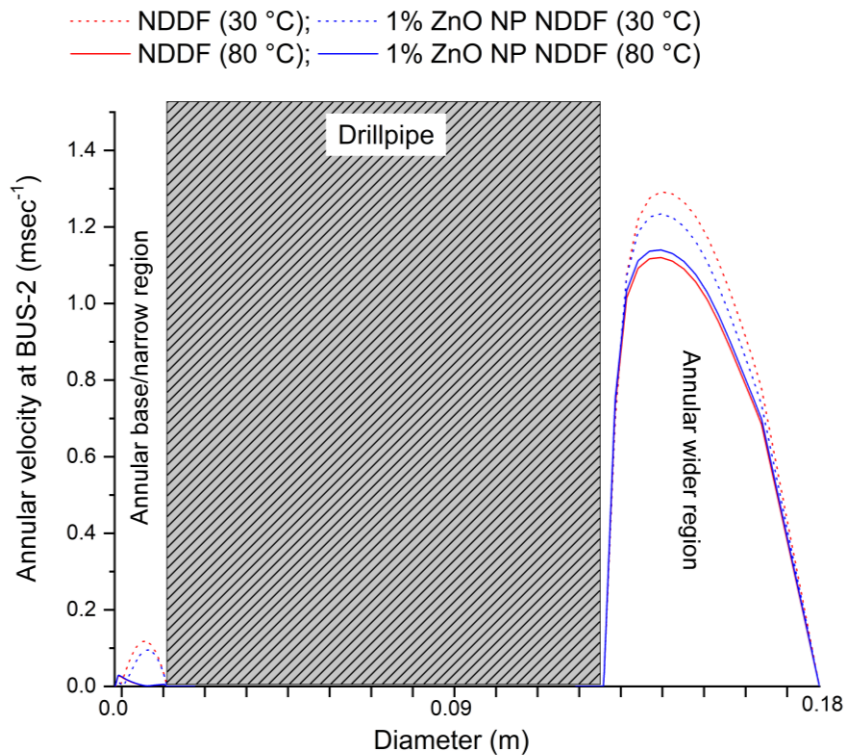


Fig. 8.12: Velocity profile at Build-up section (BUS) for base and 1% ZnO NP NDDF at 30 and 80 °C conditions

At BUS, Fig 8.12, a sharp velocity profile is observed for both fluids at 30° and 80° C. The addition of ZnO NP NDDF imparts a higher lift velocity at 80 °C with a better cutting displacement capacity. However, at lower temperatures, the base NDDF possesses superior rheological consistency thereby exhibiting lower cutting retention in the annulus.

8.3.3 EFFECT OF ZnO NPs ON PRESSURE DROP OF NDDF

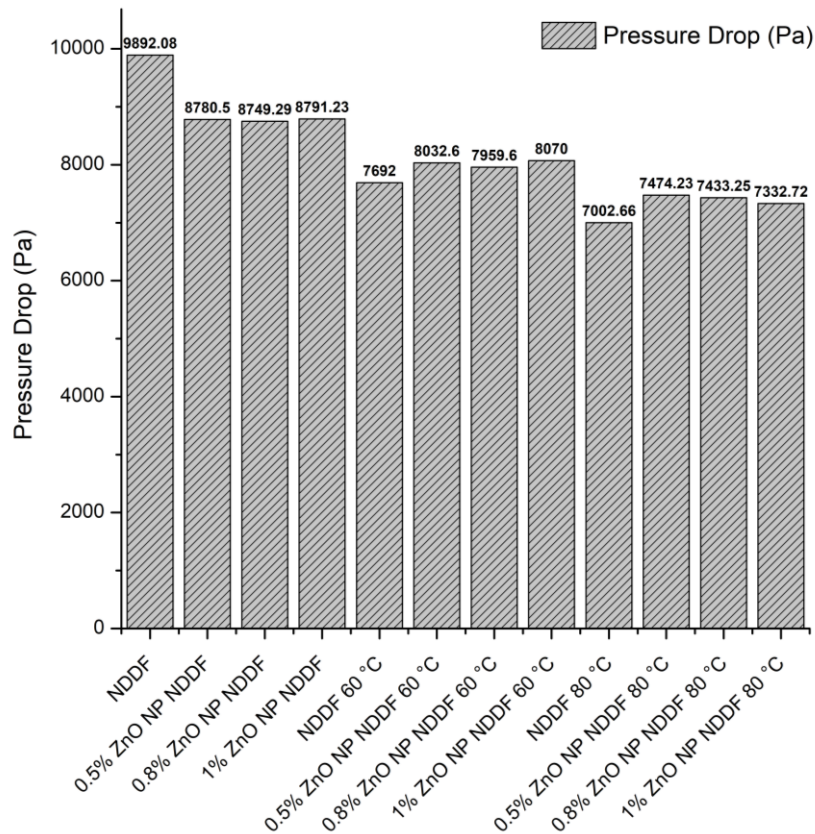


Fig. 8.13: Pressure drop of ZnO NP NP based NDDF

Fig. 8.13 reports pressure drop from CFD simulations. It can be noticed that the magnitudes of pressure drop decrease as temperature increases. This is undeniably due to degradation in rheological properties at higher temperatures especially consistency index (K). A drastic reduction in pressure drop at 30 to 80 °C can be observed for base NDDF while 0.8 and 1 wt% ZnO NP NDDF preserves the most. The range of pressure drop varies from 0.33 psi/ft to 0.46 psi/ft, which are under acceptable ranges.

8.4 CHAPTER CONCLUSION

The results from this study reveal that the addition of ZnO NP brings about a change in the viscoelastic properties of NDDF (viscoelastic liquid to viscoelastic solid). It also imparts favorable fluid loss control properties and good thermal stability with an increase in concentration. From CFD studies, it

was observed that 1 wt% ZnO NP NDDF shows a higher ability to remove cuttings; although, the change in performance amongst 0.8 and 1 wt% ZnO NP NDDF is minimal. Keeping in mind better fluid loss control ability of 1 wt% ZnO NP NDDF, it can be concluded as an apt candidate.

CHAPTER 9

CONCLUSION

This chapter presents a comparative study of all the concerned NPs that are investigated in this study. The best performing NPs are considered from each chapter's conclusions to draw relative contrast amongst themselves from rheological, fluid loss and CFD standpoint.

9.1. COMPARATIVE ANALYSIS OF ALL NP BASED NDDF

9.1.1. COMPARING STEADY STATE RHEOLOGICAL TEST MEASUREMENTS

The section discusses rheological measurement and parameters obtained from steady state rotational test at 80 °C

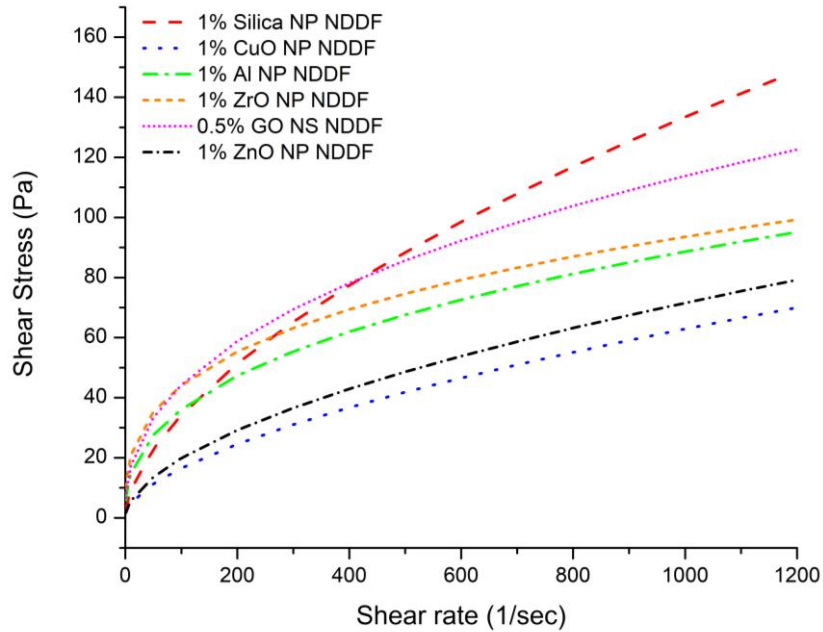


Fig. 9.1: Modelled shear stress *vs.* shear rate of different NP based NDDF considering HB parameters at 80 °C

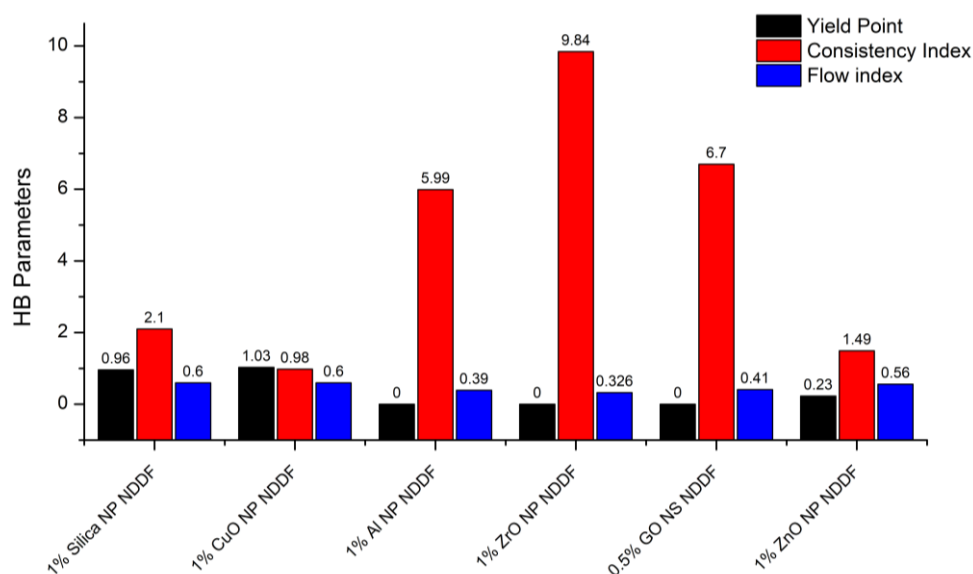


Fig. 9.2: HB parameters optimally determined from GA optimization techniques considering shear stress *vs.* shear rate values at 80 °C

Fig. 9.1 represents shear stress *vs.* shear rate values for all NP based NDDFs at 80 °C. It can be observed that 1 wt% SiO₂ NP NDDF shows the highest shear stress values at high shear rates while 1 wt% CuO NP NDDF shows the lowest of all. 1 wt% ZrO₂ NP NDDFs shows the highest consistency index (*K*) (Fig. 9.2), accompanied by the lowest value of flow index (*n*); hence it displays extreme shear thinning nature. On the other hand, 1 wt% SiO₂ NP NDDF exhibit lower consistency index (*K*) with a higher value of flow index (*n*). Consequently, the degree of shear thinning ability is notably less than 1 wt% ZrO₂ NP and 0.5 wt% GO NS NDDFs.

9.1.2 COMPARING AMPLITUDE SWEEP TEST MEASUREMENTS

Amplitude sweep oscillation test gives the nature of viscoelasticity i.e. it determines if a fluid is viscoelastic solid or liquid in nature. Elasticity has a significant contribution to cutting suspension by confirming a gel structure.

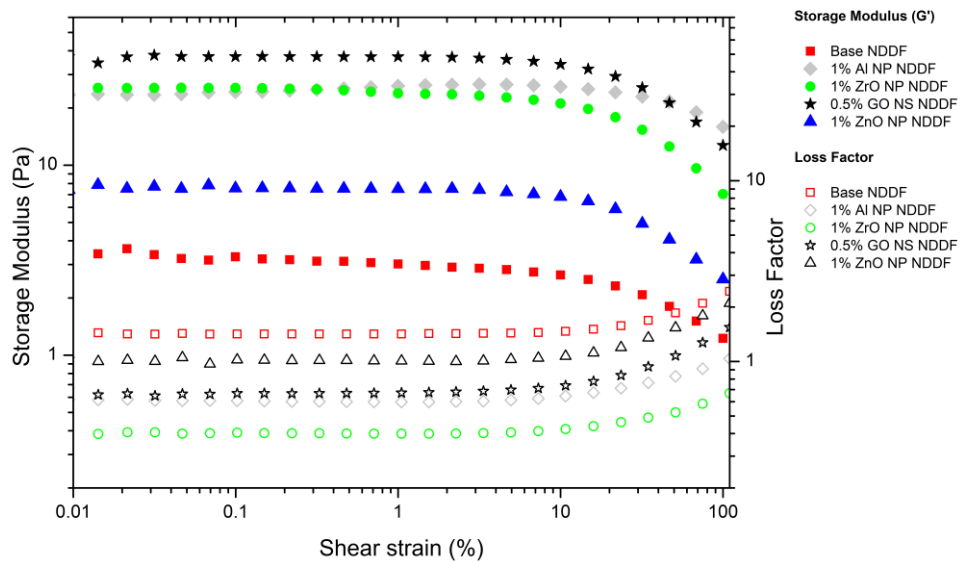


Fig. 9.3: Storage modulus (G') and loss factor vs. shear strain (%) of different NP based NDDF at 80 °C

Fig. 9.3 represents G' and loss factor data against varying shear strain (%) at 80 °C. 0.5 wt% GO NS, 1 wt% Al_2O_3 NP and 1 wt% ZrO_2 NP NDDFs shows higher values of G' demonstrating higher viscoelastic nature. It is important to note that base NDDF shows viscoelastic liquid nature. With the addition of NPs, the nature of viscoelasticity turns into solid. This can be established with values of loss factor which is less than unity in case of base NDDF and more than unity for all NP based NDDFs.

9.1.3 COMPARING FREQUENCY SWEEP TEST MEASUREMENTS

Frequency sweep quantifies the response of a fluid when subjected to a different frequency of constant deformation.

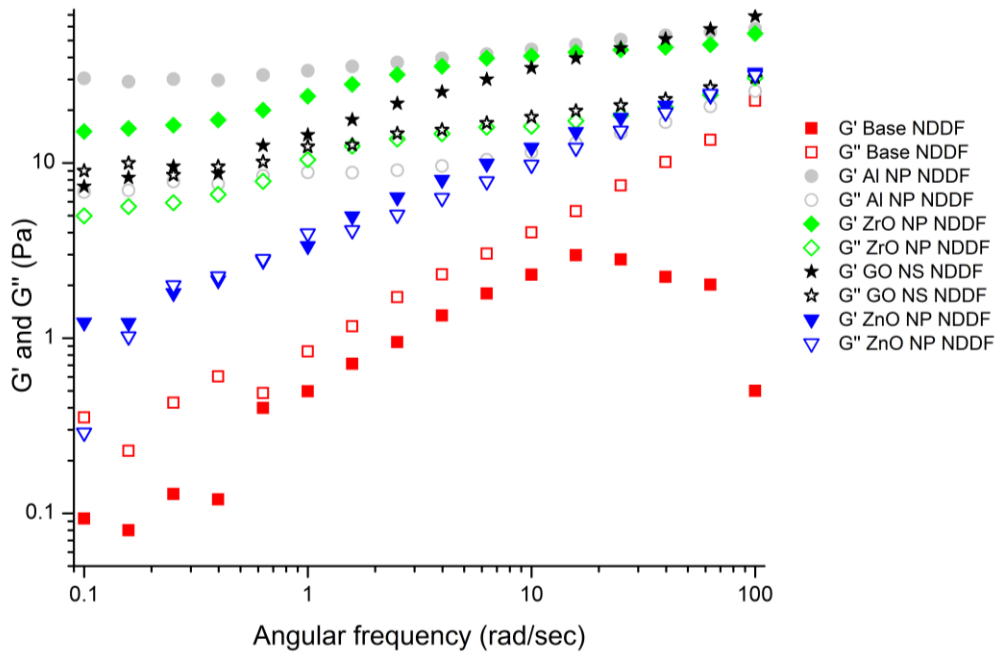


Fig. 9.4: Storage modulus (G') vs. angular frequency of different NP based NDDF at 80 °C

From Fig. 9.4, it can be observed that there is a decreasing trend in G' with a decrease in frequency (or increase in the time period between successively applied deformation). Although, this phenomenon is not firmly revealed in the case of 1 wt% Al_2O_3 NP based NDDF; rather, it follows a very less rate of decline in G' . Furthermore, complete degradation of structure can be observed for base NDDF due to its inconsistent fluid structure which is caused at high temperature. It can be admirably noticed that with the addition of NPs, the unpredictability in NDDFs behaviour is well addressed at high temperatures. In practicality, when 1 wt% Al_2O_3 NP based NDDF is left static for a prolong duration; the energy required to displace or initiate flow would be significantly higher as compared to the rest of the NP based NDDF. Although cutting holding capacity would be more efficient for the same.

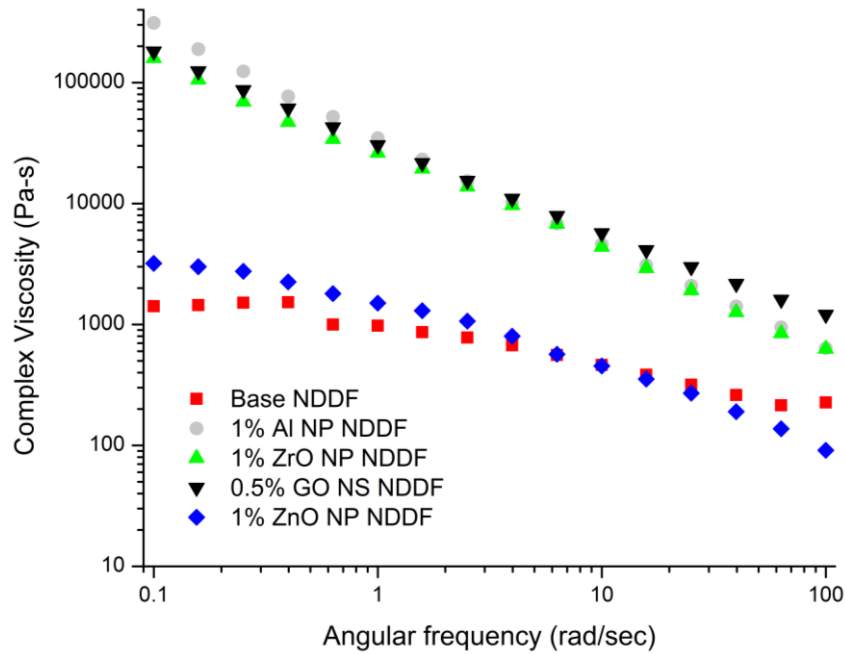


Fig. 9.5: Complex viscosity vs. angular frequency of different NP based NDDF at 80 °C

From Fig. 9.5 a plateau region can be observed for the base and 1% ZnO NP NDDF which indicates a cease of structural buildup after a certain time interval thereby limiting gel strength. Whereas, for 1 wt% Al_2O_3 NP, 0.5 wt% GO NS and 1 %wt ZrO_2 NP based NDDF shows a constant rise in the structural build-up. This is a fair indication of superior gel strength and thixotropic nature of the fluid.

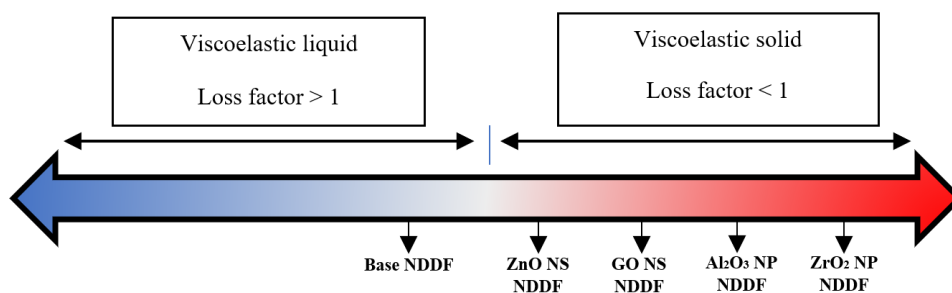


Fig. 9.6: Viscoelastic road for different NDDFs

A summary of all the base and NP based NDDF can be described in Fig. 9.6 which shows a general trend of all the concern fluids from a viscoelastic standpoint.

9.1.4 COMPARING API FLUID LOSS TEST MEASUREMENTS

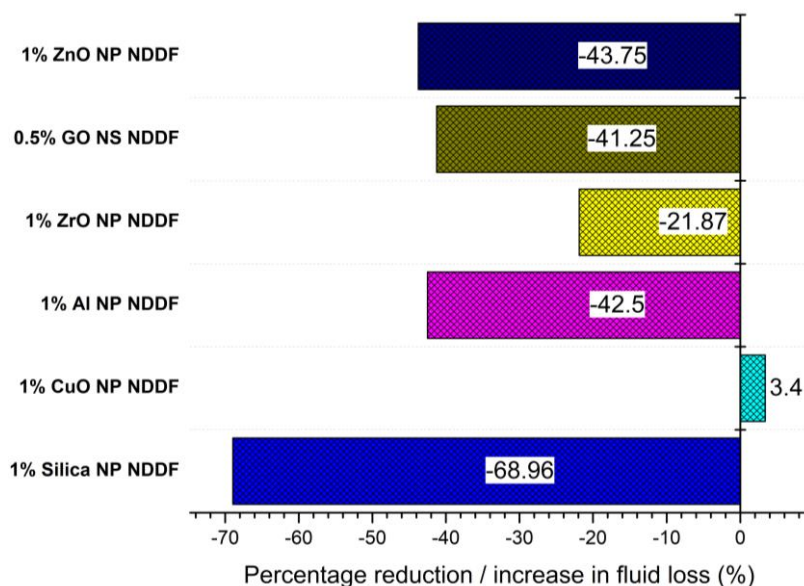


Fig. 9.7: Effect of NPs on fluid loss control compared to base NDDF ('-' values denote reduction in fluid loss %, '+' value denote increase in fluid loss %)

Fig. 9.7 represents the percentage reduction or increase in fluid loss due to the addition of NPs at a differential pressure of 100 psi and ambient conditions.

It can be concluded that 1 wt% SiO₂ NPs has the highest effect in reducing fluid loss by 68.96 %. On the other hand, 1 wt% Al₂O₃ NP, 0.5 wt% GO NS and 1 %wt ZrO₂ NP based NDDF shows the relatively same level of fluid loss control property that ranges from a reduction of 41.25 to 43.75 %.

9.1.5 COMPARING CUTTING CARRYING CAPACITY

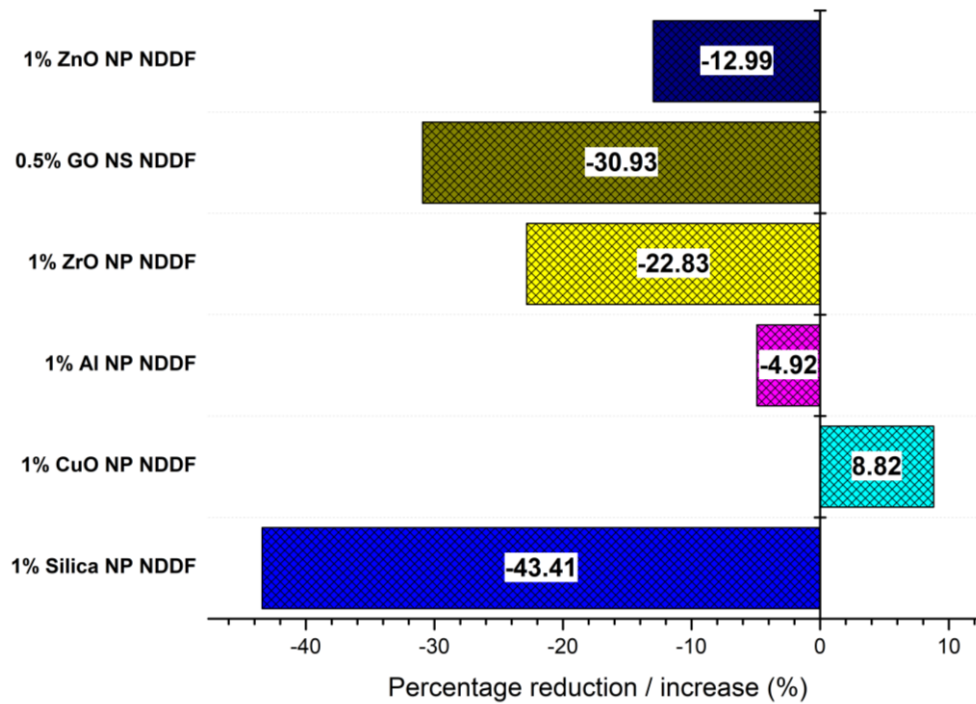


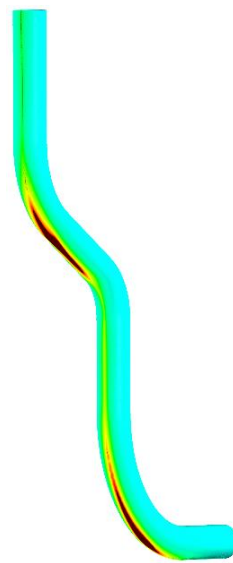
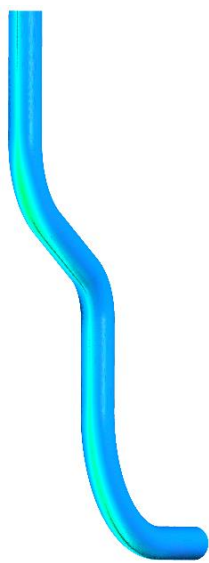
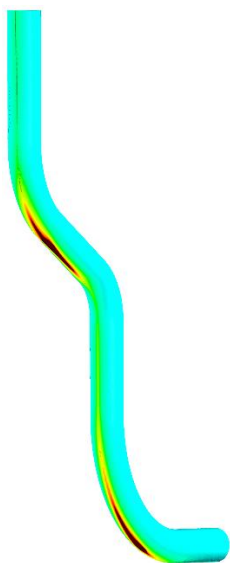
Fig. 9.8: Effect of NPs in annular cutting retention compared to base NDDF at 80 °C (‘-‘ values denote reduction cutting retention ‘+’ value denote increase cutting retention in %)

Fig. 9.8 quantifies the total percentage retention of cuttings in the annular volume for the NP based NDDFs compared to its corresponding base NDDFs. 1 wt% SiO₂ NPs clearly has a considerable effect, which increases the cutting carrying ability of NDDF by 43.41%. 0.5 wt% GO NS and 1 %wt ZrO₂ NP based NDDF has noteworthy improvement as compared to base NDDF with 30.93 and 22.83 % respectively. On the contrary, 1 wt% CuO NP has a detrimental effect on cutting retention and increases it by a margin of 8.82 %.

Base NDDF

1% SiO₂ NP NDDF

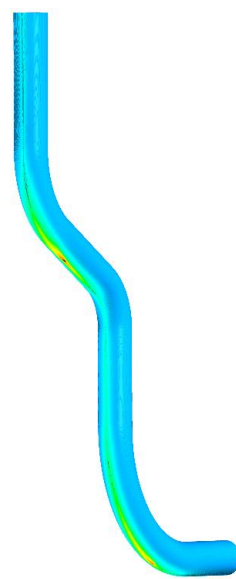
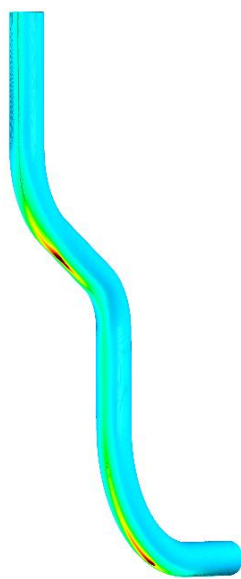
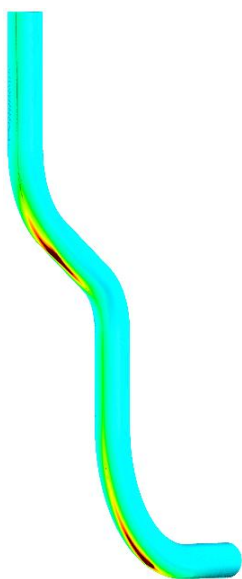
1% CuO NP NDDF



1% Al₂O₃ NP NDDF

1% ZrO₂ NP NDDF

0.5% GO NS NDDF



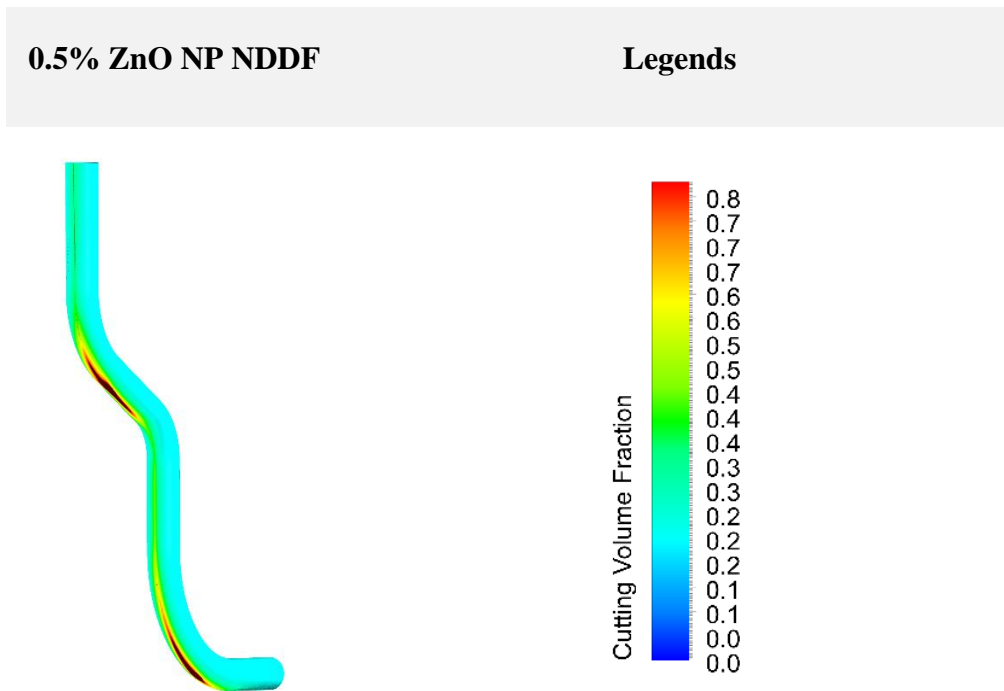


Fig. 9.9: Contours of cutting volume fraction of base and NP NDDFs in the annular region at 80 °C

Fig. 9.9 represents the volume fraction of cutting deposition throughout the wellbore. The contour scale has been widened to make a clear distinction amongst the NDDFs. Supporting the previous findings from Fig. 9.8, 1 wt% SiO₂ NP NDDF forms very marginal deposition in the localized bend sections. Small appearance in cuttings buildup can be noticed for 0.5 wt% GO NS and 1 %wt ZrO₂ NP based NDDF. These fluids promote less sagging and hence problems like mechanical pipe sticking can be better tackled while the base, 1 wt% CuO NP NDDF endorse high sedimentation issues and can pose a grave concern in operations.

9.2 CONCLUSION

In this study, the effect of NPs (SiO₂, CuO, Al₂O₃, ZrO₂, GO NS and ZnO) on rheological and fluid loss control properties of NDDF are investigated. Results from rheological measurements are further used to evaluate the hydraulic performance of all NP based NDDFs with CFD. It can be concluded that most of the NPs when used with NDDF show superior fluid loss control

properties as compared to NP based conventional bentonite drilling fluid. Additionally, this is one of the first attempts made to understand the change in viscoelastic behaviour due to the addition of NPs. One of the striking findings of this research was the change observed in the nature of viscoelasticity of NDDF from liquid to solid. Due to the evolution of a stronger structure at near rest condition, it is fair to theorize that the fluid loss was better controlled in cases where NP based NDDFs showed higher viscoelastic nature. The hydraulic performance of all the concerned drilling fluids was evaluated through CFD approach by considering HB parameters. It was observed that these parameters (τ_0 , K and n) had a significant effect on cutting carrying capacity. The value of K obtained from measurements with Al_2O_3 , GO NS and ZrO_2 NP NDDF was significantly higher than SiO_2 , CuO and ZnO NP NDDF but it yielded inferior cutting carrying ability when compared to the cutting carrying capacity of SiO_2 NP NDDF. Thus, it was noticeable that higher consistency index (K) does not signify better lifting ability or anti-sagging property. This is due to the lesser shear thinning behaviour of the former fluids and the latter having a high value of flow index (n) or less shear thinning nature.

After a thorough and holistic investigation, the following conclusions and remarks can be deduced. Summary of findings and inferences are tabulated in Table 9.1.

Table 9.1 Summary and Conclusions

Drilling fluid	Rheological properties	Hydraulic performance	Fluid loss control
Base NDDF	Degrades under moderate-high temperature.	Poor cleaning efficiency at high temperatures.	High fluid loss.
1% SiO_2 NP NDDF	Shows high thermal stability.	Excellent wellbore cleaning effect.	Reduces fluid loss by 68 %. Excellent fluid loss control agent.

1% CuO NP NDDF	No changes in rheological properties. Rather acts as thinner and reduces viscosity.	Poor hole cleaning efficiency.	Negative impact on fluid loss.
1% Al₂O₃ NP NDDF	Highly viscoelastic in nature. Manifests high gel structure.	May cause difficulty in start-up flow due to its viscoelastic nature. It has a negligible impact on hole cleaning.	High fluid loss control property. Reduces fluid loss by 42 %.
1% ZrO₂ NP NDDF	Viscoelastic and highly shear thinning in nature.	Significant increase in hole cleaning ability.	Reduces fluid loss by 21%.
0.5% GO NS NDDF	Viscoelastic and shear thinning in nature. Forms a stable gel structure. High resistance to degradation under high temperature.	Excellent hole cleaning ability.	Excellent fluid loss control. Reduces fluid loss by 41 %.
1% ZnO NP NDDF	Shows viscoelastic liquid nature under high deformation and low consistency index at high temperatures.	Fair improvement in hole cleaning.	Good fluid loss control agent.

9.3 SCOPE FOR FUTURE WORK

This research work has presented a holistic investigation of the effect of NPs on NDDFs' performance. It has been well established that NPs play a

pivotal role in enhancing different properties of NDDFs. Further scope of the study can be summarized as below:

- i. The effect of extensional flow in bends and constricted areas due to the viscoelastic nature of NP based NDDF needs to be further investigated.
- ii. CFD and microfluidic pore scale investigation into the phenomenon of fluid loss across the permeable section needs to be investigated, especially with the addition of NPs.
- iii. Rheological study to evaluate normal stresses needs to be studied further to obtain more comprehensive knowledge about the viscoelastic nature of NP based NDDFs.
- iv. High pressure high temperature (HPHT) rheological studies along with fluid loss measurements are to be carried out.
- v. Synergetic effect of NPs at various concentrations on NDDF.
- vi. Multi-objective optimization to derive at Pareto-optimal solution that includes rheological properties, hydraulic performance and fluid loss control against different controlling parameters during drilling operations.
- vii. Compatibility of different NPs used in drilling fluids with reservoir production zone: A study through return permeability and wettability alteration.

This researched work has indeed served as a foundation for further questions that are to be addressed and probed with more conviction.

CHAPTER 10

10.1 BIBLIOGRAPHY

- Abdo, J., & Haneef, M. D. (2012).** Nano-enhanced drilling fluids: pioneering approach to overcome uncompromising drilling problems. *Journal of Energy Resources Technology*, 134(1), 014501.
- Abdo, J., & Haneef, M. D. (2013).** Clay NPs modified drilling fluids for drilling of deep hydrocarbon wells. *Applied Clay Science*, 86(Dec), 76–82.
- Afolabi, R. O., Paseda, P., Hunjenukon, S., & Oyeniyi, E. A. (2018).** Model prediction of the impact of zinc oxide NPs on the fluid loss of water-based drilling mud. *Cogent Engineering*, 5(1), 1–14.
- Aftab, A., Ismail, A. R., Khokhar, S., & Ibupoto, Z. H. (2016).** Novel zinc oxide NPs deposited acrylamide composite used for enhancing the performance of water-based drilling fluids at elevated temperature conditions. *Journal of Petroleum Science and Engineering*, 146, 1142–1157.
- Aladekomo, J. B., & Bragg, R. H. (1990).** Structural transformations induced in graphite by grinding: Analysis of 002 X-ray diffraction line profiles. *Carbon*, 28(6), 897–906.
- Alcheikh, I. M., & Ghosh, B. (2017).** A comprehensive review on the advancement of non-damaging drilling fluids. *International Journal of Petrochemistry and Research*, 1(1), 61–72.
- Arkoudeas, P., Mahmoud, O., Nasr-El-Din, H., & Kelessidis, V. (2015).** Utilization of Iron Oxide NPs in Drilling Fluids Improves Fluid Loss and Formation Damage Characteristics. In *First EAGE Workshop on Well*

Injectivity and Productivity in Carbonates.

Barry, M. M., Jung, Y., Lee, J.-K., Phuoc, T. X., & Chyu, M. K. (2015).

Fluid filtration and rheological properties of NPs additive and intercalated clay hybrid bentonite drilling fluids. *Journal of Petroleum Science and Engineering*, 127, 338–346.

Bern, P. A., Zamora, M., Slater, K. S., & Hearn, P. J. (1996).

The Influence of Drilling Variables on Barite Sag. In *SPE Annual Technical Conference and Exhibition* (pp. 1–8). Colorado, U.S.A.: Society of Petroleum Engineers.

Bradshaw, R. J., Hodge, R. M., Wolf, N. O., Knox, D. A., Hudson, C. E.,

Evans, E., & Swaco, M. I. (2006). Formate-based reservoir drilling fluid resolves high-temperature challenges in the natuna sea. *Proceedings - SPE International Symposium on Formation Damage Control, 2006*, 783–790.

Caenn, R., Darley, H. C. H., & Gray, G. R. (2011).

Composition and Properties of Drilling and Completion Fluids. Composition and Properties of Drilling and Completion Fluids.

Cheraghian, G., & Hendraningrat, L. (2016).

A review on applications of nanotechnology in the enhanced oil recovery part A: effects of NPs on interfacial tension. *International Nano Letters*, 6(1), 129–138.

Committee, A. S. S. (2005).

Drilling Fluids Processing Handbook. Gulf Professional Publishing, Elsevier.

Elkatatny, S. (2019).

Enhancing the Rheological Properties of Water-Based Drilling Fluid Using Micronized Starch. *Arabian Journal for Science and Engineering*, 44(6), 5433–5442.

Elochukwu, H., Gholami, R., & Sham Dol, S. (2017).

An approach to improve the cuttings carrying capacity of nanosilica based muds. *Journal of Petroleum Science and Engineering*, 152(March), 309–316.

- Elshehabi, T., & Bilgesu, I. (2015).** Impact of Drilling With Oil Based Mud on Well Control in Horizontal Shale Gas Wells.
- Fluent, A. (2013).** *Ansys Fluent Theory Guide*. ANSYS Inc., USA (Vol. 15317). USA: Ansys Inc.
- Galindo, K. A., Zha, W., Zhou, H., & Deville, J. P. (2015).** High Temperature, High Performance Water-Based Drilling Fluid for Extreme High Temperature Wells. In *SPE International Symposium on Oilfield Chemistry* (pp. 179–188). Texas, USA: Society of Petroleum Engineers.
- García-Ochoa, F., Santos, V. ., Casas, J. ., & Gómez, E. (2000).** Xanthan gum: production, recovery, and properties. *Biotechnology Advances*, 18(7), 549–579.
- Halali, M. A., Ghotbi, C., Tahmasbi, K., & Ghazanfari, M. H. (2016).** The Role of Carbon Nanotubes in Improving Thermal Stability of Polymeric Fluids: Experimental and Modeling. *Industrial & Engineering Chemistry Research*, 55(27), 7514–7534.
- Han, S.M., Hwang, Y.K., Woo, N.S., Kim, Y.J. (2010).** Solid–liquid hydrodynamics in a slim hole drilling annulus. *J. Pet. Sci. Eng.* 70, 308–319.
- Hu, Z., Haruna, M., Gao, H., Nourafkan, E., Wen, D., (2017).** Rheological Properties of Partially Hydrolyzed Polyacrylamide Seeded by Nanoparticles. *Ind. Eng. Chem. Res.* 56, 3456–3463.
- Hummers Jr., W. S., & Offeman, R. E. (1958).** Preparation of Graphitic Oxide. *Journal of the American Chemical Society*, 80(6), 1339–1339.
- Ii, E. H. H., & Thuriere, A. (2016).** Survey of Polyamines as Prospective Shale Stabilizers. *American Association of Drilling Engineers*, (April).
- Ismail, A.R., Aftab, A., Ibupoto, Z. H., & Zolkifile, N. (2016).** The novel approach for the enhancement of rheological properties of water-based

drilling fluids by using multi-walled carbon nanotube, nanosilica and glass beads. *Journal of Petroleum Science and Engineering*, 139, 264–275.

Ismail, Abdul Razak, Seong, T. C., Buang, N. A., & Wan Sulaiman, W. R. (2014). Improve Performance of Water-based Drilling Fluids Using NPs. *The 5th Sriwijaya International Seminar on Energy and Environmental Science & Technology*, (April), 1–5.

Javeri, S. M., Haindade, Z. W., & Jere, C. B. (2011). Mitigating loss circulation and differential sticking problems using silicon NPs. In *SPE/IADC Middle East Drilling Technology Conference and Exhibition*. Muscat, Oman.

Kang, Y., She, J., Zhang, H., You, L., & Song, M. (2016). Strengthening shale wellbore with silica NPs drilling fluid. *Elsevier*, 2(2), 189–195.

Khaled, S. M., & Hassan, Z. H. (2017). Improving the Drilling Fluid Performance by Alumina Oxide NPs. *International Advanced Research Journal in Science, Engineering and Technology*, 4(November), 195–199.

Kole, M., & Dey, T. K. (2013). Investigation of thermal conductivity, viscosity, and electrical conductivity of graphene based nanofluids. *Journal of Applied Physics*, 113(8).

Kosynkin, D. V, Ceriotti, G., Wilson, K. C., Lomeda, J. R., Scorsone, J. T., Patel, A. D., Tour, J. M. (2012). Graphene Oxide as a High-Performance Fluid-Loss-Control Additive in Water-Based Drilling Fluids. *ACS Applied Materials & Interfaces*, 4(1), 222–227.

Krishnakumar, B., Prasanna Sanka, R. V. S., Binder, W. H., Park, C., Jung, J., Parthasarthy, V., Yun, G. J. (2020). Catalyst free self-healable vitrimer/graphene oxide nanocomposites. *Composites Part B: Engineering*, 184(July 2019), 107647.

Kumar, A., Badoni, R.P., Singhal, S., Agarwal, S. and Tripathi, A.R., 2018. Synthesis and characterization of zirconia-based catalyst for the

isomerization of n-hexane. *Chem. Eng. Commun.* 205(1), 92–101.

Lahalih, S. M., Dairanieh, I. S., & Division, M. (1989). Development of novel polymeric drilling mud dispersants, 25(2), 187–192.

Leaper, R., Anderson, D., Dye, W., Hansen, N., Al Ansari, A., Foreman, D., & Yadav, K. (2007). Diverse Application of Unique High Performance Water Based Mud Technology in the Middle East. *SPE/IADC Middle East Drilling Technology Conference & Exhibition*.

Li, S., Osisanya, S., & Haroun, M. (2016). Development of New Smart Drilling Fluids Using Nano-Materials for Unconventional Reservoirs. In *SPE International Petroleum Exhibition & Conference*.

Lun, C. K. K., & Savage, S. B. (1987). A simple kinetic theory for granular flow of rough, inelastic, spherical particles. *Journal of Applied Mechanics*, 54(1), 47–53.

Mahto, V., & Sharma, V. P. (2004). Rheological study of a water based oil well drilling fluid. *Journal of Petroleum Science and Engineering*, 45(1–2), 123–128.

Malviya, N., Carpenter, G., Oswal, N., & Gupta, N. (2015). Synthesis and characterization of CuO nano particles using precipitation method. *American Institute of Physics*, 050038, 050038.

Mao, H., Qiu, Z., Shen, Z., Huang, W., Zhong, H., & Dai, W. (2014). Novel hydrophobic associated polymer based nano-silica composite with core-shell structure for intelligent drilling fluid under ultra-high temperature and ultra-high pressure. *Progress in Natural Science: Materials International*, 25(1), 90–93.

Mensah, A. E., & Mukhtah, A. (2016). Effect of AL₂O₃ NPs on the Rheological Properties of Water Based Mud. *International Journal of Science and Engineering Applications*, 5(1), 7–11.

- Mme, U., & Skalle, P. (2012).** CFD Calculations of Cuttings Transport through Drilling Annuli at Various Angles. *International Journal of Petroleum Science and Technology*, 6(2), 129–141.
- Mohammed, A. S. (2017).** Effect of temperature on the rheological properties with shear stress limit of iron oxide NPs modified bentonite drilling muds. *Egyptian Journal of Petroleum*, 26(3), 791–802.
- Moraga, F. J., Larretegui, A. E., Drew, D. A., & Lahey, R. T. (2003).** Assessment of turbulent dispersion models for bubbly flows in the low Stokes number limit. *International Journal of Multiphase Flow*, 29(4), 655–673.
- Nabhani, N., & Emami, M. (2012).** The potential impact of nanomaterials in oil drilling industry. In *Nanocon* (pp. 23–26). Brno, Czech Republic, EU.
- Peng, B., Tang, J., Luo, J., Wang, P., Ding, B., & Tam, K. C. (2018).** Applications of nanotechnology in oil and gas industry: progress and perspective. *The Canadian Journal of Chemical Engineering*, 96(1), 91–100.
- Pérez, R. M., Siquier, S., Ramírez, N., Müller, A. J., & Sáez, A. E. (2004).** Non-Newtonian annular vertical flow of sand suspensions in aqueous solutions of guar gum. *Journal of Petroleum Science and Engineering*, 44(3–4), 317–331.
- Ponmani, S., Nagarajan, R., & Sangwai, J. (2013).** Applications of nanotechnology for upstream oil and gas industry. *Journal of Nano Research*, 24, 7–15.
- Ponmani, S., Nagarajan, R., & Sangwai, J. S. (2016).** Effect of Nanofluids of CuO and ZnO in Polyethylene Glycol and Polyvinylpyrrolidone on the Thermal, Electrical, and Filtration-Loss Properties of Water-Based Drilling Fluids. *SPE Journal*, 21(2).
- Pourafshary, P., Azimpour, S. S., Motamedi, P., Samet, M., Taheri, S. A.,**

- Bargozin, H., & Hendi, S. S. (2009).** Priority assessment of investment in development of nanotechnology in upstream petroleum industry. In *SPE Saudi Arabia Section Technical Symposium*. AlKhobar, Saudi Arabia: Society of Petroleum Engineers.
- Power, D., & Zamora, M. (2003).** Drilling fluid yield stress: measurement techniques for improved understanding of critical drilling fluid parameters. *AADE-03 National Technology Conference "Practical Solutions for Drilling Challenges,"* 1–9.
- Ofei, T.N., Irawan, S., Pao, W. (2014).** CFD Method for Predicting Annular Pressure Losses and Cuttings Concentration in Eccentric Horizontal Wells. *J. Pet. Eng.* 2014, 1–16.
- Rahman, I. A., & Padavettan, V. (2012).** Synthesis of Silica NPs by Sol-Gel: Size-dependent properties, surface modification, and applications in silica-polymer nanocomposites a review. *Journal of Nanomaterials*, 2012.
- Sahoo, S. K., & Mallik, A. (2015).** Simple, Fast and Cost-Effective Electrochemical Synthesis of Few Layer Graphene Nanosheets. *Nano: Brief Reports and Reviews*, 10(02), 1550019.
- Sajjad, H., Farshad, F., & Zargar Ghassem. (2016).** The Study of Effective of Added Aluminum Oxide Nano Particles to the Drilling Fluid: The Evaluation of Two Synthesis Methods. *Journal of Petroleum & Environmental Biotechnology*, 7(3), 10–12.
- Salih, A. H., Elshehabi, T. A., & Bilgesu, H. I. (2016).** Impact of Nanomaterials on the Rheological and Filtration Properties of Water-Based Drilling Fluids. *SPE Eastern Regional Meeting*.
- Scherrer, P., & Debye, P. (1918).** Werk Übergeordnetes Werk. *Nachr. Ges. Wiss. Göttingen, Math.-Physik. Klasse*, 2, 101–120.
- Schiller, L., & Naumann, A. (1935).** A drag coefficient correlation. *Zeitschrift Des Vereins Deutscher Ingenieure*, 77, 318–320.

- Shakib, J. T., Kanani, V., & Pourafshary, P. (2016).** Nano-clays as additives for controlling filtration properties of water–bentonite suspensions. *Journal of Petroleum Science and Engineering*, 138, 257–264.
- Shaygan Nia, A., Rana, S., Döhler, D., Noirfalise, X., Belfiore, A., & Binder, W. H. (2014).** Click chemistry promoted by graphene supported copper nanomaterials. *Chem. Commun.*, 50(97), 15374–15377.
- Sidik, N. A. C., Mohammed, H. A., Alawi, O. A., & Samion, S. (2014).** A review on preparation methods and challenges of nanofluids. *International Communications in Heat and Mass Transfer*.
- Srivatsa, J. T., & Ziaja, M. B. (2012).** An experimental investigation on use of NPs as fluid loss additives in a surfactant - polymer based drilling fluid. In *International Petroleum Technology Conference* (Vol. 3, pp. 2436–2454). Bangkok, Thailand.
- Syamlal, M., & O'Brien, T. J. (1988).** Computer simulation of bubbles in a fluidized bed. *International Journal of Multiphase Flow*, 14(4), 473–481.
- Vryzas, Z., Mahmoud, O., Nasr-El-Din, H., Zaspalis, V., & Kelessidis, V. C. (2016).** Incorporation of Fe₃O₄ NPs as Drilling Fluid Additives for Improved Drilling Operations. In *Volume 8: Polar and Arctic Sciences and Technology; Petroleum Technology* (Vol. 8, pp. 1–10). American Society of Mechanical Engineers.
- Wan, T., Zang, T. S., Wang, Y. C., Zhang, R., & Sun, X. C. (2010).** Preparation of water soluble Am-AA-SSS copolymers by inverse microemulsion polymerization. *Polymer Bulletin*, 65(6), 565–576.
- William, J. K. M., Ponmani, S., Samuel, R., Nagarajan, R., & Sangwai, J. S. (2014).** Effect of CuO and ZnO nanofluids in xanthan gum on thermal, electrical and high pressure rheology of water-based drilling fluids. *Journal of Petroleum Science and Engineering*, 117, 15–27.
- Wong, K. V., & De Leon, O. (2010).** Applications of nanofluids: current and

future. *Advances in Mechanical Engineering*, 2, 519659.

Xie, G., Deng, M. Y., Su, J. L., & Pu, L. C. (2013). Study on Shale Gas Drilling Fluids Technology. *Advanced Materials Research*, 868, 651–656.

Yang, X., Yue, Y., Cai, J., Liu, Y., & Wu, X. (2015). Experimental study and stabilization mechanisms of silica NPs based brine mud with high temperature resistance for horizontal shale gas wells. *Journal of Nanomaterials*, 2015, 1–9.